A Search for Physics Beyond the Standard Model using Like-Sign Muon Pairs in pp Collisions at $\sqrt{s} = 7$ TeV with the ATLAS Detector

by

Louise Anastasia Skinnari

A dissertation submitted in partial satisfaction of the

requirements for the degree of

Doctor of Philosophy

in

Physics

in the

Graduate Division

of the

University of California, Berkeley

Committee in charge:

Professor Beate H. E. Heinemann, Chair

Professor Robert G. Jacobsen

Professor Eric B. Norman

Fall 2012

A Search for Physics Beyond the Standard Model using Like-Sign Muon Pairs in pp Collisions at $\sqrt{s} = 7$ TeV with the ATLAS Detector

Louise Anastasia Skinnari

Abstract

A Search for Physics Beyond the Standard Model using Like-Sign Muon Pairs in pp Collisions at $\sqrt{s} = 7$ TeV with the ATLAS Detector

by

Louise Anastasia Skinnari

Doctor of Philosophy in Physics

University of California, Berkeley

Professor Beate H. E. Heinemann, Chair

This dissertation presents a search for physics beyond the Standard Model using pairs of muons with equal electric charge. The search is performed in a proton-proton collision data sample collected during 2011 at $\sqrt{s} = 7$ TeV by the ATLAS experiment at the Large Hadron Collider. The total data sample corresponds to an integrated luminosity of 4.7 fb^{-1}. Events are selected by requiring pairs of prompt and isolated like-sign muons with transverse momentum greater than 20 GeV. The observed dimuon invariant mass distribution is compared to the Standard Model expectation, searching for any deviation between the observed and predicted yields. No evidence for an excess beyond the Standard Model expectation is observed. The results are interpreted as inclusive cross-section limits on the production of like-sign muon pairs from non-Standard Model sources as function of the dimuon invariant mass. The cross-section limits range between 30 fb and 1.2 fb. The data sample is also searched for a new narrow resonance which decays to like-sign muon pairs. No evidence for such resonant production is observed and the results are interpreted as upper limits on the mass and production cross section of doubly charged Higgs bosons. Assuming pair-production and a 100% branching ratio to muons, masses below 398 GeV (306 GeV) are excluded assuming coupling to left-handed (right-handed) fermions.

Contents

List of Figures

List of Tables

Acknowledgments

Many people have in various ways contributed to the analysis described in this dissertation as well as to my graduate studies over the past years. First and foremost, my research advisor Beate Heinemann. I am incredibly grateful for having had the opportunity to work with and to learn from her. Not only an excellent physicist, but also the most inspiring one I know. Countless times I have found myself stuck or unmotivated, Beate always cured that with her knowledge, enthusiasm, and advice, any time I needed it. Thank you!

Martina Hurwitz has been crucial in making the like-sign dimuon analysis happen, from preparing the first results in 2011 to the final publications in Fall 2012. I learned a lot from her way of approaching a problem, always seeing the broader context and the real questions to be addressed. She is most certainly also the postdoc I have bugged the most over the years... Thanks for all the help and patience!

The like-sign dimuon analysis was carried out jointly with the electron-based channels. Thanks to the other like-sign dilepton people: Else Lytken, Dominick Olivito, Kenji Hamano (special thanks for limit-running!), Nicholas Rodd (special thanks for fiducial efficiencies!), and Anthony Hawkins. Special thanks to Jean-Francois Arguin for all his help and guidance. Both for always being willing to chat about physics and for his major and important contributions in making the like-sign analysis converge.

I want to thank Karl Jacobs, Marjorie Shapiro, and Zach Marshall for carefully reviewing our conference notes and papers, and my committee members at Berkeley, Bob Jacobsen and Eric Norman, for reviewing this dissertation.

I want to send a wider thank-you to the Berkeley-LBL ATLAS group. Since I first started with the group as an undergraduate, many former and current group members have taught me about everything from the details of our detector and software particularities, to how to carry out a successful physics analysis. I learned about the inner detector alignment from Shih-Chieh Hsu, who was always accessible to answer questions regardless of the time of the day. The older generation of students and numerous postdocs, including Lauren, Max, Seth, Andrei, Mark, Dimitris, Mike, Andreas, have helped me with everything from getting PDSF to work to advice on job applications. And to my fellow grad students, Andre with whom I shared an office for many years and David for reading parts of this dissertation, thanks! I want to also especially thank Marjorie Shapiro, partly responsible for me coming to Berkeley in the first place, for the careful review of the analysis and always being happy to share her wisdom of the field.

Lastly, thanks to my friends around the world for always being there. To Jonathan, for all your support throughout graduate school, and for always making me laugh. Sist men inte minst vill jag riktigt ett stort tack till min familj, inte minst till mamma och pappa. Tack för att ni alltid stöttat mig och uppmuntrat mig att göra vad jag drömt om!

Chapter 1

Introduction

The Standard Model of particle physics describes known elementary particles and their interactions. It has had remarkable success in explaining experimental data and has repeatedly held up to precision tests since its first formulation in the 1970s. Despite its success, many questions about our universe remain unanswered. For instance, the Standard Model does not account for observed non-zero neutrino masses nor does it provide a candidate for the constituent of dark matter.

The Large Hadron Collider (LHC) [8] and its associated experiments enable precision studies of the Standard Model as well as opportunities to probe and discover, or constrain, new physics phenomena. Since its start at a center-of-mass energy of 7 TeV in 2010, the LHC has performed remarkably well and delivered a proton-proton collision dataset of about 5 fb^{-1} in 2011 and over 20 fb^{-1} in 2012. ATLAS [4] is one of two large general-purpose experiments which were designed and constructed specifically to study these high-energy collisions. The LHC is designed to be a discovery machine and there are many reasons to believe that new physics resides within its energy reach. This dissertation probes some of the new physics phenomena which may be present at the TeV-scale.

The search described in this dissertation uses the 2011 ATLAS proton-proton (pp) collision dataset. Events containing two muons, the heavier cousin of the electron, with the same electric charge are identified and selected. Final states with pairs of *like-sign* muons is a prime search channel for new physics phenomena thanks to its low expected background from Standard Model sources since at the same time, many models of physics *beyond* the Standard Model predict an enhanced rate of such production. The search is designed to be as model-independent as possible, not targeting one particular model but instead being sensitive to a broad range of possible new physics scenarios producing like-sign muons.

The results of the like-sign dimuon search described in this dissertation are separated into two interpretations. The data is first searched for any excess beyond the Standard Model predictions, the *inclusive* search. Secondly, the data is searched for a *narrow resonance* decaying to pairs of like-sign muons using the same event selection

criteria and background estimates. The inclusive and the narrow resonance search in the like-sign dimuon final state were performed jointly with similar searches in final states containing pairs of electrons, or pairs of one electron and one muon, with the same electric charge. Both the inclusive and the narrow resonance search have been accepted for publication [10, 11]. A previous version of the analysis, performed in a smaller data sample of 1.6 fb^{-1}, was published using the like-sign dimuon final state [12].

This dissertation is organized as follows. Chapter 2 provides the theoretical background and motivation for the search. Examples of models of beyond the Standard Model physics, to which this search may be sensitive, are discussed. In particular, models producing doubly charged Higgs bosons are described. In Chapter 3, the details of the LHC and the ATLAS experiment are described. The general search strategy is explained in Chapter 4. The reconstruction of physics objects in the detector, such as muons, are discussed in Chapter 5. Chapter 6 presents studies of the alignment of the ATLAS inner tracking system. Chapter 7 describes the data sample and the event selection criteria used to identify the search signal region. Chapter 8 provides detailed descriptions of the different background sources and the techniques used to estimate their contribution to the signal region. Data control regions used to verify the background modeling are also shown. The systematic uncertainties affecting the background estimate and the signal acceptance are discussed in Chapter 9. Chapter 10 provides the results of the inclusive like-sign dimuon search. Chapter 11 similarly provides the results of the narrow resonance search. Finally, conclusions are given in Chapter 12.

Chapter 2

Theoretical Motivation

The Standard Model (SM), which describes elementary particles and their interactions, is a successful theory which has been tested experimentally to high precision over the past decades. There are, however, strong arguments for why the Standard Model cannot be the ultimate theory of nature. A wide range of new physics models has been invented over the years to address the shortcomings of the Standard Model. Some of these models predict final states with like-sign dileptons as an experimental signature, which forms the basis of the search described in this dissertation. This chapter reviews the theoretical background and presents the motivation for the search. The Standard Model is briefly discussed together with its shortcomings and resulting need for beyond the SM physics. Examples are given of new physics models which can be experimentally probed through searches for like-sign dileptons. Specifically, models producing doubly charged Higgs bosons, causing a narrow like-sign resonance, are discussed.

2.1 The Standard Model of Particle Physics

Elementary particles in the Standard Model are divided into spin-1/2 matter particles (*leptons* and *quarks*) and spin-1 force carriers (*gauge bosons*). Leptons are further divided into electrically charged and neutral leptons. The charged leptons include the electron (e), muon (μ), and tau (τ) while the neutral leptons are the three nearly massless neutrinos (ν_e, ν_μ, ν_τ)[1]. Quarks are categorized based on their electric charge as up-type ($Q = +2/3e$) and down-type ($Q = -1/3e$) quarks. The up-type quarks include the up (u), charm (c), and top (t) quarks while the down-type quarks include the down (d), strange (s), and bottom (b) quarks. All matter particles are organized into three generations as ($e\ \nu_e, u\ d$), ($\mu\ \nu_\mu, c\ s$), and ($\tau\ \nu_\tau, t\ b$). The only distinction between the generations is an increasing particle mass.

[1]The fact that neutrinos have mass, albeit small, is important in its own. Neutrino masses were not incorporated in the initial formulation of the Standard Model, as will be discussed later.

The Standard Model incorporates three of the four fundamental interactions of nature: the electromagnetic, weak, and strong interactions. The fundamental interactions are in the Standard Model mediated by gauge bosons. The neutral and massless photon (γ) is responsible for the electromagnetic interaction, acting between all electrically charged leptons and quarks. The heavy $W^{\pm}$ and Z^0 bosons mediate the weak interaction which affects both neutral and charged particles. Eight massless gluons (g) which are electrically neutral but carry *color charge* are responsible for the strong interaction. Unlike leptons, quarks have color charge, allowing them to interact through the strong interaction in addition to the electromagnetic and weak interactions.

The final particle in the Standard Model is the Higgs boson, a neutral scalar particle which is necessary to give mass to the heavy gauge bosons. A *Higgs-like* particle was discovered by the ATLAS and CMS Collaborations in July 2012 around a mass of 125–126 GeV [13, 14]. At time of writing[2], it is yet to be determined whether this particle is indeed consistent with the postulated and long-sought SM Higgs boson.

The particle content of the Standard Model is summarized in Table 2.1. In addition to the listed particles, charged leptons, quarks, and the charged gauge bosons have associated antiparticles with opposite electric charge, nearly doubling the particle content. The neutral gauge bosons are their own antiparticles[3]. Throughout this dissertation, the convention $c = \hbar = 1$ is used, resulting in that masses and momenta are measure in units of energy (eV).

2.1.1 Theoretical Formulation

This section gives a summary of the most important concepts in the theoretical formulation of the Standard Model, necessary for the later discussions of models of beyond the SM physics. Complete descriptions can be found elsewhere, see for instance Refs. [15], [16], or [7] from which information in this section were collected unless explicitly stated otherwise.

The Standard Model describes the electromagnetic, weak, and strong interactions as *gauge theories*. Gauge theories are quantum field theories for which the descriptive Lagrangian is invariant under some set of local transformations. These transformations, known as gauge transformations, form a symmetry group of the theory. Gauge fields emerge in the Lagrangian from requiring its invariance under local gauge transformations. For quantized theories, the quanta of the gauge fields are the gauge bosons.

The Standard Model is a non-Abelian gauge theory, meaning that its symmetry

[2] November 2012.

[3] It is not yet established whether neutrinos are their own antiparticles.

Type	Name	Mass	Charge [e]
LEPTONS (spin=1/2)	electron (e)	0.511 MeV	-1
	electron neutrino (ν_e)	< 2 eV	0
	muon (μ)	106 MeV	-1
	muon neutrino (ν_μ)	< 0.19 MeV	0
	tau (τ)	1.78 GeV	-1
	tau neutrino (ν_τ)	< 18.2 MeV	0
QUARKS (spin=1/2)	up (u)	2.3 MeV	+2/3
	down (d)	4.8 MeV	-1/3
	charm (c)	1.28 GeV	+2/3
	strange (s)	95 MeV	-1/3
	top (t)	174 GeV	+2/3
	bottom (b)	4.18 GeV	-1/3
GAUGE BOSONS (spin=1)	photon (γ)	0	0
	$W^\pm$	80.4 GeV	± 1
	Z^0	91.2 GeV	0
	gluons (g)	0	0
HIGGS BOSON (spin=0)	Higgs (H)	$\sim$125–126 GeV?	0

Table 2.1: Summary of the particle content of the Standard Model, including their mass, spin, and electric charge [7]. The existence of the Higgs boson as predicted within the Standard Model is yet to be confirmed experimentally.

group is non-commutative. The Standard Model symmetry group is

$$SU(3)_C \otimes SU(2)_L \otimes U(1)_Y. \tag{2.1}$$

$SU(3)_C$ is the symmetry group of the strong interaction with C being the associated conserved quantum number (color). $SU(2)_L \otimes U(1)_Y$ describes the electroweak interaction, which unites the electromagnetic and weak interactions, with L indicating left-handed helicity and Y being the hypercharge.

The Strong Interaction

The strong interaction between quarks and gluons is characterized by *Quantum Chromodynamics* (QCD). It is as an $SU(3)$ gauge theory which is invariant under local color transformations. The different color charges are typically referred to as blue, green, and red (or antiblue, antigreen, and antired). The local invariance of the governing Lagrangian is maintained by introducing eight gauge fields. These gauge fields correspond to the eight massless gluons which mediate the strong interaction. Gluons themselves carry color charge and therefore interact with quarks as well as with other gluons.

An important property of the strong interaction is the strength of its coupling constant (α_s). Despite the name, α_s is not constant but depends on the energy scale of the interaction, more specifically, on the momentum transfer Q involved in a process. To first order, the strong coupling constant decreases with energy as

$$\alpha_s(Q^2) \sim \frac{1}{\ln(\mathrm{Q}^2/\Lambda)}, \tag{2.2}$$

where Λ is the non-perturbative scale of QCD.

The energy dependence of the strong coupling constant has two important consequences: *asymptotic freedom* and *confinement*. The concept of asymptotic freedom entails the decreased interaction strength with increasing energy, resulting in that at high energies, quarks and gluons can effectively be treated as free particles. Related is the concept of confinement, resulting from an increased interaction strength with increased particle separation. The consequence is that color-charged particles such as quarks and gluons cannot exist as free particles but are confined within color-neutral hadrons, formed from two or three quarks. Hadrons can either be mesons, formed from quark-antiquark pairs in a color state of e.g. blue plus antiblue, or baryons, formed from three quarks where each quark have a different color, also resulting in a color-neutral state.

At the high energies of hadron colliders such as the LHC, quarks and gluons can be treated as free particles in interactions involving large momentum transfers. Quarks and gluons produced in the interactions will, however, due to confinement not appear as free particles in the detector. Instead, they appear as collections of

stable hadrons, known as *jets*. The process of forming hadrons from the initial quarks and gluons is called hadronization. It should be mentioned that although the strong interaction and asymptotic freedom is theoretically well described, the details of its consequences such as confinement of quarks and gluons is not fully understood. The process of hadronization is similarly not a theoretically well-characterized process.

The Electroweak Interaction

The electromagnetic interaction, which acts on all charged particles and is mediated by the photon, is described within *Quantum Electrodynamics (QED)*. The weak interaction is mediated by the $W^{\pm}$ and Z^0 bosons and acts between quarks, charged leptons, and neutral leptons. The weak interaction also allows flavor-changing transitions of quarks and leptons. Although a first theory for weak interactions was formed in the 1930s by Enrico Fermi, a successful description at both low and high energies did not exist until Glashow, Salam, and Weinberg in the 1960s developed the theory of the electroweak interaction, in which the electromagnetic and weak forces are unified.

The electroweak interaction is described by the $SU(2)_L \otimes U(1)_Y$ gauge group. The $U(1)_Y$ group has one associated gauge field, B_μ, and its conserved quantum number is the hypercharge Y. The $SU(2)_L$ group has three gauge fields, A^a_μ $(a = 1, 2, 3)$, and the conserved quantity is the weak isospin T. The coupling parameters of the $SU(2)_L$ and the $U(1)_Y$ gauge groups are denoted g and g', respectively.

Electrically charged fermions occur in both left-handed and right-handed states. The subscript L in $SU(2)_L$ denotes left-handed helicity, indicating that the weak interaction distinguishes between left-handed and right-handed states. Only left-handed fermions (right-handed antifermions) interact with the $SU(2)_L$ gauge fields. The left-handed states are organized in $SU(2)$ doublets, while the right-handed states are singlets, as shown in Table 2.2. There are no right-handed neutrinos in the Standard Model.

The gauge fields of the $SU(2)_L \otimes U(1)_Y$ group, B_μ and A^a_μ, do not represent any physical states. The problem is that in an unbroken gauge theory, all gauge bosons are massless due to gauge invariance. Within QED and QCD, the photon and the gluons are indeed massless. However, the gauge bosons associated with the weak interaction are massive and to give them mass, the symmetry must be broken. Simply adding a mass term for the gauge bosons to the Lagrangian will lead to a non-renormalizable theory. In the Standard Model, the symmetry is instead broken through *spontaneous symmetry breaking*. With spontaneous symmetry breaking, the Lagrangian remains invariant while the lowest energy state, the vacuum, is not invariant under the gauge symmetry.

Spontaneous electroweak symmetry breaking in the Standard Model is governed by the Higgs mechanism. Briefly stated, an additional complex scalar field (ϕ) in an $SU(2)$ representation is introduced. The scalar field is governed by a Lagrangian

Generation			Quantum numbers		
I	II	III	Q	T	T_3
$\begin{pmatrix} e \\ \nu_e \end{pmatrix}_L$	$\begin{pmatrix} \mu \\ \nu_\mu \end{pmatrix}_L$	$\begin{pmatrix} \tau \\ \nu_\tau \end{pmatrix}_L$	0 -1	$1/2$	$+1/2$ $-1/2$
e_R	μ_R	τ_R	-1	0	0
$\begin{pmatrix} u \\ d \end{pmatrix}_L$	$\begin{pmatrix} c \\ s \end{pmatrix}_L$	$\begin{pmatrix} t \\ b \end{pmatrix}_L$	$+2/3$ $-1/3$	$1/2$	$+1/2$ $-1/2$
u_R	c_R	t_R	$+2/3$	0	0
d_R	s_R	b_R	$-1/3$	0	0

Table 2.2: Left-handed and right-handed fermions together with their charge (Q), hypercharge (T), and third component of the hypercharge (T_3).

density with a global $U(1)$ gauge symmetry. The symmetry breaking occurs as the field ϕ acquires a vacuum expectation value (*vev*)

$$\langle \phi \rangle = \frac{1}{\sqrt{2}} \begin{pmatrix} 0 \\ v \end{pmatrix}. \tag{2.3}$$

Once the *Higgs field* acquires a vev, the gauge bosons gain mass through interactions with the Higgs field. There are now three vector fields representing massive gauge bosons, $W_\mu^\pm$ and Z_μ^0, and a fourth vector field, A_μ, orthogonal to Z_μ^0 which remains massless and is interpreted as the photon

$$\begin{aligned} W_\mu^\pm &= \frac{1}{\sqrt{2}}(A_\mu^1 \mp i A_\mu^2) \quad \text{with mass} \quad m_W = g\frac{v}{2}, \\ Z_\mu^0 &= \frac{1}{\sqrt{g^2+g'^2}}(gA_\mu^3 - g'B_\mu) \quad \text{with mass} \quad m_Z = \sqrt{g^2+g'^2}\frac{v}{2}, \\ A_\mu &= \frac{1}{\sqrt{g^2+g'^2}}(g'A_\mu^3 + gB_\mu) \quad \text{with mass} \quad m_A = 0. \end{aligned} \tag{2.4}$$

The Higgs mechanism provides mass to quarks and charged leptons in a similar procedure.

The *weak mixing angle* θ_w is introduced to relate the states (A^3, B) to the physical mass states (Z^0, A). It is defined as

$$\sin(\theta_w) = \frac{g'}{\sqrt{g^2+g'^2}}. \tag{2.5}$$

At tree-level, the $W^{\pm}$ and Z^0 boson masses are furthermore related as

$$m_W = m_Z \cos(\theta_w). \tag{2.6}$$

The complex scalar field doublet which is added to the SM Lagrangian can be written in terms of four real scalar fields. Three of the fields are absorbed to generate mass to the heavy gauge bosons while the fourth emerges as a new massive scalar boson, the *Higgs boson*. The mass of the Higgs boson is not predicted by the theory and it remains the one missing particle of the Standard Model which is yet to be experimentally verified. As mentioned earlier, a Higgs-like particle was discovered by the ATLAS and CMS Collaborations in 2012 around a mass of 125–126 GeV [13, 14]. This particle is an even-spin boson since it decays into two photons. However, it is yet to be determined whether the discovered particle indeed has spin-0 as the SM Higgs boson and whether its coupling parameters and other properties are consistent with that predicted by the theory.

2.1.2 Limitations of the Standard Model

The Standard Model has been a highly successfully theory, explaining and predicting experimental data. The theory predicted, for instance, the existence and the masses of the W and Z bosons before they were discovered in 1983 [17, 18]. Electroweak precision measurements have consistently confirmed the validity of the model. Despite its success, there are numerous shortcomings to the Standard Model which indicate that it is only a low-energy approximation of an underlying more fundamental theory.

One immediate limitation of the Standard Model as a complete theory of all elementary particles and interactions is its lack of incorporating the gravitational force. Gravity, described by Einstein's general relativity, is negligible at the distance scales studied in elementary particle physics. Attempts have been made to incorporate gravity at quantum level into the Standard Model, so far without success.

In the initial formulation of the Standard Model, neutrinos are massless particles. The discovery of neutrino oscillations [19] provided experimental evidence of non-zero neutrino masses. Massive neutrinos can be incorporated into the Standard Model by adding right-handed neutrino states, in which case neutrinos are *Dirac* neutrinos. The drawback of simply introducing right-handed states to create neutrino mass terms is that the tiny neutrino masses imply extremely weak (*unnatural?*) couplings. If neutrinos instead are their own antiparticles, then known as *Majorana* neutrinos, mass terms can be incorporated by introducing a seesaw mechanism. The seesaw mechanism explains the smallness of neutrino masses through mixing with an additional very heavy neutrino N ($m_N >> m_W$), so that $m_\nu \sim m_D^2/m_N$, where m_ν is the mass of the SM light neutrino and m_D is the Dirac mass of charged fermions of the same generation as the neutrino. As the Standard Model currently stands, it is not yet un-

derstood why neutrinos are so incredibly light compared to other elementary particles and what the mechanism is behind neutrino masses.

Quarks and leptons are divided into three generations, but why are there *three* generations? The number of generations is not predicted by the Standard Model, nor is an explanation for the mass hierarchy between the generations given. Could an additional fourth generation exist? Precision measurements of the Z boson *invisible* decay width from collider experiments only prohibits the existence of a fourth generation with neutrino masses $m_\nu < m_Z/2$.

Another question for which the Standard Model does not provide an answer is what causes the apparent matter/antimatter asymmetry observed in the universe. There is no source in the Standard Model of charge-parity (CP) violation which is strong enough to explain the asymmetry (see e.g. Ref. [7]).

From cosmological studies it is well established that the ordinary matter in the universe is not sufficient to explain the total observed mass. On the contrary, ordinary matter only constitutes about 5% of the total energy in the universe. Another 20% is due to *dark matter* [20]. There is clear experimental evidence for the existence of dark matter in the universe, for instance from studies of galaxy rotations, but *what* is dark matter? There is no viable dark matter candidate in the Standard Model. The combination of ordinary matter and dark matter still only constitutes a small fraction of the total energy in the universe. The remaining 75% is called *dark energy*, causing the expansion of the universe to accelerate [21, 22].

Questions also remain about the nature of electroweak symmetry breaking. If the recently discovered Higgs-like particle is *not* consistent with that expected from the SM Higgs boson, then what is it? Do multiple Higgs bosons and charged Higgs bosons exist? The mechanism of electroweak symmetry breaking is in itself related to a particularly severe problem with the Standard Model from a theoretical point-of-view: the *hierarchy problem*. The basis of the hierarchy problem is that in the Standard Model, the Higgs boson mass is the sum of its tree-level (*bare*) mass and quadratically divergent quantum loop corrections

$$M_H^2 = (M_H^2)_{\text{bare}} + O(\lambda_f)\Lambda, \tag{2.7}$$

where λ_f is the coupling constant to a fermion f (the largest corrections are due to top-quark loops) and Λ is interpreted as the next higher scale above which the Standard Model is no longer valid. If the next scale is that of gravity, then Λ is taken as the Planck scale $M_P \sim 10^{19}$ GeV. To then keep the Higgs mass (m_H) at the weak scale $\mathcal{O}(100)$ GeV, two large numbers must cancel to an extremely high precision. Such *fine-tuning* is considered highly unnatural [23, 24].

2.2 Physics Beyond the Standard Model

In addition to the motivation for the need of physics beyond the Standard Model, there is reason to expect new phenomena to reside around the TeV-scale [25], i.e. within the energy reach of the LHC. Many of the SM shortcomings point specifically towards the weak scale, such as the hierarchy problem. This section briefly discusses some frameworks of beyond the SM physics which can lead to experimental signatures involving pairs of like-sign leptons to which the described search may be sensitive.

2.2.1 Supersymmetry

One of the theoretically most established and well-motivated frameworks of physics beyond the Standard Model is *supersymmetry*. Supersymmetry was first formulated within four-dimensional space-time by Wess and Zumino in 1974 [26] and has since then developed as a theoretical framework. The *minimal* supersymmetric extension of the Standard Model (MSSM) was proposed in 1981 to solve the hierarchy problem [27], although there are today many incarnations of supersymmetry.

Supersymmetry introduces a supersymmetric partner to all Standard Model particles which differ by 1/2 in spin. The SM spin-1/2 fermions, quarks and leptons, receive spin-0 bosonic partners, *squarks* ($\tilde{q}$) and *sleptons* ($\tilde{l}$). Fermionic partners are similarly added to the SM gauge bosons. The supersymmetric partners of the gluons are known as *gluinos* ($\tilde{g}$) while the partners of the electroweak gauge bosons are *winos* ($\tilde{W^{\pm}}$, $\tilde{W^{0}}$) and *bino* ($\tilde{B^{0}}$). In supersymmetry, two Higgs doublets are required to give mass to all fermions. The Higgs bosons also have supersymmetric partners, *higgsinos*. The effects of electroweak symmetry breaking cause the higgsinos and gauginos to mix. The formed mass eigenstates are neutralinos ($\tilde{\chi_i^0}$), formed from mixing the neutral higgsinos and neutral gauginos, and charginos ($\tilde{\chi_i^{\pm}}$), formed from the charged higgsinos and winos. Since no supersymmetric partners to the SM particles of the same mass have been observed, the symmetry must be broken to cause a mass splitting.

Supersymmetry has potential of addressing several SM shortcomings. The hierarchy problem is solved by stabilizing the Higgs mass to radiative corrections. In introducing supersymmetric boson partners to the SM fermions, additional loop corrections to the Higgs boson mass are added. The largest SM loop corrections originate from the top quark. Its partner the *stop* will now contribute to the Higgs mass and to first order cancel the contribution from the top quark. The Feynman diagrams for the one-loop corrections are shown in Figure 2.1. To solve the hierarchy problem without any significant fine-tuning, the stop squark must not be much heavier than the top quark.

Supersymmetry may also provide a dark matter candidate. In supersymmetry, baryon numbers and lepton numbers are no longer conserved quantities. Since their conservations have been tested to very high precision, the concept of matter parity,

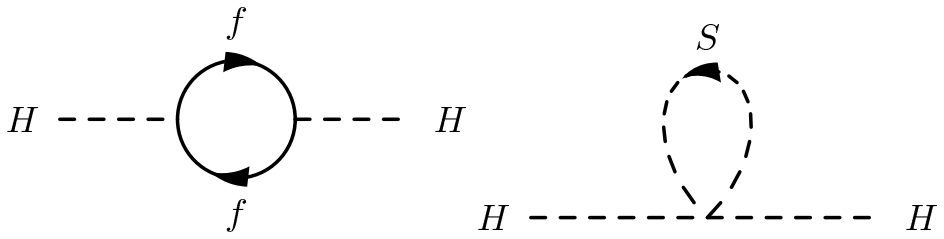

Figure 2.1: Feynman diagrams showing the one-loop corrections to the Higgs mass from a fermion f and a scalar S.

or *R-parity*, is introduced[4]. R-parity is defined as

$$R = (-1)^{3(B-L)+2s} \tag{2.8}$$

where B is the baryon number, L the lepton number, and s the spin. If R-parity is conserved, supersymmetric particles must be pair-produced and the lightest one cannot decay. The lightest supersymmetric particle may be a candidate for dark matter.

A third important motivation for supersymmetry is the possibility of gauge coupling unification. If the supersymmetric particles have mass around the TeV-scale, the gauge couplings of the three gauge groups ($U(1)$, $SU(2)$, and $SU(3)$) unify at high energies ($\sim 10^{16}$ GeV) due to the added particle content which modifies the "running" of the gauge couplings. In the Standard Model, the gauge couplings do not possess this convergence.

Like-sign dileptons constitute a powerful experimental search channel for discovering supersymmetry [28]. Events containing like-sign dileptons may be produced for instance through cascade decays of pair-produced gluinos or from direct gaugino production. Examples of like-sign dilepton production through gluino pair-production, decaying to stop-top quark pairs, and direct production of a chargino and a neutralino are illustrated in Figure 2.2.

2.2.2 Doubly Charged Higgs Bosons

Electroweak symmetry breaking as described within the Standard Model involves only one complex Higgs doublet and thus one physical, neutral Higgs boson. Other scenarios may be considered, involving multiple Higgs doublets, Higgs triplets, or other configurations with neutral and/or charged Higgs bosons. In this dissertation, the production of doubly charged Higgs ($H^{\pm\pm}$)[5] bosons is considered, predicted in several models of beyond the SM physics.

[4] A theory without baryon number constraints could result in a short-lived proton, clearly in contrast to observation. Such a theory is not viable.

[5] Among theorists, the notation $\Delta^{\pm\pm}$ is typically used instead.

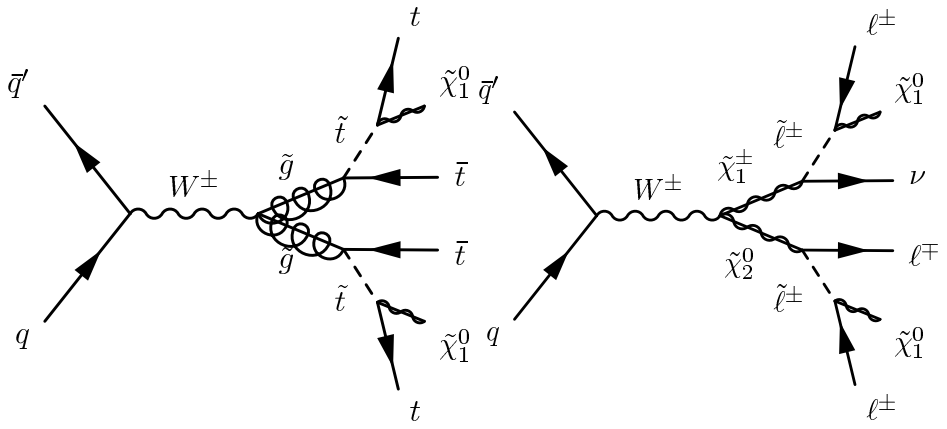

Figure 2.2: Feynman diagrams illustrating like-sign dilepton production through gluino pair production if two top quarks decay leptonically (left) and direct gaugino production (right).

Any theory involving a more intricate Higgs sector must fulfill stringent requirements from experimental observations. Models involving Higgs triplets must be designed to maintain $\rho \equiv m_W^2/[\cos^2\theta_w m_Z^2] = 1$. For models involving only doublets, as the SM Higgs mechanism, this occurs naturally at tree-level. For a Higgs triplet representation, it results in constraints on the vev of the neutral member of the triplet. Other constraints include the absence of flavor-changing neutral currents [29, 30].

At the LHC, doubly charged Higgs bosons can be produced through pair-production via the Drell-Yan process or associate production with a singly-charged Higgs boson. The Feynman diagrams for these processes are shown in Figure 2.3. As the cross section of associate production depends on the mass of the singly-charged boson, which is generally unknown, this search considers only the pair-production process. An additional production mode could be single production through WW fusion. However, such production is typically absent due to the theoretical constraints discussed above [30]. Similarly, decays of $H^{\pm\pm}$ bosons to pairs of W bosons may be suppressed. The branching ratio of lepton flavor violating decay modes, $H^{\pm\pm} \to \ell^{\pm}\ell^{\pm}$, may instead be large. Such decays give rise to the experimentally striking signature of a narrow like-sign dilepton resonance.

The narrow like-sign resonance search described in this dissertation is interpreted within the left-right symmetric model [31, 32, 33, 34]. The presence of Higgs triplets is not, however, limited to left-right symmetric models. Models exist with only one Higgs triplet [35, 36, 37], where the couplings may differ compared to the left-right symmetric model but the phenomenology affecting this search is otherwise unchanged. Doubly charged Higgs bosons also occur within the little Higgs model, a model which predicts the Higgs boson as a pseudo-Goldstone boson of an approximate broken symmetry [38]. Finally, a doubly charged boson can occur as a singlet as proposed

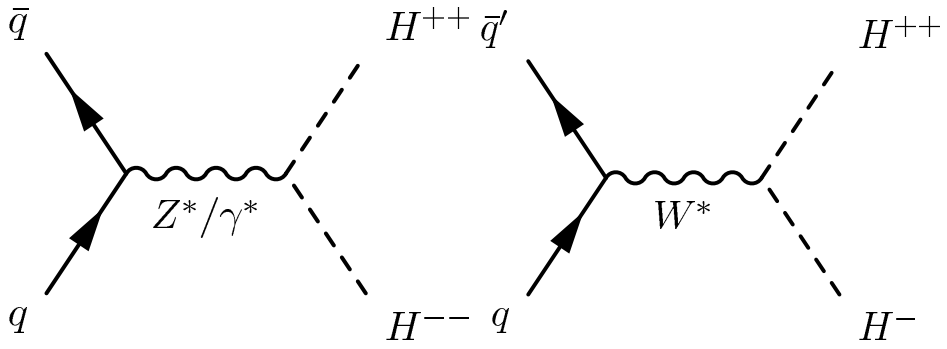

Figure 2.3: Feynman diagrams showing pair production of doubly charged Higgs bosons (left) and associated production involving a singly-charged state (right).

within the Zee-Babu model [39, 40, 41].

Left-Right Symmetric Model

The left-right symmetric model (LRSM) introduces an additional right-handed symmetry, $SU(2)_R$, to the Standard Model Lagrangian at a scale well above the electroweak symmetry breaking scale. The modified symmetry group is expressed as

$$SU(3)_C \otimes SU(2)_L \otimes SU(2)_R \otimes U(1)_{B-L}, \tag{2.9}$$

which conserves the quantity $(B - L)$, where B is baryon number and L lepton number. The model results in additional right-handed gauge bosons (Z_R^0 and $W_R^\pm$) as well as right-handed neutrinos (ν_R).

Within LRSM, the Higgs fields are described in a triplet representation with separate triplets coupling to left-handed and right-handed fermions. This results in the presence of two doubly charged Higgs bosons, one which couple to left-handed fermions ($H_L^{\pm\pm}$) and one to right-handed fermions ($H_R^{\pm\pm}$). The model predicts singly-charged and neutral Higgs bosons as well. Masses are generated to the neutrinos at tree-level through a type-II seesaw mechanism[6] [43, 44, 45, 46]. The constraint of keeping $\rho = m_W^2/[\cos^2\theta_w m_Z^2]$ to unity is maintained by assigning a very small vev to the neutral member of the left-handed triplet.

This search considers the pair-production process of doubly charged Higgs bosons. The cross sections depend only on the masses of the $H^{\pm\pm}$ bosons and the electroweak quantum numbers [47]. The cross section for $pp \to H_L^{\pm\pm}H_L^{\mp\mp}$ is about 2.5 times higher than that for $pp \to H_R^{\pm\pm}H_R^{\mp\mp}$ because the former can proceed through both Z/γ, while the latter proceeds only through γ.

[6]Three different types of seesaw mechanisms can occur [42]. Type-I seesaw generates neutrino masses through Dirac Yukawa couplings to additional right-handed neutrinos. Type-II seesaw instead involves an SU(2) bosonic triplet with Majorana-type couplings. Type-III involves an SU(2) fermionic triplet, also with Dirac Yukawa couplings.

The partial decay width of doubly charged Higgs bosons into pairs of like-sign leptons is described by

$$\Gamma(H^{\pm\pm} \to \ell^{\pm}\ell'^{\pm}) = k\frac{h^2_{\ell\ell'}}{16\pi}m(H^{\pm\pm}), \tag{2.10}$$

where $k = 2$ if the leptons have the same flavor ($\ell = \ell'$) and $k = 1$ is the leptons are of different flavor [30]. $h^2_{\ell\ell'}$ is the coupling parameter and $m(H^{\pm\pm})$ the doubly charged Higgs boson mass. For this search, only cases where the $H^{\pm\pm}$ boson decays promptly, here defined as having a lifetime of $c\tau < 10$ μm, are considered.

2.2.3 Other Models Producing Like-Sign Dileptons

Like-sign dilepton production is a probe of many scenarios of beyond the SM physics other than models of supersymmetry and doubly charged Higgs bosons. The left-right symmetric model, discussed within the context of doubly charged Higgs boson production, can produce like-sign dileptons from decays of the right-handed W_R through a heavy Majorana neutrino N_R as

$$q\bar{q}' \to W_R \to lN_R \to llW^*_R \to lljj. \tag{2.11}$$

The resulting final state, illustrated in Figure 2.4, contains two like-sign leptons and two jets, potentially with very high transverse momentum.

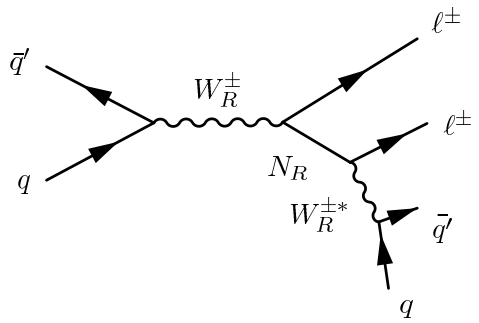

Figure 2.4: Feynman diagram of the production of a heavy Majorana neutrino (N_R) through a right-handed W boson, resulting in a final state with like-sign dileptons.

Pair-production of heavy fourth-generation down-type quarks (b') can also give rise to like-sign dileptons [48]. A dominant decay mode for produced b' quarks is

$$b' \to Wt \to WWb. \tag{2.12}$$

When the b's are pair-produced, the resulting final state thus contains four W bosons and two b quarks. If two W bosons with equal charge decay leptonically, like-sign dileptons are produced. This process is illustrated in Figure 2.5.

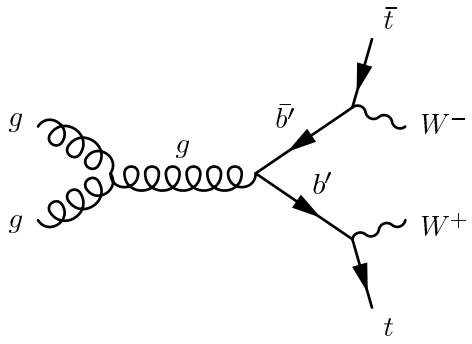

Figure 2.5: Feynman diagram of pair production of heavy fourth-generation down-type quarks.

A similar final state is pair-production of like-sign top quarks which may occur if a new flavor-changing Z' boson, coupling to u and t quarks, is exchanged in the t-channel as illustrated in Figure 2.6. This was proposed [49] to explain a forward-backward asymmetry (A_{FB}) observed in $t\bar{t}$ production at the Tevatron [50, 51]. If both top quarks decay leptonically, the final state contains two like-sign leptons.

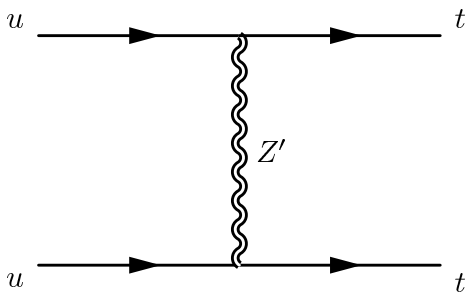

Figure 2.6: Feynman diagram of like-sign top-quark production through a flavor-changing Z' boson.

2.3 Previous Searches

Searches for both inclusive like-sign dilepton production and direct searches for doubly charged Higgs bosons have previously been performed at various high-energy collider experiments. The CDF Collaboration has performed inclusive searches at the Tevatron [52, 53]. The ATLAS Collaboration previous performed an inclusive search for new physics in the like-sign dilepton final state, using an integrated luminosity of 34 pb^{-1} [54]. As mentioned in the introduction, an initial version of the search was performed in a data sample corresponding to 1.6 fb^{-1} [12]. None of the inclusive searches for pairs of prompt, high transverse momentum leptons with the same electric

charge observed any evidence for new physics.

Direct Searches for Doubly Charged Higgs Bosons

Direct searches have been performed at collider experiments for doubly charged Higgs bosons. The pair-production process $e^+e^- \rightarrow H^{++}H^{--}$ was searched for at LEP in final states with four charged, prompt leptons [55, 56, 57]. These searches placed lower bounds on the $H^{\pm\pm}$ boson mass within the left-right symmetric model between 95 GeV and 100 GeV. Direct searches for $H^{\pm\pm}$ bosons have also been performed at the Tevatron by the CDF [53, 58] and D0 [59] Collaborations, excluding masses between 112 GeV and 245 GeV, depending on the final state. The most stringent limits were set by the CMS Collaboration using a data sample corresponding to an integrated luminosity of 5 fb^{-1} [60]. Here, $H^{\pm\pm}$ bosons are excluded at 95% confidence level for masses below 382 GeV, 395 GeV, and 169 GeV for the same-flavor final states ee, $\mu\mu$, and $\tau\tau$, assuming pair production and left-handed couplings. Additionally, masses below 391 GeV, 293 GeV, and 300 GeV are excluded for $e\mu$, $e\tau$, and $\mu\tau$. The previous ATLAS search using like-sign dimuons excluded masses below 355 GeV and 251 GeV for $H^{\pm\pm}$ bosons coupling to left-handed and right-handed fermions, respectively, assuming pair production and a branching ratio to muons of 100%.

Indirect Constraints on Doubly Charged Higgs Bosons

There are additional constraints on doubly charged Higgs bosons from Bhabha scattering. The presence of a $H^{\pm\pm}$ boson would modify the Bhabha scattering cross section through its contribution in the t-channel exchange. Results from the OPAL [56] and L3 Collaborations [57] placed constraints on the Yukawa coupling to electrons (h_{ee}) for $H^{\pm\pm}$ bosons masses into the TeV-range. The limits range from about $h_{ee} < 0.15$ at a mass of 100 GeV to about $h_{ee} < 0.75$ at 1 TeV, assuming pair-production of the $H^{\pm\pm}$ bosons.

Stringent limits also result from the 90% upper limits on the muon decay branching ratio $BR(\mu^+ \rightarrow e^+e^-e^+) < 1.0 \times 10^{-12}$ [61]. This constrains the product of the h_{ee} and $h_{e\mu}$ couplings as [62]

$$h_{ee}h_{e\mu} < 4.7 \times 10^{-11} GeV^{-2} \times m(H^{\pm\pm})^2. \tag{2.13}$$

Chapter 3

The ATLAS Experiment at the Large Hadron Collider

The Large Hadron Collider (LHC) [8], located outside Geneva on the border between Switzerland and France, is the most powerful accelerator ever constructed for conducting high-energy physics research. It is designed to accelerate and collide protons to a beam energy of 7 TeV (a center-of-mass energy $\sqrt{s} = 14$ TeV), with capability of also accelerating heavy ions, such as lead ions (Pb^{82+}), at a center-of-mass energy of 2.76 TeV per nucleon pair. The LHC has two counter-circulating beams, kept in their orbits using strong superconducting electromagnetic fields, which intersect at four points along the beam paths. At each interaction point, the beams collide at the center of a large detector which records and studies the collision products.

The ATLAS detector [4] is one of four large experiments analyzing the LHC collision data. It is designed as a large cylinder with an onion-type structure of different detector subsystems. It contains an inner tracking system surrounded by electromagnetic and hadronic calorimeters, followed by an outermost muon spectrometer. The inner tracking system detects and measures trajectories of charged particles. The calorimeters identify and measure the energy of photons, electrons, and jets, while the muon spectrometer is responsible for detecting and measuring the properties of muons. A magnet system, with an inner solenoid and three outer toroids, bends the trajectories of charged particles to allow their momenta to be measured.

This chapter gives an overview of the motivation and design of the LHC and provides a summary of the ATLAS detector and its different subsystems. Full details can be found in the ATLAS Technical Design Reports [63, 64] as well as in the first ATLAS detector publication [4].

3.1 The Large Hadron Collider

The LHC is installed in the tunnel which previously hosted the electron-positron collider LEP in the 1990s. The tunnel measures 26.7 km in circumference and is situated between 45 m and 170 m underground, on a plane inclined at an angle of 1.4%, sloping towards Lake Geneva. It was first approved for construction by the CERN Council in 1994 as the next generation discovery machine. The decision to build a high-energy hadron collider at CERN and its subsequent chosen design was largely driven by the possibility of its installation in the former LEP tunnel, allowing for significantly reduced costs since both the tunnel and the LEP injection chain could be re-used.

Four large detectors have been constructed to study the LHC collisions. ATLAS [4] and CMS [65] are both general-purpose detectors. They are designed to make precision Standard Model measurements up to the TeV scale, probe the mechanism behind electroweak symmetry breaking and search for the Higgs boson, as well as to search for a wide range of new physics phenomena. LHCb [66] is an experiment targeted to study the physics of the b quark, making Standard Model precision measurements as well as performing direct and indirect searches for new physics signatures in the b-quark sector. One of the main goals of LHCb is understanding the matter/antimatter asymmetry present in the universe. ALICE [67] is specifically designed to study heavy-ion collisions, exploring conditions resembling those of the universe a few microseconds after the Big Bang. This state of matter is referred to as the quark-gluon plasma, and ALICE aims to probe and understand its properties.

3.1.1 Design

The LHC is a large superconducting synchrotron which accelerates protons to a maximum energy of 7 TeV per beam. It is preceded by a series of smaller accelerators which produces the protons and accelerates them to an energy of 450 GeV when they can be injected into the main LHC ring. The LHC ring consists of eight straight sections and eight arcs, following the LEP tunnel design. Protons are focussed and kept in their orbit using strong superconducting magnets. To minimize beam losses through interactions of protons with gas molecules and to keep the beam background minimal for the LHC experiments, the beams are kept in an ultrahigh vacuum (10^{-13} atm).

To achieve the target beam energy and intensity necessary to probe the rare physics phenomena for which the LHC is constructed, a proton-proton machine is preferred over a proton-antiproton one due to limitations in producing antiprotons in large enough quantities. In contrast to its predecessor at Fermilab, the Tevatron, which collided protons with antiprotons and could use a design with two beams in a single ring, the LHC must be constructed with two separate rings for the counter-circulating beams. The physical size of the former LEP tunnel made installing two

physically distinct rings with separate magnet systems challenging. Instead, a two-in-one dipole magnet design was used which allowed both beam-pipes to be contained in one dipole.

Accelerator Chain

Producing high-energy and high-intensity proton-proton collisions at the LHC begins with the creation of protons from hydrogen atoms and is followed by a chain of accelerators, each step with increasing energy. An illustration of the CERN accelerator complex is shown in Figure 3.1.

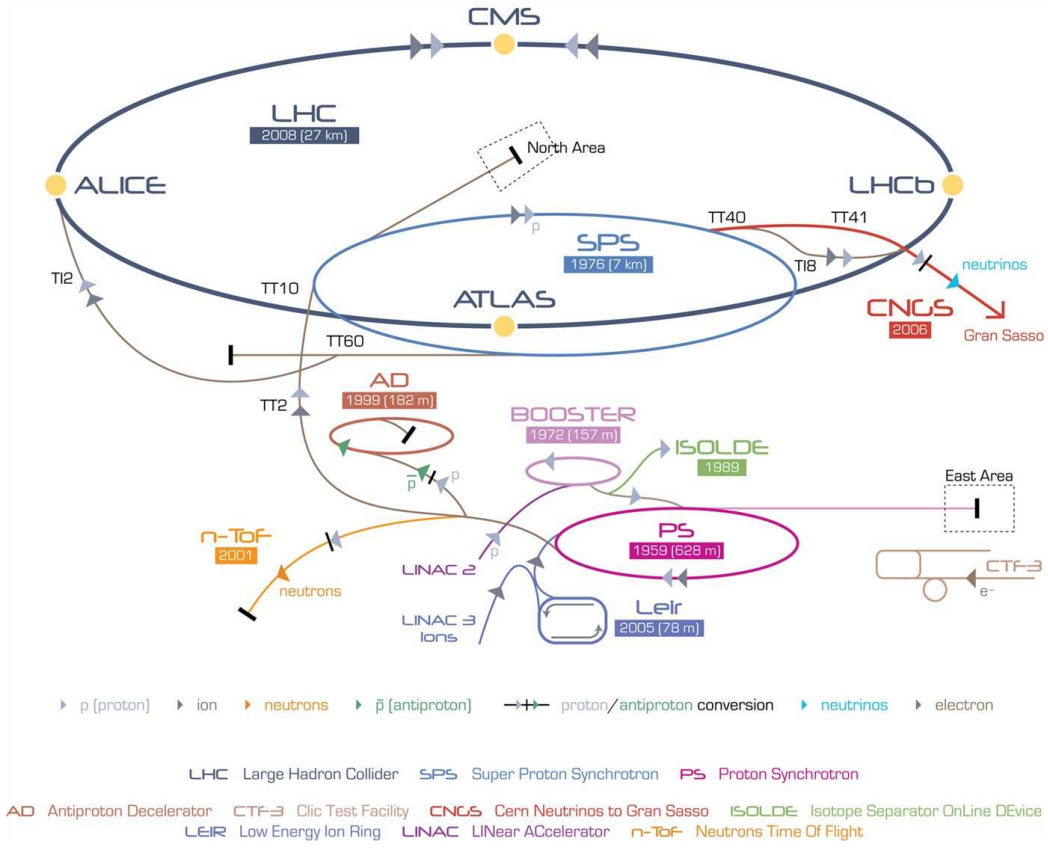

Figure 3.1: Illustration of the CERN accelerator complex showing the LHC, its four main experiments, and the accelerator chain responsible for creating and accelerating protons and ions before injection into the main LHC ring [1].

During the first step of the process, electrons are stripped off hydrogen atoms to create protons in an ion source. Protons enter a linear accelerator (Linac2) where they are accelerated to an energy of 50 MeV. From Linac2 the protons continue to the Proton Synchrotron Booster (PSB), a small synchrotron of 157 m in circumference, which accelerates protons to 1.4 GeV. Next, the beam is injected to the Proton

Synchrotron (PS), 628 m in circumference and operating since 1959, where protons reach an energy of 25 GeV. The final, pre-LHC stage is the Super Proton Synchrotron (SPS) which further accelerates protons to 450 GeV, after which they can be injected into the main LHC ring. The SPS, nearly 7 km in circumference, was first switched on in 1976 and is historically an important synchrotron. It is responsible for the discoveries of the W [17] and Z [18] bosons in 1983 during a time when it operated as a proton-antiproton machine. The PS and the SPS both use room-temperature (i.e. non-superconducting) electromagnets to bend and focus the proton beams.

The creation of heavy-ion beams proceeds analogously. Lead ions are created from lead atoms by heating a lead sample and ionizing the lead vapor using an electron current. The produced lead ions have a maximum charge of Pb^{29+}. The ions are collected and sent through a first linear accelerator (Linac3), after which they pass a carbon foil further stripping electrons off the ions. The lead ions are accelerated in the Low Energy Ion Ring (LEIR) and then injected to the PS. Another stage of electron-stripping is performed before the ions are injected into the SPS by a second carbon foil to obtain Pb^{82+}.

Protons in the LHC beams are grouped in *bunches*, each containing up to 1.15×10^{11} protons. The LHC and the preceding synchrotrons (PSB, PS, SPS) all use radio-frequency (RF) systems to capture and accelerate protons. The RF system at the LHC operates at a 400 MHz frequency, resulting in 35640 *RF buckets*, local minima of the RF electromagnetic waves. At design intensity, proton bunches (i.e. filled RF buckets) will be spaced 25 ns apart, corresponding to a beam-crossing frequency of 40 MHz. There is 3564 possible bunch places per ring at 25 ns spacing but in practice, maximally 2808 filled bunches can be stored per beam due to the beam filling scheme and the RF systems. Proton bunches in each beam are organized in *bunch trains* of 72 bunches, followed by a minimum of eight empty bunches. Longer bunch gaps are also required to allow for instance to turn on the kicker magnets which are used to safely dump the LHC beams.

Superconducting Magnets

The counter-circulating LHC beams are accelerated in separate beam pipes in a strong magnetic field, created using superconducting electromagnets. The magnets are built with a technology using superconducting coils made from Niobium-Titanium (NbTi) cables cooled to 1.9 K using superfluid helium. The superconducting magnets produce fields with maximal strength of 8.33 T and operate at a current of 11.8 A at design energy.

The space limitations of the LEP/LHC tunnel led to the use of a two-in-one design for the superconducting magnets. This design allows the windings for both beams to be contained within the same cold mass (all components that need to be cooled by the superfluid helium) and cryostat, while generating magnetic fields in opposite directions to bend the two beams simultaneously. The LHC ring contains a total of

1232 dipole magnets, used to keep the beams in the circular orbit, and 392 quadrupole magnets to focus the beams. Figure 3.2 shows an illustration of a typical LHC dipole magnet.

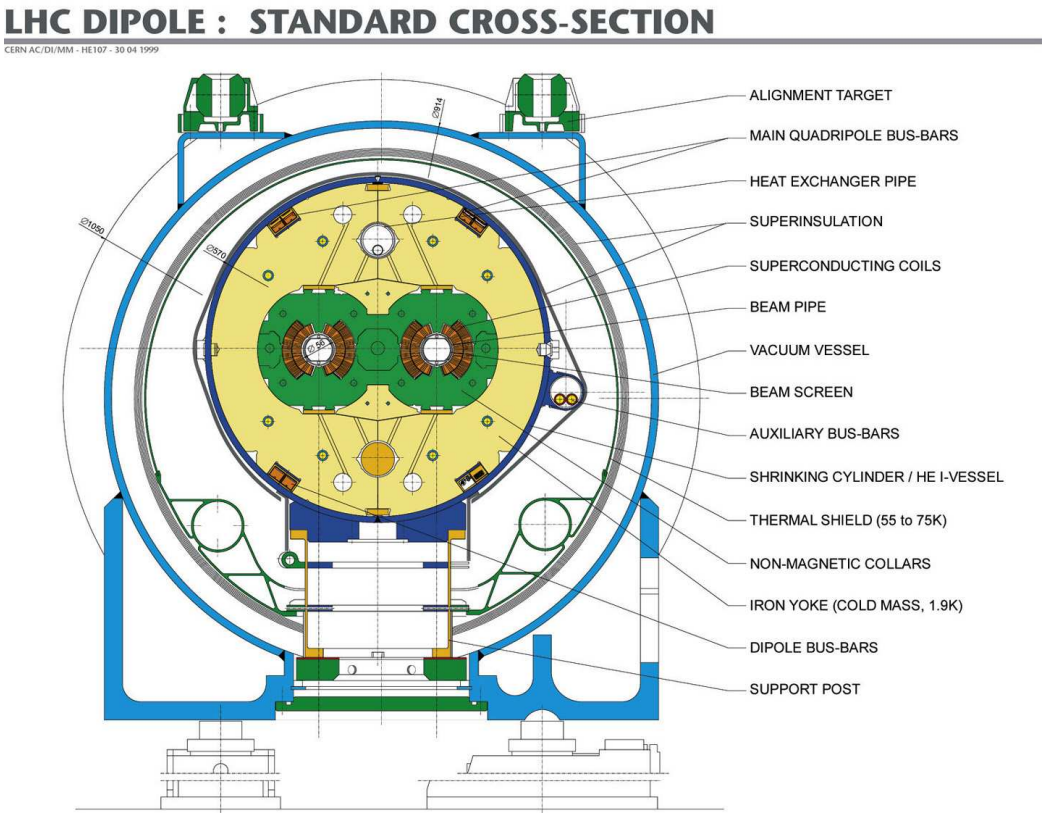

Figure 3.2: Illustration of a superconducting dipole magnet used at the LHC to keep the beams in their orbit, with two beam pipes contained in the same cold mass [2].

Definition of Luminosity and Cross Section

An important property for characterizing hadron collisions is the concept of luminosity. The *instantaneous luminosity*, $\mathcal{L}$, is measured per unit area and second [$\mathrm{cm}^{-2}\mathrm{s}^{-1}$] and describes the collision rate. It depends on both the frequency of the beam crossings as well as the proton density and the beam overlap area. The instantaneous luminosity relates the number of produced events, N_{event}, to the event production cross section, σ_{event}, as

$$\frac{dN_{\mathrm{event}}}{dt} = \mathcal{L} \cdot \sigma_{\mathrm{event}}. \tag{3.1}$$

The instantaneous luminosity is a function of the beam parameters and can be written as

$$\mathcal{L} = \frac{N_1 N_2 n_b f_{\text{rev}}}{A}, \tag{3.2}$$

where N_1 and N_2 are the number of protons per colliding bunch in each beam, n_b the number of bunches per beam, f_{rev} the revolution frequency of the beams (11 kHz), and A the cross-sectional area of the beams at the collision point. The cross-sectional area can in turn be expressed as

$$A = \frac{4\pi\epsilon_n\beta^*}{\gamma_r F}, \tag{3.3}$$

where ϵ_n is the normalized transverse beam emittance (a measure of the average spread of the protons in position and momentum phase space), β^* the beta function (a measure of the width of the beam) at the collision point, γ_r the relativistic gamma factor, and F a geometric factor to account for the non-zero beam-crossing angle at the interaction point. The luminosity can also be expressed in terms of the average number of inelastic interactions per bunch crossing (μ) and the pp inelastic cross section (σ_{inel}) [68] as

$$\mathcal{L} = \frac{\mu n_b f_{\text{rev}}}{\sigma_{inel}}. \tag{3.4}$$

The design instantaneous luminosity is 10^{34} cm^{-2}s^{-1} for proton-proton collisions and 10^{27} cm^{-2}s^{-1} for lead-lead collisions.

Closely related to the instantaneous luminosity is the *integrated luminosity*, which is the instantaneous luminosity integrated over time. The integrated luminosity describes the total collected data, usually measured in units of inverse barn, while cross sections are measured in barn (1 barn = 10^{-24} cm^2)[1].

LHC Operation and 2011 Run Conditions

Proton beams were first circulated in the LHC on September 10, 2008. Shortly after, however, a magnet quench occurred due to a faulty electric connection, resulting in mechanical damage and release of helium [69]. Several magnets were repaired and an improved magnet protection system was installed, but it was decided to limit the machine energy until further upgrades could be made. First collisions at injection energy ($\sqrt{s}$ = 900 GeV) were achieved on November 23, 2009. On March 30, 2010, the LHC began proton-proton collisions at the record energy $\sqrt{s}$ = 7 TeV, with subsequent rapidly increasing instantaneous luminosity during 2010 and 2011. During 2012, the center-of-mass energy was further increased to 8 TeV while the design energy of 14 TeV is expected to be achieved after a long shutdown period in 2013–2014 involving additional magnet training and installation of further quench protection systems to ensure safe operation at the highest energies.

[1] More commonly, picobarn [pb] and femtobarn [fb] are used.

The search described in this dissertation was performed using data collected in 2011 at $\sqrt{s} = 7$ TeV. The total integrated luminosity delivered by the LHC and recorded by the ATLAS experiment during this time is shown in Figure 3.3. The total recorded luminosity during 2011 was 5.25 fb^{-1}, with an ATLAS data-taking efficiency of 93.6%. The efficiency loss takes into account the time to switch on high voltage for certain detector subsystems, as well as inefficiencies in the data acquisition and individual isolated problems with different detectors. Figure 3.3 also shows the peak instantaneous luminosity per LHC fill, the maximum during 2011 was 3.65×10^{33} cm^{-2}s^{-1}.

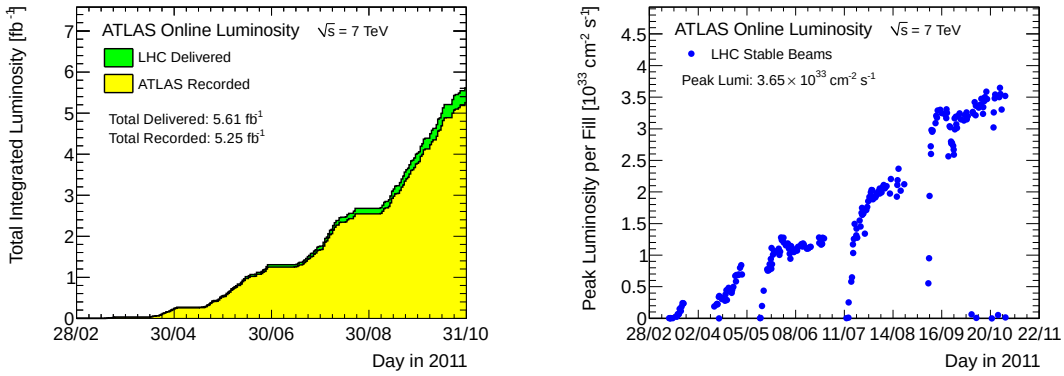

(a) (b)

Figure 3.3: Figures showing (a) the total integrated luminosity delivered by the LHC and recorded by ATLAS and (b) the peak instantaneous luminosity per LHC fill during 2011 [3].

Before the experiments can begin data-taking, a series of steps must be completed. When protons have been injected into the LHC and both beams are filled, the energy of the beams is ramped up successively to the target beam energy. Next, the bunches are squeezed, meaning that the physical size of the bunches are reduced to increase the likelihood of collisions, i.e. the proton density is increased. The beams are then adjusted and optimized to prepare for collisions, for instance to deliver the same instantaneous luminosity to both ATLAS and CMS and to ensure low beam background. The latter is crucial for the innermost detector components which could otherwise suffer severe damage. When preparations for collisions are complete, LHC declares *stable beams* and only then does data-taking begin.

The run conditions of the LHC operation during 2011 varied significantly throughout the year. Initially, the LHC operated with a bunch spacing of 75 ns but after a month it was successfully decreased to 50 ns. The run conditions during 2011 are listed in Table 3.1 and compared to those for nominal operation.

At the high LHC luminosity, multiple pp interactions occur for each bunch crossing. Even at high luminosities though, maximally one hard collision will occur for a

Parameter	Nominal	2011
Beam energy [TeV]	7	3.5
Number of protons/bunch (N_b)	1.15×10^{11}	up to 1.45×10^{11}
Number of colliding bunches (n_b)	2808	1380
Bunch spacing [ns]	25	75, 50
β^* [m]	0.55	1.5, 1.0
Stored energy per beam [MJ]	362	110
Peak luminosity [$\text{cm}^{-2}\text{s}^{-1}$]	1.0×10^{34}	3.7×10^{33}
Mean interactions per crossing	20	6(12) at $\beta^* = 1.5(1.0)$ m

Table 3.1: The LHC run conditions comparing nominal and 2011 operation [8, 9].

given bunch crossing, but with multiple simultaneous low-energy interactions. Multiple interactions within the same bunch crossing is known as *in-time pileup*. Overlapping interactions also result from previous bunch crossings, *out-of-time pileup*, due to the short bunch spacing compared to the readout response of many detector subsystems. Pileup is a challenge for the detectors, affecting among others the trigger operation, missing transverse momentum determination, and lepton isolation. Figure 3.4 shows the peak number of interactions per bunch crossing, averaged over all bunch crossings, as function of time during 2011. It ranges from about three in the beginning of 2011 data-taking to over 15 interactions per bunch crossing by the end of the year.

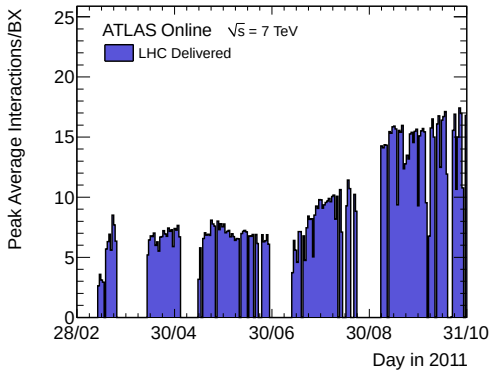

Figure 3.4: The peak number of interactions per bunch crossing, averaged over all bunches, during 2011 [3].

3.2 The ATLAS Detector

ATLAS is a general-purpose detector, measuring 25 m in height and 44 m in length with an overall weight of approximately 7000 tonnes. The high collision energy and expected integrated luminosity delivered by the LHC will allow ATLAS and the other experiments to perform precision tests of the Standard Model as well as probing a wide range of phenomena of beyond the Standard Model physics. One of the main goals is understanding the mechanism of electroweak symmetry breaking and to find or exclude the existence of a Higgs boson. ATLAS was designed to have sensitivity over the entire allowed Higgs boson mass range. Other benchmark scenarios include searches for supersymmetry and new heavy gauge bosons and Standard Model precision measurements such as of the W-boson or top-quark masses.

The ATLAS detector, shown schematically in Figure 3.5, comprises an inner tracking system, electromagnetic and hadronic calorimeters, and a muon spectrometer. A magnet system, with an inner solenoid and three outer toroids, bends charged-particle trajectories to measure their momenta. The solenoid is located between the inner detector and the electromagnetic calorimeter and provides a 2 T axial magnetic field to deflect electrically charged particles traversing the inner detector. Its design was optimized to keep the material thickness in front of the calorimeter to a minimum. The air-core superconducting toroids, one barrel and two endcaps, provide magnetic bending for the muon detectors through a toroidal magnetic field of approximately 0.5 T and 1 T in the barrel and endcaps, respectively.

Fulfilling its physics goals while operating in the presence of high interaction rates and radiation doses places strict requirements on the detector capabilities [63, 64]. The detector subsystems must use fast electronics and radiation-hard sensors. Fine detector granularity is required to achieve high track reconstruction efficiency and momentum resolution also at the highest luminosities. Accurate identification and high-precision measurements of electrons, photons, and muons over a wide momentum range are crucial for many physics analyses, including Higgs boson searches. Excellent secondary-vertex resolution for reconstruction of tau-lepton decays and b quarks, as well as good energy resolution for jet and missing transverse momentum measurements are necessary. The detector must have large acceptance in pseudorapidity for full event reconstruction and nearly full acceptance in the azimuthal direction to measure the total transverse energy. High trigger efficiency is required for both low-p_{T} and high-p_{T} objects to reduce the event rate while keeping events of interest.

The performance goals of the ATLAS detector are summarized in Table 3.2, indicating the required resolution and η coverage, which differs for the range in which trigger capability is provided and the range in which measurements are possible. The detector resolution is described with a constant term and one term which varies with energy or momentum.

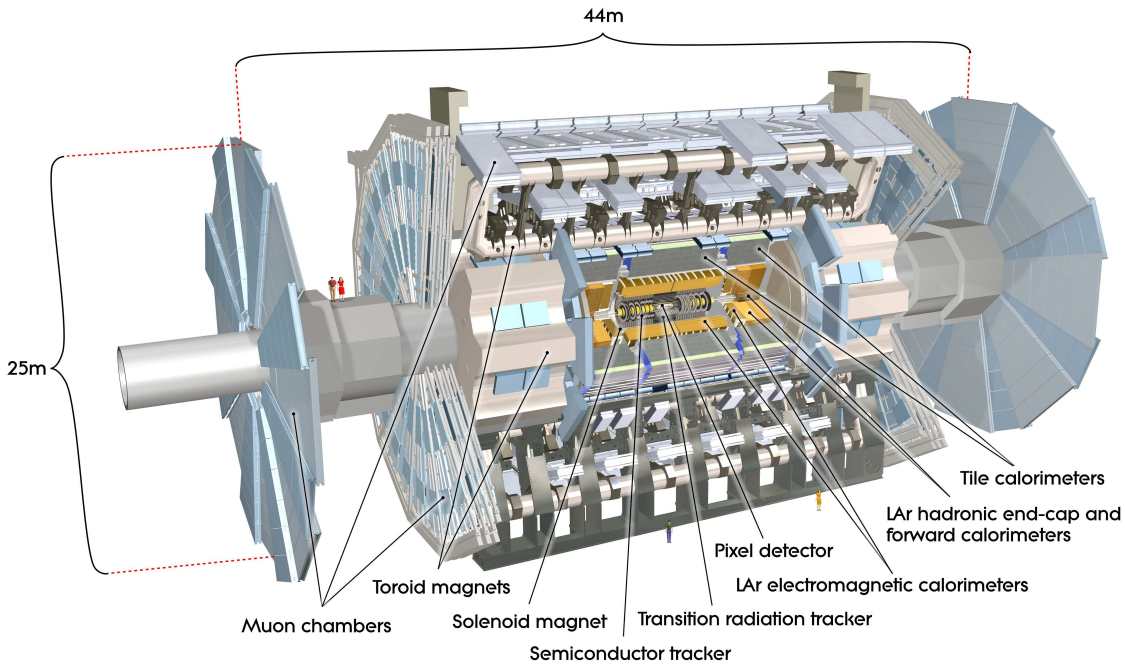

Figure 3.5: Illustration of the ATLAS detector with its various subsystems.

3.2.1 Coordinate System

The ATLAS coordinate system is here briefly summarized. The nominal interaction point is the origin of the coordinate system and the beam direction defines the z-axis with the x-y plane transverse to the beam axis. The positive x-axis points from the interaction point to the center of the LHC ring and the positive y-axis points upwards away from the beam, the positive z-direction then points counter-clockwise if viewed from above. ATLAS is constructed with a central cylindrical barrel and two outer endcaps, often referred to as endcap A and endcap C, where the A (C) side is defined with positive (negative) z. From the rectangular coordinate system (x, y, z), spherical (r, ϕ, θ) and cylindrical (r, ϕ, z) coordinates are defined as usual with the azimuthal angle ϕ measured around the beam axis and the polar angle θ with respect to the beam axis. Particle momenta and energies are generally measured in the transverse x-y plane, for instance, transverse momentum (p_{T}) and missing transverse momentum ($E_{\mathrm{T}}^{\mathrm{miss}}$).

The pseudorapidity η, an important quantity as it is measurable and a Lorentz invariant, is defined in terms of the polar angle

$$\eta = -\ln(\tan(\theta/2)). \tag{3.5}$$

Detector component	Required resolution	$\lvert\eta\rvert$ coverage	
		Measurement	Trigger
Tracking	$\sigma_{p_T}/p_T = 0.05\% p_T \oplus 1\%$	2.5	-
EM calorimetry	$\sigma_E/E = 10\%/\sqrt{E} \oplus 0.7\%$	3.2	2.5
Hadronic calorimetry			
barrel & endcap	$\sigma_E/E = 50\%/\sqrt{E} \oplus 3\%$	3.2	3.2
forward	$\sigma_E/E = 100\%/\sqrt{E} \oplus 10\%$	3.1–4.9	3.1–4.9
Muon spectrometer	$\sigma_{p_T}/p_T = 10\%$ at $p_T = 1$ TeV	2.7	2.4

Table 3.2: Summary of the performance goals for the ATLAS detector [4].

For massive particles, the rapidity y is used instead

$$y = \frac{1}{2}\ln(\frac{E + p_z}{E - p_z}), \tag{3.6}$$

where E is the particle energy and p_z its momentum along the z-axis. In the limit of massless particles the rapidity is identical to the pseudorapidity (electrons, muons, and photons can all be considered massless). The distance ΔR in (η,ϕ) space will be used frequently and is defined as

$$\Delta R = \sqrt{(\Delta\eta)^2 + (\Delta\phi)^2}. \tag{3.7}$$

3.2.2 Inner Detector

The inner detector (ID) is the innermost subsystem of ATLAS, responsible for detecting trajectories of charged particles, measuring their momenta, and constructing track vertices. It is immersed in a 2 T solenoidal magnetic field which bends charged particles, allowing their momenta to be measured. To achieve the required momentum and vertex resolutions as driven by the experiment's benchmark physics processes, the ID is designed with three independent and complementary subsystems: a pixel detector (pixel), a silicon strip detector (SCT), and a transition radiation tracker (TRT).

The inner detector has a central barrel ($|\eta| < 1.05$) and two outer endcaps ($1.05 < |\eta| < 2.5$). Charged particles traversing the ID will typically cross three pixel layers, eight SCT layers, and more than 30 straw tubes in the TRT. Tracks are generally reconstructed for $p_T > 400$ MeV within the pseudorapidity coverage of $|\eta| < 2.5$ ($|\eta| < 2.0$ for the TRT). The inner detector also provides electron identification through the TRT for $|\eta| < 2.0$. Figure 3.6 shows an illustration of the barrel region of the inner detector with the sensors and structural elements traversed by a 10 GeV charged particle. Figure 3.7 similarly shows an illustration of one of the endcaps,

together with two 10 GeV particles, one at $\eta = 1.4$ traversing both the silicon detectors and the TRT, and one at $\eta = 2.2$ which is outside the TRT coverage.

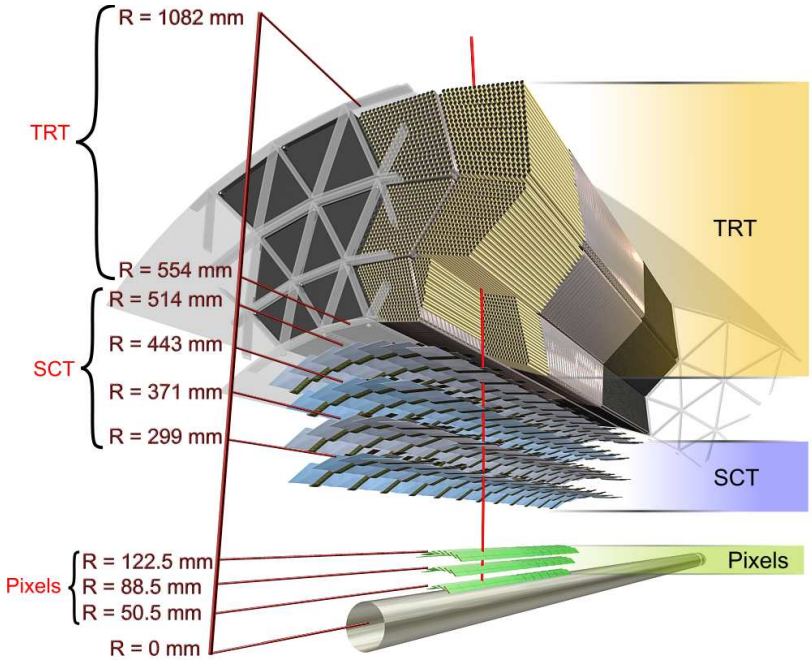

Figure 3.6: Illustration of the barrel region of the inner detector, showing sensors and structural elements traversed by a charged track with $p_{\mathrm{T}} = 10$ GeV ($\eta = 0.3$).

The ID is subject to high radiation doses which place strict requirements on the sensor elements. To minimize radiation damages, the silicon-based detector sensors must be cooled to about -5 C to -10 C when operating, while the TRT is operated at room temperature.

Pixel Detector

The innermost subsystem of ATLAS, the pixel detector, is located directly surrounding the beryllium beam-pipe. It is constructed based on silicon pixel technology, which provides the pattern recognition capabilities necessary to meet the required track reconstruction performance in presence of the high LHC radiation doses and interaction rates [70]. The ATLAS pixel detector contains a total of approximately 80 million pixels.

The pixel detector is designed to provide three measurement points for tracks traversing within the covered pseudorapidity range ($|\eta| < 2.5$). It consists of a central barrel and two outer endcaps, as shown in Figure 3.8. The barrel has three cylindrical layers at radii $R = 50.5$ mm, 88.5 mm, and 122.5 mm and each endcap contains three disks oriented transverse to the beam line at $|z| = 495$ mm, 580 mm, and 650 mm.

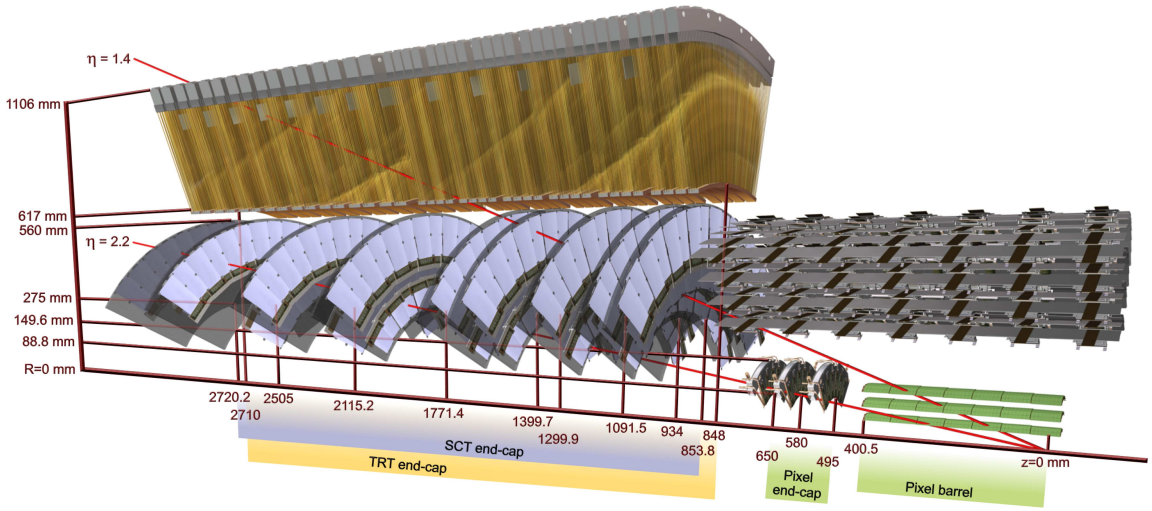

Figure 3.7: Illustration of one of the inner detector endcap regions, showing sensors and structural elements traversed by two charged tracks with $p_{\mathrm{T}} = 10$ GeV ($\eta = 1.4$ and $\eta = 2.2$).

There are 1744 identical modules in the pixel detector which each cover an active area of 16.4×60.8 mm^2 and contain 47232 pixels. Each module is read out by 16 radiation-hard front-end chips, bump-bonded to the module. The pixel detector has a total of 80.4 million readout channels. Most pixel sensors measure 50×400 μm^2 in $R\phi \times z$, although a smaller fraction which are located in the regions of the module front-end readout chips are 50×600 μm^2. The intrinsic resolutions of the pixel modules are 10 μm in $R\phi$ and 115 μm in z (barrel) or R (endcaps).

The pixel sensors are made of 250 μm thick n-type silicon wafers, with negative charge (n^+) implants on the readout side of the sensor and positive charge (p^+) implants on the opposite side, forming the p-n junction [70]. The depletion region is operated in reverse-bias, initially with a voltage of 150 V. As radiation damage of the sensors occurs, the n-type bulk will slowly convert to p-type. The design with n^+ implants on the readout side allows the sensor to continue to operate also after irradiation.

Hits in the pixel sensors are read out if the signal exceeds a predefined, tunable threshold on the number of electrons. Currently, the pixel detector is operated with a threshold at 3500 electrons. The deposited charge is related to the time interval for which the signal is above the set threshold. This relationship is used to measure the deposited charged, the *time-over-threshold* technique. For a minimum ionizing particle, the expected signal is about 20,000 electrons (as compared to the employed threshold of 3500 electrons).

The innermost pixel layer (the B-layer) which is of crucial importance for performing track vertexing is particularly exposed to the high radiation rates from the LHC

collisions. The B-layer will be complemented during the LHC shutdown in 2013-2014 by inserting an additional inner fourth pixel layer outside a new, narrower beam-pipe. Development of this *insertable B-layer* (IBL) is currently in progress within ATLAS.

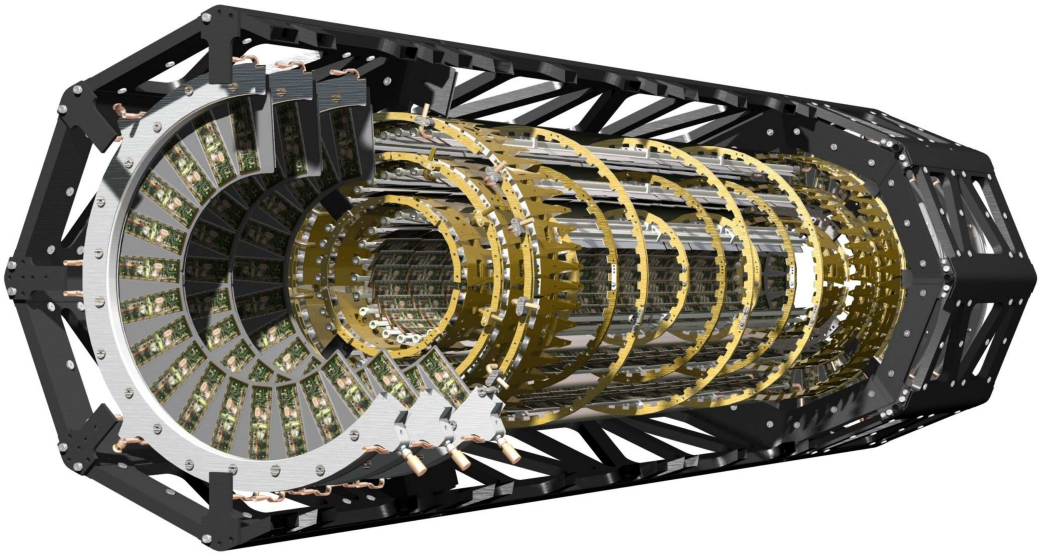

Figure 3.8: The ATLAS pixel detector [4].

Semiconductor Tracker

The semiconductor tracker (SCT) is centered around the pixel detector and designed to provide precision tracking. Due to its increased distance from the interaction region compared to the pixel detector, the requirements on its design due to high interaction and radiation rates are less stringent. Instead of silicon pixels, the SCT is based on a technology with silicon microstrips which are 6 cm long with a pitch of 80 μm. The sensors use a traditional p-in-n technology. The SCT consists of a total of 4088 modules, arranged in four barrel layers with radii ranging from $R = 299$ mm to $R = 514$ mm, and two endcaps, each with nine disks.

For a typical track originating from near the interaction point, the SCT provides eight strip measurements. In the barrel this is achieved through the use of double-sided layers, where two sensors are glued together back-to-back at a stereo angle of 40 mrad. The double-sided design allows for the one-dimensional sensors to give a resolution of 580 μm in the z (barrel) or R (endcap) direction, in addition to a 17 μm intrinsic accuracy in the $R\phi$ plane. The strips are read out by front-end chips, with a total of approximately 6.3 million SCT readout channels. Unlike the pixel detector, the SCT does not provide information of the amount of deposited charge but uses a binary readout.

Transition Radiation Tracker

Surrounding the SCT is the transition radiation tracker (TRT), which consists of nearly 300,000 proportional straw drift tubes. The straws are 4 mm in diameter and filled with a $Xe/CO_2/O_2$ gas mixture. When a charged particle traverses, the gas is ionized, resulting in charge drifting to the central anode (made of tungsten). The charge drift time measures the particle's distance from the central wire.

Similar to the silicon-based detectors, the TRT has a central barrel and two outer endcaps. Straws in the TRT barrel are arranged along the beam line in three cylindrical layers, divided into 32 sectors in ϕ. In each of the two endcaps, straws are oriented radially in two sets of wheels, with a total of 160 layers of straws. In the barrel, straws are 144 cm long, while in the endcaps they measure 37 cm. The TRT is designed such that a typical charged particle with $|\eta| < 2.0$ will traverse more than 30 straws.

In addition to allowing track following, the TRT provides electron identification by producing and detecting transition radiation photons. Transition radiation photons are distinguished from the tracking signals through the use of a low and high threshold in the front-end readout electronics. The low threshold is set such that any charged particle produces hits above that threshold with very high efficiency, while the high threshold is set such that electrons have a significantly higher probability of producing hits than pions. The number of high threshold hits on a track therefore provides discrimination between electron and pion tracks.

The total number of readout channels in the TRT is about 351,000. The TRT provides information only in the $R\phi$ direction with an intrinsic resolution of 130 μm.

Beam Conditions Monitor

In addition to the main ID subsystems, a beam conditions monitor (BCM) is constructed in the center of the detector. The BCM consists of four small diamond sensors on each side of the ATLAS interaction point, at $|\eta| = 4.2$, and is primarily designed to monitor the beam background levels to ensure that the run conditions are safe for ATLAS operation (the innermost pixel detector being the most targeted subsystem). It also, however, proved powerful for luminosity measurements.

3.2.3 Calorimetry

The ATLAS calorimeter system, depicted in Figure 3.9, covers a large pseudorapidity range of $|\eta| < 4.9$ using a variety of technologies. Electromagnetic calorimetry, covering an η range similar to that of the inner detector, provides precision measurements of electrons and photons. Hadronic calorimetry, covering the full η range, allows for jet reconstruction and measurements of the missing transverse momentum, crucial for many Standard Model measurements and new physics searches.

The electromagnetic and hadronic calorimeters are both sampling detectors, with altering layers of a dense energy absorber and an active material producing the read-out signal. Energy measurements are based on the production of electromagnetic or hadronic *showers* which result from the interactions of an incoming particle, charged or neutral, with an electron or an atomic nuclei in the absorber material through the electromagnetic or strong force.

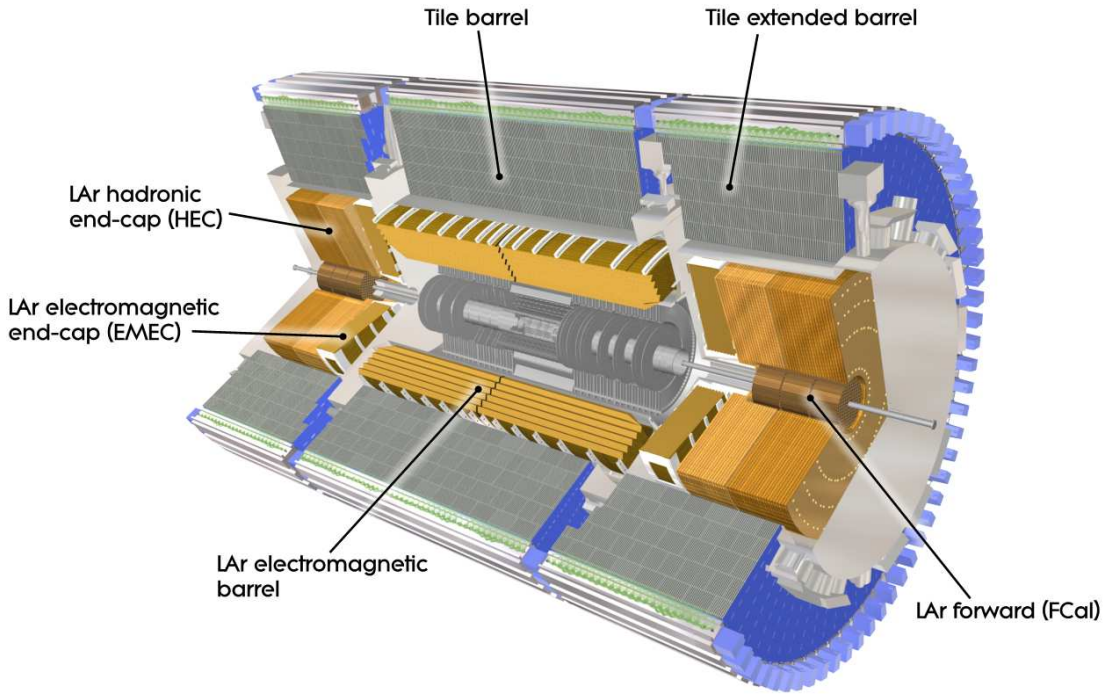

Figure 3.9: Illustration of the ATLAS calorimeter system with electromagnetic and hadronic sections.

Electromagnetic Calorimeter

The electromagnetic (EM) calorimeter is a sampling detector with lead as the dense absorber and liquid argon (LAr) as the active material. The energy of an incoming particle, for instance an electron or a photon, is measured as the particle interacts with the absorber material, creating an electromagnetic shower proportional to the energy of the primary particle. LAr is used as the active material due to its intrinsic radiation hardness, linear behavior, and stability of response over time [4].

The EM calorimeter consists of a barrel ($|\eta| < 1.475$) and two endcaps ($1.375 < |\eta| < 3.2$), where each endcap is divided into two wheels ($1.375 < |\eta| < 2.5$ and $2.5 < |\eta| < 3.2$). The barrel is further split in two halves at $z = 0$ and extends

radially from about 1.4 m to 2.0 m. The EM calorimeter is designed with accordion-shaped kapton electrodes and lead absorbers plates. For the barrel, the accordion waves are axial and run in ϕ, while for the endcaps the waves are parallel to the radial direction and run axially. The accordion-geometry design gives complete ϕ symmetry with uniform resolution. The thickness of the lead plates varies with η to optimize the performance of the calorimeter energy resolution, but is around 1–2 mm.

High-precision measurements are provided through a fine segmenting in η of the first calorimeter layer. An illustration of a barrel module is found in Figure 3.10, showing the accordion structure and the granularity of the three layers. The fine granularity in the longitudinal direction of the inner layer provides separation power between photons and neutral pions. The largest fraction of the total energy is collected in the second layer, while the third layer picks up the tail of the electromagnetic shower and is less segmented. The total thickness of the electromagnetic calorimeter is >22 radiation lengths (X_0) in the barrel and >24 in the endcaps.

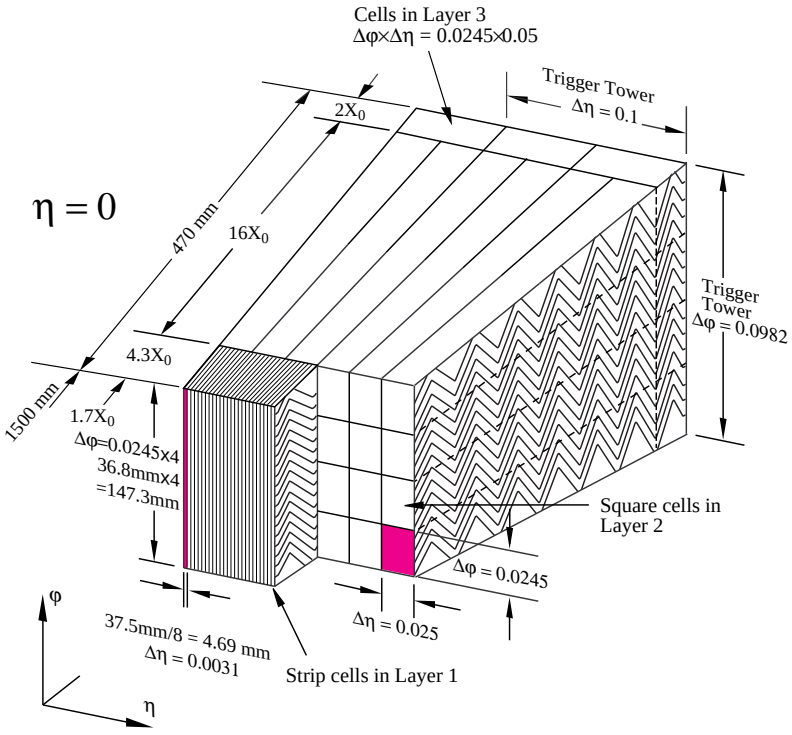

Figure 3.10: Sktech of a barrel model in the electromagnetic cloarimeter.

In the η range covering the ID acceptance, the EM calorimeter is segmented in three sections in depth to provide precision measurements, whereas at high η, only two layers are available. For $|\eta| < 1.8$, the calorimeter is complemented by a presampler detector to correct for energy lost by electrons or photons upstream of the calorimeter in the inner detector, solenoid, or cryostat wall. The presampler acts as a

thin (11 mm) active layer of LAr, providing a first sampling of the showers in front of the calorimeter. Since it is only used to improve the energy resolution, the presampler has a coarser granularity than the rest of the calorimeter ($\Delta\eta \times \Delta\phi = 0.025 \times 0.1$).

The liquid argon used as active material must be cooled in order to maintain its liquid state. The barrel and the two endcaps are contained within separate cryostats, each made of two aluminum vessels (an outer warm and an inner cold vessel). The barrel cryostat is shared with the solenoid to reduce the amount of material in front of the calorimeter. Each of the two endcap cryostats is shared between the EM endcap calorimeter and the LAr-based hadronic endcap and forward calorimeters.

Hadronic Calorimeter

The hadronic calorimeter consists of a central tile calorimeter, a liquid-argon hadronic endcap calorimeter, and a liquid-argon forward calorimeter. The tile calorimeter is a sampling detector with steel absorbers and scintillating tiles as the active material, covering the barrel ($|\eta| < 1.0$) and extended barrel ($0.8 < |\eta| < 1.7$) regions, radially extending from about 2.3 m to 4.3 m. Each barrel consists of 64 modules, designed as wedges in $\Delta\phi \sim 0.1$. The tile calorimeter is segmented in depth in three layers, with a granularity in $\Delta\eta \times \Delta\phi$ of 0.1×0.1 for the two inner layers and 0.2×0.1 for the outer layer. The total radial depth corresponds to about 7.4 interaction lengths (λ). The signal is produced as ionizing particles cross the tiles and produce ultraviolet scintillation light in the base material. The scintillating tiles are read out on two sides into two photomultiplier tubes after converting the ultraviolet light to visible light using wavelength-shifting fibers.

The liquid-argon hadronic endcap calorimeter, covering the range $1.5 < |\eta| < 3.2$, consists of two independent wheels per endcap. Each endcap is located just outside the electromagnetic endcap calorimeter, with which it shares cryostat. The wheels are made of 25 mm (inner wheel) or 50 mm (outer wheel) thick copper plates which are interleaved with LAr as the active material. Each wheel is constructed from 32 wedge-shaped modules. The provided granularity in $\Delta\eta \times \Delta\phi$ is 0.1×0.1 (0.2×0.2) for $1.5 < |\eta| < 2.5$ ($2.5 < |\eta| < 3.2$).

The liquid-argon based forward calorimeter provides both electromagnetic and hadronic measurements. It covers the $|\eta|$ range 3.1–4.9 and is segmented in three layers. On each side, the forward calorimeter is integrated to the main endcap cryostat. The three modules per endcap, one for each layer, use different absorber materials. The inner layer is made of copper and optimized for electromagnetic measurements, while the outer two are made of tungsten and primarily measure the energy of hadronic interactions. Each module is constructed as a metal matrix, with LAr interleaved as the active medium. The total depth is about 10 interaction lengths.

3.2.4 Muon Spectrometer

The ATLAS muon spectrometer consists of large air-core superconducting toroid magnets together with trigger and high-precision tracking chambers. It is designed to provide fast triggering of muons with $|\eta| < 2.4$ and to perform precision tracking and momentum measurements out to $|\eta| = 2.7$. The performance goal in terms of momentum resolution ranges from about 3% for muon tracks at 100 GeV to 10% at 1 TeV, as measured by the muon system alone. The latter corresponds to measuring a sagitta along the beam axis of 500 μm with a resolution of less than 50 μm. The muon energy loss in the calorimeters is about 3–4 GeV, and consequently muons only reach the muon system if the transverse momentum is greater than 3–4 GeV.

Each of the three large toroids consists of eight coils. The toroidal fields are responsible for magnetic bending of muon tracks, with the bending plane oriented parallel to the beam axis. For $|\eta| < 1.4$, the barrel toroid provides the magnetic bending, while for $1.6 < |\eta| < 2.7$, it is primarily achieved by the endcap toroids. In the intermediate region, the transition region, both barrel and endcaps contribute. The resulting field configuration is mostly orthogonal to the muon trajectories. In the barrel region, the bending power is 1.5–5.5 Tm, whereas for the endcap regions it is between 1–7.5 Tm. The bending power in the transition regions is lower.

Muon chambers are arranged in three cylindrical structures in the barrel region ($|\eta| < 1.05$), corresponding to radii $R = 5$ m, 7.5 m, and 10 m. In the endcaps ($|\eta| > 1.05$), the muon chambers are arranged in wheels perpendicular to the beam axis at around $|z| = 7.4$ m, 10.8 m, 14 m, and 21.5 m. In the center of the detector around $|\eta| = 0$, a gap is present to give space for detector services to the inner detector, solenoid, and calorimeters. Additional acceptance gaps are present in the lower parts due to detector support structure. An overview of the muon spectrometer is shown in Figure 3.11.

Triggering on muon candidates is provided by Resistive Plate Chambers in the barrel and Thin Gap Chambers in the endcap regions. In addition to providing triggering, the trigger chambers measure muon coordinates in both the bending (η) and non-bending (ϕ) plane, whereas the tracking chambers provide precision coordinate determination in the bending plane only (the coordinate in the bending plane is the one required for performing precision measurements of muon momenta). Precision tracking is performed primarily with Monitored Drift Tubes in the full η range, except for the range $2.0 < |\eta| < 2.7$ in the innermost layer where Cathode Strip Chambers are used instead. The latter have higher granularity and time resolution and are chosen due to the large muon track density and background rates in this region. The placements of the different muon subsystems can be seen in Figure 3.12.

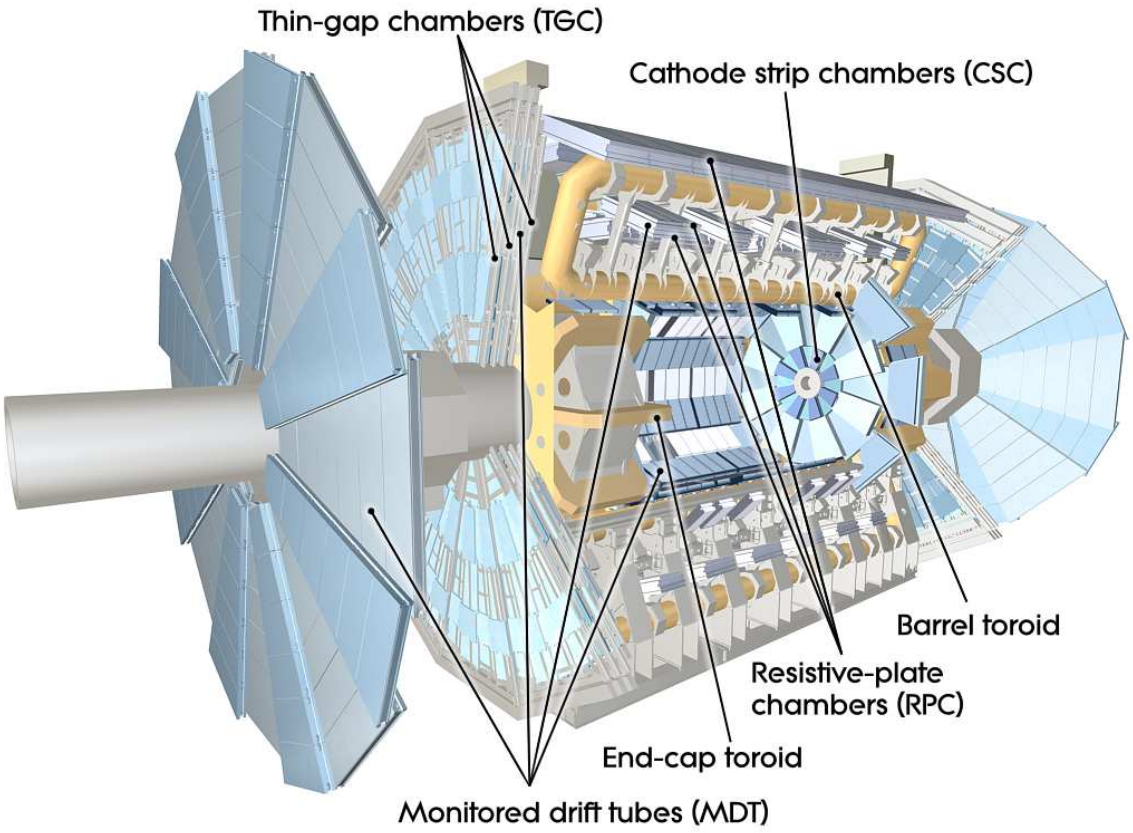

Figure 3.11: Illustration of the ATLAS muon spectrometer.

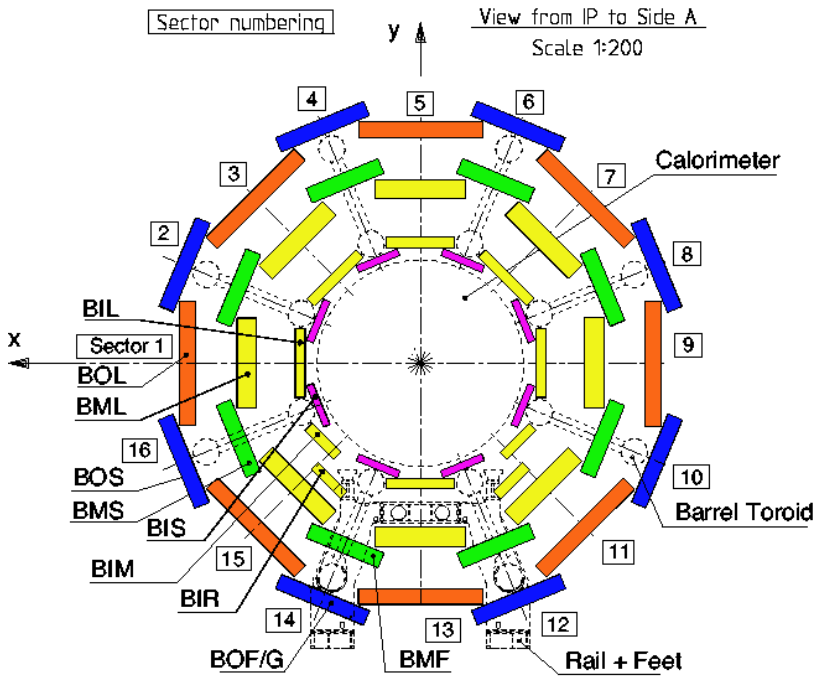

(a)

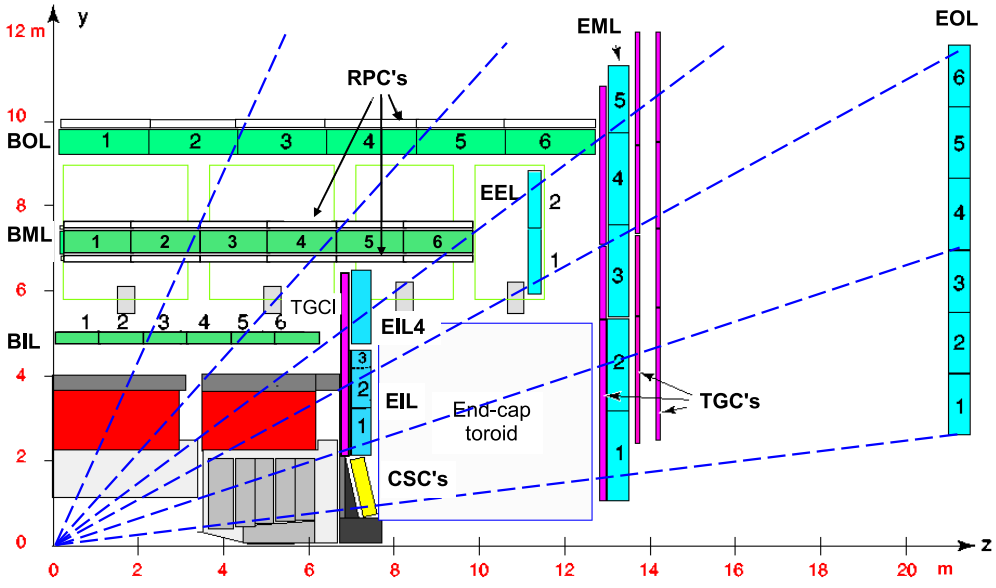

(b)

Figure 3.12: Cross-sectional view of (a) the muon spectrometer barrel region transverse to the beam line (the non-bending plane) and (b) one quarter of the muon spectrometer in the plane containing the beam line (the bending plane) [4].

Monitored Drift Tubes

The Monitored Drift Tube (MDT) chambers are designed with pressurized, gas-filled (Ar/CO_2) aluminum drift tubes with a diameter of 30 mm. In the center of the tube, a thin (50 μm diameter) tungsten-rhenium anode wire is held at a potential of 3 kV. The outer cathode tube is held at ground potential, creating a radial electric field. When a muon traverses a tube, the gas is ionized and the released electrons drift towards the central wire where they are collected. The design using multiple individual tubes provides high precision, yet a robust mechanical structure. Several hits per traversing track are generally created. The relevant time measure is the arrival time at the wire of charges originating from closest to the track rather than those at the periphery. The maximal drift time for electrons from the cathode wall to the wire is about 700 ns.

An MDT chamber consists of two multi-layers of tubes, each with 3–4 layers of tubes, which are separated by a mechanical spacer as shown in Figure 3.13. The two multi-layers are mounted on a solid aluminum support frame. The typical width of a chamber is 1–2 m with a length of 1–6 m. The tubes are oriented along ϕ in both barrel and endcaps. The MDTs provide measurements only in the bending plane (z coordinate), for which the chamber resolution is about 35 μm.

The chambers are arranged in alternating large and small sectors in ϕ with slight overlap, allowing a relative alignment of adjacent sectors using tracks traversing a nearby large and small sector. This can be seen from the cross-sectional view of the barrel region in Figure 3.12.

The MDT chambers have an internal optical alignment system located in the mechanical spacer between the two multi-layers. Additional sensors provide chamber-to-chamber and in-between-layer alignment. Only variations in the relative position can be determined with sufficient precision using the optical alignment system. To achieve required precision, the optical system must be combined with track-based alignment algorithms.

Cathode Strip Chambers

The Cathode Strip Chambers (CSC) are multi-wire proportional chambers which are employed at high pseudorapidity ($2.0 < |\eta| < 2.7$) in the innermost endcap layer of the muon chambers. They are located about 7 m from the interaction point. The CSCs are chosen in this high particle flux region for their fine granularity and fast response time.

The CSCs consist of cathode planes, segmented into strips in orthogonal directions, with a gas-filled ($Ar/CO_2/CF_4$) gap between the planes. Central anode wires, oriented in the radial direction, are held at 1.9 kV. The orientation of the two cathode planes orthogonal to each other allows both track coordinates to be measured simultaneously. The distance between the wire plane and the cathode planes is 2.5 mm.

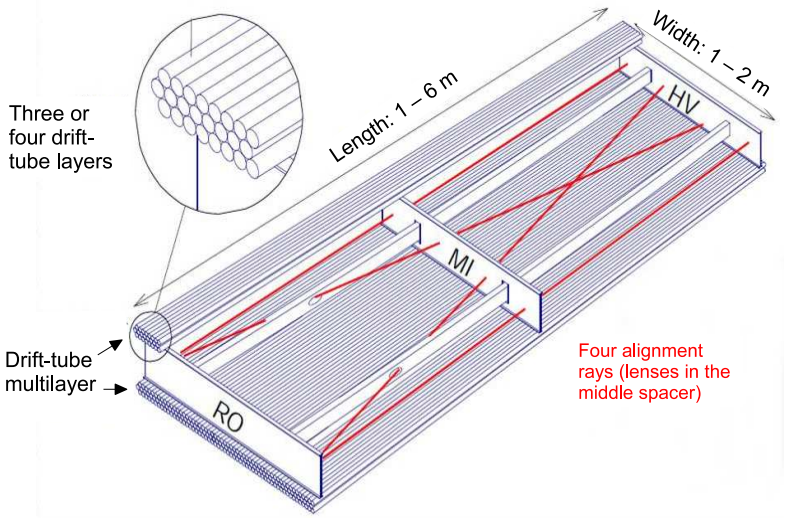

Figure 3.13: Illustration of a MDT chamber with the two multi-layers of drift tubes, mounted on an aluminum frame. The four optical alignment rays are shown as well. RO and HV indicate the location of the readout electronics and high voltage supplies, respectively [4].

The distance between two wires in a wire plane is also 2.5 mm. The plane with strips perpendicular to the wires measures the precision coordinate (R), while the plane parallel to the anode wires gives the transverse coordinate (ϕ). The coordinates are measured through the charge induced on the cathodes by the avalanche formed on the anode wire. The signals on the central wire are not read out. The chamber resolution is 40 μm in R and 5 mm in ϕ. The small cathode-to-wire distance gives a maximal drift time of about 30 ns with a resulting time resolution of 7 ns.

Each CSC endcap has altering small and large chambers in ϕ, with a total of 16 chambers per endcap. Each chamber in turn contains four CSC planes and consequently provides four measurements in (η,ϕ) for a given track.

Resistive Plate Chambers

The muon trigger chambers have three purposes. They must give a rough momentum estimate for the trigger, be sufficiently fast to provide timing information to associate an event to a particular bunch crossing, and to measure the second, non-bending coordinate. Different technologies are used in the barrel and endcap regions partly to achieve similar p_{T} resolutions across different η and due to significantly higher radiation levels in the endcaps. The endcap regions also suffer from inhomogenous fields in the barrel-endcap toroid transition region.

The Resistive Plate Chambers (RPC) are gaseous, parallel electrode-plate detectors. The RPCs do not use any wires which simplifies their construction. The

chambers are made of two 2.0 mm thick resistive plates, made from plastic laminate, which are kept parallel to each other with a 2.0 mm gas-filled (primarily $C_2H_2F_4$) gap between. The gap is subject to a strong electric field of $\sim$ 5 kV/mm allowing avalanches to form towards the anode as a ionizing muon track traverses. The signal is read out on both sides of the detector from two orthogonal series of strips which provide information for both the η and ϕ coordinates.

The RPCs are located in three cylindrical layers around the beam axis, usually referred to as three trigger stations. Two inner stations are located on each side of the middle MDT layer and are responsible for low-p_{T} muon triggering, while a third layer is located at the third and outermost MDT layer. The resulting longer lever arm between the outer station and the inner two stations allows high-p_{T} tracks to be measured. The RPC has a 10 mm precision for both the η and ϕ coordinates and an excellent time resolution of 1.5 ns.

Thin Gap Chambers

Triggering in the endcap regions is performed using Thin Gap Chambers (TGC). This technology is chosen over of the more cost-optimized RPCs due to the finer granularity and higher rate capabilities. The TGCs are similar to multi-wire proportional chambers, but with a shorter wire-to-cathode plane distance of 1.4 mm compared to the wire-to-wire distance of 1.8 mm. Anode wire planes, kept at a high voltage of 2.9 kV, are sandwiched between two planes with graphite cathodes. The area between the planes is gas-filled (CO_2/C_5H_{12}). The anode wires, 50 μm in diameter, run parallel to the MDT wires and provide information about the bending coordinate for the trigger. Additional readout strips run perpendicular to the wires and measure the non-bending coordinate.

The TGCs are constructed in doublets and triplets of chambers. The triplets have three wire layers (which measure the bending coordinate) and two strip layers (measuring the non-bending coordinate). Each doublet has two wire layers and two strip layers. The inner station has one doublet of TGCs, while the middle station has a total of seven layers (one triplet and two doublets). The trigger is based on requiring hit coincidences between the layers in two doublets or a triplet. The small wire-to-wire distance gives a precise time resolution of 4 ns, while the spatial resolution is 2–6 mm in R and 3–7 mm in ϕ.

3.2.5 Forward Detectors and Luminosity

In addition to the main subsystems, ATLAS has a set of forward detectors. A Cherenkov detector, LUCID (LUminosity measurement using Cherenkov Integrating Detector), located at a distance of $\pm$17 m from the interaction point (pseudorapidity range $5.6 < |\eta| < 6.0$), is used as a relative luminosity monitor. A Zero-Degree Calorimeter (ZDC), located $\pm$140 m from the interaction point (where the LHC beam-

pipe is divided to two separate pipes), is designed primarily to detect forward neutrons during heavy-ion collisions. A third forward detector system is ALFA (Absolute Luminosity For ATLAS), ±240 m from the center of ATLAS, which is designed to provide an absolute luminosity calibration for ATLAS.

Luminosity Measurement

An accurate luminosity measurement is a key component for all cross-section measurements as well as any searches which rely on background modeling using simulated data, with predicted background yields normalized to the integrated luminosity. For measurements, the luminosity uncertainty is also often the dominant systematic uncertainty.

The measurement of the ATLAS luminosity and its associated systematic uncertainty is performed using measurements from several luminosity detectors as well as comparing different methods for its determination. The general strategy is to calibrate the luminosity detectors with a measurement as determined from the LHC beam parameters. Event counts from the luminosity detectors can then be used to measure the luminosity both online for monitoring purposes and offline for physics analyses.

For the absolute luminosity measurement, ATLAS relies on *event counting*, i.e. counting the fraction of bunch crossings for which a particular detector observes an event under a given set of requirements (such as a given number of hits). LUCID and BCM were used in 2011 to make luminosity measurements. The luminosity scale is calibrated from dedicated van der Meer (vdM) scans in which the beams are scanned, one at a time, to estimate the vertical and horizontal beam profiles (compare the expression for the luminosity in Equation 3.2). For the full 2011 data, the preliminary luminosity uncertainty was estimated to be 3.9% [71].

3.2.6 Trigger and Data-Acquisition System

The ATLAS trigger system [72] is crucial for identifying and selecting events associated with rare physics processes from the vast background of low-energy interactions. ATLAS uses a three-level trigger system to reduce the event rate from about 40 MHz, the LHC bunch-crossing rate at design luminosity, to about 400 Hz which can be stored for offline event reconstruction. Trigger decisions are based on *trigger signatures*, for instance candidate physics objects such as muons, electrons, photons, jets, or b-jets. Additional triggers are based on global event properties such as the total transverse energy in an event or the missing transverse momentum. Four main physics *data streams* are defined based on the trigger type: Muon, Egamma, JetTauEtmiss, and MinBias. Offline physics analyses will use the data stream(s) corresponding to the chosen trigger(s).

The three-level trigger system consists of a combination of hardware-based and

software-based triggers. The first-level trigger (L1) is a hardware-based, fast, and coarse trigger. The trigger decision is made in less than 2.5 μs and reduces the event rate to about 75 kHz which is the maximum rate that the detector readout systems can process. The second-level trigger (L2) and the event filter (EF) further reduce the event rate to about 3.5 kHz and 400 Hz, respectively. The L2 and the EF, both implemented as software-based triggers, together form the High-Level Trigger (HLT).

First Level Trigger

The L1 trigger decision is based on information from a subset of the detectors. It searches for high-transverse momentum muons using reduced-granularity information from the muon triggers (the RPC and TGC), and for electrons/photons, jets, or hadronically decaying tau leptons using coarse information from the electromagnetic and hadronic calorimeters. Other L1 trigger signatures are large missing transverse momentum or large total transverse energy, again based on inputs from the calorimeters.

During the time it takes the trigger system to form and distribute the L1 trigger decision, event information from the detector subsystems is temporarily stored in detector-specific pipeline memories. In order not to exceed the maximum pipeline memory storage, the L1 trigger must take no longer than 2.5 μs from the bunch crossing to the L1 accept. To achieve this, the L1 trigger is implemented as a system of hardware processes. The L1 trigger identifies Regions-of-Interest (RoIs) which indicate the coordinates in (η,ϕ) of the trigger objects, defining detector regions to be further investigated by the HLT. The muon RoIs measure about 0.1×0.1 in $\Delta\eta \times \Delta\phi$.

The overall L1 trigger decision is made by the Central Trigger Processor (CTP) which combines information for different object types and decide whether to accept the event. The trigger decision is then sent from the CTP to the detector front-end and readout systems. The L1 trigger must have the ability to uniquely identify the bunch crossing of interest - a challenge with a bunch-crossing interval of merely 25 ns at design luminosity. For the L1 calorimeter trigger, complication arises from the width of the calorimeter signal which typically extends over several bunch crossings.

The L1 calorimeter trigger uses coarse granularity information in *trigger towers*, typically 0.1×0.1 in $\Delta\eta \times \Delta\phi$, and the trigger decision is based on the multiplicity of hits for programmable E_{T} thresholds. Already a L1, it can be required that the electron/photon or tau trigger objects have a minimum angular separation from any large energy deposits in the same trigger as a crude method of identifying isolated objects.

The L1 muon trigger uses information from the RPCs in the barrel and the TGCs in the endcap regions, all based on three trigger stations. The trigger algorithm looks for hit patterns consistent with a muon originating from the interaction point by searching for coincidences of hits in the different trigger stations within a *road*. The road is a straight line, with the width of the road depending on the p_{T} threshold in

question (higher p_{T}, narrower road). Three low-p_{T} and three high-p_{T} (programmable) thresholds are defined. The trigger decision is defined in terms of the multiplicity of muons for a given p_{T} threshold.

For the barrel region, the L1 muon trigger algorithm is initiated by a hit in the second of the three RPC doublets, referred to as the *pivot plane*. A search is then made for a matching hit in the first doublet within a trigger road defined between the initial hit and the interaction point. Coincidence is required in three of four layers in the two doublets. This defines the low-p_{T} triggers. The high-p_{T} muon triggers use the third station as well, requiring an additional coincidence hit in one of the two layers in the outermost RPC doublet. In the endcap regions, the outermost doublet is used as the pivot plane. Similar coincidences are required to define the triggers (in the endcaps the innermost station is less relied upon due to limited coverage).

Second Level Trigger

If an event is accepted by the L1 trigger, data from the subdetectors are transferred to detector-specific Readout Buffers (ROB) which stores the event information until the L2 decision is made. ROBs are accessible to the HLT through Readout Systems (ROS). The L2 trigger use information only from the RoIs, while the event filter takes advantage of the full event, provided through the Event Builder which assembles event fragments from the ROBs. The L2 trigger use all available information about coordinates and energy deposits within the RoIs to make the trigger decision in order to further reduce the event rate. The processing time available for the L2 trigger is about 40 ms.

Event Filter

The event filter runs full event reconstruction, using the same reconstruction algorithms as the offline reconstruction. The event-filter decision takes on average 4 s, reducing the event rates to about 400 Hz which can be written to storage and used for offline analysis. At each trigger level, a smaller fraction of a trigger menu item can be selected through pre-scaling of a certain item. For example, with a pre-scaling of 100, only 1 event in 100 passing that trigger item would be kept.

Chapter 4

Search Strategy

Many models of physics beyond the Standard Model predict final states containing pairs of leptons with the same electric charge (*like-sign dileptons*), discussed in detail in Chapter 2. The event characteristics and kinematics vary substantially between models. Some models predict events with little activity other than the like-sign lepton pair, an example is pair production of doubly charged Higgs ($H^{\pm\pm}$) bosons where each $H^{\pm\pm}$ boson subsequently decays to two charged leptons. Other models predict high event activity with several hadronic jets or large missing transverse momentum, for instance pair production of like-sign top quarks. Another characterizing event property is the momentum spectrum of produced leptons.

The general strategy of this search is to have sensitivity to a wide range of scenarios of beyond the Standard Model physics, rather than targeting and optimizing towards one particular model. The search is performed in the like-sign dimuon final state, although it was published jointly with analyses of the $e^{\pm}e^{\pm}$ and $e^{\pm}\mu^{\pm}$ final states, following the same search strategy [10, 11]. To maximize the model independence, the event selection criteria rely solely on the muon properties. No requirements are placed on the number of reconstructed jets or the missing transverse momentum of the event. The final state requiring only two like-sign muons has low background contribution from Standard Model sources. Consequently, it is possible to perform a powerful search which is sensitive to a large variety of models of new physics phenomena despite the inclusive event selection which is not optimized for a specific model.

The search is limited to *promptly* produced leptons, here defined as leptons originating from decays of short-lived states, such as W and Z bosons, or from a new elementary particle with lifetime (τ) less than approximately 3×10^{-14} seconds ($\tau c < 10$ μm). The search is also limited to the phase space where both muons have transverse momentum $p_{\mathrm{T}} > 20$ GeV.

4.1 Like-Sign Dileptons at Hadron Colliders

Pairs of leptons with the same electric charge are rarely produced in the Standard Model. Three like-sign dilepton categories can be distinguished based on the production source. The categories include Standard Model production of pairs with two promptly produced leptons, pairs with at least one non-prompt lepton, and pairs of prompt leptons where the charge of one lepton is misreconstructed.

Pairs of prompt leptons with *opposite* electric charge are produced abundantly at hadron colliders. The dominant sources are production of Z bosons which decay to pairs of oppositely-charged leptons (e^+e^-, $\mu^+\mu^-$, $\tau^+\tau^-$) and production of top-antitop quark pairs ($t\bar{t}$) where both top quarks subsequently decay to leptons

$$t\bar{t} \rightarrow W^{\pm}b\ W^{\mp}\bar{b} \rightarrow \ell^{\pm}\nu b\ \ell^{\mp}\nu\bar{b}. \tag{4.1}$$

Events containing pairs of promptly produced leptons with the *same* electric charge are, on the contrary, quite rare in the Standard Model. The dominant source is production of two gauge bosons, WZ or ZZ production, where both gauge bosons decay leptonically

$$\begin{aligned} W^{\pm}Z &\rightarrow \ell^{\pm}\nu\ell^{\pm}\ell^{\mp} \\ ZZ &\rightarrow \ell^{\pm}\ell^{\mp}\ell^{\pm}\ell^{\mp}. \end{aligned} \tag{4.2}$$

Smaller contributions result from production of like-sign W bosons in association with two jets and from associate production of top-quark pairs with a W or Z boson

$$\begin{aligned} W^{\pm}W^{\pm}jj &\rightarrow \ell^{\pm}\nu\ell^{\pm}\nu jj \\ t\bar{t}W^{\pm} &\rightarrow W^{\pm}b\ W^{\mp}\bar{b}\ W^{\pm} \\ &\rightarrow \ell^{\pm}\nu b\ jj\bar{b}\ \ell^{\pm}\nu \ \text{(alternatively } \ell^{\pm}\nu b\ \ell^{\mp}\nu\bar{b}\ \ell^{\pm}\nu) \\ t\bar{t}Z &\rightarrow W^{\pm}b\ W^{\mp}\bar{b}\ Z \\ &\rightarrow \ell^{\pm}\nu b\ jj\bar{b}\ \ell^{\pm}\ell^{\mp} \ \text{(alternatively } \ell^{\pm}\nu b\ \ell^{\mp}\nu\bar{b}\ \ell^{\pm}\ell^{\mp}). \end{aligned} \tag{4.3}$$

Like-sign dileptons can also be produced from sources where one or both leptons are non-prompt. Non-prompt *muons* arise primarily from semi-leptonic decays of heavy-flavor (b or c) hadrons. They are typically produced with significant hadronic activity around the muon in the tracking and calorimeter systems. As a result, non-prompt muons are on average less well isolated than prompt muons. Muons from heavy-flavor decays have another characteristic property: they originate from a particle with finite lifetime. For instance, the mean lifetime of $B^{\pm}$ hadrons is about 1.6 ps, corresponding to a mean traveled distance of $c\tau = 0.5$ mm [7]. Muons from heavy-flavor decays are therefore typically produced before reaching the innermost layer of the pixel detector, while the mean lifetime is sufficiently long for the muon to originate from a non-negligible distance away from the primary event vertex. The transverse impact parameter (d_0) of the muon track with respect to the primary

vertex, or the impact parameter *significance* ($d_0/\sigma(d_0)$, where $\sigma(d_0)$ is the estimated uncertainty on the d_0 measurement), can be used to differentiate between prompt muons and muons originating from heavy-flavor decays.

Non-prompt muons can also be produced in decays of pions or kaons ($\pi^{\pm}/K^{\pm} \rightarrow \mu^{\pm}\nu_{\mu}$). The mean lifetimes of pions and kaons are 26 ns and 12 ns, respectively [7], i.e. they may travel several meters before decaying. Pions or kaons that decay to muons between the inner detector and the muon spectrometer can be reconstructed with an ID track segment from the initial meson and an MS track segment from the decay muon. In the decays, a fraction of the energy is lost to neutrinos so the momentum of the MS track segment will be lower than the momentum of the ID track segment. This property can be exploited to explicitly target muons from decay-in-flights of pions and kaons. Another source of non-prompt muons involves misidentified ("fake") muons, resulting from hadronic showers in the calorimeter which reach the muon spectrometer and are incorrectly matched to a reconstructed track in the inner detector. The relative occurrence of fake muons as well as muons from early decays (before the inner detector) of $\pi^{\pm}/K^{\pm}$ are small compared to muons from heavy-flavor in the momentum range considered in this analysis [73]. For electrons, non-prompt and fake sources include hadrons that are misidentified as electrons, photon conversions, and semi-leptonic decays of b or c hadrons to electrons. Non-prompt and fake leptons are hereafter referred to jointly as non-prompt leptons.

A third source of like-sign dilepton production involves pairs of prompt opposite-sign leptons where the charge of one lepton is mismeasured in the detector. Charge-misidentification occurs particularly for high momentum tracks when the tracking system is incapable of correctly reconstructing the lepton charge. Another source of charge misidentification, affecting electrons but not muons, is radiation of a high-momentum photon which subsequently converts into an e^+e^- pair. Electron candidates associated with a photon conversion vertex are typically rejected by the electron identification algorithms [74]. However, for asymmetric conversions it may occur that only the track from one of the radiated electrons is reconstructed, and that this track has a different charge than the original electron causing charge misidentification. Another source of background is production of $W\gamma$ and $Z\gamma$ which can similarly give charge misidentification for electrons due to photon conversions.

4.2 Identifying Like-Sign Muon Pairs

The signal region of the search is defined by selecting pairs of prompt, well-reconstructed muons with equal electric charge. Both muons are required to have transverse momentum greater than 20 GeV. This limits the probed phase space but significantly reduces the non-prompt background, consequently enhancing the search sensitivity, compared to allowing the subleading muon to have $p_{\mathrm{T}} > 10$ GeV. Requiring at least one muon with $p_{\mathrm{T}} > 20$ GeV is motivated by the trigger selection (an

18 GeV muon is required at the event filter).

The selection criteria are based on the muons only, with no requirements on other event activity. The main available handles for identifying a clean dimuon sample and reducing background from non-prompt sources are isolation and impact parameter significance. Selected muons must be isolated from nearby tracks in the inner detector and be separated from reconstructed jets. Muons are also required to originate from near the primary event vertex, enforced by placing tight cuts on the transverse and longitudinal impact parameters. Additionally, the transverse impact parameter significance must be less than three, which has high efficiency for prompt muons while it further reduces contributions from non-prompt sources.

Standard Model processes that produce prompt, like-sign leptons (dominated by WZ and ZZ production) constitute an irreducible and dominant background in the search. The prompt background is estimated using predictions from Monte Carlo simulation. Pairs where at least one muon originates from a non-prompt source is another important background in the search. It is a reducible background source which can largely be suppressed using stringent muon selection criteria. It is estimated using data-driven techniques. The third background source is charge misidentification which for muons is small. After all event selection criteria, prompt muons constitute about 80% of the total background while the remaining 20% is due to sources with at least one non-prompt muon.

The challenges of the search lie almost entirely in deriving accurate background predictions. Monte Carlo simulation is used to make predictions of the prompt muon background with dominant systematic uncertainties related to cross-section uncertainties and limited statistics at high dimuon mass. The non-prompt background is estimated directly from the data, extrapolating from control samples with altered lepton selection. Numerous cross-checks of the non-prompt background estimate are performed; these also form the basis for the derived systematic uncertainty. The background estimates, in particular the non-prompt background, are studied in a variety of data control regions, defined by modifying the isolation requirement, inverting the impact parameter significance cut, or loosening the transverse momentum selection. Verifying the background modeling in several control regions before "opening the box" and looking at the signal region is a crucial component of the analysis.

4.3 Results and Interpretations

The signal region with like-sign muon pairs is analyzed in a few different ways. The dimuon invariant mass distribution is studied for any discrepancy between the observation in data and the background estimate. Five mass ranges are defined from $m > 15$ GeV to $m > 400$ GeV for which the data and background yields are compared. The data observation and background predictions are further studied separately for $\mu^+\mu^+$ and $\mu^-\mu^-$.

The observed yield in data are used to derive upper limits on the possible number of prompt muons originating from non-Standard Model sources in each mass bin. Limits are placed both inclusively and separately for positive and negative-charged pairs. The upper limits on the number of muon pairs are further translated to constraints on the production cross section for sources of new physics contributing to the sample. Cross-section limits are placed with respect to a region of phase space, defined to closely emulate the criteria used to select the reconstructed dimuon sample. This phase-space region is referred to as the *fiducial region*.

In addition to the inclusive search, the data is searched for a narrow like-sign dimuon resonance, as predicted for instance from the production of doubly charged Higgs bosons. For the narrow resonance search, mass windows are defined to ensure optimal signal sensitivity across the full mass range considered. In each mass window, the number of observed events is compared to the total expected background and signal yield to derive a limit on the signal contributions.

Chapter 5

Object Reconstruction and Performance

Physics objects are reconstructed using inputs from the different detector subsystems. Trajectories of charged particles traversing the detector, *tracks*, are reconstructed from hit information in the inner detector. Muons are detected by the muon spectrometer and reconstructed using a combination of inner-detector track information, muon-spectrometer measurements, and information about energy deposits in the calorimeters. Electrons and photons, which are not directly used in the search, are identified and measured by the calorimeters and the inner detector. Track and muon reconstruction, crucial to this search, are described in detail in this chapter. The reconstruction of jets and missing transverse momentum from calorimeter information, used indirectly in the search, is summarized as well. Finally, the performance of muon properties which are important for identifying prompt muons, such as muon isolation, is discussed.

5.1 Track Reconstruction

Charged particles with transverse momentum $p_{\mathrm{T}} > 400$ MeV and pseudorapidity $\eta < 2.5$ are reconstructed and measured with the inner detector and its surrounding solenoidal magnetic field. The track reconstruction begins by forming three-dimensional hit objects from hit information in the silicon detectors. The actual track finding is performed using the three-dimensional hit objects as input. During a post-processing stage following the track finding, primary vertices are formed from the reconstructed tracks.

Raw hit data from neighboring pixel sensors and silicon microstrips are grouped into pixel and SCT *clusters* [75]. Pixel and strip hits that are classified as noisy by either an online calibration or the offline detector monitoring are rejected during the cluster formation stage [76]. The input to the succeeding track finding is

three-dimensional hit objects, *space-points*. Since pixel modules measure local two-dimensional coordinates, pixel clusters can be transformed to a three-dimensional space-point representation by adding information of the radius of the pixel layer. For SCT modules, which are double-sided with separate sensors on the two module sides, clusters from the two sides are grouped together to form three-dimensional space-points. For the TRT, raw timing information is converted into calibrated *drift circles*, defined as the radial distance between the central wire in a TRT straw to the position of the traversing particle.

The default track reconstruction begins by identifying *track seeds*. They are formed by combining space-points from any three of the inner four silicon layers (three pixel plus one SCT layer), with a constraint of originating from near the interaction region. By fitting and including additional silicon hits, seeds are extended through the remaining SCT layers to construct track candidates.

Before extending tracks into the TRT, ambiguities in associating clusters to tracks must be solved and fake tracks be rejected. This is achieved by imposing track quality requirement such as limiting the maximum allowed number of clusters that are shared with other tracks and limiting the number of active sensors which are crossed by a track without generating hits, *holes*. Silicon track candidates are extended into the TRT by searching for hits around the extrapolated track path. The full combined track is thereafter refitted. If the TRT-extended track gives an improved fit result, the combined track is kept, otherwise the original silicon track is stored.

This inside-out tracking scheme is not ideal for reconstructing tracks originating from secondary vertices, such as long-lived particles or photon conversions. An alternative procedure is employed as a complement to the default tracking, *back tracking*. Here, TRT track segments which are not already associated to a silicon track are used and extended back into the silicon by assigning clusters not associated to existing tracks [75].

5.1.1 Track Parametrization

Charged particles in a uniform magnetic field follow helical trajectories. Reconstructed tracks of such particles can be described with five helix parameters. The parametrization used in ATLAS [63] is

$$(d_0, z_0, \phi_0, \cot\,\theta, q/p_{\mathrm{T}}), \tag{5.1}$$

where the different parameters are defined below.

- d_0: The transverse impact parameter, defined as the distance of closest approach between the track and the beam axis in the x-y plane. The sign of the transverse impact parameter is determined by the reconstructed angular momentum of the track about the beam axis.

- z_0: The longitudinal impact parameter, defined as the z position of the track at the point of closet approach in the R-z plane.
- ϕ_0: The azimuthal angle between the track and the tangent of closest approach, with $\tan \phi_0 = p_y/p_x$.
- $\cot \theta$: Cotangent of the polar angle, with $\cot \theta = p_z/p_{\mathrm{T}}$.
- q/p_{T}: The track curvature, defined as the inverse of the transverse momentum (p_{T}) multiplied by the charge of the track.

5.1.2 Primary Vertex Reconstruction

The reconstruction of primary vertices from tracks in the inner detector proceeds in two steps [77]. First, tracks are associated to vertex candidates by a primary vertex finding algorithm, and secondly, a vertex fitting algorithm is used to reconstruct the vertex position. Reconstructed ID tracks are additionally refitted with a constraint that they originate from the primary vertex.

During 2011, the primary vertex reconstruction used tracks with $p_{\mathrm{T}} > 400$ MeV. Tracks were required to fulfill a minimal set of silicon and TRT hit requirements and to originate from close to the luminous region, known as the *beam spot*. These track quality cuts are placed to minimize the fraction of fake tracks and tracks originating from secondary interactions rather than from the primary interaction vertex.

The *iterative vertex finding* approach is used to reconstruct vertices from pre-selected tracks [77]. A vertex seed is defined using the global maximum in the distribution of the z coordinate for these tracks, as determined with respect to the center of the beam spot. The actual vertex position is determined using the *adaptive vertex fitting* algorithm [78]. This is a robust χ^2-based fitting algorithm which uses the seed positions and their surrounding tracks. Outlying tracks are down-weighted based on their compatibility with the vertex. Tracks which are incompatible with the primary vertex by more than 7σ are used to seed a new vertex. The association of tracks to vertices is repeated until all tracks have been assigned to vertices or no additional seed vertices can be formed.

Several primary vertices can be reconstructed for a given event. The primary event vertex is usually defined as the vertex corresponding to the highest $\sqrt{\sum p_{\mathrm{T}}^2}$ value, the scalar p_{T} sum of all tracks associated to the vertex. For Z bosons decaying to electrons or muons, the efficiency of requiring a primary event vertex reconstructed with at least three tracks (the requirement used for the like-sign dimuon search) is close to 100%.

5.2 Muon Reconstruction

Muons are reconstructed using a combination of tracks in the inner detector, hits and tracks in the muon spectrometer, and information about the energy loss in the calorimeter. There are three primary types of muon reconstruction in ATLAS, each with varying purity and reconstruction efficiency [4]. These are:

Stand-alone muons: Stand-alone muon reconstruction only uses information from the muon spectrometer, reconstructing tracks with $|\eta| < 2.7$. Tracks are reconstructed from at least two local MS track segments and constrained to originate from near the interaction region. The momentum measurement in the muon spectrometer is corrected for the muon energy loss in the calorimeters.

Combined muons: Combined muons are the highest-purity muons, formed by requiring independently reconstructed ID and MS tracks. Combined muon reconstruction is restricted to $|\eta| < 2.5$, limited by the ID acceptance. The reconstruction efficiency is driven by the efficiency of reconstructing a MS-only track and varies with η and ϕ. The efficiency is lower around $\eta = 0$ due to limited detector coverage in this region resulting from services extending down to the calorimeters and the inner detector. The reconstruction efficiency is also lower in the transition region between the barrel and endcap sections of the muon system, around $|\eta| = 1.2$, where muons only traverse one chamber.

Segment-tagged muons: Segment-tagged muons are formed based on a track in the inner detector and a local track segment in the muon spectrometer (unlike combined muons for which a complete track extrapolated through the entire muon system is required). Segment-tagged muons are constructed within $|\eta| < 2.5$ and are particularly useful for identifying very low-p_{T} muons which do not reach the outer muon stations and therefore do not form an MS track. Segment-tagged muons are also complementary to the stand-alone reconstruction in low-efficiency η regions.

All types of muon reconstruction need to take into account the muon energy loss in the calorimeters. Energy losses occur due to ionization, bremsstrahlung, and electron pair-production (e^+e^-). Ionization is the primary source of energy loss below about 100 GeV, while bremsstrahlung and electron pair-production, jointly referred to as radiative energy losses, become more dominant at higher p_{T} [79]. The energy loss is about 3 GeV for muons traversing the central barrel region, while at higher pseudo-rapidity it is larger as a consequence of the increased amount of material traversed. The energy loss is estimated by an algorithm which uses either a parametrization of the most probably energy-loss value or the measured calorimeter energy. The latter is

used only for isolated tracks with a significantly larger measured calorimeter energy compared to the parametrized energy loss [63].

ATLAS has two separate algorithm chains for performing track reconstruction in the muon system. The chain employed by this analysis use `Muonboy` for reconstructing stand-alone muon tracks and `STACO` to form combined muons [80]. This search relies solely on combined muons, as they provide the highest muon purity and also allow the rate of muon charge misidentification to be constrained by requiring the charge of the ID-only and MS-only tracks to agree. With this requirement, muons must be mismeasured by both subsystems in order to result in charge misidentifications.

The reconstruction of tracks in the muon spectrometer using `Muonboy` proceeds as follows. First, local regions of activity with at least one RPC/TGC hit in both the bending and non-bending directions are identified. These regions measure about 0.4×0.4 in (η, ϕ). Within each of the three muon stations, local straight track segments are reconstructed around the regions of activity by combining hits in adjacent MDT multi-layers. For a given station, a local straight track approximation is valid. The local track segment is required to point back towards the interaction region to reduce contributions of fake tracks. Constructing local track segments before performing global track fits simplifies the complicated task of track fitting over the large distances that separate different muon stations. Global muon track candidates are first formed by combining local track segments. Inhomogeneities in the muon system magnetic field are taken into account at this stage. A global fit is then performed of the track candidates using individual hit information rather than the combination of local track segments.

The `STACO` combined muon reconstruction performs a statical combination of the individual ID-track and MS-track measurements using their respective track parameters and covariance matrices. The track combination initially searches for ID-MS pairs that are roughly consistent in (η, ϕ). If the parameter vectors of the two tracks are P_1 and P_2 with covariance matrices C_1 and C_2, and the parameter vector of the combined track is P, then the χ^2 of the combination is

$$\chi^2 = (P - P_1)^T \times C_1^{-1} \times (P - P_1) + (P - P_2)^T \times C_2^{-1} \times (P - P_2). \tag{5.2}$$

Only track combinations with a global match χ^2 below a pre-defined maximum value are considered. For muons used in the search, $\chi^2 < 150$ was required. If multiple combinations are possible, the one with lowest χ^2 is chosen. The combined muon momentum resolution is dominated by the ID measurement for $p_{\mathrm{T}} < 80(20)$ GeV in the barrel (endcap), and by the MS for $p_{\mathrm{T}} > 100$ GeV. In the intermediate range of transverse momentum, the two measurements have comparable weights [81].

5.3 Jets and Missing Transverse Momentum

The search relies only indirectly on reconstructed hadronic jets and missing transverse momentum. Jets are used as part of the isolation criteria, requiring muons to be well separated from reconstructed jets to suppress background due to hadronic decays. The missing transverse momentum is used as one variable of study for control regions verifying the non-prompt background estimate.

Jet Reconstruction

Jet candidates are formed from topological clusters in the calorimeter [82]. Topological clusters are groups of neighboring calorimeter cells which are formed starting from a seed cell to which nearby cells are added iteratively, ensuring that the cell energy is above a predefined noise threshold. Jet candidates are reconstructed from such topological clusters using the anti-k_t algorithm [83] with a distance parameter R of 0.4. The anti-k_t algorithm is used as it is infrared and collinear safe, meaning that neither soft emissions nor collinear splittings significantly change the jet energy.

Jet energy measurements are corrected for various instrumental effects. These include calorimeter non-compensation (partial measurement of hadron energy deposits), energy losses due to inactive detector regions, and leakage of particles to outside the calorimeter. Energy measurements are also affected by energy deposits within the jet cone from particles not associated with the jet. Furthermore, quality criteria are applied to remove reconstructed jets not arising from hard-scattering interactions [84].

Missing Transverse Momentum Reconstruction

The missing transverse momentum in an event is defined as the momentum imbalance in the transverse plane (where momentum balance is expected in contrast to in the z-direction). Momentum imbalance in the transverse plane is expected as a result of neutrinos escaping the detector but it is also an important signature of new stable particles which neither interacts electromagnetically nor hadronically in the detector.

The vectorial momentum imbalance is the negative sum of the momentum of all detected particles and $E_{\mathrm{T}}^{\mathrm{miss}}$ refers to its magnitude, defined as

$$E_{x(y)}^{\mathrm{miss}} = E_{x(y)}^{\mathrm{miss,calo}} + E_{x(y)}^{\mathrm{miss},\mu} \tag{5.3}$$

$$E_{\mathrm{T}}^{\mathrm{miss}} = \sqrt{(E_x^{\mathrm{miss}})^2 + (E_y^{\mathrm{miss}})^2}. \tag{5.4}$$

The `MET_RefFinal` algorithm was used to reconstruct the missing transverse momentum. It calculates $E_{\mathrm{T}}^{\mathrm{miss}}$ by including contributions from energy deposits in the calorimeters ($|\eta| < 4.9$), calibrating cells to the objects with which they are associated, and tracks reconstructed in the muon spectrometer ($|\eta| < 2.7$). More details can be found in Ref. [85].

5.4 Muon Isolation and Impact Parameter

Muons selected for the search are required to be prompt, originating directly from the hard interaction. Muon isolation and impact parameter significance are two main variables for selecting prompt muons with high efficiency while rejecting muons from non-prompt sources, thus minimizing the background contributions. The definition of these variables, their use in rejecting background, and motivation for the selection criteria chosen for the search are discussed in the remainder of this chapter.

5.4.1 Track Quality Selection

The muon track in the inner detector must fulfill a set of hit quality requirements, as recommended by the ATLAS muon combined performance group [86]. If the muon traverses an active module in the innermost pixel layer, a hit must be registered in this layer. An active pixel module is one for which the high voltage and preamplifiers are turned on, and which is registering hits without readout issues, timing errors, or other problems. A module is classified as active or inactive on an event-by-event basis. The requirement removes muons originating from hadronic decays occurring after the innermost pixel layer.

The number of recorded hits summed with the number of dead sensors crossed by the muon must be greater or equal to two in the pixel detector and greater or equal to six in the SCT. Furthermore, the total number of pixel and SCT holes, i.e. the number of non-registered hits where a hit is expected, must be less than three.

A successful extension from the silicon-based detectors to the TRT is required where expected. Denote the number of TRT hits by n_{TRT}^{hits}, the number of TRT outliers (hits not associated with a track) by $n_{TRT}^{outliers}$, and set $n = n_{TRT}^{outliers} + n_{TRT}^{hits}$. The TRT track extension requirement can then be summarized as:

- For $|\eta| < 1.9$: Require $n > 5$ and $n_{TRT}^{outliers} < 0.9n$
- For $|\eta| \geq 1.9$: If $n > 5$, then require $n_{TRT}^{outliers} < 0.9n$

5.4.2 Muon Isolation

Isolation is the main handle for reducing background due to non-prompt muon sources. Different type of isolation variables can be defined which rely on either the calorimeter or the inner tracking system. Calorimeter-based isolation uses information from calorimeter clusters inside a cone around the muon direction. Track-based isolation instead measures the combined transverse momentum of tracks within a cone around the muon track in the inner detector. An alternative track-based isolation method is to count the number of tracks within a cone around the muon, although this latter method is not commonly used in ATLAS.

The calorimeter-based isolation variable ($E_{\mathrm{T}}^{\mathrm{cone}\Delta\mathrm{R}_{\mathrm{iso}}}$) is defined as the sum of calorimeter cluster energies deposited in a given cone of size ΔR_{iso} surrounding the cell in which the muon deposited energy. Typically, cone sizes of $\Delta R_{\mathrm{iso}} = 0.2$, 0.3, or 0.4 are considered. Only cells above a predefined noise threshold are used, currently corresponding to an RMS of 3σ. The default track-based isolation variable ($p_{\mathrm{T}}^{\mathrm{cone}\Delta\mathrm{R}_{\mathrm{iso}}}$) is defined as the sum of transverse momenta of all tracks with $p_{\mathrm{T}} > 1$ GeV, excluding the muon track itself, within a cone of ΔR_{iso}.

Loose impact parameter and track quality requirements are placed on tracks used in defining the track-based isolation variable, listed below. These cuts help reduce the dependence of the isolation variable on pileup.

- $d_0 < 10$ mm
- $z_0 < 10$ mm
- Number of silicon hits $(N_{pixel} + N_{SCT}) \geq 4$

Pileup Effects

Defining a clean isolation variable in the presence of high pileup is non-trivial. Calorimeter-based isolation is particularly sensitive to these effects. Both in-time pileup, resulting from overlapping interactions in the same bunch crossing, and out-of-time pileup, due to interactions in adjacent bunch crossings, are of concern. Track-based isolation is less sensitive to in-time pileup as only tracks associated to the primary event vertex are used to determine the isolation variable. Out-of-time pileup is of no concern at all since hits from previous crossings do not confuse the track reconstruction.

For calorimeter isolation, in-time pileup results in a general increase of activity in the calorimeter as particles from overlapping interactions deposit their energy. This increases the measured energy in the isolation cone, in turn resulting in that also muons that would otherwise be considered as isolated will have a significant amount of activity in nearby calorimeter cells. Contributions from activity in previous bunch crossing are of concern due to the long readout pulse of the liquid-argon electromagnetic calorimeter of about 600 ns, significantly longer than the LHC bunch-spacing. The pulse is shaped with an initial peak followed by a long negative tail, as illustrated in Figure 5.1, designed to integrate to zero so that for a particular bunch crossing, contributions due to interactions in previous bunch crossings are effectively canceled out with the in-time pileup. As a consequence of the LHC bunch-train structure, bunches in the beginning of a train do not see a net negative contribution from out-of-time pileup but only the positive contribution from in-time pileup.

The dependence on in-time pileup for different isolation variables is evaluated by studying isolation efficiencies as function of the number of reconstructed primary vertices per event. The number of primary vertices is strongly correlated with the

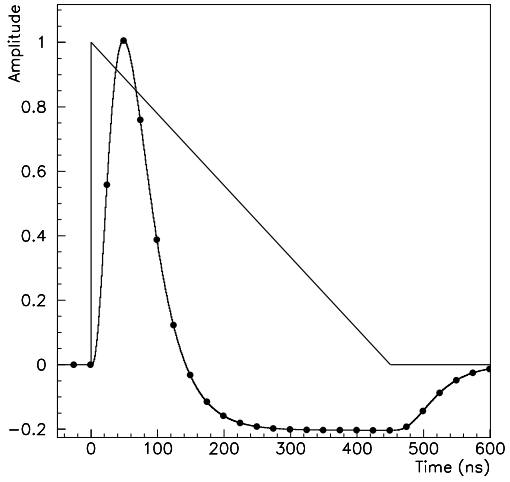

Figure 5.1: Pulse shape of the output signal from the front-end readout electronics of the liquid-argon electromagnetic calorimeter as function of time (dotted line) for a triangular pulse [4].

number of interactions, although not a direct measure thereof due to a finite efficiency. All primary vertices that are reconstructed with at least two tracks are counted. These studies required the isolation energy to be less than 8% of the muon transverse momentum. Cone sizes of $\Delta R_{\text{iso}} = 0.2$ and 0.4 are considered and both calorimeter-based and track-based isolation are studied. Figure 5.2 shows the isolation efficiency as function of the number of reconstructed primary vertices for muons in simulated $Z \to \mu\mu$ events, generated with Pythia, and selected by requiring a pair of opposite-sign muons with $p_{\text{T}} > 20$ GeV in an invariant mass window around the Z mass (81–101 GeV). Also shown are similar efficiencies for muons from simulated $b\bar{b}/c\bar{c}$ events, generated with Pythia. Here, dimuon events are selected with invariant mass above 15 GeV and the leading (subleading) muon must have $p_{\text{T}} > 20(10)$ GeV.

The calorimeter-based isolation variables show large dependence on in-time pileup, particularly for the large cone size. The result is a significantly reduced isolation efficiency for prompt muons in presence of high pileup. With a narrow cone size, the pileup dependence is reduced, however, a narrow isolation cone is also significantly less powerful in rejecting non-prompt muons. Track-based isolation show no or minimal dependence on pileup. For a large cone size, its rejection power is similar to that of the calorimeter-based variable. Table 5.1 shows the efficiency for prompt and non-prompt muons, integrated over p_{T}, to pass a track-based isolation selection of 5%, 8%, or 10%, as estimated from Monte Carlo.

The isolation dependence on out-of-time pileup is studied by comparing the aver-

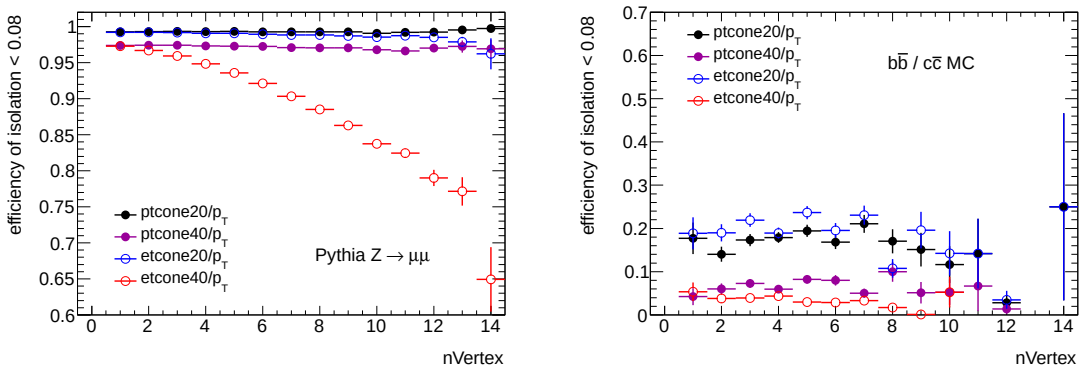

(a) (b)

Figure 5.2: Efficiency of an 8% relative isolation cut for different isolation variables as a function of the number of reconstructed primary vertices in the event, shown for (a) prompt muons from simulated $Z \to \mu\mu$ events and (b) non-prompt muons from simulated $b\bar{b}/c\bar{c}$ events.

age isolation energy as function of bunch crossing identification (BCID). Figure 5.3 shows the mean isolation energy for simulated $Z \to \mu\mu$ events for calorimeter-based and track-based isolation, respectively, with three different sizes of the isolation cone as function of the BCID[1]. As expected, track-based isolation is independent of out-of-time pileup effects. Calorimeter-based isolation, on the other hand, shows large biases depending on the bunch position in a train.

In conclusion, track-based isolation offers high isolation efficiency for prompt muons while keeping good rejection of muons from non-prompt sources. Additionally, the variable has almost no dependence on either in-time or out-of-time pileup. Track-based isolation, with a large cone of $\Delta R_{\text{iso}} = 0.4$, is therefore chosen for this analysis. Placing p_{T}-dependent isolation criteria is also powerful as it results in a tight cut for low p_{T} where the non-prompt background contribution is most dominant, while it gives a looser isolation criteria at high muon p_{T}.

[1]The spikes in Figure 5.3 is a non-physical artifact from the analysis.

Prompt muons ($Z \to \mu\mu$)			
Isolation variable	$< 10\%$	$< 8\%$	$< 5\%$
$p_{\mathrm{T}}^{\mathrm{cone0.2}}/p_{\mathrm{T}}$	99.5	99.3	98.5
$p_{\mathrm{T}}^{\mathrm{cone0.4}}/p_{\mathrm{T}}$	98.1	97.3	94.7

Non-prompt muons (bb / $c\bar{c}$)			
Isolation variable	$< 10\%$	$< 8\%$	$< 5\%$
$p_{\mathrm{T}}^{\mathrm{cone0.2}}/p_{\mathrm{T}}$	12.0	9.9	6.8
$p_{\mathrm{T}}^{\mathrm{cone0.4}}/p_{\mathrm{T}}$	5.0	3.4	1.8

Table 5.1: Efficiency of isolation cut as obtained from Monte Carlo simulation of PYTHIA $Z \to \mu\mu$ and $b\bar{b}/c\bar{c}$ events.

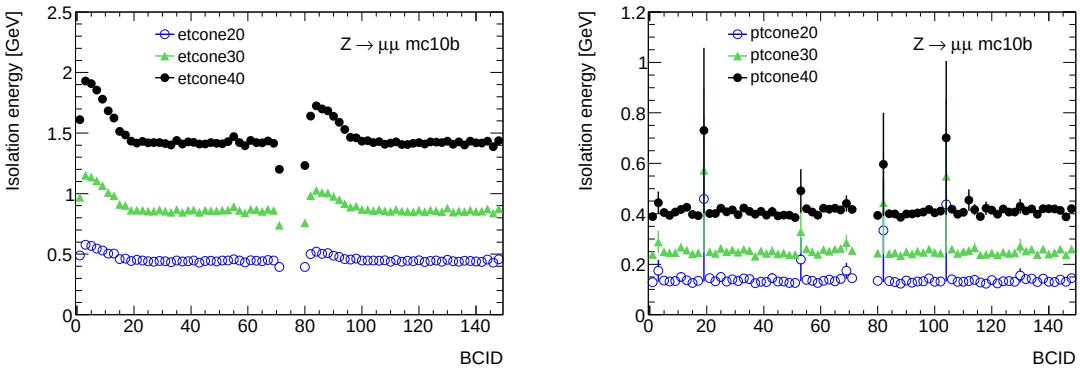

(a) (b)

Figure 5.3: Mean isolation energy for (a) calorimeter-based isolation and (b) track-based isolation, with three different sizes of the isolation cone as function of the bunch crossing identification (BCID), shown for prompt muons from simulated $Z \to \mu\mu$ events.

5.4.3 Impact Parameter Significance

Another powerful muon selection variable for reducing background contributions due to non-prompt muons from heavy-flavor decays is the impact parameter significance. Figure 5.4 shows the impact parameter significance, $|d_0|/\sigma(d_0)$, for prompt muons selected from Monte Carlo simulated $t\bar{t}$ events, explicitly requiring muons to originate directly from the decay of a W boson. The impact parameter significance is also shown for non-prompt muons, selected from a simulated sample of $b\bar{b}/c\bar{c}$ events. Non-prompt muons from heavy-flavor decays are expected to have a broader impact parameter significance distribution because the decay-muons originate from a non-negligible distance away from the primary vertex (see discussion in Section 4.1). A cut on $|d_0|/\sigma(d_0) < 3$ is highly efficient for prompt muons, while it rejects a significant fraction of non-prompt muons from heavy-flavor decays. According to MC, 97% of prompt muons are retained while 40% of muons from b-hadron decays are rejected.

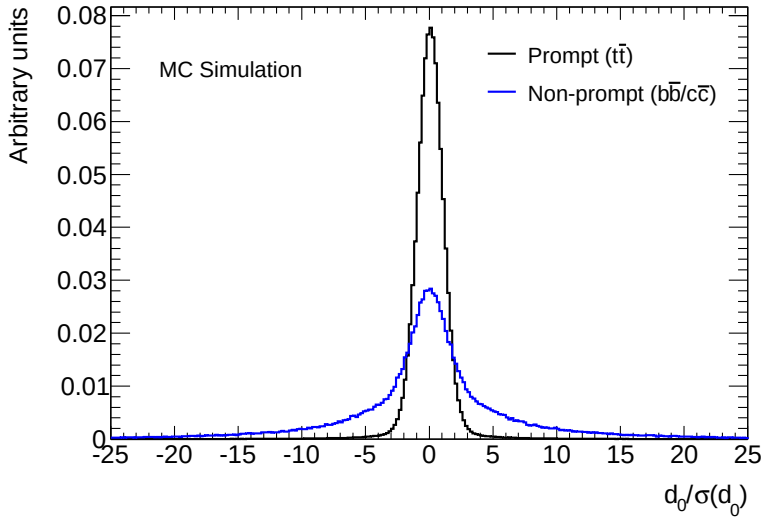

Figure 5.4: Impact parameter significance for prompt muons from simulated $t\bar{t}$ events and non-prompt muons from simulated $b\bar{b}/c\bar{c}$ events.

Chapter 6

Alignment of the Inner Detector

Correctly reconstructing trajectories of charged particles and precisely measuring their momenta, as well as performing accurate vertex finding, is of crucial importance for nearly all ATLAS physics analyses. The search presented in this dissertation relies, for instance, on well-measured track impact parameters to reduce background from non-prompt sources, precise momentum measurements for the reconstruction of the dimuon invariant mass, and correct charge assignments to accurately select like-sign dimuons and to minimize background from charge misidentification.

Many effects can cause a degradation of the inner detector tracking performance, such as an incomplete understanding of the detector material or the locations of detector sensor elements. An important part of achieving the required performance, driven by the physics goals of the experiment, is performing an *alignment* of the inner detector. The goal of the alignment is to accurately determine the positions and orientations of individual detector modules as well as the locations of larger detector structures relative to each other. The alignment procedure is vital in minimizing misalignment effects which degrade measurements of physics quantities. Both random module-by-module misalignments and global systematic detector distortions can be present. Random misalignments are efficiently removed by the alignment procedure. Standard track-based alignment algorithms are, however, often incapable of resolving global distortions which introduce systematic biases of track measurements. Eliminating such distortions requires special techniques to be applied during the alignment.

The Z resonance with its decay to oppositely-charged muons provides a clean event signature and a powerful tool for studying the alignment performance and probing associated systematic effects. Its intrinsic width has been measured with high precision to $\Gamma_Z = 2.4952 \pm 0.0023$ GeV at LEP [7]. The experimental dimuon mass resolution is therefore a direct measure of detector effects. Other abundantly produced dimuon resonances such as the J/ψ can be used for the same purpose. However, the Z boson has a strong advantage because its decay muons have considerably higher transverse momentum compared to muons from low-mass resonances. Muons from Z decays are thus less sensitive to systematic effects in the inner detector material

description as material effects are relevant particularly at low p_{T}. The measured resolution of the reconstructed Z-boson mass is instead directly sensitive to alignment effects.

This chapter discusses the alignment of the inner detector within the context of performance studies using $Z \to \mu^+\mu^-$ decays. An overview of the general alignment procedure is given, with particular focus on the alignment during 2011 when significant systematic detector distortions emerged as larger data samples became available. Systematic distortions are discussed as well as techniques for how to probe and correct for them, with examples shown where systematic misalignments have been introduced for Monte Carlo simulated Z events. Finally, results of the alignment performance in the data processing used for the like-sign dimuon search are shown.

6.1 Alignment Overview

Aligning the inner detector requires determining almost 35,000 degrees-of-freedom for the silicon detectors and 700,000 for the TRT [87]. This impressive number of degrees-of-freedom follows from the large number of individual silicon modules and TRT straws. Table 6.1 shows a summary of the alignable structures and their properties. The alignment is performed using a combination of isolated, high-p_{T} collision tracks and cosmic-ray tracks collected between periods of collision data taking. The baseline goal of the alignment is to determine the positions and orientations of detector modules with high precision such that any limited knowledge of sensor locations should not degrade the resolution of track parameters by more than 20% with respect to the intrinsic tracker resolution. This requires aligning the silicon pixel (strip) modules to a precision of 7 (12) μm in the $R\phi$ direction [76]. Precision measurements require even higher accuracy. For instance, measuring the W-boson mass requires an understanding of module positions at an accuracy level of 1 μm [4].

Subdetector	Alignable structures	Element size	Intrinsic resolution
Pixel	1774 modules	50 μm $\times$ 400 μm	10 μm ($R\phi$), 115 μm (Rz)
SCT	4088 modules	80 μm $\times$ 12 cm	17 μm ($R\phi$), 580 μm (Rz)
TRT	350,848 straws	4 mm (diameter)	130 μm ($R\phi$)

Table 6.1: Details of the aligned detector components.

6.1.1 Alignment Procedure

The alignment is performed in three stages with increasing granularity at each stage [87]:

- *Level (1)* Relative alignment of different subdetectors with respect to each other.
- *Level (2)* Alignment of separate layers in a given subdetector.
- *Level (3)* Alignment of individual modules or straws in each detector layer.

To minimize effects due to multiple scattering which are significant at low momentum, the alignment relies on high-p_{T} tracks from both collision and cosmic-ray events.

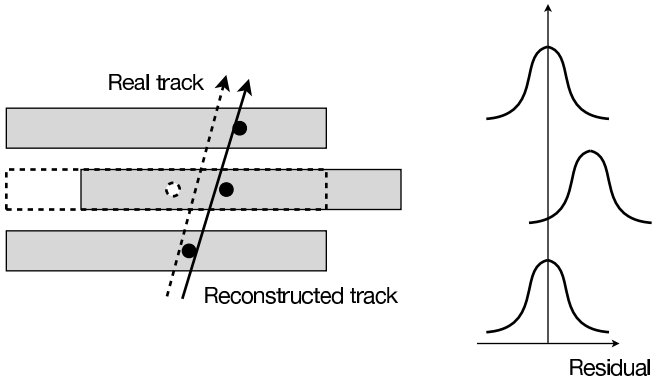

Figure 6.1: Principle of track-hit residuals.

The alignment is based on measuring and minimizing track-hit residuals, defined as the distance between the extrapolated track position on a given module to the actual recorded hit position in the same module, illustrated in Figure 6.1. Two independent alignment algorithms have been developed:

- *Global* χ^2 *alignment* involves a simultaneous fit of all track and alignment parameters by minimizing a χ^2, resulting in a linear system with a size corresponding to the number of alignment degrees-of-freedom.
- *Local* χ^2 *alignment* is instead based on aligning each detector module separately which requires solving a system of up to six linear equations for each module.

Each alignable structure, from individual modules to entire layers and disks, has a total of six degrees-of-freedom: three translations (T_x, T_y, T_z) determining the position and three rotations (R_x, R_y, R_z) for the orientation[1]. The *alignment constants* define the alignment which minimizes a χ^2 of the track-hit residuals. Helical

[1]Pixel and SCT modules as well as TRT endcap wires are aligned using six degree-of-freedom while TRT barrel wires use five degrees-of-freedom.

trajectories of charged particles are parametrized, as discussed in Section 5.1.1, using

$$\boldsymbol{\tau} = (d_0, z_0, \phi_0, \theta, q/p). \tag{6.1}$$

The χ^2 is then constructed as

$$\chi^2 = \sum \boldsymbol{r}^{\mathrm{T}} V^{-1} \boldsymbol{r}, \tag{6.2}$$

where the sum is over all tracks used in the alignment and $\boldsymbol{r} = \boldsymbol{r}(\boldsymbol{\tau}, \boldsymbol{a})$ is the vector of track-hit residuals for a track, which depends on the track parameters ($\boldsymbol{\tau}$) and the alignment parameters ($\boldsymbol{a}$). The alignment parameters contain all parameters which are aligned, corresponding to three translations and three rotations for each structure. For global χ^2 alignment, all structures are aligned simultaneously, while for local χ^2, each module is aligned separately. V is the covariance matrix of the hit measurements. The χ^2 minimization is performed with respect to $\boldsymbol{a}$. Further details on local and global χ^2 alignment and the complex problem of solving the alignment can be found in Ref. [87].

Different constraints may be enforced during the alignment. Tracks can be constrained to originate from the beam spot or from a primary vertex. Information of pixel module deformations from a survey of the detector elements, taken during the assembly and installation of the detector, are considered.

6.1.2 Global Systematic Distortions

The track-based alignment algorithms are powerful in eliminating random residual misalignments. However, global systematic distortions of the detector may remain. The presence of systematic distortions is a consequence of the cylindrical symmetry of the detector combined with using tracks originating from a common interaction point. Track-hit residuals are left unbiased for tracks from a common origin and are thus unaffected by standard alignment algorithms. This is not the case for cosmic-ray tracks, however, aligning the detector using only cosmic rays is of limited power. Specifically the endcap regions of the detector are difficult to constrain with cosmic-ray muons since these typically traverse the detector vertically. Eliminating systematic distortions is vital for accurate momentum measurements and charge determinations.

To distinguish different modes of systematic distortions, a simplified parametrization scheme is constructed with shifts in radial, azimuthal, or z directions (ΔR, $\Delta\phi$, Δz) as function of corresponding global cylindrical coordinates (R, ϕ, z). The nine modes are summarized in Table 6.2, with descriptive names indicating the resulting type of distortion.

Different approaches can be considered to remove systematic biases. These include running the alignment algorithms with a different track sample, for instance tracks from cosmic-ray or beam-halo events or tracks collected during times when the solenoid field surrounding the inner detector was turned off. Without the magnetic

	ΔR	$\Delta\phi$	Δz
R	Radial expantion	Curl	Telescope
ϕ	Elliptical	Clamshell	Skew
z	Bowing	Twist	z expansion

Table 6.2: Schematic overview of different global systematic distortions.

field, all tracks of charged particles are expected to be straight. Another alternative is to enforce constraints during the alignment procedure. The momentum as measured by only the muon spectrometer can be used to constrain the momentum as measured by the inner detector, assuming that any misalignment in the MS is uncorrelated with biases present in the ID. Constraints derived using the ratio of the electron energy as measured by the calorimeter to the electron momentum as measured by the inner detector (E/p) can also be imposed. Alignment using constraints derived from the E/p ratio for positively and negatively-charged electrons was successfully employed during 2011. The goal was to reduce large charge-dependent momentum biases that were observed in particularly the endcap regions. This will be discussed further in Section 6.2.3.

6.2 Alignment Performance with $Z \to \mu\mu$ Decays

The Z resonance is in many aspects a powerful calibration tool for the LHC experiments; abundantly produced with clean final states as well as a well-known mass and intrinsic width. Here it is used for evaluating the alignment performance and probing global systematic detector distortions. For these studies, high-quality tracks of muons from Z decays are selected in the inner detector. The dimuon invariant mass is reconstructed and its mean value and measured width are used as probes to study the alignment performance.

6.2.1 Event Selection

$Z \to \mu\mu$ candidates are selected by identifying pairs of oppositely-charged muons that have high-quality tracks in the inner detector. The data used for these studies were collected during pp collisions at a center-of-mass energy of 7 TeV between March and July of 2011. The data were collected using a single muon trigger with a transverse momentum threshold of 10 GeV at the Level-1 trigger and 18 GeV at the event filter. The total data sample corresponds to an integrated luminosity of 1.2 fb^{-1}.

Events are required to have a primary vertex reconstructed with at least five tracks. Muon candidates are identified using both the muon spectrometer and the inner detector. Only combined muons are selected, while the track parameters are

determined using only the inner detector track segment. The track segment in the inner detector must fulfill the track-quality requirements described in Section 5.4.1 to ensure well-measured tracks. Muon candidate must have $p_{\mathrm{T}} > 20$ GeV, $|\eta| < 2.5$, and be isolated from other nearby tracks to reduce background from non-prompt muons. The exact requirement is $p_{\mathrm{T}}^{\mathrm{cone0.40}}/p_{\mathrm{T}}(\mu) < 0.2$. The track impact parameters determined with respect to the primary event vertex must be small as well: $|d_0| <$ 0.2 mm and $|z_0| < 1.0$ mm.

Events containing two oppositely-charged muons, satisfying the above selection criteria, are used to reconstruct Z candidates. The dimuon invariant mass must be between 60 GeV and 120 GeV. When fitting mass distributions, a narrower mass window of 71–111 GeV is used.

Fitting Procedure

A fit of the reconstructed dimuon invariant mass is performed in order to extract the mean and width of the distribution. The shape of the reconstructed Z mass is a combination of the intrinsic Z-boson mass distribution and the experimental detector resolution.

The non-relativistic Breit-Wigner distribution is used to describe the intrinsic Z-mass distribution

$$f(x;\mu,\Gamma_Z) = \frac{1}{(x-\mu)^2 + 1/4\Gamma_Z^2}, \tag{6.3}$$

where μ is the mean mass and Γ_Z is the intrinsic Z width, kept fixed at its well-determined value of 2.495 GeV. To describe the resolution effects, a Crystal-Ball function is used. The Crystal-Ball function consists of a Gaussian core and a one-sided polynomial tail which takes the radiative energy loss into account. The point where the Gaussian and the polynomial functions meet can be written in terms of a parameter α as $(\mu_0 - \sigma \times \alpha)$, where μ_0 is the mean and σ the resolution:

$$f(x;\alpha,n,\mu_0,\sigma) = N \cdot \begin{cases} \exp(-\frac{(\mathrm{x}-\mu_0)^2}{2\sigma^2}), & \text{for } \frac{(\mathrm{x}-\mu_0)^2}{2\sigma^2} > -\alpha \\ A \cdot (B - \frac{(x-\mu_0)^2}{2\sigma^2})^{-n}, & \text{for } \frac{(\mathrm{x}-\mu_0)^2}{2\sigma^2} \leq -\alpha \end{cases} \tag{6.4}$$

The slope of the polynomial tail is described by the parameter n, and the variables N, A, and B are overall normalization constants. In these fits, α is kept fixed at a value determined from Monte Carlo simulation ($\alpha = 2.0$) whereas σ and n are allowed to float. μ_0 is fixed to zero since the mean mass is determined by the mean of the Breit-Wigner in the combined fit to the convolution of the two functions. The fit is performed as an unbinned maximum-likelihood fit, and the mean (μ from the Breit-Wigner) and resolution (σ from the Crystal-Ball) are extracted for subsequent studies.

An example of the mass fit is shown in Figure 6.2 for $Z \to \mu\mu$ candidates in data, reconstructed with the spring 2011 alignment. Shown are both fits of Z candidates

where (a) both muons fall in the central barrel region ($|\eta| < 1.05$) and (b) events where both muons are in endcap A ($1.05 < \eta < 2.5$). For the barrel, the mass fit agrees well with the observed distribution. For the endcap regions, the fit does not always give a perfect description of the data but it still provides a reasonable estimate of the mean Z mass and the mass resolution.

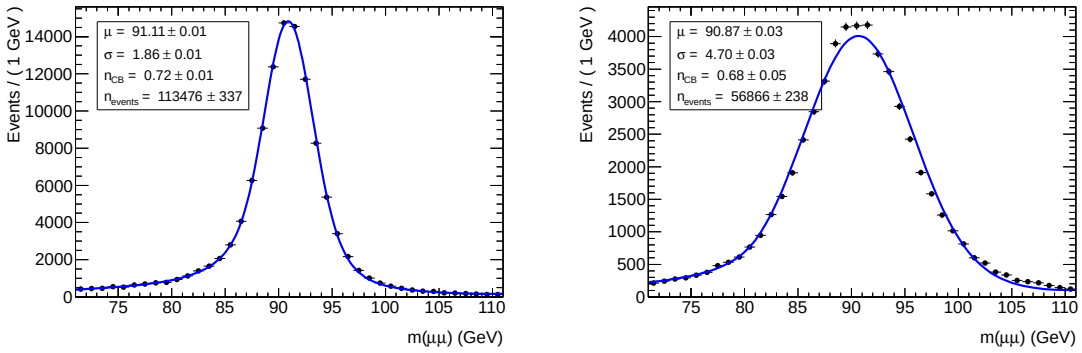

(a) (b)

Figure 6.2: Invariant mass of $Z \to \mu\mu$ candidates together with resulting fit distribution (spring 2011 alignment). Shown are (a) events where both muons are in the central barrel region ($|\eta| < 1.05$) and (b) events where both muons are in endcap A ($1.05 < \eta < 2.5$).

6.2.2 Systematic Distortions in Simulation

The expected impact of systematic distortions on the reconstructed Z-boson mass is studied using Monte Carlo. Simulated samples of $Z \to \mu\mu$ decays were produced with enforced *misaligned* detector geometries, following the simplified scheme outlined in Section 6.1.2. These misaligned constants introduce global systematic shifts of the module positions, on top of a perfectly aligned detector. Here, the focus is on the effect of $\Delta\phi$ misalignments, particularly *curl* and *twist* which are illustrated schematically in Figure 6.3. Misalignments in $\Delta\phi$ are charge-asymmetric, they bias the track curvature and hence affect positively-charged tracks differently from negatively-charged ones. The produced alignment constants for $\Delta\phi$ misalignments correspond to a maximum detector movement of 50 μm at the outer SCT radius.

The curl misalignment ($R\Delta\phi$) affects the track curvature by introducing a global curl around the z axis with increasing movements at increasing radius. Its effect on the reconstructed Z-boson mass can be probed through mass shifts as function of the difference in curvature between the positive and negative muon. The twist misalignment ($z\Delta\phi$) can be visualized as a global twist of the detector along the z direction and can be probed through mass shifts dependent on the difference in η between the positive and negative muon.

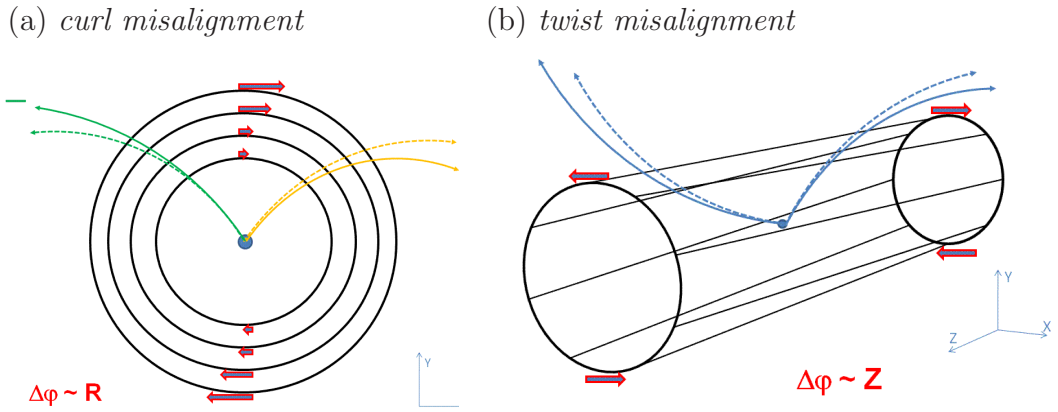

Figure 6.3: Schematic illustrations of the charge-antisymmetric curl and twist misalignments, showing both the detector deformations and the impact on reconstructed particle momenta. The true particle trajectories are shown as dashed lines and the reconstructed trajectories as continuous lines [5].

Figure 6.4 shows Z-mass distributions for simulated data reconstructed in grey with perfectly aligned Monte Carlo and for the colored markers with different $\Delta\phi$-misaligned geometries. With all misaligned geometries, a slight degradation of the Z mass resolution can be seen.

Figure 6.5 shows the mean Z mass as function of the difference in pseudorapidity $(\eta(+) - \eta(-))$. Plots are shown separately for when both muons are in the barrel region ($|\eta| < 1.05$) and where both muons are in endcap A ($1.05 < \eta < 2.5$) or endcap C ($-2.5 < \eta < -1.05$). For simulation with an applied twist misalignment (shown in blue filled markers), clear systematic effects are visible. The effects are largest in the endcap regions of the detector (a consequence of the global twist which is largest at higher η).

Figure 6.6 shows the mean Z mass as function of the difference in curvature between the positively and negatively-charged muon $(1/p_{\mathrm{T}}(+) - 1/p_{\mathrm{T}}(-))$. The plots are again separated for $Z \to \mu\mu$ decays where both muons are in the barrel or endcap A/C. For all detector regions, muons reconstructed with applied curl misalignment show clear systematic biases. In the endcap regions, also the twist misalignment is visible.

To summarize, it is shown that systematic biases as applied to simulated Z decays can give large systematic mass biases which may be probed by studied the mean reconstructed Z mass as function of kinematic quantities. The biases applied to Monte Carlo simulated data give, however, a simplified picture. It is not necessarily expected that real detector biases are as "clean", but they provide a starting point for probing systematic effects in real data.

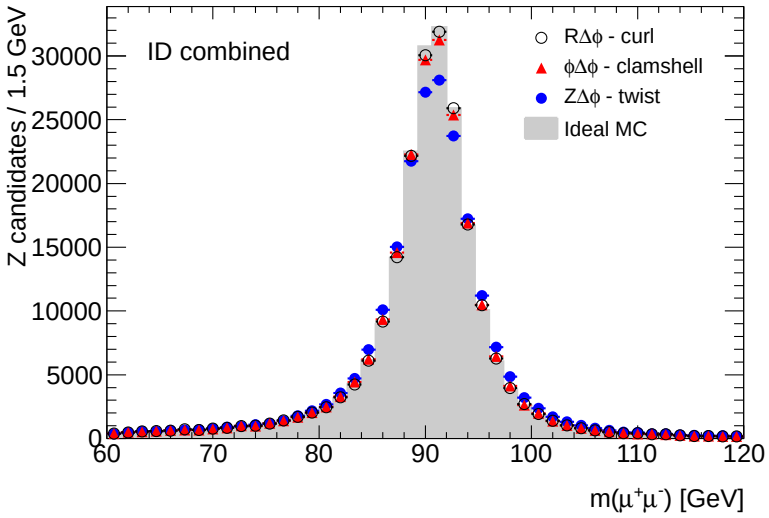

Figure 6.4: Reconstructed dimuon invariant mass distribution showing perfectly aligned Monte Carlo together with three misaligned samples.

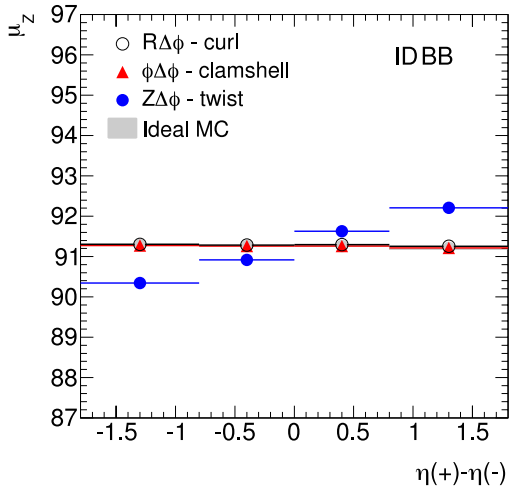

(a) Both muons in barrel ($|\eta| < 1.05$)

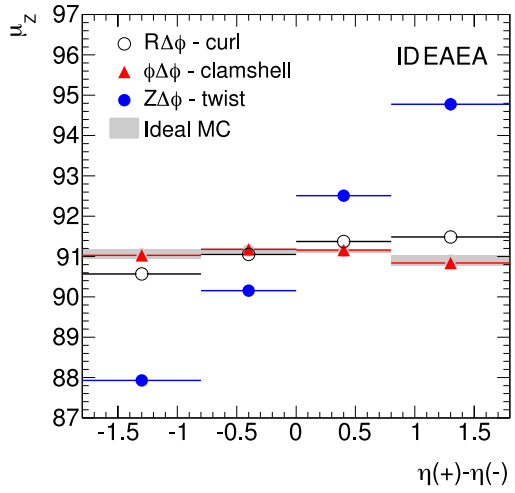

(b) Both muons in endcap A ($1.05 < \eta < 2.5$)

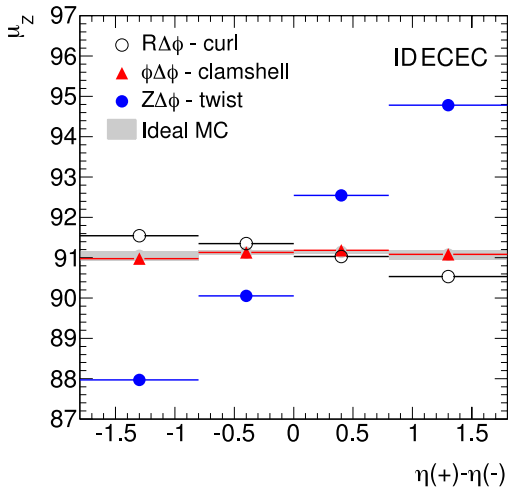

(c) Both muons in endcap C ($-2.5 < \eta < -1.05$)

Figure 6.5: Mean Z mass as function of the difference in pseudorapidity between the positively and negatively-charged muon. Shown in grey is Monte Carlo simulated data assuming a perfectly aligned detector, and in color, assuming misaligned detector geometries.

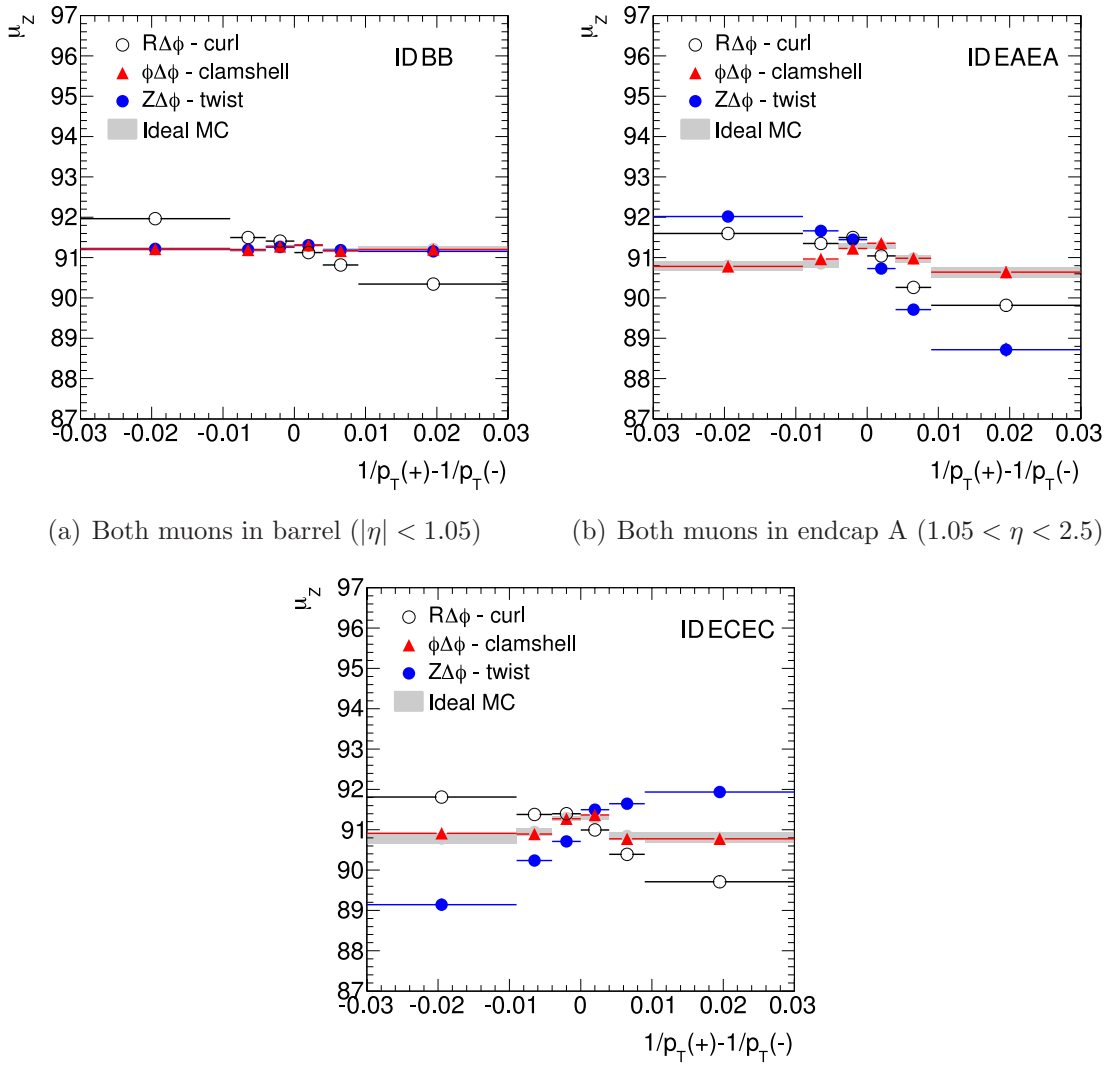

(a) Both muons in barrel ($|\eta| < 1.05$)

(b) Both muons in endcap A ($1.05 < \eta < 2.5$)

(c) Both muons in endcap C ($-2.5 < \eta < -1.05$)

Figure 6.6: Mean Z mass as function of the difference in curvature ($1/p_{\mathrm{T}}$) between the positively and negatively-charged muon. Shown in grey is Monte Carlo simulated data assuming a perfectly aligned detector, and in color, assuming misaligned detector geometries.

6.2.3 Alignment Performance in Data

The performance of the alignment during 2011 is studied with $Z \rightarrow \mu\mu$ candidates, selected as outlined in Section 6.2.1, in a data sample corresponding to an integrated luminosity of 1.2 fb^{-1}. The figures in this section shows data processed using two different set of alignment constants. The first one, referred to in the plots as *Initial 2011 alignment*, was, as the name indicates, the alignment used for initial 2011 data taking. As more data were collected, large systematic, charge-dependence momentum biases were observed using $Z \rightarrow \mu\mu$ decays and using the E/p ratio for high-p_{T} electrons. An updated, improved alignment was derived to remove the observed biases. Data processed using the updated alignment is labelled in the plots as *Updated alignment*. The observations in data are compared to predictions assuming a perfectly aligned detector using Monte Carlo simulation. The PYTHIA event generator was used to generate the $Z \rightarrow \mu\mu$ sample.

This section shows distributions of the reconstructed invariant mass of the Z boson for data, using the initial and the updated alignments, and Monte Carlo simulation of a perfectly aligned detector. Systematic misalignment effects are probed by searching for biases of the invariant mass as function of various kinematic quantities, such as the difference in curvature (probing curl misalignments) or difference in η (probing twist misalignments) between the two decay muons. The ϕ of positively and negatively-charged muons are also considered to probe sagitta-type *phi*-dependence distortions.

To probe the general alignment performance, as measured by the Z mass resolution, the distribution of the reconstructed Z-boson invariant mass is shown in Figure 6.7. The mass distribution is shown for all Z candidates combined and separately for events where both muons fall within the barrel region ($|\eta| < 1.05$), endcap A ($1.05 < \eta < 2.5$), and endcap C ($-2.5 < \eta < -1.05$). Comparing the performance between the initial and updated alignments, a significant improvement of the mass resolution is observed, achieved as a result of the updated detector geometry. For both the combined distribution and those shown separately for different detector regions, the agreement between data and Monte Carlo simulation is significantly improved although not quite perfect.

The fitted mean of the dimuon mass distribution and corresponding mass resolution are plotted as functions of muon η, shown in Figure 6.8. A clear improvement for the updated alignment can be observed compared to the initial 2011 alignment.

Figure 6.9 shows the curvature difference, probing the curl misalignment, and Figure 6.10 shows the difference in η between the two muons, probing the twist misalignment. The initial 2011 alignment showed indications of a twist-type systematic bias in endcap A, but this misalignment was largely removed during the updates to the detector geometry. The most significant improvements can be seen in Figure 6.11, which shows the mean invariant mass as function of ϕ for positively and negatively-charged muons.

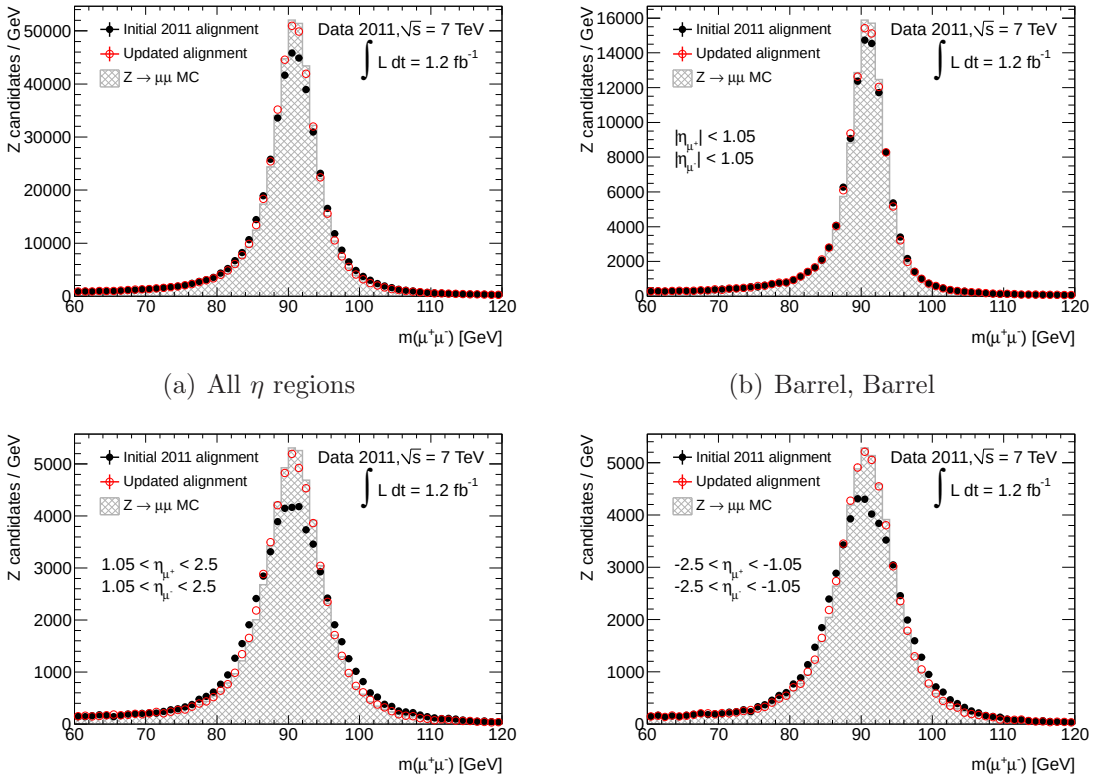

(a) All η regions

(b) Barrel, Barrel

(c) Endcap A, Endcap A

(d) Endcap C, Endcap C

Figure 6.7: Reconstructed Z mass distributions showing data and perfectly aligned Monte Carlo.

Alignment using the E/p Ratio

Detector deformations that are orthogonal to the trajectories of charged particles, referred to as *sagitta* deformations, bias the track curvatures with an opposite effect for positively and negatively-charged tracks. The effect on a track with curvature q/p_{T} can be expressed in terms of a bias parameter, $\delta_{\mathrm{sagitta}}$, according to

$$q/p_{\mathrm{T}} \rightarrow q/p_{\mathrm{T}} + \delta_{\mathrm{sagitta}}, \tag{6.5}$$

or alternatively, since the reconstructed polar angle of the track is unchanged, this relation can be reformulated as

$$p \rightarrow p \times (1 + qp_{\mathrm{T}}\delta_{\mathrm{sagitta}})^{-1}. \tag{6.6}$$

In order to correct for charge-dependent momentum biases that were observed in the initial 2011 alignment, the E/p ratio for electrons and positrons was used [5]. The

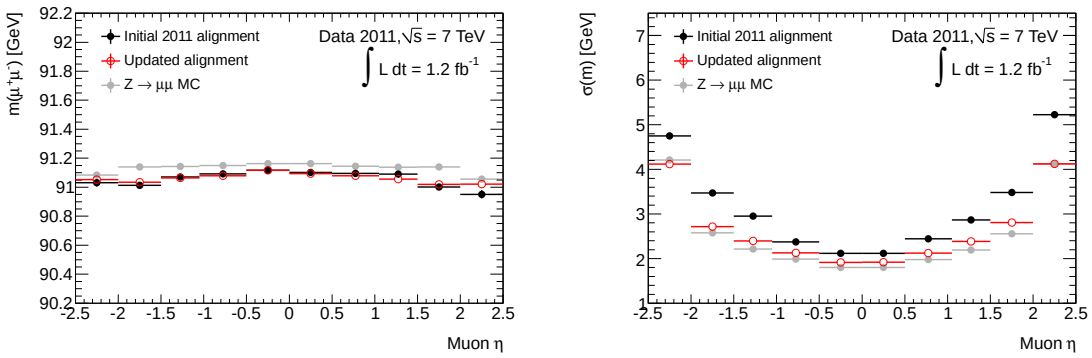

(a) Mean (b) Resolution

Figure 6.8: Fitted mean Z mass and resolution as a function of muon η for data and perfectly aligned Monte Carlo.

E/p ratio, the measured energy deposited in the calorimeter (E) to the measured ID momentum (p), is used under the assumption that the calorimeter response is independent of the charge of the particle which deposits energy. From Equation 6.6, a sagitta-type deformation affecting the inner detector measurements will have a similar effect on the E/p. Assuming that the true mean E/p is independent of charge, the bias parameter can be expressed as

$$\delta_{\text{sagitta}} = \frac{\langle E/p \rangle^{+}_{\text{reco}} - \langle E/p \rangle^{-}_{\text{reco}}}{2\langle p_{\text{T}} \rangle}, \tag{6.7}$$

where $\langle E/p \rangle^{\pm}_{\text{reco}}$ represents the reconstructed E/p.

The E/p ratios were derived using a high-purity electron sample from W and Z decays [5]. The E/p distribution for electrons and positrons is fitted to derive the mean values and consequently derive the bias parameter δ_{sagitta}. To remove the observed biases, tracks used in the alignment are constrained to the a corrected momentum measurement using δ_{sagitta} as derived using the E/p. From Equation 6.6, the track momentum correction can be written as

$$q/p_{\text{corr}} = q/p_{\text{reco}} \times (1 - q p_{\text{T}}^{\text{reco}} \delta_{\text{sagitta}}). \tag{6.8}$$

where p_{corr} and p_{reco} represents the corrected and the original reconstructed track momentum, respectively.

6.2.4 Conclusion

The Z resonance with its clean decays to final states with two opposite-charged muons is an excellent probe for studying detector effects. Measuring the mean and

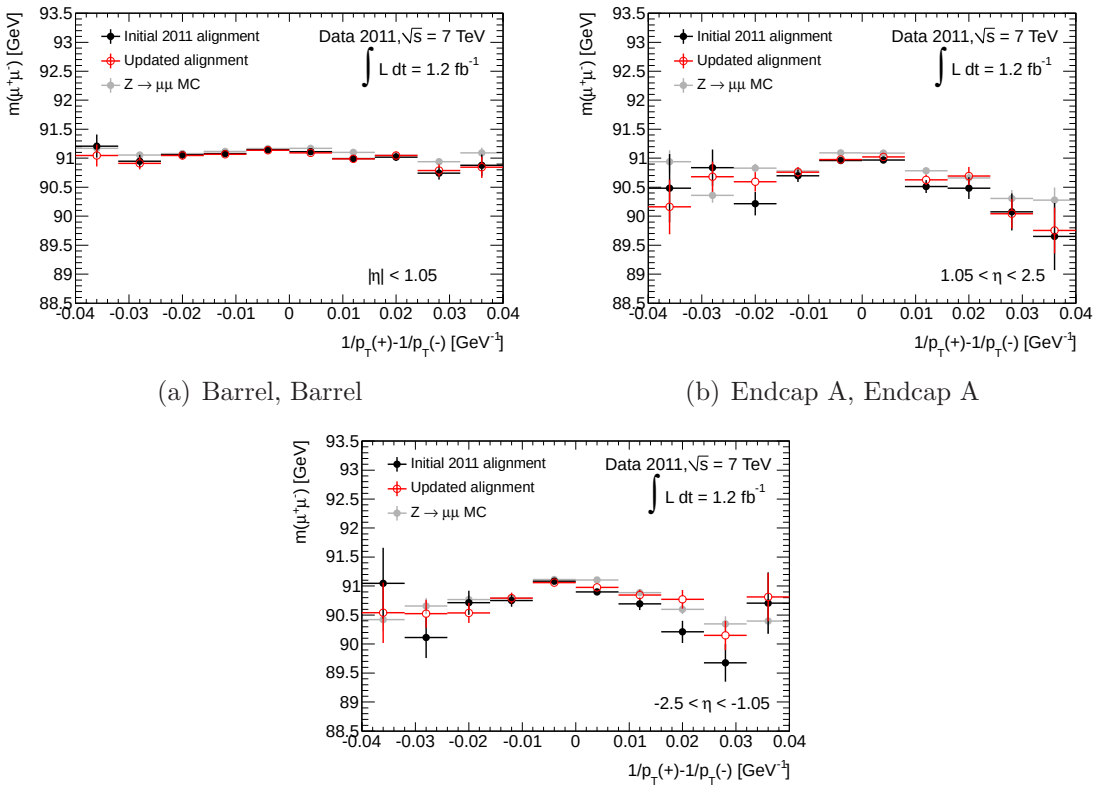

(a) Barrel, Barrel

(b) Endcap A, Endcap A

(c) Endcap C, Endcap C

Figure 6.9: Fitted mean Z mass as a function of curvature difference between the two muons.

width of the dimuon mass distribution around the Z peak, as reconstructed using track parameters from the inner detector only, provides information of the performance of the alignment as high-p_{T} muon tracks from Z decays are primarily sensitive to exactly (mis)alignment effects.

Large biases were observed during early 2011 data taking using $Z \to \mu\mu$ decays and E/p ratio measurements. By deriving momentum corrections using the E/p ratio and applying these to tracks used in the alignment, tightly constraining them to the corrected momentum measurements, a greatly improved alignment was derived. To quantify the comparison of the alignment performance using the Z resonance for tracks reconstructed with the initial and the updated alignments, the mass distributions are fitted for each detector region using the fit function from Section 6.2.1. The resulting mass resolutions due to detector effects (i.e. not including the intrinsic Z width) are listed in Table 6.3. The improvement correspond to about 6% in the barrel, 30% in endcap A, and 25% in endcap C.

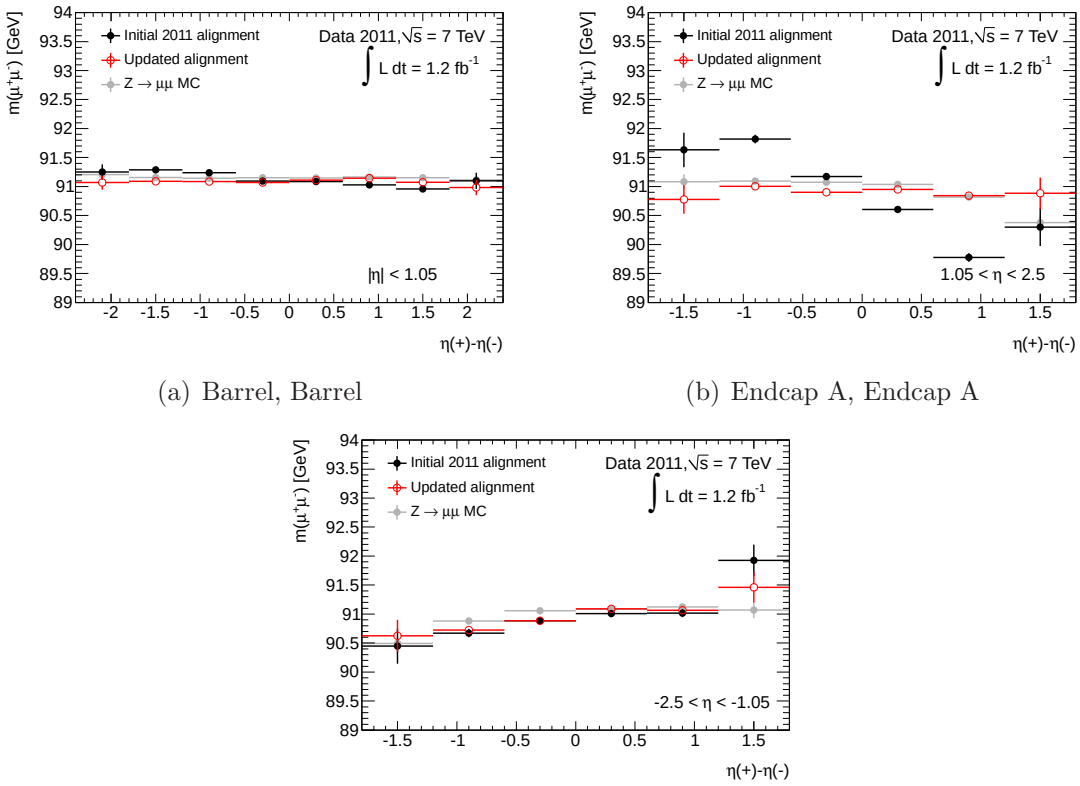

(a) Barrel, Barrel

(b) Endcap A, Endcap A

(c) Endcap C, Endcap C

Figure 6.10: Fitted mean Z mass as a function of difference in η between the two muons.

	Resolution [GeV]		
Detector region	Data (Initial)	Data (Updated)	Monte Carlo
Full detector	2.90 ± 0.01	2.46 ± 0.01	2.34 ± 0.00
Barrel, Barrel	1.86 ± 0.01	1.75 ± 0.01	1.65 ± 0.01
Endcap A, Endcap A	4.70 ± 0.03	3.63 ± 0.03	3.42 ± 0.01
Endcap C, Endcap C	4.51 ± 0.03	3.60 ± 0.03	3.43 ± 0.01

Table 6.3: Resolution of the fitted Z invariant mass distribution due to detector effects, i.e. not including the intrinsic Z width. The resolution is listed for the full detector and separately for when both muons are in the barrel region ($|\eta| < 1.05$), both in endcap A ($1.05 < \eta < 2.5$), or both in endcap C ($-2.5 < \eta < -1.05$). Results from data using the initial 2011 alignment and the updated alignment are compared to the fitted resolution from perfectly aligned Monte Carlo.

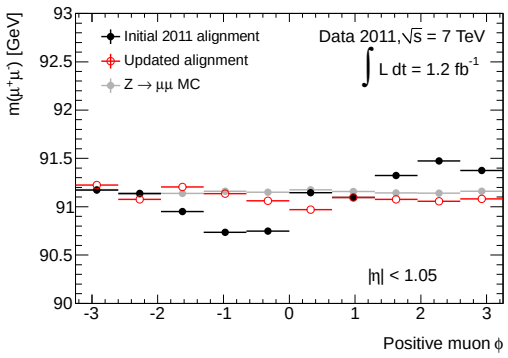

(a) Barrel, Barrel - Positive muon ϕ

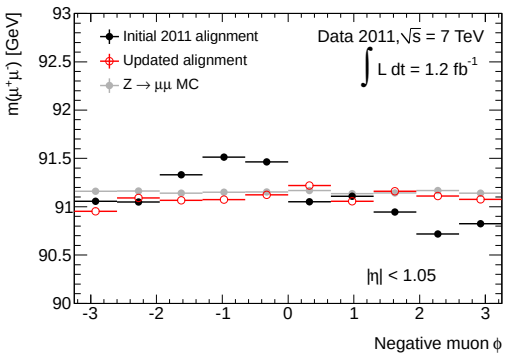

(b) Barrel, Barrel - Negative muon ϕ

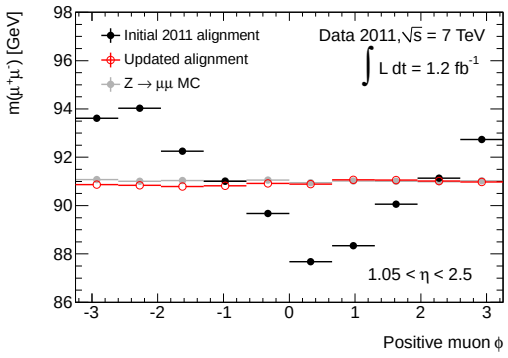

(c) Endcap A, Endcap A - Positive muon ϕ

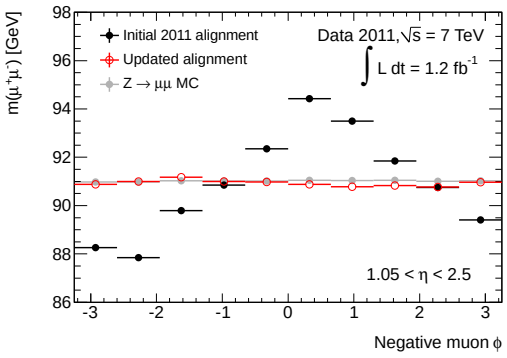

(d) Endcap A, Endcap A - Negative muon ϕ

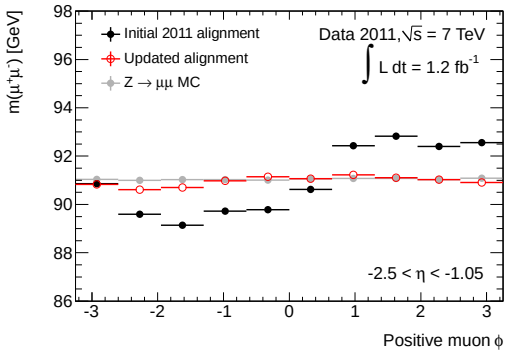

(e) Endcap C, Endcap C - Positive muon ϕ

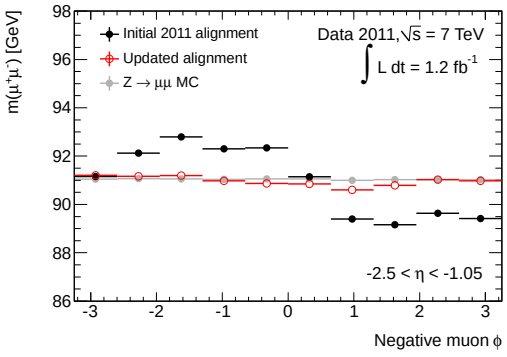

(f) Endcap C, Endcap C - Negative muon ϕ

Figure 6.11: Fitted mean Z mass as a function of ϕ for positively and negatively-charged muons.

Chapter 7

Data Sample and Event Selection

The like-sign dimuon search is performed using data collected between March and October of 2011, corresponding to the full 2011 proton-proton dataset. This chapter described the criteria used to select like-sign muon pairs. Event candidates are first identified with the muon trigger system and selected if they contain at least two good muons. The analysis selection is based only on the muon properties, no requirements are imposed on the missing transverse momentum or the number of reconstructed jets, with tight identification requirements placed on the muons. Muons must be well reconstructed with tracks in both the inner detector and the muon spectrometer, and be isolated from other nearby tracks. The signal region is defined as pairs of good muons with the same electric charge.

7.1 Event Selection

The data are selected using single-muon triggers requiring a muon with $p_{\mathrm{T}} > 18$ GeV at the event filter (see Section 7.1.1). The data must pass a *Good Run List* (GRL) which ensures that the data were acquired during run periods where the beam conditions were good, all parts of the detector needed for physics object measurements were fully operational, and basic data-quality requirements were fulfilled. The resulting integrated luminosity is 4.7 fb^{-1}.

7.1.1 Trigger

The dimuon search uses a data sample selected by requiring a single muon with high transverse momentum. At the software-based, high-level trigger, a muon with $p_{\mathrm{T}} > 18$ GeV is required for the full 2011 data sample. The hardware-based Level-1 trigger seeding this 18 GeV threshold trigger chain was, however, changed during the year to keep the collected data within its allocated bandwidth. The transverse momentum threshold at the Level-1 trigger is 10 GeV. For about the first third of

the data sample, corresponding to data collected between March and July of 2011, the L1_MU10 trigger was used, while the succeeding part of the year used the L1_MU11 trigger. The L1_MU10 trigger requires a two-station (three-station) coincidence trigger in the barrel (endcap) region, whereas L1_MU11 uses coincidences of hits from three stations in both barrel and endcaps [6]. The event-filter triggers seeded by L1_MU10 and L1_MU11 are referred to as EF_MU18 and EF_MU18_medium, respectively. With a trigger p_{T} threshold of 18 GeV, the subsequent analysis always requires a muon with transverse momentum greater than 20 GeV in each event to ensure a high and flat trigger efficiency, well above the trigger turn-on region (see discussion of trigger efficiency in Section 7.2.2). The details of the triggers used for different run periods are summarized in Table 7.1.

Run ranges	Level-1 trigger	Event-filter trigger	Luminosity [fb^{-1}]
177986 - 186493	L1_MU10	EF_mu18	1.5
186516 - 191933	L1_MU11	EF_mu18_medium	3.2

Table 7.1: Muon triggers used for different run periods.

7.1.2 Muon Selection

A variety of identification and quality requirements are imposed on muons selected for the search. Muon are identified using the STACO reconstruction algorithm [80], as described in Section 5.2. To ensure accurate charge measurements, only combined muons are used. The charge of the muon track as measured in the inner detector (Q_{ID}) must equal the charge of the extrapolated track in the muon system (Q_{MS})

$$Q_{ID} = Q_{MS}.$$

This requirement helps reduce the rate of muon charge misidentification, discussed further in Section 8.4.

Muons with transverse momentum $p_{\mathrm{T}} > 10$ GeV and pseudorapidity $|\eta| < 2.5$ are selected. At least one muon with $p_{\mathrm{T}} > 20$ GeV must match an event-filter level trigger object within $\Delta R < 0.15$. The trigger matching requirement result in that effectively at least one muon must have $|\eta| < 2.4$ (the pseudorapidity range where muon triggering is provided).

Impact Parameters

Muons are required to originate from close to the primary event vertex. This is implemented by requiring the transverse (d_0) and longitudinal ($z_0 \sin\theta$) distances of the inner detector track with respect to the primary event vertex to be small. A tight

cut is also placed on the transverse impact parameter significance ($d_0/\sigma(d_0)$). Placing a requirement on the impact parameter significance is powerful in removing muons originating from heavy-flavor decays. The specific impact parameter cuts are listed below.

- $|d_0| < 0.2$ mm
- $|z_0 \sin\theta| < 1.0$ mm
- $|d_0/\sigma(d_0)| < 3$

The impact parameter requirements also remove any potential contamination of cosmic-ray muons. Cosmic-ray muons which traverse the detector near the interaction region may falsely be reconstructed as a pair of muons: one muon originating from the interaction point which has correctly assigned charge and one muon, reconstructed as traveling *upwards* from the interaction point with opposite charge to the original *downward* traveling muon. Since such pairs typically have opposite charge, they are not expected to have any impact on the signal region.

Muon Isolation

Muons selected for this search are required to be isolated from other tracks and separated from reconstructed jets. Imposing tight criteria on the muon track isolation is a powerful way to reduce background from non-prompt sources (see Section 5.4.2). The track isolation ($p_{\mathrm{T}}^{\mathrm{cone}\Delta\mathrm{R}_{\mathrm{iso}}}$) is defined as the scalar p_{T} sum of all good tracks with $p_{\mathrm{T}} > 1$ GeV within a cone $\Delta R_{\mathrm{iso}} < 0.40$ of the muon direction, with the muon track itself removed from the isolation variable.

For this analysis, track isolation criteria which depend on the muon p_{T} are used. The cuts are chosen to be stringent at low p_{T} where the non-prompt muon background is most severe and to result in a flat efficiency for prompt muons at high p_{T}. The isolation selection is:

- $p_{\mathrm{T}}(\mu) < 100$ GeV: $\quad p_{\mathrm{T}}^{\mathrm{iso}}/p_{\mathrm{T}}(\mu) < 0.06$
- $p_{\mathrm{T}}(\mu) \geq 100$ GeV: $\quad p_{\mathrm{T}}^{\mathrm{iso}} < (4 + 0.02 \times p_{\mathrm{T}}(\mu))$ GeV

Figure 7.1 shows a schematic illustration of the maximum allowed isolation as function of muon p_{T}.

To further suppress background from hadronic decays, muons must be isolated from reconstructed jets. Jet candidates are for this purpose selected if they fulfill $|\eta| < 2.8$, $p_{\mathrm{T}} > 25$ GeV, and have 75% of the combined momentum of tracks within the jet originating from the primary vertex. The jet-vertex cut selects jets from the hard scatter and suppresses jets from pileup interactions. Selected muons must be separated from jets which pass these selection cuts and have $p_{\mathrm{T}}(\mathrm{jet}) > 25 + 0.05 \times p_{\mathrm{T}}(\mu)$ GeV by $\Delta R(\mu, \mathrm{jet}) > 0.40$. The non-constant cut value on the jet p_{T} is placed

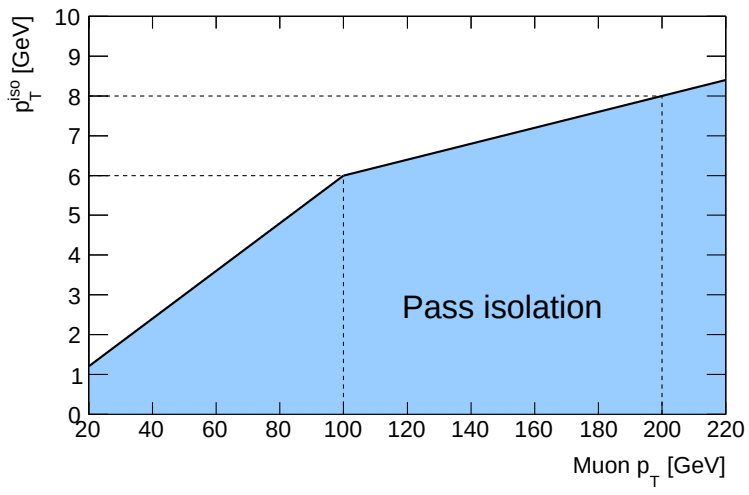

Figure 7.1: Schematic illustration of the track isolation energy as function of the muon transverse momentum.

in order to achieve an approximately flat efficiency for the muon-jet separation criteria for prompt high-p_{T} muons (see Section 7.2.4).

7.1.3 Signal Region Definition

All events are required to have a primary vertex determined with three or more tracks, where the primary vertex is that with the highest $\sqrt{\sum p_{\mathrm{T}}^2}$ value. The events must contain at least two good muons, as defined in Section 7.1.2, with transverse momentum greater than 20 GeV and equal electric charge. Any combination of two muons is considered, i.e. more than one muon pair per event can be included in the signal region. The invariant mass of the two muons is required to be larger than 15 GeV to avoid the region of phase space with low-mass hadronic resonances such as the J/ψ and Υ. The criteria used for defining the signal region are summarized in Table 7.2.

7.2 Muon Efficiencies

The efficiency of the muon trigger, reconstruction, and identification cuts are measured in data and compared to the estimated efficiencies in simulation. Any differences are corrected for in the simulation to ensure that the simulation closely emulates the data. The simulation is also corrected to reproduce the momentum resolution observed in data.

All efficiency measurements are based on the *tag-and-probe* method. The method uses $Z \rightarrow \mu\mu$ events, selected by requiring two opposite-charge muons with invari-

Event preselection	
Primary vertex	$N_{vtx} \geq 1$ with $N_{tracks} \geq 3$
Trigger	`EF_mu18` or `EF_mu18_medium`
Muon selection	
Kinematics	$\lvert\eta\rvert < 2.5$
	$p_{\mathrm{T}} > 20$ GeV
Impact parameter	$\lvert d_0\rvert < 0.2$ mm
	$\lvert z_0 \times \sin\theta\rvert < 1$ mm
	$\lvert d_0\rvert/\sigma(d_0) < 3$
Isolation	$p_{\mathrm{T}}^{\mathrm{iso}}/p_{\mathrm{T}}(\mu) < 0.06$
	$p_{\mathrm{T}}^{\mathrm{iso}} < (4 + 0.02 \times p_{\mathrm{T}}(\mu))$ GeV
	$\Delta R(\mu, \mathrm{jet}) > 0.40$
Signal region	
Muon pairs	$Q(\mu_1) = Q(\mu_2)$
	$m(\mu^{\pm}\mu^{\pm}) > 15$ GeV
Trigger	One muon match EF trigger object

Table 7.2: Summary of the selection criteria used to define the signal region.

ant mass in a narrow window around the Z mass. One defines a *tag* muon which is required to be well-reconstructed, used to tag the event, and a *probe* muon, for which the efficiency in question is measured. The efficiency of the muon trigger and reconstruction are provided centrally in ATLAS through the muon combined performance group, as is the correction in simulation of the muon momentum scale. The efficiencies of the muon selection cuts which are unique to this particular analysis must, however, be evaluated.

7.2.1 Reconstruction Efficiency

The muon reconstruction is performed by combining measurements from the inner detector and the muon spectrometer. To measure the reconstruction efficiency for each system, the tag-and-probe method is used with $Z \to \mu\mu$ decays for which one decay muon is reconstructed in both systems (the tag muon) and the other is reconstructed using only one system to measure the efficiency of the other (the probe muon). The method as it was used with 2010 data is described in detail in Refs. [88, 81]. It is here briefly summarized with updated results for the 2011 dataset.

The combined muon reconstruction efficiency is a product of three components:

- (1) The muon reconstruction efficiency in the inner detector.
- (2) The muon reconstruction efficiency in the muon spectrometer.

- (3) The matching efficiency between the two systems.

Through the tag-and-probe method, component (1) is measured separately while components (2) and (3) are measured jointly. In both cases, the tag must be a combined muon. When measuring the ID efficiency, the probe is a standalone muon, whereas in measuring the MS plus matching efficiency, the probe is an ID track. The ID efficiency is determined as the fraction of standalone probes that can be associated with an ID track while the combined MS plus matching efficiency is the fraction of ID probes that can be associated to a combined muon.

Efficiencies are derived for data using the full 2011 sample and for simulated $Z \to \mu\mu$ events. The sample typically has a purity of $> 99\%$ but small background contributions from $Z \to \tau\tau$, $W \to \mu(\tau)\nu$, $b\bar{b}$, $c\bar{c}$, and $t\bar{t}$ are corrected for [81]. Candidate events are selected with the regular single-muon trigger. Muons must be prompt, isolated, fulfill the track hit requirements in Section 5.4.1, and have $p_{\mathrm{T}} > 20$ GeV. The tag muon must have $|\eta| < 2.4$ and match the trigger object to avoid any trigger bias in the efficiency measurement. The probe muon must have $|\eta| < 2.5$ and be associated to the same vertex as the tag. The tag and the probe must additionally have opposite charge, an invariant mass within ± 10 GeV around the Z mass, and be back-to-back ($\Delta\phi > 2.0$). When matching the ID probe to form a combined muon, the probe and the combined muon must have the same electric charge and $\Delta R < 0.01$. In matching a standalone probe to a muon track, $\Delta R < 0.05$ is required.

The measured efficiency of the ID muon reconstruction, including the imposed track hit cuts, is shown in Figure 7.2 for part of the 2011 dataset as function of the muon pseudorapidity. The combined muon reconstruction efficiency with respect to the ID efficiency is also shown in Figure 7.2 as function of pseudorapidity. For both figures, the lower part of the plots show the scale factors, defined as the ratio between the efficiencies as measured in data to those predicted by the simulation.

The ID efficiency is roughly independent of muon p_{T} and ϕ but has a dependence on η. The reduction in efficiency around $\eta = 0$ and $|\eta| = 1.2$ are due to the imposed track hit quality requirements. Around $\eta = 0$, tracks traverse a region where TRT straws give no hits. Around $|\eta| = 1.2$, tracks pass a transition region between the SCT barrel and endcap parts where less SCT sensors are crossed than what is required by the track quality cuts. The resulting scale factor comparing data and simulation is within 1%.

The combined efficiency for muon reconstruction in the muon system and the ID-MS matching shows strong dependence on pseudorapidity. The efficiency is lower around $\eta = 0$ due to detector services extending down to the inner detector and the calorimeters and in the transition regions between the barrel and endcap sections of the muon system. The efficiency also has a dependence on muon ϕ, resulting from the detector geometry, such as the feet of the muon system.

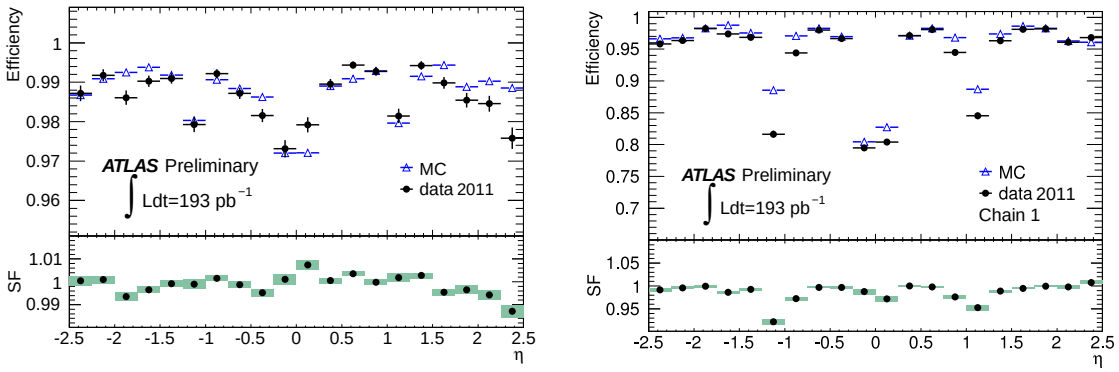

(a) ID efficiency

(b) MS + matching efficiency

Figure 7.2: Measurement of (a) the inner detector reconstruction efficiency and (b) the combined muon reconstruction efficiency with respect to the ID efficiency, parametrized versus muon η. The bottom parts of each plot show the ratio of the efficiency as measured in data to that in Monte Carlo.

7.2.2 Trigger Efficiency

The muon trigger efficiency is determined with respect to isolated, offline reconstructed, combined muons using the tag-and-probe method with $Z \rightarrow \mu\mu$ events [6]. The Level-1 trigger efficiency as function of muon p_{T} is shown in Figure 7.3 for the barrel and endcap regions. The left plot shows in filled circles `L1_MU10`, requiring two-station coincidences, and in open circles `L1_MU11`, requiring three-station coincidences. In the trigger plateau region, well above the trigger threshold, the efficiency is about 6% lower for `L1_MU11` compared to `L1_MU10`. The right plot shows only the three-station coincidence trigger, as this is required for both Level-1 triggers in the endcap regions.

The efficiency of the `EF_mu18_medium` trigger, seeded by the `L1_MU11`, with respect to isolated, combined muons is shown in Figure 7.4 for barrel and endcap regions. Efficiencies measured in data are compared to those in Monte Carlo. The bottom part of the plots show the ratio of data compared to Monte Carlo. In general the Monte Carlo models the data well, any small observed differences are corrected for to ensure accurate modeling by the simulation.

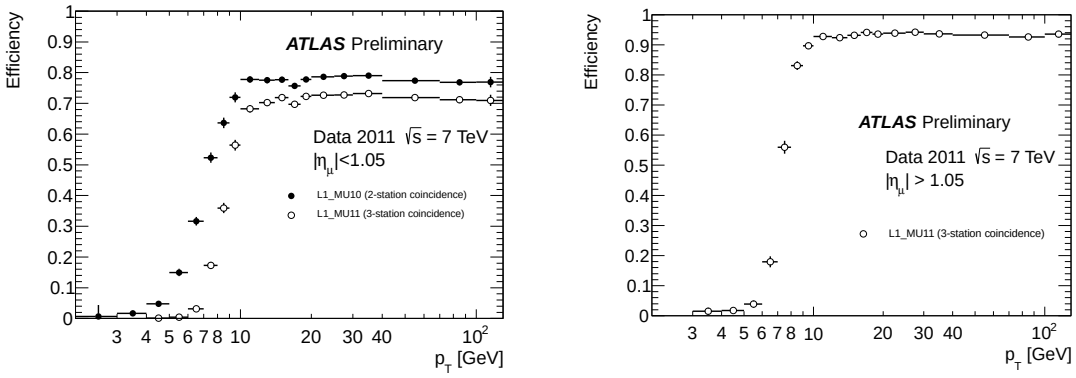

(a) (b)

Figure 7.3: Level-1 trigger efficiency for (a) the barrel region and (b) the endcap regions [6].

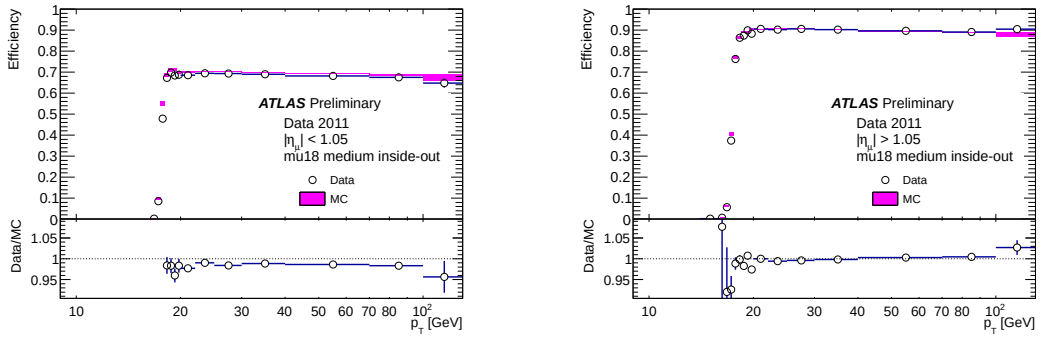

(a) (b)

Figure 7.4: Event-filter trigger efficiency for (a) the barrel region and (b) the endcap regions [6].

7.2.3 Momentum Scale and Resolution

The muon momentum scale and momentum resolution are derived from data using the invariant mass distribution of muons from Z decays. Information of the muon momentum scale is extracted from the peak of the dimuon invariant mass distribution around the Z pole while the momentum resolution is derived from the width of the distribution. For combined muons, the momentum resolution is primarily affected by misalignments and miscalibrations in the ID and the MS, as well as by any relative misalignment between the two systems. The scale and resolution is measured for both data and simulation, and the simulation is consequently scaled and smeared to reproduce what is observed for data. The method is described in detail in Ref. [89] and is here briefly summarized with updated results as applied to the full 2011 dataset.

For these studies, Z candidate events are selected with two combined, opposite-sign muons with $p_{\mathrm{T}} > 15$ GeV. Four regions of pseudorapidity are defined: $|\eta| < 1.05$ (*barrel*), $1.05 < |\eta| < 1.7$ (*transition region*), $1.7 < |\eta| < 2.0$ (*endcap*), and $2.0 < |\eta| < 2.5$ (*CSC/no TRT*). The width of the dimuon invariant mass distribution is a convolution of the intrinsic Z width and the momentum resolution. The increased width due to resolution effects is studied separately for the MS and ID in the four η regions, requiring both decay muons to be within the same region. The mass distribution is fitted using a convolution of the Z lineshape[1] and two gaussians, describing the detector resolution effects.

The combined momentum resolution is derived for the ID and the MS using a Monte Carlo template technique where distributions of the mass resolution are formed for different resolution values and then matched to those observed in data by minimizing a χ^2 fit to the input values. The muon momentum measurements in the MS and the ID are smeared according to

$$p_{\mathrm{T}}^{MS,smear} = p_{\mathrm{T}}^{MS}(1 + \Delta^{MS}) \tag{7.1}$$

$$p_{\mathrm{T}}^{ID,smear} = p_{\mathrm{T}}^{ID}(1 + \Delta^{ID}) \tag{7.2}$$

where Δ^{MS} and Δ^{ID} are expressed as

$$\Delta^{MS} = f(0,1)\Delta p_1^{MS} + f(0,1)\Delta p_2^{MS} p_{\mathrm{T}}, \tag{7.3}$$

$$\Delta^{ID} = \begin{cases} f(0,1)\Delta p_2^{ID} p_{\mathrm{T}} & \text{for } |\eta| < 1.9 \\ f(0,1)\Delta p_2^{ID} p_{\mathrm{T}} / \tan^2(\theta) & \text{for } |\eta| > 1.9. \end{cases} \tag{7.4}$$

For the ID, the regions $|\eta| < 1.9$ and $|\eta| > 1.9$ (near the edge or outside the TRT acceptance) are distinguished due to a difference in the amount of traversed material. The term p_1^{MS} is the multiple scattering term in the MS, while the terms p_2^{MS} and p_2^{ID} represent the intrinsic resolutions in the MS and ID, respectively. The resolution terms for the 2011 dataset as applied to the like-sign dimuon search are summarized in Table 7.3.

[1] The description of the Z lineshape includes the natural Z boson width and radiation terms [89].

Region	p_1^{MS} [%]	p_2^{MS} [TeV^{-1}]	p_2^{ID} [TeV^{-1}]
$\|\eta\| < 1.05$	1.95 ± 0.04	0.100 ± 0.015	0.193 ± 0.009
$1.05 < \|\eta\| < 1.7$	3.97 ± 0.06	0.473 ± 0.020	0.245 ± 0.034
$1.7 < \|\eta\| < 2.0$	2.88 ± 0.14	0.201 ± 0.009	0.498 ± 0.020
$2.0 < \|\eta\| < 2.5$	1.82 ± 0.20	0.150 ± 0.048	0.015 ± 0.004

Table 7.3: Momentum resolution terms for the ID and the MS. The uncertainties are statistical only.

The combined muon momentum is corrected based on the resolution measurements from the ID and the MS, as well as by applying a correction of the momentum scale S, according to

$$p_{\mathrm{T}}^{CB,smear} = S \times p_{\mathrm{T}}^{CB} \left[1 + \frac{\frac{\Delta^{MS}}{\sigma_{MS}^2} + \frac{\Delta^{ID}}{\sigma_{ID}^2}}{\frac{1}{\sigma_{MS}^2} + \frac{1}{\sigma_{ID}^2}} \right], \tag{7.5}$$

where σ_{MS} (σ_{ID}) is the momentum resolution for a given value of p_{T}^{MS} (p_{T}^{ID}). The correction of the muon momentum scale is close to unity for all regions of pseudorapidity, as listed in Table 7.4.

Region	Scale correction (S)
$\|\eta\| < 1.05$	0.999223
$1.05 < \|\eta\| < 1.7$	0.998684
$1.7 < \|\eta\| < 2.0$	0.998207
$2.0 < \|\eta\| < 2.5$	0.997724

Table 7.4: Scale correction of the combined muon momentum.

7.2.4 Additional Selection Efficiencies

The efficiency of the muon isolation and impact parameter selection cuts, which are specific to this analysis, are also evaluated using the tag-and-probe method. The specific selection cuts for which the efficiency is derived are:

- Equal charge of the ID and MS track segments: $Q_{ID} = Q_{MS}$
- Impact parameter selection: $|d_0| < 0.2$ mm, $|z_0 \sin\theta| < 1.0$ mm, $|d_0|/\sigma(d_0) < 3$
- Track isolation requirement:

  - $p_{\mathrm{T}}(\mu) < 100$ GeV: $p_{\mathrm{T}}^{\mathrm{iso}}/p_{\mathrm{T}}(\mu) < 0.06$
  - $p_{\mathrm{T}}(\mu) \geq 100$ GeV: $p_{\mathrm{T}}^{\mathrm{iso}} < (4 + 0.02 \times p_{\mathrm{T}}(\mu))$ GeV
- Jet-muon separation: $\Delta R(\mu, \text{jet}) > 0.40$ for jets with $p_{\mathrm{T}}(\text{jet}) > (25 + 0.05 \times p_{\mathrm{T}}(\mu))$ GeV

For the tag-and-probe efficiency measurement, events with two oppositely-charged muons are selected. Both muons must be combined, fulfill the track quality hit requirements, and have $p_{\mathrm{T}} > 20$ GeV and $|\eta| < 2.5$. The dimuon invariant mass must be within a ± 10 GeV window around the Z-boson mass. The two muons are considered one at a time as a potential tag muon. The tag must fulfill all muon selection cuts in Section 7.1.2, except the requirement on muon-jet separation. The other muon, the probe, is used to measure the efficiency for a particular selection cut.

The efficiency for each of the charge, impact parameter, and isolation cuts are measured separately for data and Monte Carlo simulated $Z \to \mu\mu$ decays. The Z sample used is simulated with the ALPGEN generator [90]. The resulting efficiencies are shown for data and Monte Carlo as functions of the muon p_{T} and η in Figure 7.5. The resulting scale factors are shown as functions of p_{T} and η in Figure 7.6.

The scale factors are largest at low muon p_{T}, primarily driven by a difference between data and Monte Carlo in the modeling of muon isolation. For 20 GeV muons, the scale factor is about 0.97 and increases up to about 0.99 for 50 GeV muons. For muons with $p_{\mathrm{T}} > 150$ GeV, the available statistics in the Monte Carlo is limited. There is some indication of an increase in the scale factor in this p_{T} range, but due to the large statistical uncertainty in this range the scale factor is kept constant at 0.99 for $p_{\mathrm{T}} > 110$ GeV with an uncertainty of ± 0.02 to cover observed fluctuations from this value.

The efficiency of the requirement on muon-jet separation, $\Delta R(\mu, \text{jet}) > 0.4$, is additionally compared between data and Monte Carlo as function of the number of reconstructed jets in the event, parametrized versus muon p_{T}. The scale factors are shown in Figure 7.7. For low-p_{T} muons in events with three or more jets, the scale factor increases to 0.95–0.96. Since the analysis does not place any jet requirements and the main backgrounds which are estimated from simulation, WZ and ZZ production, are expected to have similar event activity outside the muon pair, this variation is not taken as any additional uncertainty. Differences in the efficiency between data and simulation are also considered for potential signals as part of the *fiducial efficiency*, discussed later in Section 10.2.2.

To cross-check the efficiency of the selection cuts for muons with very high p_{T}, a simulated Z' template sample is used. This special simulation sample is created by removing the Breit-Wigner peak to flatten out the mass spectrum. Consequently, a wide muon p_{T} range is covered. The efficiencies as function of muon p_{T} using this sample are shown in Figure 7.8. As expected, the efficiency is approximately flat versus p_{T}.

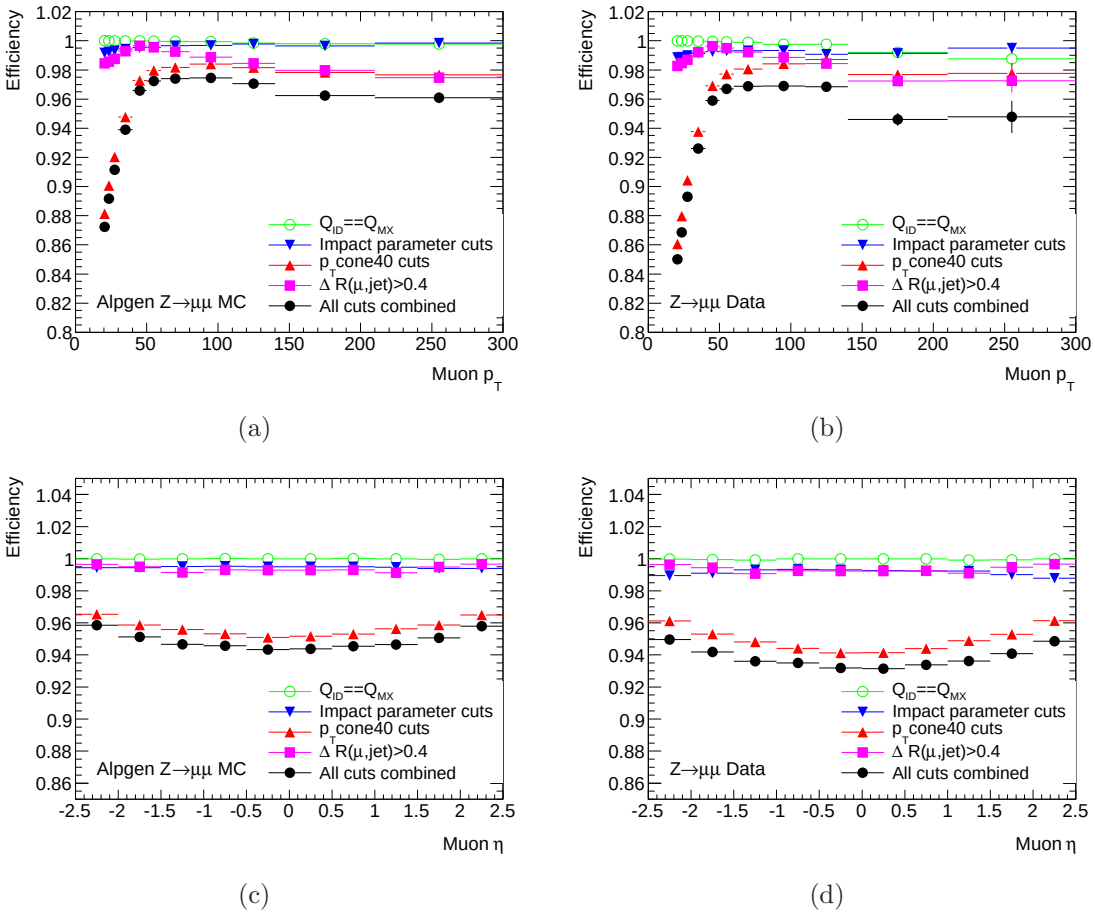

Figure 7.5: Muon efficiency with respect to combined muons in Monte Carlo (left) and data (right) as a function of p_{T} (top) and η (bottom).

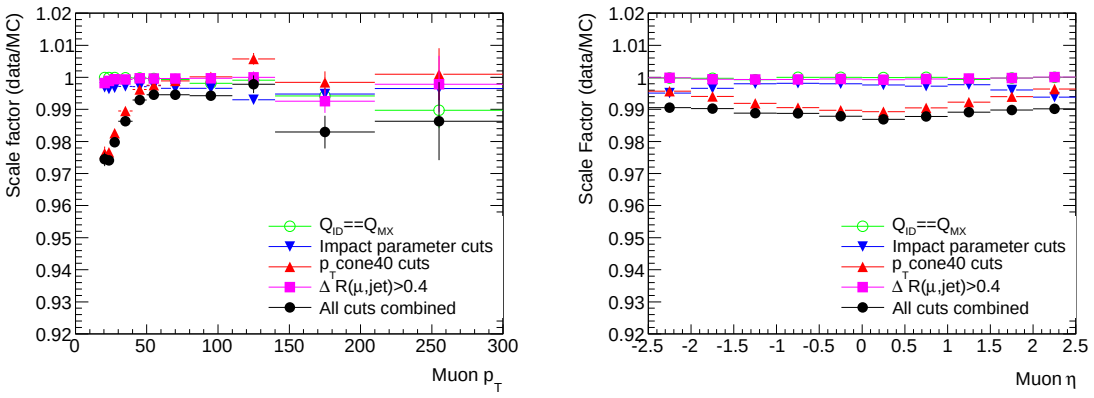

(a) (b)

Figure 7.6: Muon scale factors (efficiency in data divided by efficiency in MC) as a function of p_{T} (left) and η (right).

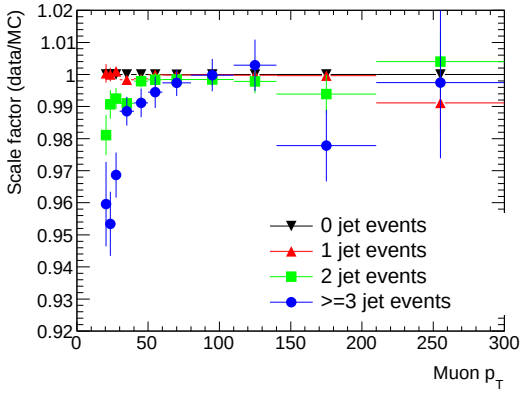

Figure 7.7: Muon scale factors (efficiency in data divided by efficiency in MC) as a function of p_{T} for events with 0, 1, 2, and ≥ 3 jets.

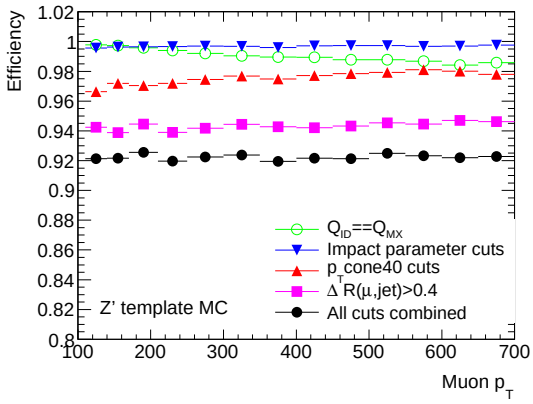

Figure 7.8: Muon efficiency versus p_{T} in the Z' template Monte Carlo sample.

Chapter 8

Background Estimation

The sources of background contributing to the like-sign dimuon final state in this search can be divided into three categories. The first and largest category is Standard Model production of prompt, like-sign muon pairs where the dominant process contributing is diboson (WZ/ZZ) production. Prompt muons constitute the largest source of background in this search. The second background category is muon pairs where at least one muon originates from a non-prompt source. Non-prompt muons come from b- and c-hadron decays (*heavy-flavor*) and from decay-in-flights of pion and kaons (*light-flavor*). The third and final background category is Standard Model production of opposite-sign muon pairs where the charge of one of the muons is mismeasured. Background due to charge misidentification is nearly negligible for muons. The prompt background is an irreducible background source in the search while non-prompt muons can largely be suppressed with tight muon identification criteria.

The methods used for estimating the different background contributions are described in detail in this chapter. Contribution from prompt like-sign muon pairs is estimated from Monte Carlo simulation. The non-prompt background is determined using data-driven techniques, extrapolating from control samples in data with altered lepton selection. The charge misidentification background is estimated using Monte Carlo simulation with a systematic uncertainty assessed using a data-driven method.

8.1 Prompt Background

The dominant source of prompt muons with the same electric charge in the Standard Model is diboson production, $WZ \to \ell^{\pm}\nu\ell^{\pm}\ell^{\mp}$ or $ZZ \to \ell^{\pm}\ell^{\mp}\ell^{\pm}\ell^{\mp}$, as discussed in Section 4.1. Smaller contributions come from like-sign W production which proceeds via a t-channel exchange of a gluon and results in two jets in the final state in addition to the W bosons, $W^{\pm}W^{\pm}jj$, and pair production of top quarks in association with a W or Z boson, $t\bar{t}W$ and $t\bar{t}Z$. The contribution from these background

processes to the signal region is estimated from Monte Carlo simulation.

The detector response to the generated events is simulated with the ATLAS simulation framework [91] using GEANT4 [92], and the events are reconstructed with the same software used to process the data. Simulated minimum bias interactions, generated with PYTHIA, are overlaid on the hard scatter events to closely emulate the multiple pp interactions present in the current and in adjacent bunch crossings (pileup) present in the data. The Monte Carlo samples are reweighted to fully reproduce the pileup profile in data. The reweighting is performed through an ATLAS standardized procedure using the average number of interactions $\langle\mu\rangle$ [93]. The average number of interactions is related to the luminosity as shown in Equation 3.4. The reweighting to reproduce the $\langle\mu\rangle$ distribution in data ensures that the simulation accurately describes the data. The Monte Carlo samples are corrected for the small differences in the trigger and muon reconstruction efficiencies and in momentum resolution, as discussed in Section 7.2.

For the simulated samples, only muons which originate directly from W and Z/γ^* bosons or from τ leptons are considered prompt. Muons originating from other sources are not considered in the prompt background estimation to avoid double-counting with the data-driven non-prompt background estimate.

8.1.1 WZ and ZZ Production

Background due to WZ and ZZ production is estimated using samples generated with the SHERPA event generator [94]. The samples include the contribution from off-shell $\gamma^* \to \ell^+\ell^-$, originating from bremsstrahlung of final-state leptons or quarks, for $m(\ell^+\ell^-) > 0.1$ GeV. This means that the singly resonant W and Z production diagrams ($W \to \ell\nu \to \ell\gamma^*\nu \to \ell\ell\ell\nu$ and $Z \to \ell\ell \to \ell\ell\gamma^* \to \ell\ell\ell\ell$) are included.

The predicted yield and invariant mass spectrum from SHERPA for WZ and ZZ are normalized to predictions from MCFM[1] [95]. The cross sections from SHERPA include the next-to-leading order (NLO) corrections due to real emissions, but it is not a true NLO generator. Cross sections from MCFM are, on the other hand, calculated at next-to-leading order. The normalization is derived as function of the like-sign dilepton mass. To identify events with kinematics close to that in the signal region, it is required for both SHERPA and MCFM that leptons forming the like-sign pair have $p_{\mathrm{T}} > 20$ GeV and $|\eta| < 2.5$ at particle level. Charged final-state leptons are also required to be separated from each other by $\Delta R > 0.4$.

The ratio of the cross section from MCFM to the cross section from SHERPA as function of the like-sign dilepton mass is shown in Figure 8.1 for W^+Z, W^-Z, and ZZ production. For W^+Z and W^-Z events, the ratio is fitted using a linear parametriza-

[1] Version 6.2 of MCFM is used, which includes the singly resonant W and Z production processes.

tion to derive the following normalization factors:

$$W^+Z: \quad 1.075 - 0.0003019 \times m \tag{8.1}$$

$$W^-Z: \quad 1.044 - 0.0007088 \times m \tag{8.2}$$

where m is the like-sign dilepton mass measured in GeV. The uncertainty of the fits are taken into account as an additional statistical uncertainty on these backgrounds. For ZZ events, a flat normalization of 1.0 is used, i.e. no normalization correction is applied to the SHERPA sample. An additional 5% uncertainty is assigned for this process to take into account observed deviations from a flat line at 1.0.

The resulting cross section times branching ratio to leptons for $WZ \to \ell^\pm\nu\ell^\pm\ell^\mp$ or $ZZ \to \ell^\pm\ell^\mp\ell^\pm\ell^\mp$, requiring two charged leptons (electrons, muons, or taus) with the same electric charge, $p_{\mathrm{T}} > 20$ GeV, and $|\eta| < 2.5$ are 372 fb and 91 fb, respectively.

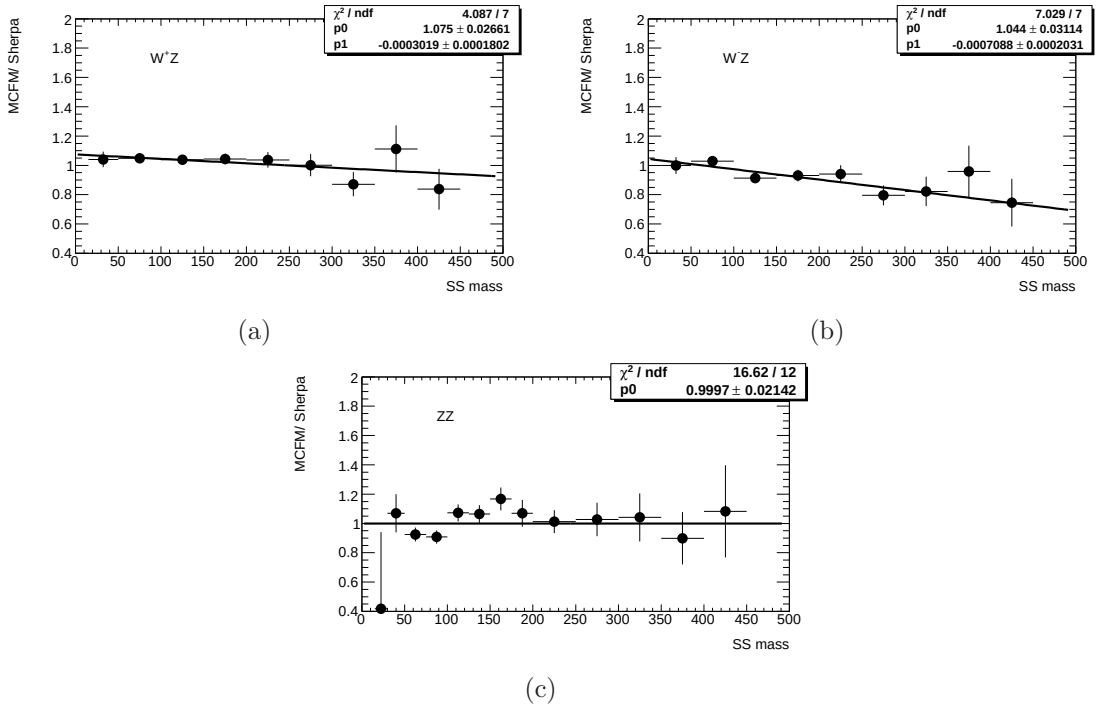

Figure 8.1: Ratio of the cross section derived using MCFM to that derived from SHERPA for (a) W^+Z, (b) W^-Z, and (c) ZZ events as a function of the like-sign dilepton mass in GeV.

8.1.2 $WWjj$, $t\bar{t}W$, and $t\bar{t}Z$ Production

To estimate the background contribution from $W^\pm W^\pm jj$, a sample generated with MADGRAPH is used [96]. The sample was generated with a jet p_{T} cut of 20 GeV

imposed while for the analysis, no jet selection is applied. The inclusive cross section without any jet p_{T} cut was evaluated using MADGRAPH to be 30% larger than that with a 20 GeV jet p_{T} cut. The $W^{\pm}W^{\pm}jj$ contribution as estimated using this sample is therefore scaled up accordingly by 30%.

Full higher-order corrections have not yet been calculated for $W^{\pm}W^{\pm}jj$ production. The QCD corrections at next-to-leading order have, however, been shown to be small for the process involving vector-boson fusion (VBF) production [97, 98], which accounts for approximately 60% of the total cross section. Based on this information, the leading-order (LO) cross section is used without any additional correction applied (NLO/LO K-factor of 1.0). The sample used includes the process $W^{\pm}W^{\mp}W^{\pm}$, where one of the W bosons decay hadronically and result in the final state of two like-sign W bosons plus two jets. The process where all three W bosons decay leptonically is not included but is largely suppressed due to the relatively small W branching ratio to leptons.

Background from $t\bar{t}W$ and $t\bar{t}Z$ production is also estimated using MADGRAPH. NLO cross-section corrections have been calculated for $t\bar{t}W$ production [99], resulting in a NLO cross section of 0.169 pb. The LO cross section from MADGRAPH is 0.124 pb, and a K-factor of 1.36 is consequently applied for this process. For $t\bar{t}Z$ production the NLO/LO cross-section correction was calculated initially at a center-of-mass energy of 14 TeV [100], predicting a K-factor of 1.35. This K-factor is applied to the MADGRAPH LO cross section of 0.096 pb. The cross section at next-to-leading order was calculated more recently for a center-of-mass energy of 7 TeV [101, 102] with a resulting value of 0.139 pb, indicating a somewhat larger K-factor. However, this analysis used the earlier K-factor calculation. The difference is small compared to the cross-section uncertainty discussed in Section 8.1.4.

Parton distribution functions (PDFs) taken from CTEQ6L1 [103] are used for the MadGraph samples. For the generation of diboson samples with Sherpa, the CTEQ10 [104] parameterization is used.

8.1.3 Prompt Opposite-Sign Dimuon Production

Prompt opposite-sign dimuon production from Z/γ^*, $t\bar{t}$, and $W^{\pm}W^{\mp}$ processes is used for some control samples and to estimate the charge-misidentification background. These are modeled using Monte Carlo. The production of Z/γ^* is modeled using Pythia[2], with the cross section calculated at next-to-next-to-leading order (NNLO) using PHOZPR [106]. The ratio of this cross section to the LO cross sec-

[2] A non-optimal agreement of the Z-boson p_{T} distribution is observed between data and simulation for the sample used, attributed to the Monte Carlo tuning. A Z-boson p_{T} reweighting was derived by the ATLAS Z' working group [105], and is here applied for this analysis. The reweighting has a negligible effect on the Z-boson invariant mass distribution, but improves the muon p_{T} modeling. This consequently has no effect on the results of the search described in this dissertation, but improves the prompt control region agreement (see Section 8.5.1).

tion is used to determine a mass dependent QCD K-factor which is applied to the output of the leading-order simulation [107]. Higher-order electroweak corrections (beyond the photon radiation included in the simulation) are calculated using HORACE [108, 109] and yield an electroweak K-factor due to virtual heavy gauge-boson loops and radiation radiation of W and Z bosons.

The production of $t\bar{t}$ is modeled using MC@NLO [110], with HERWIG [111] used for the parton showering and hadronization. The cross-section normalization is obtained from approximate NNLO QCD calculations using HATHOR [112]. The production of $W^{\pm}W^{\mp}$ is generated using HERWIG, and the cross section is normalized to the NLO value calculated with MCFM.

For the samples generated with PYTHIA or HERWIG, the MRST2007 LO** [113] PDF set is used. For the $t\bar{t}$ MC@NLO sample, CTEQ6.6 [114] PDFs are used.

8.1.4 Cross-Section Uncertainties

Uncertainties on the WZ and ZZ cross sections at next-to-leading order are evaluated using MCFM. The uncertainty due to higher-order QCD corrections is estimated to be $\pm 10\%$ by varying the renormalization and factorization scales by a factor of two. The uncertainty associated with parton distribution functions (PDFs) are evaluated using eigenvectors provided by the CTEQ10 [104] PDF error sets using the prescription from Ref. [115]. The difference between the central cross-section value obtained using the CTEQ10 set and that obtained from the MRST2008NLO [113] PDFs are added in quadrature, giving a resulting uncertainty due to PDFs of $\pm 7\%$. The combined cross-section uncertainty is $\pm 12\%$.

The cross-section uncertainty on $W^{\pm}W^{\pm}jj$ production, for which the full next-to-leading order corrections have not yet been calculated, is taken as 50%. Also for the processes $t\bar{t}W$ and $t\bar{t}Z$, a 50% uncertainty is quoted. The uncertainty on NLO calculations is typically lower than 50% but since the NLO cross sections were not validated for $t\bar{t}W$ and $t\bar{t}Z$ for the particular set of kinematic cuts used in this analysis, a larger uncertainty is assigned.

Table 8.1 summarizes the LO cross sections, NLO/LO K-factors, and the cross-section uncertainties used for the prompt, like-sign background processes. The additional uncertainties on WZ and ZZ production resulting from the cross-section normalization are also listed (mass-dependent for WZ and a flat 5% for ZZ).

8.2 Non-Prompt Background

Non-prompt muons constitute an important background for this search. They are predominantly real muons originating from semi-leptonic decays of b and c hadrons or from decay-in-flights of pions and kaons. Non-prompt muons also arise from fake sources, such as hadronic showers in the calorimeters which reach the muon spec-

Process	Generator	$\sigma_{LO} \times \epsilon_{\text{filter}}$ [pb]	K-factor	Uncertainty
$W^{\pm}Z$	SHERPA	6.26 (NLO)	mass-dep.	12% $\oplus$ mass-dep.
ZZ	SHERPA	4.62 (NLO)	1.0	12% $\oplus$ 5%
$W^{\pm}W^{\pm}jj$	MADGRAPH	0.287	1.0	50%
$t\bar{t}W^{\pm}$	MADGRAPH	0.124	1.36	50%
$t\bar{t}Z$	MADGRAPH	0.096	1.35	50%

Table 8.1: Cross sections and K-factors for the different background processes giving rise to prompt, like-sign dileptons.

trometer and are incorrectly matched to a reconstructed track in the inner detector, resulting in a misidentified muon. The non-prompt background is defined to include all processes where at least one of the two muons originates from a non-prompt source. The dominant process is QCD multi-jet production (including $b\bar{b}$ and $c\bar{c}$ production), with smaller contributions from W/Z+jets production and from top-quark pair production.

The non-prompt background is estimated with data-driven methods. The motivation for using data-driven techniques is that the rate with which jets are misidentified as leptons is not necessarily accurately described in simulation. There are significant theoretical uncertainties associated with heavy-flavor production and the kinematics of such events are difficult to assess theoretically. Relying on simulation for the non-prompt dimuon background also poses a computational difficulty since the production cross sections for relevant processes such as QCD multi-jet production are huge.

8.2.1 Method Overview

The non-prompt background estimate is based on defining a data control region enhanced in non-prompt muons by inverting some selection criteria. The background contribution is then derived by extrapolating from this region into the signal region. The extrapolation relies on measuring the ratio of the number of muons passing all analysis-level selection cuts (*selected muons*, N_S) to the number of muons failing some of these cuts and instead fulfilling a less stringent set of criteria (*anti-selected muons*, N_A). This ratio, the *fake factor* (f), is defined in terms of N_S and N_A as

$$f \equiv \frac{N_S}{N_A}. \tag{8.3}$$

The ratio of selected to anti-selected muons is measured as function of p_{T} and η in an independent, high-statistics data sample enhanced in non-prompt muons. The actual background prediction is derived by applying f to pairs where one or both muons fail the selected definition but instead fulfill the anti-selected criteria. The

resulting background contribution to the signal region is given by

$$N_{\text{non-prompt}} = \sum_{i=1}^{N_{A+S}} f(p_{\text{T1}}, \eta_1) + \sum_{i=1}^{N_{S+A}} f(p_{\text{T2}}, \eta_2) - \sum_{i=1}^{N_{A+A}} f(p_{\text{T1}}, \eta_1) f(p_{\text{T2}}, \eta_2), \quad (8.4)$$

where N_{A+S} (N_{S+A}) is the number of pairs for which the subleading (leading) muon fulfills the full selection criteria and the other lepton fulfills the anti-selected criteria. Similarly, N_{A+A} is the number of pairs where both muons are anti-selected. The last term of Equation 8.4 is necessary to remove double-counting of the background where both muons are non-prompt. Possible contamination from prompt muons to N_{A+S}, N_{S+A}, and N_{A+A} are subtracted using predictions from simulation. The variables p_{T1} and η_1 (p_{T2} and η_2) refer to the kinematic properties of the leading (subleading) muon.

Figure 8.2 shows a schematic illustration of the method, indicating the control regions and how these are scaled using the fake factor to determine the combined background prediction.

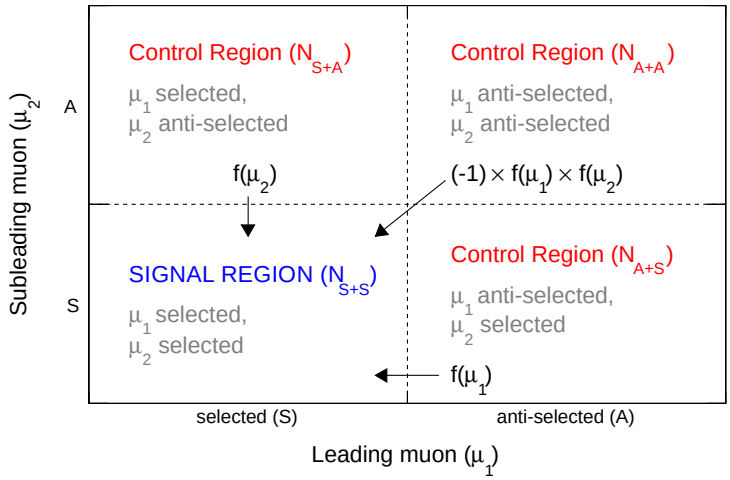

Figure 8.2: Schematic illustration of the method used for estimating the non-prompt background.

The most important step in determining the non-prompt background estimate is to accurately measure the fake factor and determine the associated systematic uncertainty. The fake factor is measured in a sample enhanced in non-prompt muons, ideally resembling the signal region as close as possible in terms of the overall event kinematics. The steps for measuring the fake factor are listed below.

- (1) Determine the selection criteria which is inverted, i.e. define selected and anti-selected muons. For this analysis, the track isolation criterion is inverted.

- (2) Define an independent sample in which the fake factor is derived. Here, muons with large impact parameter significance are used.
- (3) Subtract contamination from prompt muons in the numerator and denominator of the fake factor measurement in Equation 8.3 using simulation.
- (4) Study and derive corrections for any bias in using muons with high impact parameter significance while muons in the signal region have low impact parameter significance.
- (5) Parametrize the fake factor due to low statistics for high muon p_{T}.

Many different data control regions are used in deriving the non-prompt background estimate. Their use and distinction are summarized below.

- *Fake-factor derivation:* Independent control regions are used in which the actual fake factor is derived. They are defined by using muons with large impact parameter significance in a region orthogonal to the signal region and the regions used to derive the background estimate.
- *Non-prompt background derivation:* Data regions with one or two anti-selected muons are defined by inverting the track isolation criteria. These regions are then scaled using the fake factor to derive background estimates.
- *Verifying background prediction:* Additional control regions are defined in which the non-prompt background estimate is verified, comparing the observation in data to the background prediction.

8.2.2 Definition of Selected and Anti-Selected Muons

The definition of selected muons is identical to the standard muon selection criteria, outlined in Section 7.1.2. Anti-selected muons are required to fulfill the same selection except the track isolation criteria. Anti-selected muons must fail the regular track isolation requirement but instead fulfill a less stringent requirement $p_{\mathrm{T}}^{\mathrm{iso}}/p_{\mathrm{T}}(\mu) < 1.0$. Anti-selected muons are required be separated from reconstructed jets as usual.

Definitions for Intermediate Isolation

Several control regions which are used to validate the non-prompt background prediction apply a different isolation requirement than the signal region, referred to as *intermediate isolation*. For any given muon p_{T}, the intermediate isolation criteria always corresponds to a 4 GeV looser cut value than for the signal region:

- Fail signal track isolation

- Pass looser track isolation cut:
  - if $p_{\mathrm{T}} < 100$ GeV: $p_{\mathrm{T}}^{\mathrm{iso}} < (4 + 0.06 \times p_{\mathrm{T}}(\mu))$ GeV
  - if $p_{\mathrm{T}} > 100$ GeV: $p_{\mathrm{T}}^{\mathrm{iso}} < (8 + 0.02 \times p_{\mathrm{T}}(\mu))$ GeV

Since the isolation selection is modified, a separate fake factor must be derived for intermediate isolation. For this purpose, selected muons must fulfill the intermediate isolation criteria and pass all other analysis-level muon selection cuts. Anti-selected muons are required to fail both the signal and intermediate isolation selections, but pass the loose requirement of $p_{\mathrm{T}}^{\mathrm{iso}}/p_{\mathrm{T}}(\mu) < 1.0$. For intermediate isolation, anti-selected muons must be separated from the closest jet by $\Delta R > 0.40$, similarly as for regular isolation.

8.2.3 Derivation of the Fake Factor

The fake factor is measured directly from data using a sample enhanced in non-prompt muons which by construction is orthogonal to both the signal region and to the control regions used to derive the actual background prediction. Since anti-selected muons must pass all signal selection cuts except the track isolation requirement, the fake factor is interpreted as the ratio of passing versus failing the isolation cut for muons that are separated from jets by $\Delta R > 0.40$.

The fake factor strongly depends on the non-prompt muon source as well as the overall event kinematics, discussed further later in this section. To derive an accurate prediction of the non-prompt background, the fake factor should be derived in a region closely resembling the signal region. The fake factor is for this reason measured in dimuon events.

Sample Definition

Events are selected with a trigger requiring two muons with $p_{\mathrm{T}} > 10$ GeV[3]. Using a lower-threshold trigger allows deriving the fake factor also for low-p_{T} muons. Although both muons must satisfy $p_{\mathrm{T}} > 20$ GeV in the signal region, a set of control regions for verifying the background modeling are defined using muon pairs where the p_{T} threshold is loosened to 10 GeV for the subleading muon, resulting in control regions with improved statistics.

Muons are required to be combined and pass the track quality criteria listed in Section 7.1.2. They must additionally have $|\eta| < 2.5$, $p_{\mathrm{T}} > 10$ GeV, and pass a loose set of impact parameter cuts ($|d_0| < 10$ mm and $|z_0 \sin\theta| < 1$ mm). Events containing at least two such muons are used. Events with both like-sign and opposite-sign muon pairs are used to derive the fake factor. To remove contamination from

[3]The `EF_2mu10_loose` trigger is used to select dimuon events.

Z/γ^* production and from low-mass resonances (J/ψ and Υ), a set of invariant-mass requirements must be satisfied:

- *Like-sign:* $m(\mu^{\pm}\mu^{\pm}) > 15$ GeV
- *Opposite-sign:* $m(\mu^{+}\mu^{-}) > 15$ GeV and $m(\mu^{+}\mu^{-}) \notin [60, 120]$ GeV

All muons with impact parameter significance $|d_0|/\sigma(d_0) > 5.0$ among pre-selected dimuon events are used to measure the fake factor. Selecting muons with large impact parameter significance specifically targets muons from non-prompt sources. The transverse impact parameter cut is also loosened compared to the signal region ($|d_0| < 10$ mm instead of < 0.2 mm). The fake factor is then measured by counting the number of muons that fulfill the selected definition (N_S) and the number of muons that fulfill the anti-selected definition (N_A) among those with large impact-parameter significance. The measurement of the fake factor is thus performed in a dimuon sample which probes non-prompt muons through the modified $d_0/\sigma(d_0)$ selection and is completely orthogonal to the signal region and the control samples.

Prompt Contamination

Despite using an event selection designed to explicitly target non-prompt muons, muons from prompt sources may still contaminate the samples used to measure the fake factor. Contamination of prompt muons from W/Z+jets and $t\bar{t}$ production is therefore removed from the sample using Monte Carlo predictions[4]. The prompt contamination in the numerator (N_S) and denominator (N_A) of the fake factor is shown in Figure 8.3 as function of muon p_{T}. The contamination originates primarily from Z+jets production. Contributions to anti-selected muons (the denominator) are small, while for selected muons (the numerator) the contamination is more prominent, particularly at higher p_{T}. The fake factor before and after subtraction of prompt contamination is shown as function of muon p_{T} in Figure 8.4.

The prompt subtraction is verified by comparing its effect on opposite-sign and like-sign pairs. While the prompt subtraction is important for events with opposite-sign pairs, it has almost no impact on events with like-sign pairs since prompt contamination is mostly due to either opposite-sign Drell-Yan or $t\bar{t}$ events. Figure 8.5 shows the fake factor derived in events with opposite-sign muon pairs and in events with like-sign muon pairs, with or without applying the prompt subtraction. The opposite-sign and like-sign fake factors agree well after prompt subtraction which validates the subtraction.

[4]Production of $t\bar{t}$ is generated with MC@NLO [110], as in Section 8.1.3, while the production of W/Z+jets is modeled with ALPGEN [90].

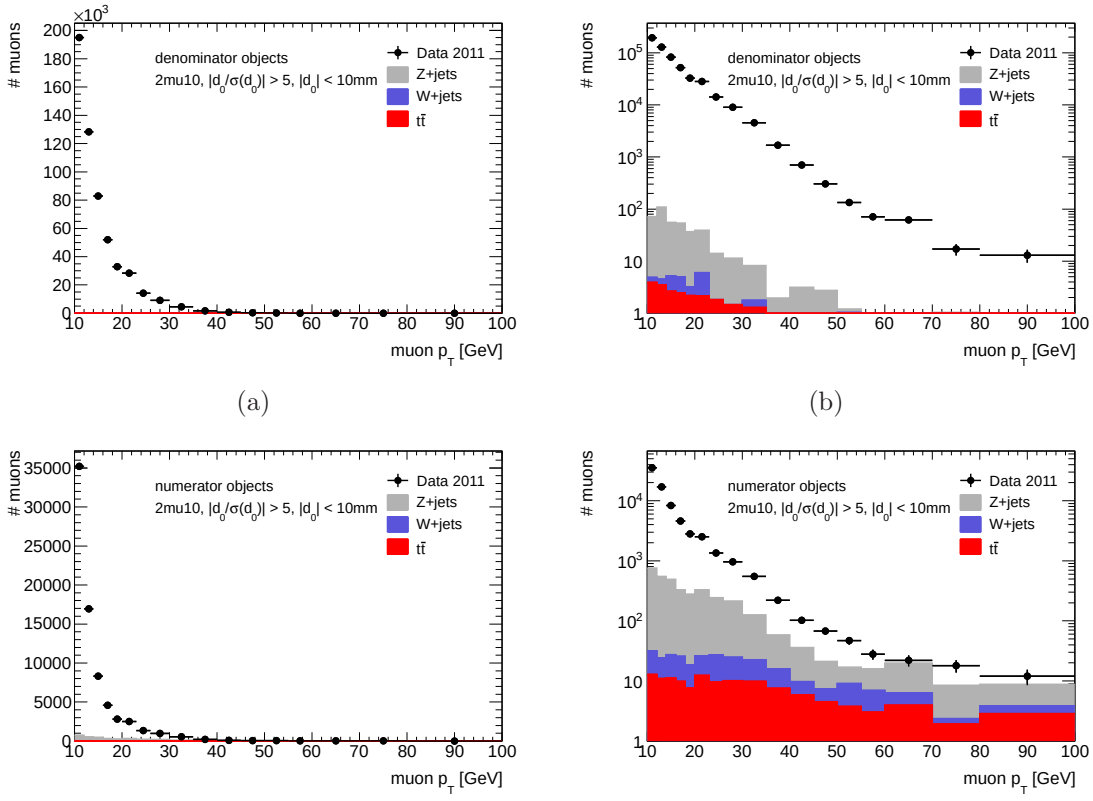

Figure 8.3: The sample of anti-selected and selected muons used to measure the fake factor, denominator and numerator objects, respectively, shown in (a) and (c) on linear scale and in (b) and (d) on logarithmic scale. The filled points represent the data counts without subtraction of prompt contamination, and the stacked histograms show the contributions from different prompt sources.

Dependence on Event Kinematics

The fake factor is measured in dimuon events, a sample similar to the signal region in the overall event kinematics. Clear differences are observed in fake factors derived from single muon and dimuon events, shown in Figure 8.6. At low muon p_{T}, the fake factor derived in single-muon events is significantly higher than that observed for dimuon events.

The dimuon trigger is used for selecting events to be able to derive the fake factor down to 10 GeV. To ensure that observed differences between single muon and dimuon events is related to the event kinematics rather than a trigger bias, the fake factor is measured separately for dimuon events triggered with a dimuon trigger and dimuon events triggered with the single muon trigger used in the main analysis. The result

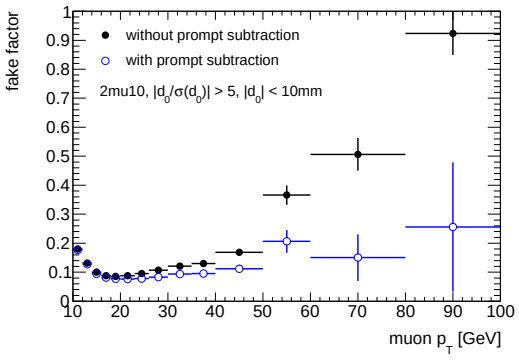

Figure 8.4: The fake factor, as measured using muons with $|d_0|/\sigma(d_0) > 5.0$ in dimuon events, before and after subtraction of prompt contributions from W/Z+jets and $t\bar{t}$ production.

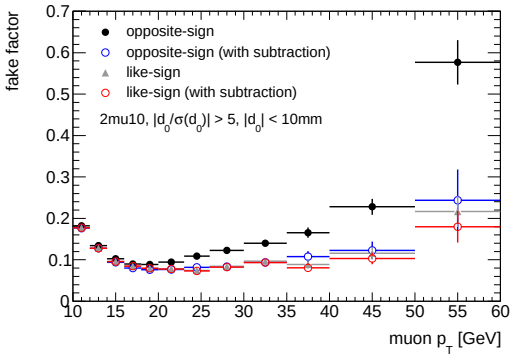

Figure 8.5: Fake factor for dimuon opposite-sign and like-sign events, with and without applying subtraction of prompt contamination.

is shown in Figure 8.7, clearly illustrating that no trigger bias is present. This is expected, since the kinematics of *dimuon events* should be the same regardless of whether one or two muons were required at trigger level.

The fake factor, or the rate with which non-prompt muons fulfill the track isolation criteria, consequently differs between single muon and dimuon events due to the event kinematics. Since the fake factor is applied to dimuon events in deriving the non-prompt background prediction, a dimuon rather than single-muon sample should be used.

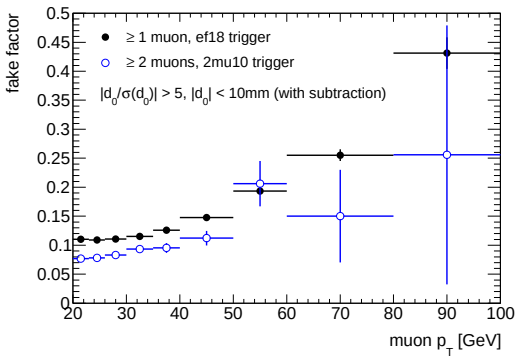

Figure 8.6: Fake factor as determined from single-muon events (selected with the regular analysis triggers) compared to dimuon events (selected with a dimuon trigger). Significant difference are observed between the two type of events.

8.2.4 Correlation between Isolation and Impact Parameter

From studies using Monte Carlo simulation, the fake factor is observed to depend somewhat on the muon impact parameter significance. Determining the fake factor using muons with $|d_0|/\sigma(d_0) > 5$ and $|d_0| < 10$ mm while in the signal region applying it to muons with $|d_0|/\sigma(d_0) < 3$ and $|d_0| < 0.2$ mm therefore introduces a bias in the measurement. This difference in fake factor for muons with high versus low impact parameter significance must be corrected for.

A correction factor is derived from simulated dimuon events with $m(\mu\mu) > 15$ GeV and $p_{\mathrm{T}}(\mu) > 10$ GeV, comparing the fake factor for muons with low and high impact parameter significance. A simulated $b\bar{b}/c\bar{c}$ sample, generated using Pythia [116], is used. Fake factors from Monte Carlo, integrated over η and p_{T}, are shown together with corresponding correction factor in Table 8.2. The correction factor is derived separately for signal and intermediate isolation.

Isolation type	$\|d_0\|/\sigma(d_0) > 5$, $\|d_0\| < 10$ mm	$\|d_0\|/\sigma(d_0) < 3$, $\|d_0\| < 0.2$ mm	Correction factor
Signal isolation	0.119 ± 0.002	0.159 ± 0.001	1.34 ± 0.02
Intermediate isolation	0.684 ± 0.003	0.918 ± 0.002	1.34 ± 0.01

Table 8.2: Fake factors derived from dimuon events in Monte Carlo simulated data, for muons with low and high impact parameter significance. The fake factors and the resulting correction factor are shown separately for signal and intermediate isolation. The uncertainties quoted are statistical only.

The p_{T} dependence of the correction factor is studied by comparing the average

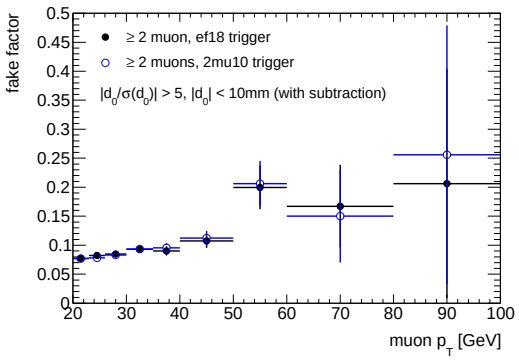

Figure 8.7: Fake factor as determined from dimuon events selected using the single muon triggers compared to dimuon events selected using the dimuon trigger. As expected, no trigger dependence is observed.

correction to the fake factor ratio as function of p_{T}, shown in Figure 8.8. The ratio as function of p_{T} is consistent with the average correction factor within the available statistics for signal isolation. For intermediate isolation, small deviations are observed. The average correction is used for both signal and intermediate isolation, but the full correction is applied as a conservative uncertainty on the correction, i.e. 1.34 ± 0.34.

Muons with $d_0/\sigma(d_0) > 5$ rather than > 3 are used for deriving the fake factor as the prompt contamination is then less severe at high muon p_{T}. To verify the correction factor procedure the fake factor is additionally derived using muons with $d_0/\sigma(d_0) > 3$, applying a correction to translate from muons with $d_0/\sigma(d_0) > 3$ to $d_0/\sigma(d_0) < 3$. The result is shown in Figure 8.9. At low muon p_{T}, the fake factor is nearly unchanged compared to that derived for $d_0/\sigma(d_0) > 5$. At higher muon p_{T}, it is completely dominated by prompt contamination and the central value should not be trusted in that region. This cross-check gives confidence in the procedure.

8.2.5 Results

The fake factor measured in data is corrected for the observed dependence on impact parameter significance by applying a correction factor derived from simulation. The final fake factors after this correction are shown in Figure 8.10 for signal and intermediate isolation as function of muon p_{T} and η.

The fake factor increases significantly at low-p_{T} for signal isolation. This is a consequence of the fact that the isolation variable only uses tracks with transverse momentum larger than 1 GeV. As an example, the signal isolation requirement ($p_{\mathrm{T}}^{\mathrm{cone0.4}}/p_{\mathrm{T}} < 0.06$) translates to $p_{\mathrm{T}}^{\mathrm{cone0.4}} < 0.06 \times 17 = 1.0$ GeV for muons with $p_{\mathrm{T}} = 17$ GeV, while for muons with $p_{\mathrm{T}} = 10$ GeV, the requirement is $p_{\mathrm{T}}^{\mathrm{cone0.4}} < 0.06 \times 10 = 0.6$ GeV.

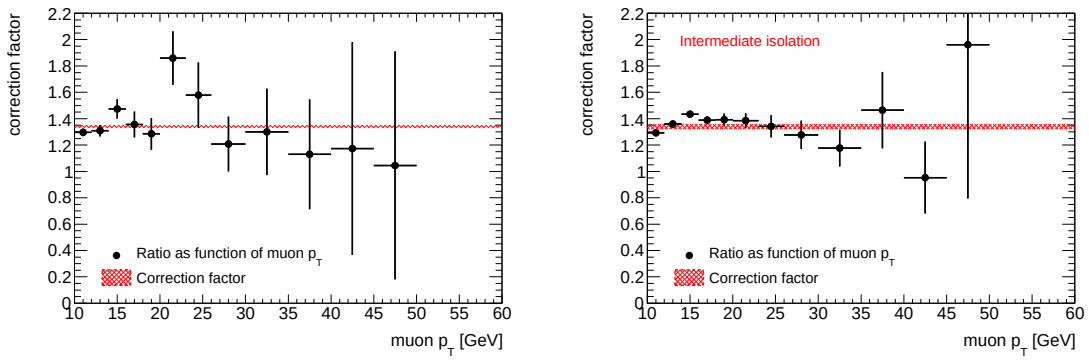

(a) (b)

Figure 8.8: Ratio of the fake factor for muons with low impact parameter significance to the fake factor for muons with high impact parameter significance as estimated from MC simulation. The red line shows the resulting average correction factor. The signal region isolation is shown on the left and the intermediate isolation is shown on the right.

However, due to the minimum track p_{T} used to define the isolation variable, any cut value of < 1 GeV is in reality equivalent to a cut at 1.0 GeV.

Fake Factor Parametrization as Function of p_{T}

The derivation of the fake factor in data suffers from low statistics at high muon p_{T}. Since a roughly linear dependence on p_{T} is observed above 20 GeV, the fake factor is parametrized. For signal isolation, the fake factor is parametrized with a first-order polynomial for $p_{\mathrm{T}} > 20$ GeV. For intermediate isolation, the fake factor is instead fitted to a zeroth-order polynomial for $p_{\mathrm{T}} > 30$ GeV. At lower p_{T}, the statistics is sufficient and no parametrization is necessary. The resulting parameterizations for signal and intermediate isolation are shown in Table 8.3. Figure 8.11 additionally shows the measured fake factors together with the parameterizations.

Isolation type	Parameterization
Signal isolation	$0.05920 + 0.00197 \times p_{\mathrm{T}}(\mu)$
Intermediate isolation	0.353

Table 8.3: Muon fake factor parametrizations for signal isolation and intermediate isolation.

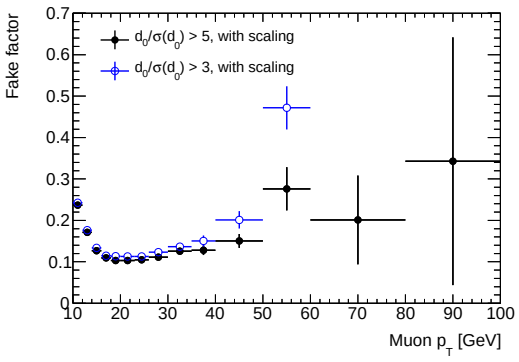

Figure 8.9: The central value of the fake factor (black filled markers) shown together with (blue open markers) the central value had it been derived using muons with $d_0/\sigma(d_0) > 3$ instead of > 5.

Dependence on η

The fake factors are evaluated as function of both p_{T} and η, assuming the variables to be uncorrelated. The final fake factor for a given muon (p_{T}, η) is determined as

$$f(p_{\mathrm{T}}, \eta) = f(p_{\mathrm{T}}) \cdot \frac{f(\eta)}{< f >}, \tag{8.5}$$

where $< f >$ is the average fake factor in the p_{T} range for which $f(\eta)$ is measured. The fake factor shape as function of η is roughly independent of the p_{T} threshold used, based on comparing 10 GeV and 20 GeV thresholds. Since the statistics is significantly better using the lower threshold, the η dependence is determined from muons with $p_{\mathrm{T}} > 10$ GeV. The η dependence is shown in Figure 8.12 for signal isolation and intermediate isolation.

8.3 Systematic Uncertainty on the Non-Prompt Muon Background

Several systematic effects may bias the measured fake factor and the predicted non-prompt background. The following effects are taken into account when determining the systematic uncertainty associated with the fake factor:

- Statistical uncertainty on the data due to limited number of denominator objects particularly at high muon p_{T}. This uncertainty is given directly from data and ranges between $\pm$(0.5–87)%. For muon p_{T} above 100 GeV, the statistics is highly limited and a $\pm$100% systematic uncertainty is assigned.

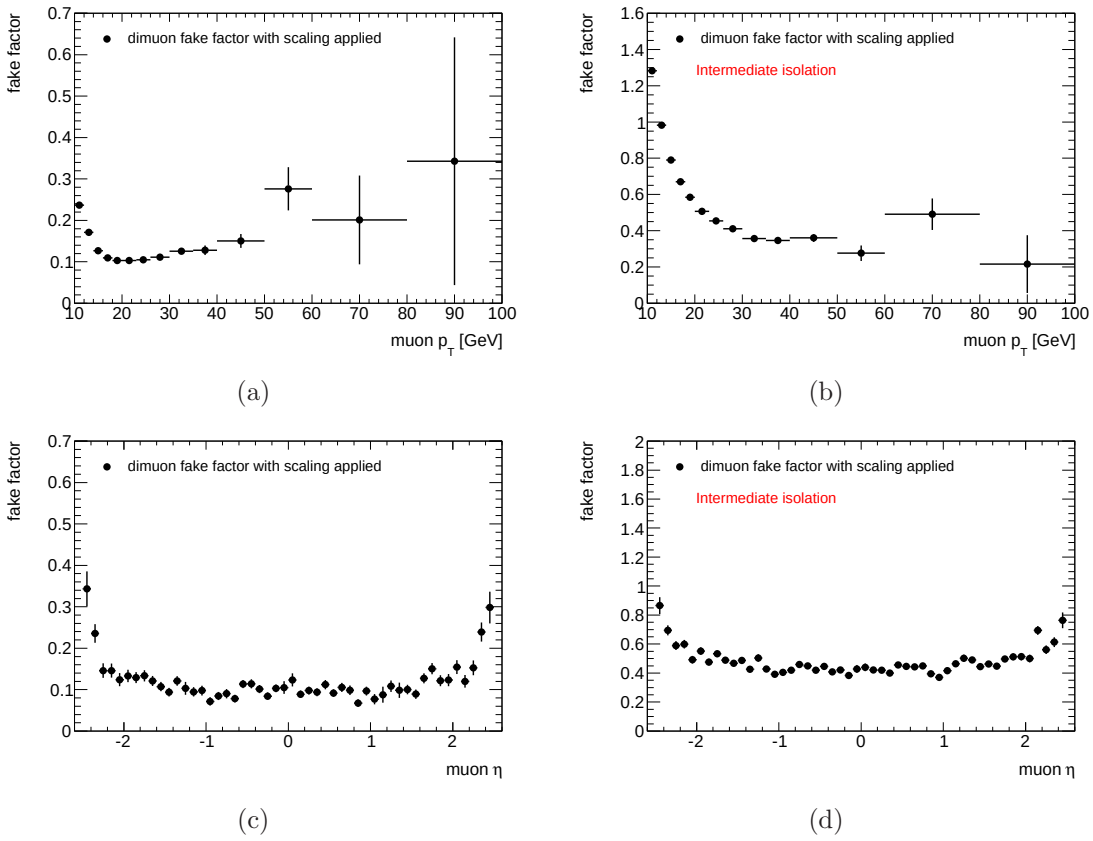

Figure 8.10: Fake factor as function of muon p_{T} and η after applying the correction factor for high vs low impact parameter significance.

- Uncertainty on the subtraction of prompt contamination. This source of systematic uncertainty is determined by varying the MC prediction by ±10%, an amount which covers the cross-section and luminosity uncertainties. The resulting uncertainty ranges between ±0.2% (for $p_{\mathrm{T}} \sim 10$ GeV) and ±27% (for $p_{\mathrm{T}} \sim 100$ GeV).

- Uncertainty associated with the correction factor from low to high impact parameter significance. The applied correction factor is 1.34 for both signal and intermediate isolation. The full correction is taken as a systematic uncertainty, giving a ±34% uncertainty due to this source.

- Uncertainty associated with non-prompt muons originating from heavy-flavor compared to light-flavor decays. This is described in detail in the section below, and results in a systematic uncertainty of ±15% on the fake factor.

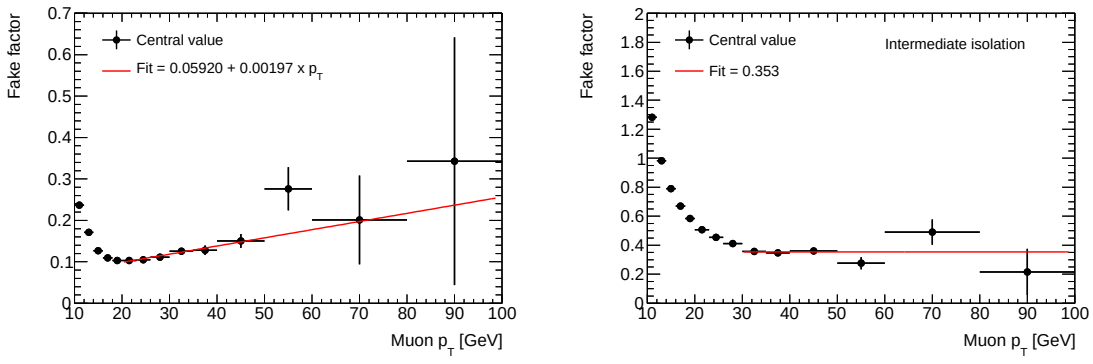

(a) (b)

Figure 8.11: Fake factor as function of muon p_{T} for signal and intermediate isolation together with the parameterizations used at high muon p_{T} where the available statistics is limited.

8.3.1 Uncertainty Associated with Light-Flavor Muons

The fake factor derivation use muons with large impact parameter significance. This is designed to particularly target non-prompt muons from heavy-flavor decays which for dimuon events is dominant in the momentum range considered (see Section 4.1). Targeting heavy-flavor decays only becomes a problem if the composition of heavy-flavor versus light-flavor is different in the region used to derive the fake factor compared to the signal region.

To get a handle on the fraction of light-flavor muons in the signal region compared to the region where the fake factor is estimated, the fractional difference in muon momentum between the inner detector and the muon spectrometer is used. The fractional momentum loss is defined as

$$\Delta p = \frac{p^{ID} - p^{MX}}{p^{ID}}, \tag{8.6}$$

where p^{ID} is the muon momentum as measured in the ID and p^{MX} is the momentum measured in the MS extrapolated back to the interaction point, correcting for the expected energy loss in the calorimeter.

For prompt muons or non-prompt muons from heavy-flavor decays, the fractional momentum loss is expected to be symmetric around $\Delta p = 0$ since when correcting for the muon energy loss in the calorimeter, the momentum measurement in the inner detector should be the same as that measured in the muon spectrometer (up to resolution effects). However, for muons originating from light-flavor sources such as pions or kaons which decay *between* the inner detector and the muon spectrometer, a large positive momentum loss is expected. For a pion/kaon decay-in-flight ($\pi/K \rightarrow$

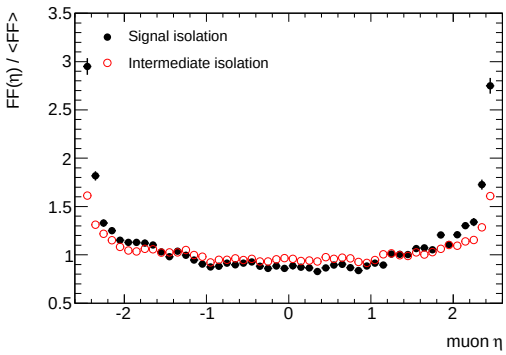

Figure 8.12: Fake factor η-correction for signal isolation and intermediate isolation.

$\mu\nu_\mu$), where the decay occurs around the calorimeter, the momentum measured in the inner detector will be that of the initial pion or kaon, while the momentum measured in the muon spectrometer will be that of the decay muon. Since the decay also involves a neutrino, the momentum is expected to be lower for the decay muon, as discussed in Section 4.1. The difference in fractional momentum loss for heavy-flavor and light-flavor muons is illustrated in Figure 8.13 using fully simulated $t\bar{t}$ events.

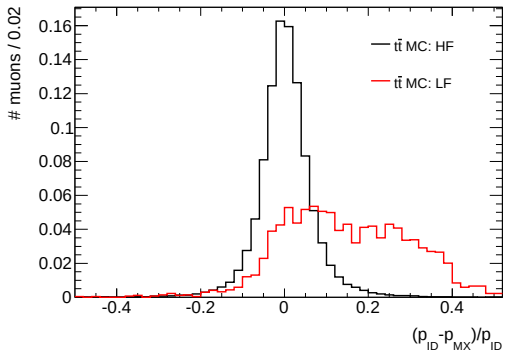

Figure 8.13: Fractional momentum loss for muons from heavy-flavor and light-flavor, respectively, in Monte Carlo simulated $t\bar{t}$ events.

This different behavior of heavy-flavor versus light-flavor is used to derive a systematic uncertainty on the fraction of light-flavor among the anti-selected muons used to determine the actual non-prompt background prediction. The fractional momentum-loss asymmetry is first defined as

$$\Delta p^{asym} = \frac{N(\Delta p > 0.10) - N(\Delta p < -0.10)}{N(\Delta p)}, \tag{8.7}$$

where $N(\Delta p > 0.10)$ and $N(\Delta p < -0.10)$ are the number of muons with fractional momentum loss larger than 0.10 and less than -0.10. $N(\Delta p)$ is the total number of muons. Using the asymmetry of the fractional momentum loss means that the component from prompt muons and muons from heavy-flavor cancels to first order - the asymmetry is then directly probing the light-flavor component.

The momentum-loss asymmetry is determined for anti-selected muons in the signal region and for anti-selected muons with $p_{\mathrm{T}} > 20$ GeV in the sample where the fake factor is derived. Figure 8.14 shows the momentum-loss distribution for muons used to determine the fake factor and anti-selected muons in the signal region, i.e. those that are used to make the non-prompt background prediction. Using Monte Carlo templates of the momentum-loss asymmetry for heavy-flavor and light-flavor muons, a given momentum-loss asymmetry can be translated into a corresponding light-flavor fraction. The measured asymmetries and corresponding estimated light-flavor fractions are shown in Table 8.4.

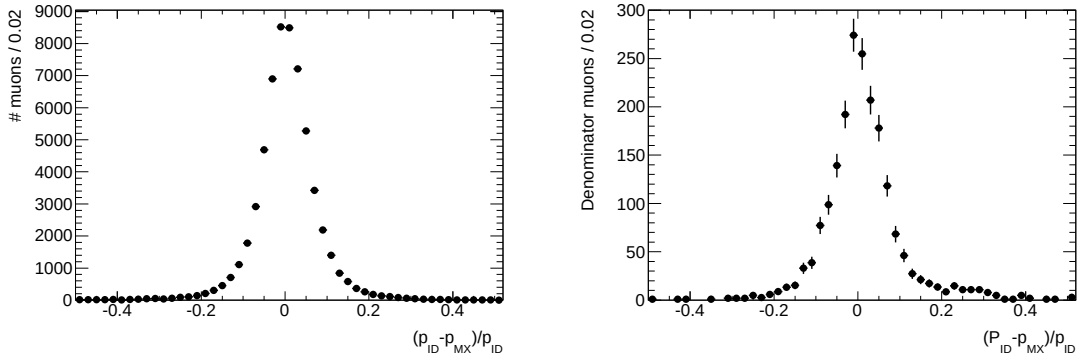

(a) (b)

Figure 8.14: Momentum-loss distributions for (a) muons used to determine the fake factor and (b) anti-selected muons in the signal region.

Region	Δp^{asym}	Light-flavor fraction
Signal region	$3.9 \pm 0.8\%$	$7.6 \pm 1.6\%$
Fake factor	$1.1 \pm 0.1\%$	$1.8 \pm 0.3\%$

Table 8.4: Momentum-loss asymmetry and corresponding light-flavor fraction for denominator muons in the signal region and in the control sample where the fake factor is determined. The uncertainties are statistical only.

An upper systematic uncertainty due to the difference in light-flavor fraction is

derived as a correction to the central value. It is defined as

$$f_{LF}^{\text{systematic}} = f^{\text{central}} \cdot (1 - x_{LF}) + f_{LF} \cdot x_{LF}, \tag{8.8}$$

where f^{central} is central value of the fake factor, x_{LF} is the 1σ upper systematic on the light-flavor fraction measured using momentum-loss asymmetry from data, and f_{LF} is the fake factor for light-flavor muons. The 1σ upper systematic on the light-flavor fraction follows from comparing the 1σ upper light-flavor fraction in the signal region to the estimated fraction for the fake factor central value in Table 8.4, and results in $x_{LF} = 7.5\%$.

The fake factor for light-flavor muons is derived from data, using single-muon events with at least one jet with $p_{\text{T}} > 25$ GeV and transverse mass $m_{\text{T}} < 10$ GeV[5] to avoid prompt muons due to W+jets production. Among muons in these events, the light-flavor fake factor is defined as

$$f_{LF} = \frac{N_S(\Delta p > 0.10) - N_S(\Delta p < -0.10)}{N_A(\Delta p > 0.10) - N_A(\Delta p < -0.10)}, \tag{8.9}$$

where N_S (N_A) is the number of selected (anti-selected) muons for a given fractional momentum loss range. Prompt muons and muons from heavy-flavor are again assumed to be symmetric around $\Delta p = 0$ and should cancel with this definition, isolating a sample largely dominated by light-flavor muons. Figure 8.15 shows the fake factor central value, and light-flavor fake factors using two different cuts on Δp of 0.10 and 0.20. The results are very similar for the two.

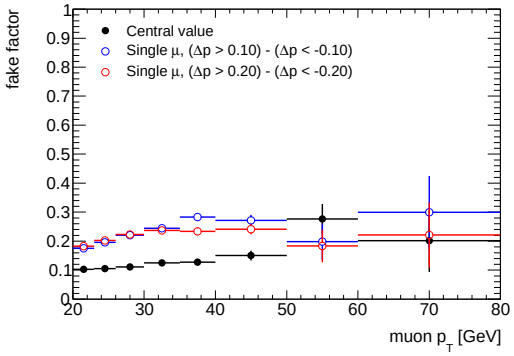

Figure 8.15: Light-flavor fake factor compared to the central value.

To probe f_{LF} also in dimuon events, an additional control sample is defined, completely orthogonal to the signal region, where one muon fails the impact parameter

[5]The transverse mass is defined as $m_{\text{T}} = \sqrt{2 p_{\text{T}} E_{\text{T}}^{\text{miss}} (1 - \cos(\phi^{\mu} - \phi^{E_{\text{T}}^{\text{miss}}}))}$.

significance cut. For the second muon in these events, f_{LF} is determined as in Equation 8.9. Due to poor statistics the values are integrated for $p_{\mathrm{T}} > 20$ GeV. The results are shown in Table 8.5. The largest observed light-flavor fake factor is three times higher than the central value, and as an upper systematic, $f_{LF} = 3 \times f^{\mathrm{central}}$ is therefore used.

Control sample	Average fake factor ($p_{\mathrm{T}} > 20$ GeV)
Central value	0.109 ± 0.002
Single μ, $\Delta p > 0.10$	0.193 ± 0.001
Single μ, $\Delta p > 0.20$	0.198 ± 0.001
Dimuon, $\Delta p > 0.10$	0.305 ± 0.046
Dimuon, $\Delta p > 0.20$	0.192 ± 0.070

Table 8.5: Light-flavor fake factors.

The systematic uncertainty is finally obtained from Equation 8.8 using the light-flavor fraction, $x_{LF} = 7.5\%$, and the light-flavor fake factor, $f_{LF} = 3 \times f^{\mathrm{central}}$ as

$$f_{LF}^{\mathrm{systematic}} = f^{central} \cdot (1 - 0.075) + 3 \cdot f^{\mathrm{central}} \cdot 0.075 = 1.15 \cdot f^{\mathrm{central}}. \tag{8.10}$$

Consequently, the systematic uncertainty associated with the light-flavor component is $\pm 15\%$.

8.3.2 Total Systematic Uncertainty

Table 8.6 shows the systematic uncertainty in bins of muon p_{T} for the different sources together with the central value and the total uncertainty. For high muon p_{T}, the uncertainty is dominated by the statistical uncertainty on the fake factor. For low muon p_{T}, the uncertainty is dominated by the uncertainty on the impact parameter correction factor. Figure 8.16 shows the central value of the fake factor, with all corrections applied, together with its parametrization and total systematic uncertainty.

p_{T} [GeV]	Central value	Total error	Statistics	Prompt sub	$d_0/\sigma(d_0)$	LF/HF
[10, 12]	0.237	37.2%	0.5%	0.2%	34.0%	15.0%
[12, 14]	0.171	37.2%	0.8%	0.3%	34.0%	15.0%
[14, 16]	0.127	37.2%	1.2%	0.6%	34.0%	15.0%
[16, 18]	0.110	37.2%	1.6%	0.8%	34.0%	15.0%
[18, 20]	0.103	37.2%	2.3%	1.1%	34.0%	15.0%
[20, 23]	0.102	37.3%	2.3%	1.5%	34.0%	15.0%
[23, 26]	0.107	37.4%	3.5%	2.2%	34.0%	15.0%
[26, 30]	0.114	37.5%	4.5%	2.8%	34.0%	15.0%
[30, 35]	0.123	37.7%	5.4%	3.0%	34.0%	15.0%
[35, 40]	0.133	38.4%	8.9%	3.6%	34.0%	15.0%
[40, 50]	0.148	39.1%	11.2%	5.0%	34.0%	15.0%
[50, 60]	0.168	42.4%	18.9%	7.8%	34.0%	15.0%
[60, 80]	0.197	69.3%	53.2%	24.1%	34.0%	15.0%
[80, 100]	0.236	98.6%	87.3%	26.9%	34.0%	15.0%
[100, ...]	0.256	100%	-	-	-	-

Table 8.6: Different sources of systematic uncertainty on the fake factor.

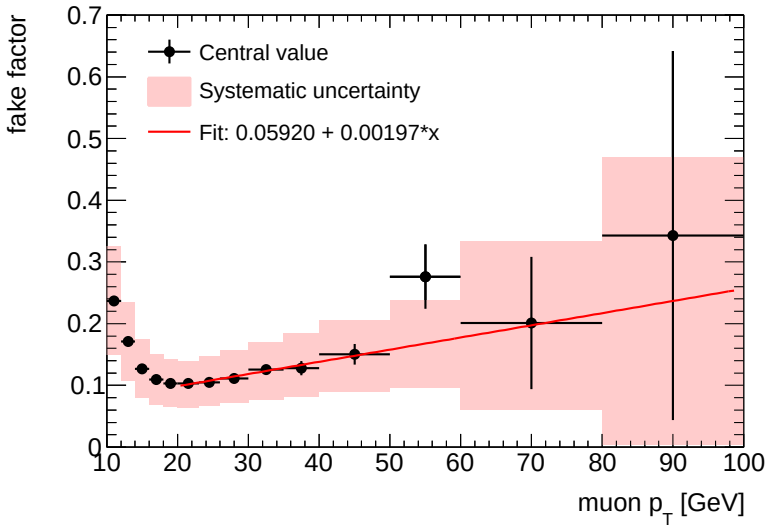

Figure 8.16: Fake factor central value and combined total systematic uncertainty.

8.4 Charge-Misidentification Background

Pairs of oppositely-charged leptons constitute a source of background if the charge of one lepton is misreconstructed. Such *charge misidentification* can occur for both electrons and muons if the tracking system is unable to correctly resolve the track curvature. This affects primarily high-momentum tracks which have small curvature and appear nearly straight in the detector, for which the tracking resolution is worse. Another source of charge misidentification which affects only electrons is radiation of a high-p_{T} photon which converts into an e^+e^- pair. The remainder of this section is focused on muon charge misidentification resulting from limited curvature resolution for high-p_{T} tracks.

Muons used for the search are required to have consistent charge measurements in the inner detector (ID) and the muon spectrometer (MS). Charge misidentification can consequently only occur if the muon track is misreconstructed in *both* the ID and the MS. The combined probability for muon charge misidentification to occur is the product of the probabilities for each of the two subsystems. The charge misidentification rate in the ID (MS) is estimated directly from data by selecting Z candidates using information from the MS (ID) only.

A sample of $Z \to \mu^+\mu^-$ event candidates is selected by identifying pairs of combined, oppositely-charged muons with the charge measured by either only the ID or only the MS. Muons must have $p_{\mathrm{T}} > 20$ GeV, $|\eta| < 2.5$, and pass the track hit quality criteria from Section 7.1.2. To ensure high-quality muons, those selected must additionally have impact parameters consistent with originating from the primary vertex ($|d_0| < 0.2$ mm, $|z_0 \sin\theta| < 1.0$ mm, and $|d_0|/\sigma(d_0) < 3.0$) and be isolated from nearby tracks ($p_{\mathrm{T}}^{\mathrm{iso}}/p_{\mathrm{T}}(\mu) < 0.1$ and $p_{\mathrm{T}}^{\mathrm{iso}} < 3$ GeV). Next, the dimuon invariant mass, as measured by either the inner detector (m_{ID}) or the muon spectrometer (m_{MS}), is formed using information from only that given subsystem. For instance, to form m_{ID}, muon track parameters as measured by the inner detector ($p_{\mathrm{T},ID}$, η_{ID}, ϕ_{ID}) only are used. A sample of $Z \to \mu^+\mu^-$ candidates can then be selected in a mass window as measured by one subsystem to probe the charge of the other so that the charge misidentification rate of the ID (MS) is estimated from muons in a Z-mass window measured by the MS (ID) only. The dimuon invariant mass distributions as reconstructed using only inner-detector or muon-spectrometer information are shown in Figure 8.17.

Event candidates are selected in the mass ranges 76 GeV $< m_{ID}, m_{MS} <$ 106 GeV to derive estimates of the charge misidentification rates. The charge measurement of the system probed is compared to the reference system, an opposite charge measurement means a charge misreconstruction in that system under the assumption that the reference system, used to select Z candidates from good opposite-charge muon pairs, has correct charge measurements. Both muons forming the Z candidate are used independently.

Resulting charge-misidentification rates for the ID and the MS are shown in Fig-

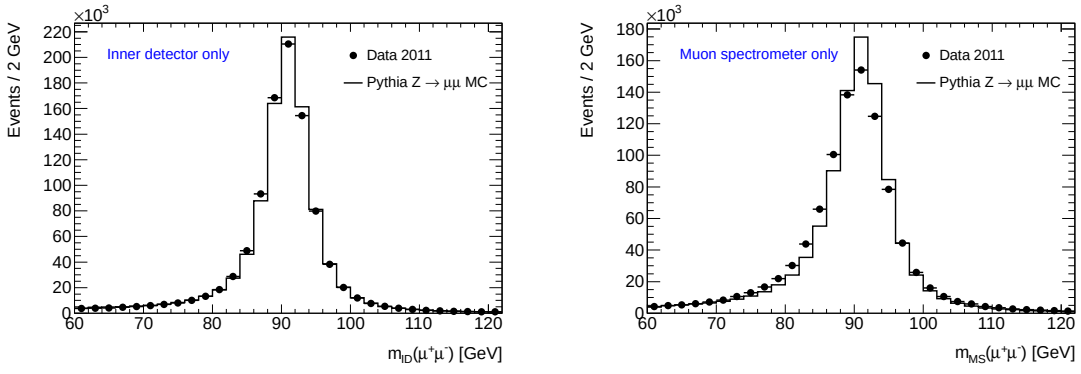

Figure 8.17: Distribution of the dimuon invariant mass based on (a) only the ID momentum reconstruction and (b) only the MS momentum reconstruction. The filled circles show data and the histogram show estimates using a Monte Carlo simulated $Z \to \mu^+\mu^-$ sample generated with PYTHIA. The Monte Carlo is normalized to the total number of events observed in data.

ure 8.18. For the ID, the charge-misidentification rate measured in data is less than 10^{-6} at low p_{T} and consistent with zero for higher p_{T} values. For the MS, the fraction of charge-misidentified muons as measured in data is about 2×10^{-4} in the lowest p_{T} range (20–50 GeV) and of the order of 10% in the highest p_{T} range (350–400 GeV). The measured charge-misidentification rates are observed to typically be a factor of two lower in simulation. Charge-misidentification primarily occurs for muons in the region $1.2 < |\eta| < 1.6$ where the alignment and instrumentation in the muon system is not yet ideal. Upper limits at 67% confidence level (CL) are derived using the charge misidentification rates observed in data and Monte Carlo. The observed upper limit in data for the highest p_{T} range is 18% for the ID and 38% for the MS. These values are limited by the available statistics in data. Limited statistics is also the constraining factor for parametrizing the charge-misidentification rates only as function of muon p_{T} rather than as functions of both p_{T} and η.

The combined upper limit on the probability for a muon to be charge misidentified, which requires a charge mismeasurement of both the inner detector and the muon spectrometer tracks, is given by the product of the individual charge mismeasurement rates. The resulting upper limit is shown in Figure 8.19. The combined upper limit at 67% CL on the charge misidentification ranges from around 10^{-10} at low muon p_{T} to 7×10^{-2} for $p_{\mathrm{T}} \approx 375$ GeV.

To derive predictions of the background due to charge misidentification (*charge-flip*) in the signal region, Monte Carlo simulation is used to determine the central value. The MC samples include $Z \to \mu^+\mu^-$ and $Z \to \tau^+\tau^-$ production, where the τ lepton subsequently decays to muons, generated using PYTHIA, and $t\bar{t}$ production,

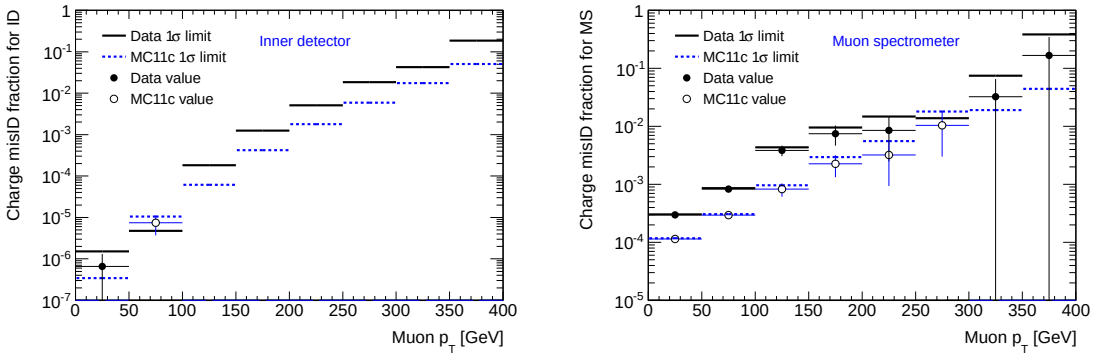

(a) (b)

Figure 8.18: Probability of muon charge misidentification as function of muon p_{T} for (a) the inner detector and (b) the muon spectrometer. The filled and open circles show the measurement in data and MC, respectively. The solid and dashed lines similarly show the upper limits at 67% confidence level for data and MC.

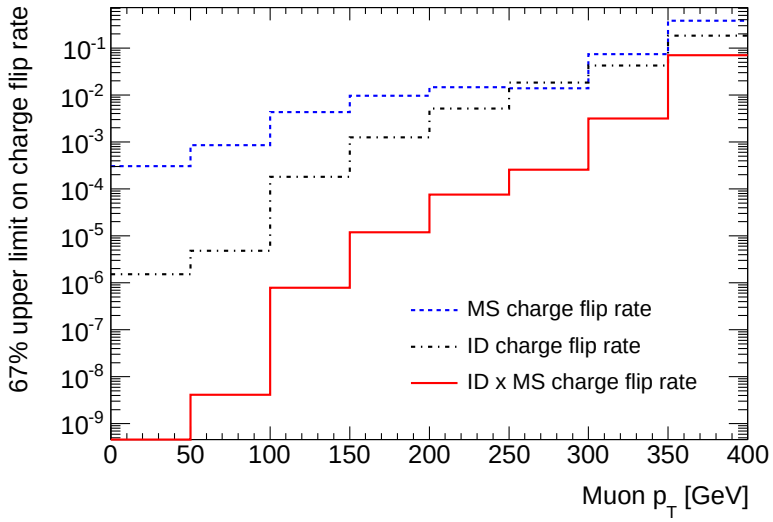

Figure 8.19: Probability for muon charge misidentification as function of muon p_{T} for the ID, the MS, and the product of the two (ID×MS). The limits are derived at 67% confidence level from the observation in data.

generated with MC@NLO. The predicted central value is zero charge-flipped muon pairs. A systematic uncertainty on the prediction is derived using the upper limits at 67% CL on the ID×MS charge-flip probability measured in data. The combined upper limit as function of muon p_{T}, shown in Figure 8.19, is applied to the MC samples, selecting opposite-sign muon pairs that pass all other event selection cuts:

$$N_{\mathrm{charge-flip}} = N_{OS} \times r_{ID\times MS}(\mu_1) + N_{OS} \times r_{ID\times MS}(\mu_2) \tag{8.11}$$

where $N_{\mathrm{charge-flip}}$ is the number of like-sign muon pairs due to charge misidentification, N_{OS} the number of opposite-sign pairs, and $r_{ID\times MS}$ is the upper limit on the ID×MS charge-flip probability. Only opposite-sign pairs where both muons are classified as prompt are used to avoid double-counting with the non-prompt background estimate.

8.5 Control Regions

The modeling of prompt muons in simulation and the data-driven background estimates are validated in different control regions orthogonal to the signal region. A region with opposite-sign muons is used to validate the modeling of prompt, isolated muons. The data-driven non-prompt muon background estimate is validated in control regions with pairs of like-sign muons where some of the muon identification criteria are reversed. The control regions are described in detail below.

8.5.1 Control Regions with Prompt Muons

To verify the modeling of prompt muons in simulation, a control region is defined by selecting pairs of isolated, oppositely-charged muons. Both muons must have $p_{\mathrm{T}} > 20$ GeV and fulfill exactly the same muon identification criteria as for the signal region, described in Section 7.1.2, except that the muons must have opposite charge. This control region is completely dominated by Z/γ^* production, where the Z boson subsequently decays to pairs of opposite-sign leptons ($\mu^+\mu^-$ or $\tau^+\tau^-$ where the taus in turn decay to muons). This region tests the modeling in simulation of the trigger and reconstruction efficiencies, the muon momentum scale and resolution, and the efficiencies of the applied isolation and impact parameter cuts.

The observed number of opposite-sign muon pairs in data is compared to the background prediction in Table 8.7. The observation in data is about 4% higher than the prediction from simulation. This level of disagreement is, however, within the theoretical cross-section uncertainties and experimental luminosity uncertainty. The distribution of the invariant mass reconstructed from the two opposite-charged muons is shown in Figure 8.20. The p_{T} and η distributions of the leading and subleading muon in each pair are shown in Figure 8.21. The agreement in the shape of the invariant-mass distribution and the kinematic distributions are good.

Process	Number of muon pairs
Non-prompt muons	1750 ± 563
WW	988 ± 128
WZ	1290 ± 166
ZZ	824 ± 106
$t\bar{t}W$	7.2 ± 3.6
$t\bar{t}Z$	12.0 ± 6.1
$t\bar{t}$	3840^{+323}_{-423}
$Z/\gamma*$	1580000 ± 108000
Sum of predictions	1590000 ± 109000
Observation in data	1655557

Table 8.7: Observed and predicted number of oppositely-charged muon pairs. The quoted uncertainties are the total systematic and systematic uncertainties.

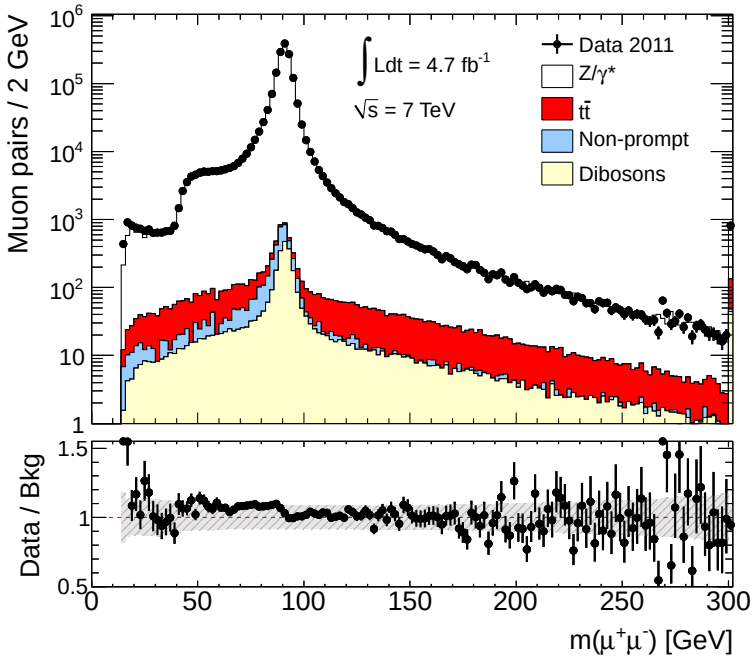

Figure 8.20: Invariant-mass distributions for pairs of prompt, isolated muons with opposite electric charge. The filled circles show the observation in data and the stacked histograms show the combined background prediction. The uncertainty bands show the total statistical and systematic uncertainty.

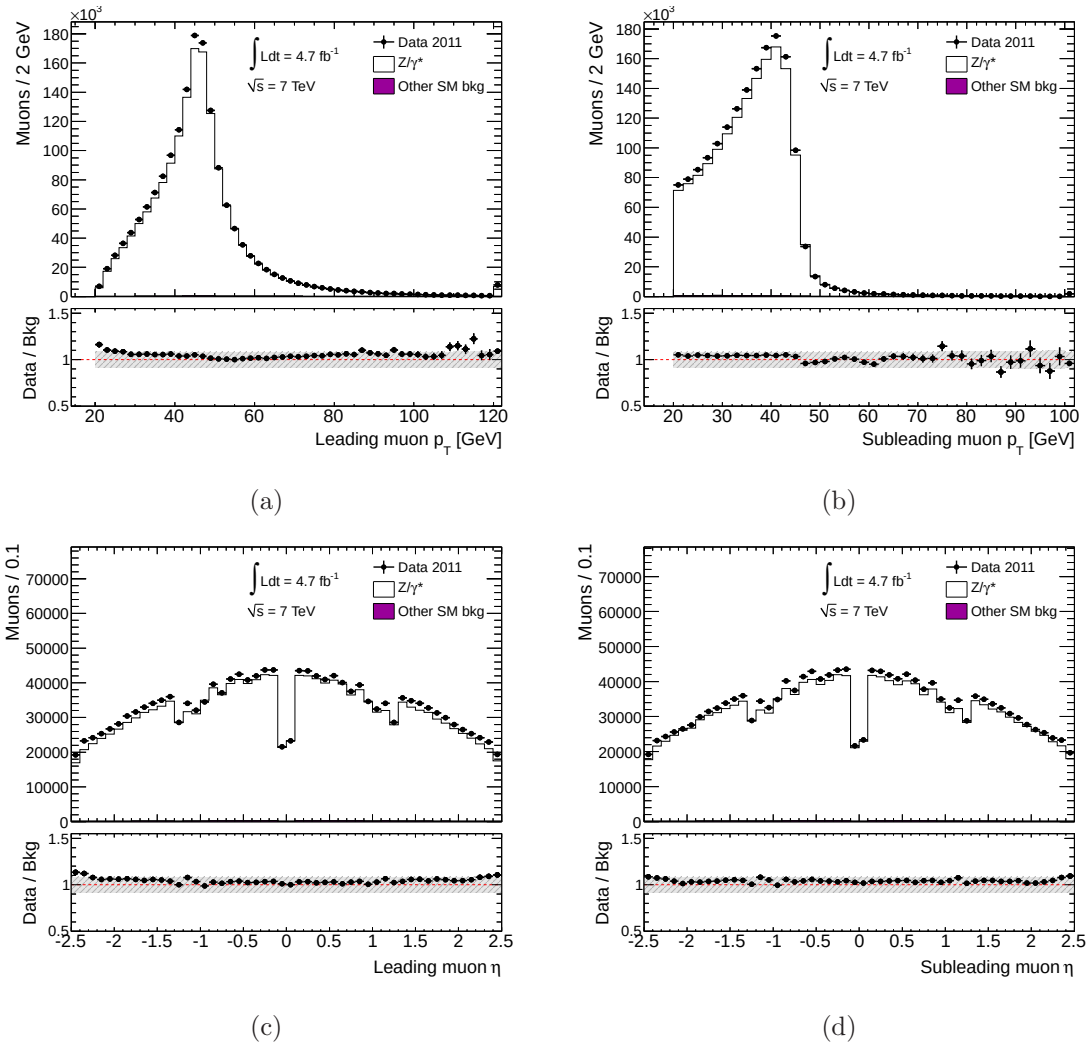

(a) (b)

(c) (d)

Figure 8.21: Distributions of (a) the leading and (b) the subleading muon p_{T} distributions, and (c) the leading and (d) the subleading muon η distributions, for the opposite-sign control region with two isolated muons.

8.5.2 Control Regions with Non-Prompt Muons

A variety of control regions enhanced in non-prompt muons are defined to test the data-driven estimates of this background. Verifying the non-prompt muon prediction in independent data samples is crucial in ensuring valid background modeling within quoted systematic uncertainties. Five control regions are defined, selecting pairs of like-sign muons by either relaxing the isolation requirement or by using muons that fail the transverse impact parameter significance cut. The regions are summarized below:

- **$|d_0|/\sigma(d_0) > 3$ for ≥ 1 muon:** Like-sign muon pairs where both muons pass the signal region isolation requirement but at least one muon fails the impact parameter significance cut. Additionally, the $|d_0|$ cut is loosened to 10 mm to gain better statistics.
- **Intermediate isolation, $|d_0|/\sigma(d_0) > 3$ for ≥ 1 muon:** Like-sign muon pairs with both muons failing the signal region isolation requirement but instead passing a looser intermediate isolation cut. At least one muon must fail the impact parameter significance cut (and $|d_0|$ cut loosened to 10 mm).
- **Intermediate isolation:** Like-sign muon pairs where both muons pass the signal impact parameter selection, but fails the signal region requirement and pass a looser intermediate isolation cut instead.
- **Leading isolated, subleading intermediate isolated:** Like-sign muon pairs where both muons pass the signal region impact parameter selection. The leading muon must pass the signal isolation cut while the subleading muon fails the signal region isolation and instead passes the looser intermediate isolation cut.
- **Leading intermediate isolated, subleading isolated:** Like-sign muon pairs where both muons pass the signal region impact parameter selection. The subleading muon must pass the signal isolation cut, while the leading muon passes the looser intermediate isolation cut.

The expected and observed number of muon pairs in these five control regions are shown in Tables 8.8 and 8.9. The quoted uncertainties include statistical and systematic uncertainties. For the uncertainty on the predictions of the non-prompt background, this includes the uncertainty associated with limited statistics in the regions used to predict the non-prompt background together with the resulting fractional systematic uncertainty on the fake factor as propagated through for the signal region. For the systematic uncertainty associated with the fake factor, a value of 32% is used (which is the effect of the systematic uncertainty on the fake-factor as propagated through to the fake prediction in the signal region).

Process	Number of muon pairs
$\|d_0\|/\sigma(d_0) > 3$ for ≥ 1 muon	
Non-prompt muons	37 ± 12
Prompt muons	8.0 ± 1.1
Sum of predictions	45 ± 12
Observation in data	39
Data - prediction	-0.4σ
Intermediate isolation, $\|d_0\|/\sigma(d_0) > 3$ for ≥ 1 muon	
Non-prompt muons	139 ± 45
Prompt muons	< 1
Sum of predictions	139 ± 45
Observation in data	157
Data - prediction	$+0.4\sigma$
Intermediate isolation	
Non-prompt muons	63 ± 21
Prompt muons	1.7 ± 0.3
Sum of predictions	64 ± 21
Observation in data	60
Data - prediction	-0.2σ

Table 8.8: Expected and observed numbers of like-sign muon pairs for control regions with high impact parameter significance or both muons being intermediately isolated. The uncertainties on the predictions include the statistical and systematic uncertainties. For the fake predictions, the systematic uncertainty on the as derived for the signal region is assumed ($\pm 32\%$).

Process	Number of muon pairs
Leading isolated, subleading intermediate isolated	
Non-prompt muons	83 ± 27
Prompt muons	25.8 ± 3.4
Sum of predictions	109 ± 28
Observation in data	130
Data - prediction	$+0.7\sigma$
Leading intermediate isolated, subleading isolated	
Non-prompt muons	27.0 ± 9.4
Prompt muons	10.7 ± 1.5
Sum of predictions	37.7 ± 9.5
Observation in data	57
Data - prediction	$+1.6\sigma$

Table 8.9: Expected and observed numbers of like-sign muon pairs for the control regions where one muon is intermediately isolated and the other pass the signal region isolation. The uncertainties on the predictions include the statistical and systematic uncertainties. For the fake predictions, the systematic uncertainty on the as derived for the signal region is assumed ($\pm 32\%$).

Figure 8.22 shows the dimuon invariant mass for each control regions. The agreement between observation and prediction is generally good. The largest observed discrepancy is in the control region where the leading muon is intermediately isolated and the subleading muon isolated. The discrepancy corresponds to 1.8σ, taking into account the full systematic uncertainty on the prediction and the statistical uncertainty on data. The leading and subleading muon p_{T} spectra for the five control regions are shown in Figures 8.23-8.24.

Control Regions with $p_{\mathrm{T}} > 10$ GeV

As the statistics is limited in the non-prompt muon enhanced control regions, control regions are additionally defined, similar to the five described above, but where the subleading muon p_{T} cut is lowered to 10 GeV. The invariant mass distributions for these control regions with p_{T} cuts 20/10 GeV are shown in Figure 8.25. The leading and subleading muon p_{T} spectra for these control regions are shown in Figures 8.26-8.27. The agreement between observation and predictions are generally very good for these statistically improved control regions.

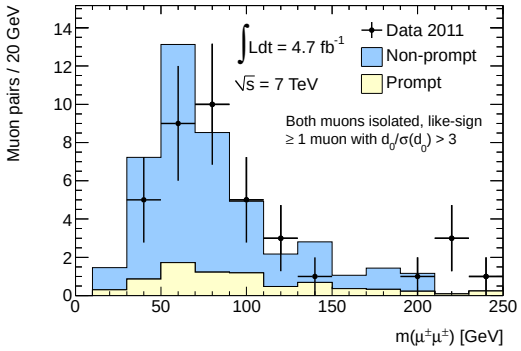

(a) $|d_0|/\sigma(d_0) > 3$ for ≥ 1 muon

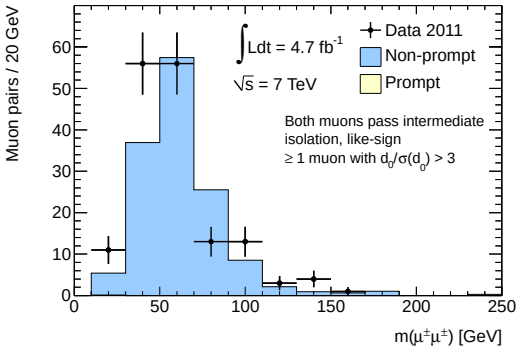

(b) Intermediate isolation, $|d_0|/\sigma(d_0) > 3$ for ≥ 1 muon

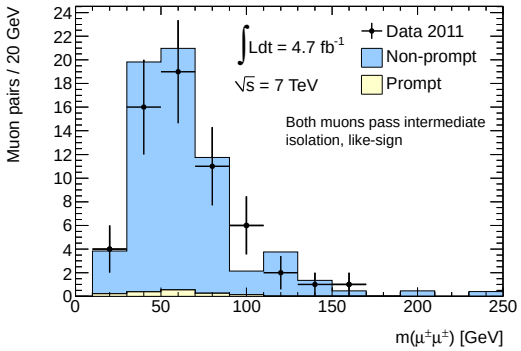

(c) Intermediate isolation

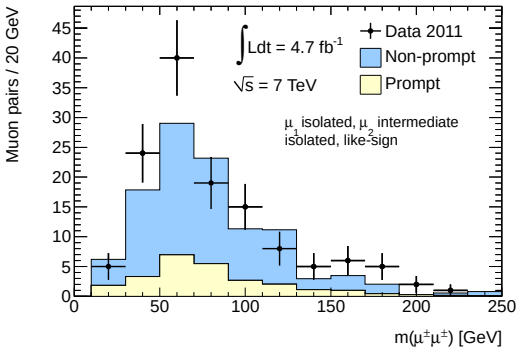

(d) Pairs with leading muon isolated and subleading muon intermediately isolated

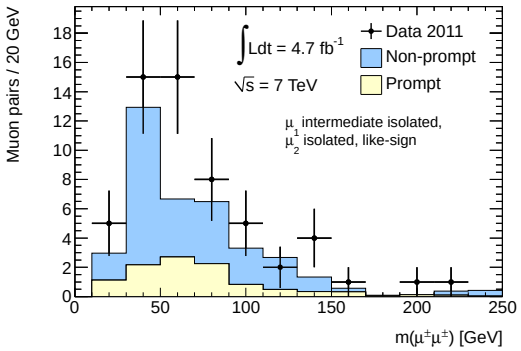

(e) Pairs with leading muon intermediately isolated and subleading muon isolated

Figure 8.22: Invariant mass distributions for different control regions with like-sign muon pairs enhanced in non-prompt background.

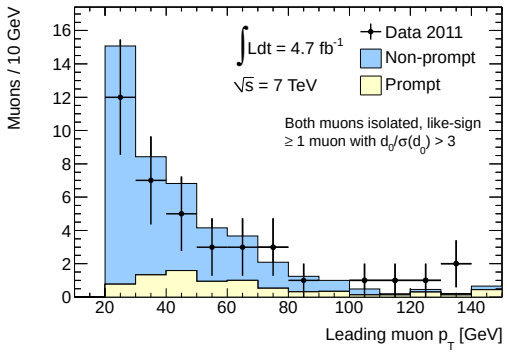

(a) Like-sign $\sigma(d_0)/d_0 > 3$ for ≥ 1 muon

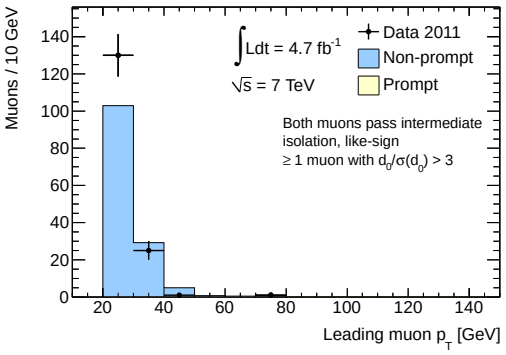

(b) Like-sign intermediate isolation, $\sigma(d_0)/d_0 > 3$ for ≥ 1 muon

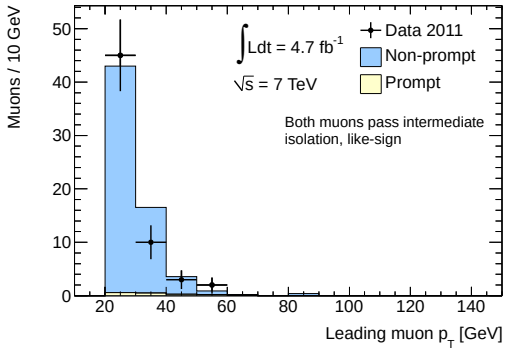

(c) Like-sign intermediate isolation

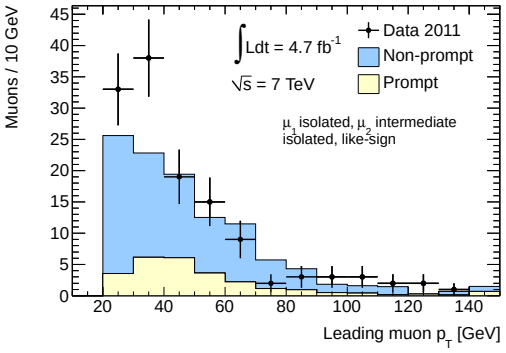

(d) Like-sign muon pairs with leading muon isolated and subleading muon intermediately isolated

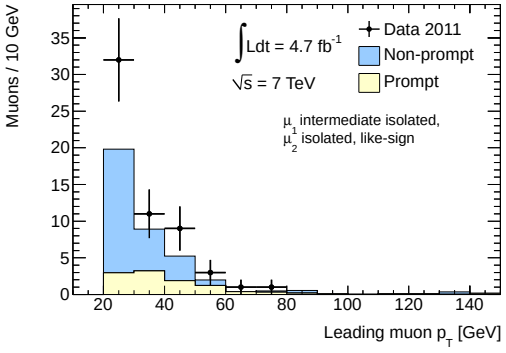

(e) Like-sign muon pairs with leading muon intermediately isolated and subleading muon isolated

Figure 8.23: Leading muon p_{T} spectrum for the five control regions that are sensitive to the non-prompt muon background.

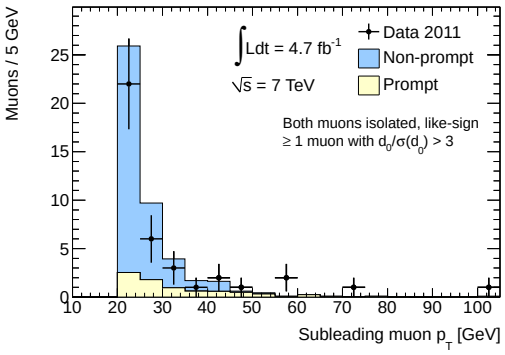

(a) Like-sign $\sigma(d_0)/d_0 > 3$ for ≥ 1 muon

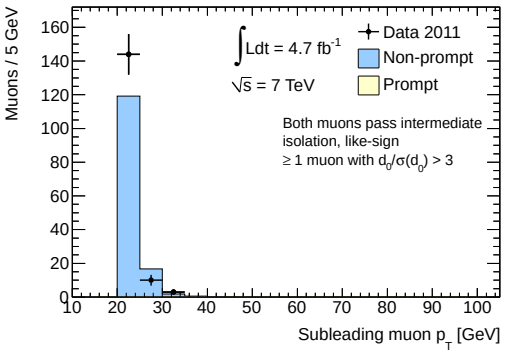

(b) Like-sign intermediate isolation, $\sigma(d_0)/d_0 > 3$ for ≥ 1 muon

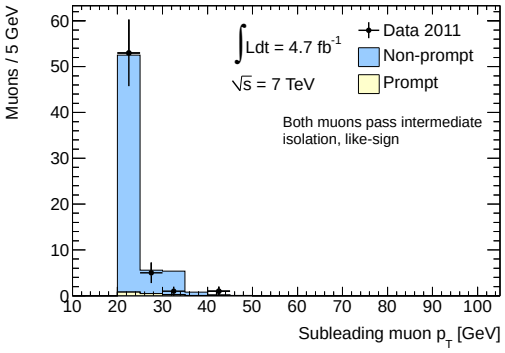

(c) Like-sign intermediate isolation

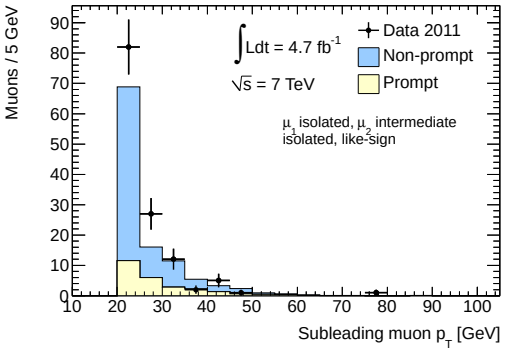

(d) Like-sign muon pairs with leading muon isolated and subleading muon intermediately isolated

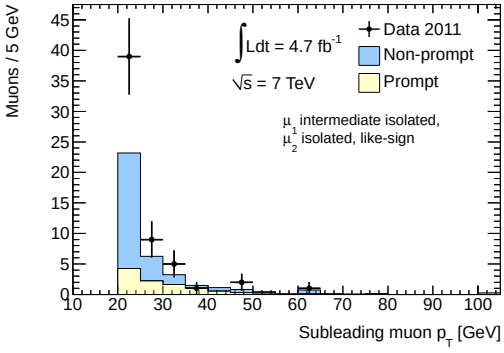

(e) Like-sign muon pairs with leading muon intermediately isolated and subleading muon isolated

Figure 8.24: Subleading muon p_{T} spectrum for the five control regions that are sensitive to the non-prompt muon background.

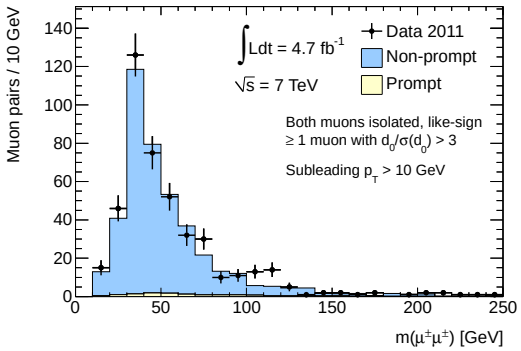

(a) Like-sign $\sigma(d_0)/d_0 > 3$ for ≥ 1 muon

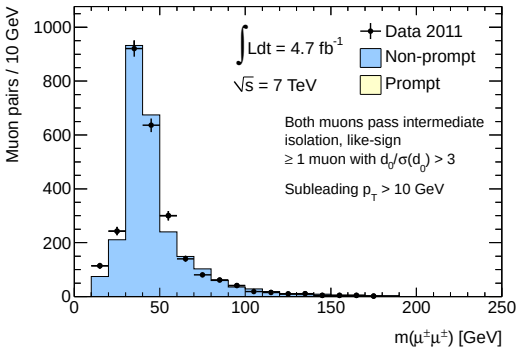

(b) Like-sign intermediate isolation, $\sigma(d_0)/d_0 > 3$ for ≥ 1 muon

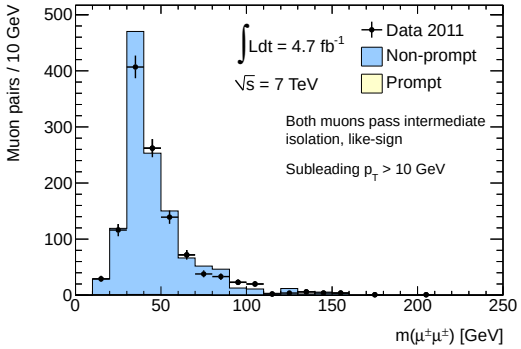

(c) Like-sign intermediate isolation

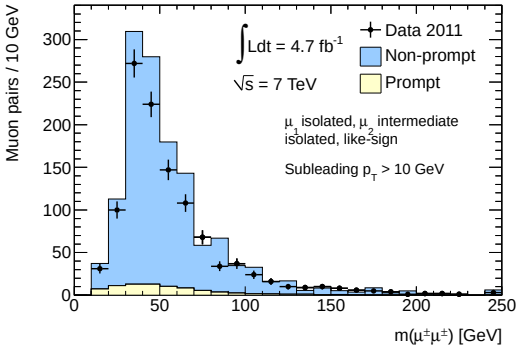

(d) Like-sign muon pairs with leading muon isolated and subleading muon intermediately isolated

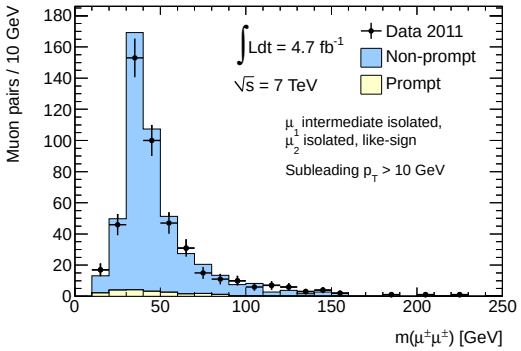

(e) Like-sign muon pairs with leading muon intermediately isolated and subleading muon isolated

Figure 8.25: Invariant mass distributions for different $\mu\mu$ control regions enhanced in fake background, where additionally the subleading muon p_{T} threshold is lowered to 10 GeV.

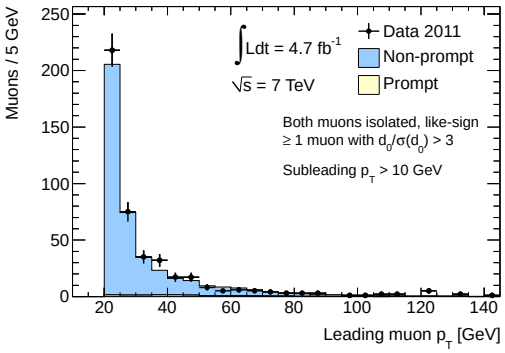

(a) Like-sign $\sigma(d_0)/d_0 > 3$ for ≥ 1 muon

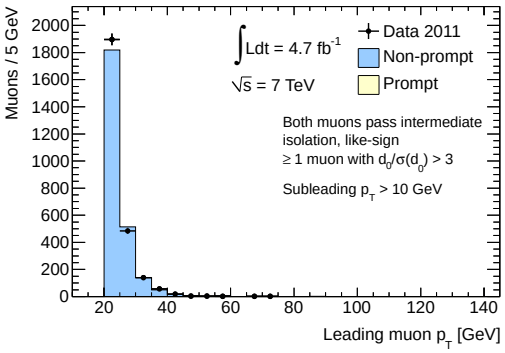

(b) Like-sign intermediate isolation, $\sigma(d_0)/d_0 > 3$ for ≥ 1 muon

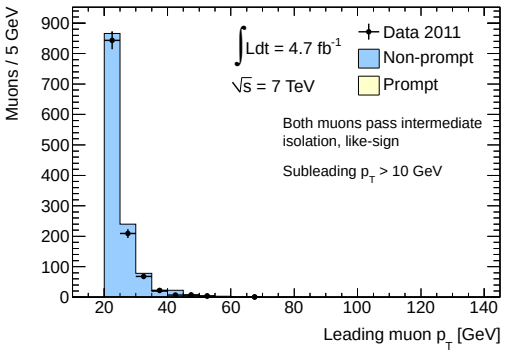

(c) Like-sign intermediate isolation

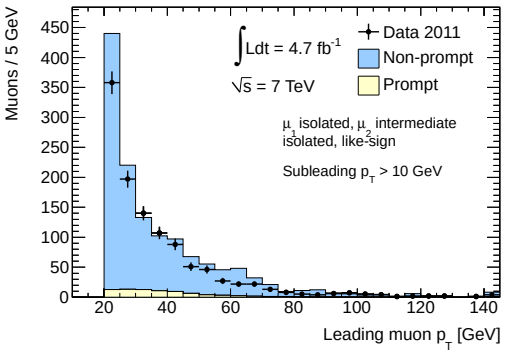

(d) Like-sign muon pairs with leading muon isolated and subleading muon intermediately isolated

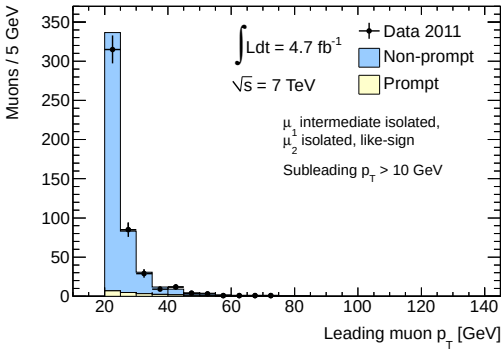

(e) Like-sign muon pairs with leading muon intermediately isolated and subleading muon isolated

Figure 8.26: Leading muon p_{T} spectrum for the five control regions that are sensitive to the non-prompt muon background, where additionally the subleading muon p_{T} threshold is lowered to 10 GeV.

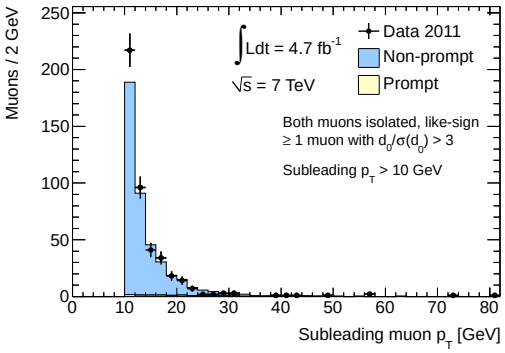

(a) Like-sign $\sigma(d_0)/d_0 > 3$ for ≥ 1 muon

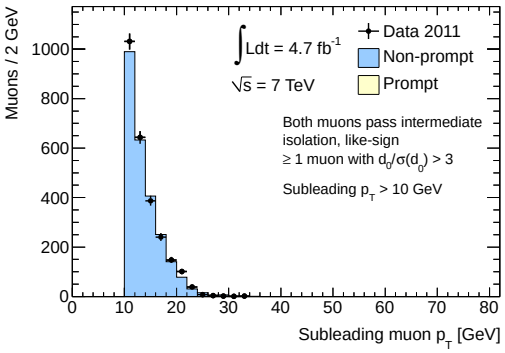

(b) Like-sign intermediate isolation, $\sigma(d_0)/d_0 > 3$ for ≥ 1 muon

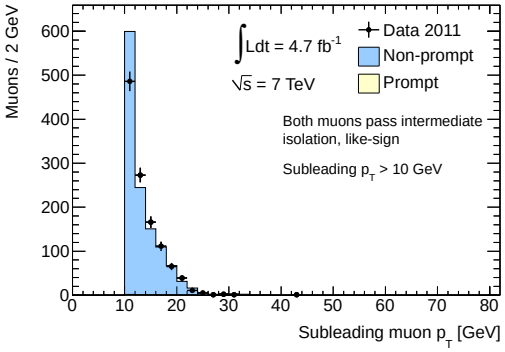

(c) Like-sign intermediate isolation

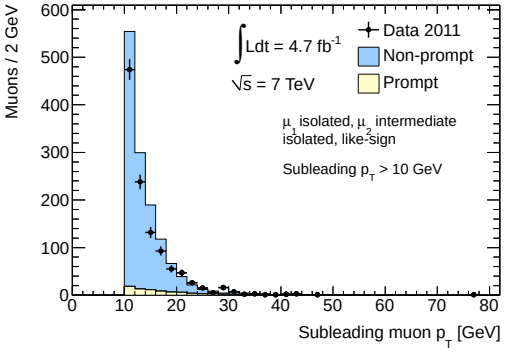

(d) Like-sign muon pairs with leading muon isolated and subleading muon intermediately isolated

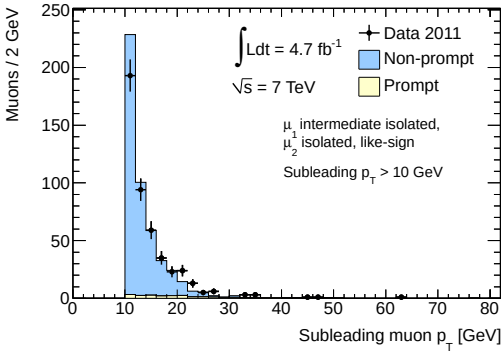

(e) Like-sign muon pairs with leading muon intermediately isolated and subleading muon isolated

Figure 8.27: Subleading muon p_{T} spectrum for the five control regions that are sensitive to the non-prompt muon background, where additionally the subleading muon p_{T} threshold is lowered to 10 GeV.

Chapter 9

Systematic Uncertainties

Several sources of systematic uncertainties may affect the signal acceptance and the background estimates. The dominant uncertainty on the predicted signal yield is the uncertainty on the integrated luminosity. Smaller sources of systematic effects include uncertainties on the muon trigger and identification efficiencies. These uncertainties also affect the prompt background prediction. The systematic uncertainty on the prompt background is, however, dominated by theoretical uncertainties on the production cross sections of the relevant processes. The systematic uncertainties associated with the data-driven non-prompt background estimate were described in detail in Section 8.3. The background contribution due to charge misidentification was estimated to be negligible with an upper systematic uncertainty derived directly from data, described in Section 8.4. Remaining sources of systematic uncertainties are described in detail below.

9.1 Muon Efficiency Uncertainties

Uncertainties associated with the muon trigger and identification efficiencies affect the signal acceptance and the prompt background which is estimated from simulation. Common muon efficiency uncertainties, such as on the trigger and reconstruction efficiencies, are provided through the ATLAS muon combined performance group and are used here wherever applicable.

9.1.1 Muon Identification Efficiency

Uncertainty on the muon identification efficiency is evaluated in a few stages. First, the uncertainty associated with requiring the muon to be combined and to fulfill the track-quality requirements outlined in Section 7.1.2 is evaluated. The measurement of the muon reconstruction efficiency was discussed in Section 7.2.1. The uncertainty on the muon reconstruction efficiency is evaluated by varying the muon

transverse momentum cut and the size of the Z mass window used for the tag-and-probe method, as well as varying the predicted background yields [88]. The resulting uncertainty is dependent on muon p_{T} and η but is generally $< 1\%$. The effect of this uncertainty on the prompt muon background estimates is evaluated by propagating the per-muon identification uncertainty through the analysis, which results in a $\pm 0.6\%$ uncertainty.

An additional uncertainty associated with the efficiency of the muon impact parameter and isolation cuts is evaluated. Efficiency scale factors, correcting the Monte Carlo efficiency to that observed in data, were evaluated in Section 7.2.4. The full size of the scale factor is taken as a p_{T}-dependent systematic uncertainty, ranging between 0–2.5% per muon. This uncertainty result in maximally a 2.4% effect on the prompt background predictions, and this uncertainty is used for all prompt background processes. For signal processes, a larger uncertainty of 4% is assigned due to the signal processes often having higher-p_{T} muons (for muons with $p_{\mathrm{T}} > 100$ GeV, the uncertainty per muon is 2%, resulting in maximally a 4% effects for muon pairs).

9.1.2 Muon Trigger Efficiency

The efficiency of the muon trigger and its difference between data and simulation was studied in Section 7.2.2. The uncertainty on the difference in trigger efficiency between data and simulation is estimated by the muon trigger group by taking into observed differences with p_{T} as well as biases due to the tag and probe selections [6]. The resulting efficiency is estimated to be $< 1\%$. Either one of the two muons can act as the triggering object and the trigger uncertainty is propagated through the analysis, resulting in an uncertainty on the prompt backgrounds of $\pm 0.7\%$.

9.1.3 Muon Momentum Scale

Uncertainty on the muon momentum scale affects the number of selected pairs with two muons with $p_{\mathrm{T}} > 20$ GeV. The determination of the momentum scale and momentum resolution was covered in Section 7.2.3. Systematic uncertainties on the momentum resolution are evaluated by taking into account by modifying the applied constraints used in determining the resolution [89]. These include multiple scattering in the inner detector and alignment accuracy in the transition region of the muon spectrometer. Uncertainties on the inner-detector and muon-spectrometer momentum measurements are propagated through the analysis, resulting in maximally $\pm 0.1\%$ uncertainty. This is used for all prompt backgrounds and the signal efficiency.

9.2 Luminosity Uncertainty

The measurement of the ATLAS integrated luminosity and the associated systematic uncertainty was summarized in Section 3.2.5. The uncertainty is dominated by the van-der-Meer scan calibration [68, 117]. The uncertainty was evaluated to be 3.7% for about the first half of the 2011 dataset, and 4.1% for about the second half, resulting in a total uncertainty of 3.9%.

9.3 Summary of Uncertainties on the Background Estimate

The sources of systematic uncertainties affecting the signal acceptance and the different background estimates are summarized in Table 9.1.

Source of uncertainty	Processes affected	Effect on prediction
Muon identification	Signal	±0.6%
	Prompt backgrounds	
Muon isolation efficiency	Signal	±4.0%
	Prompt backgrounds	±2.4%
Muon momentum measurement	Signal	±0.1%
	Prompt backgrounds	
Trigger efficiency	Signal	±0.7%
	Prompt backgrounds	
Non-prompt muon estimate	Non-prompt background	34−100%
WZ and ZZ cross section	WZ, ZZ	12%
$W^{\pm}W^{\pm}$ and $t\bar{t}W$ cross section	$W^{\pm}W^{\pm}$, $t\bar{t}W$, $t\bar{t}Z$	50%
Charge-flip rate	Z/γ^{*}, $t\bar{t}$, WW	see Section 8.4
MC statistics	Prompt backgrounds	2−25%
Data control-region statistics	Non-prompt background	6−100%
Luminosity	Signal	±3.9%
	Prompt backgrounds	

Table 9.1: Sources of systematic uncertainty and their effect on the signal region predicted yields. The variation in numbers reflects their relative impact in different bins of invariant mass.

Chapter 10

Results of the Inclusive Search for $\mu^{\pm}\mu^{\pm}$ Production

This chapter shows the results of the inclusive like-sign dimuon search. The observed yield in data is first compared to the background expectation. Distributions of the like-sign dimuon invariant mass as well as the transverse momentum and pseudorapidity of the two muons are shown. Muon pairs are considered both inclusively ($\mu^{\pm}\mu^{\pm}$) and separately for positive ($\mu^{+}\mu^{+}$) and negative ($\mu^{-}\mu^{-}$) pairs. No statistically significant deviation is observed in data with respect to the background estimate. Constraints are derived on the possible contributions from processes of physics beyond the Standard Model. The like-sign dimuon search was published jointly with similar searches in the $e^{\pm}e^{\pm}$ and $e^{\pm}\mu^{\pm}$ final states. The results from these additional search channels are summarized in Appendix B.

10.1 Comparison of Data Observation to the Background Expectation

The observed number of like-sign muon pairs in data is compared to the background expectation in Table 10.1. The yields are listed for five ranges of invariant mass, defined by a lower bound on the mass, ranging from 15 GeV to 400 GeV. The background from prompt muon sources constitutes about 83% of the total background for the most inclusive mass bin, $m(\mu^{\pm}\mu^{\pm}) > 15$ GeV, with the remaining 17% due to non-prompt sources. In the highest mass bin, prompt muons constitute nearly 100% of the total background. The combined background uncertainty ranges from 12% for $m(\mu^{\pm}\mu^{\pm}) > 15$ GeV, dominated by the non-prompt uncertainty and the prompt cross-section uncertainties, to about 80% for $m(\mu^{\pm}\mu^{\pm}) > 400$ GeV where it is dominated by cross-section uncertainties on the prompt backgrounds and limited statistics in both data and simulation samples. No indication of physics from non-SM sources contributing to the final state is observed. On the contrary, the observation

is in agreement with the background estimate in all mass bins within the statistical and systematic uncertainties.

Sample	Number of muon pairs with $m(\mu^{\pm}\mu^{\pm})$				
	> 15 GeV	> 100 GeV	> 200 GeV	> 300 GeV	> 400 GeV
Non-prompt	42 ± 14	12.1 ± 4.6	1.00 ± 0.62	$0.00^{+0.28}_{-0.00}$	$0.00^{+0.28}_{-0.00}$
Charge flips	$0.0^{+4.9}_{-0.0}$	$0.0^{+2.5}_{-0.0}$	$0.0^{+1.8}_{-0.0}$	$0.0^{+1.7}_{-0.0}$	$0.0^{+1.7}_{-0.0}$
WZ	146 ± 19	67.4 ± 8.9	15.7 ± 2.2	3.96 ± 0.65	1.43 ± 0.29
ZZ	47.5 ± 6.6	15.6 ± 2.2	3.67 ± 0.55	0.99 ± 0.17	0.38 ± 0.08
$W^{\pm}W^{\pm}jj$	5.8 ± 2.9	3.9 ± 2.0	1.47 ± 0.75	0.64 ± 0.33	0.28 ± 0.15
$t\bar{t}W$	3.6 ± 1.8	2.0 ± 1.0	0.56 ± 0.29	0.15 ± 0.08	0.04 ± 0.03
$t\bar{t}Z$	1.9 ± 1.0	1.20 ± 0.61	0.39 ± 0.20	0.10 ± 0.05	0.02 ± 0.02
Total	247^{+30}_{-29}	102 ± 12	$22.8^{+3.4}_{-2.9}$	$5.83^{+1.92}_{-0.85}$	$2.16^{+1.72}_{-0.37}$
Data	264	110	29	6	2

Table 10.1: Expected and observed numbers of pairs of isolated like-sign muons for various cuts on the dimuon invariant mass. The uncertainties shown are the quadratic sum of the statistical and systematic uncertainties.

A variety of kinematic distributions are studied to evaluate the agreement between data observation and background estimate. The dimuon invariant mass is shown in Figure 10.1 and the distributions of transverse momentum and pseudorapidity for the leading and subleading p_{T} muon are shown in Figure 10.2. The observation in data is again consistent with the Standard Model background estimate in all studied variables.

Tables 10.2 and 10.3 show the data and background predictions separately for positively and negatively-charged muon pairs. The background is higher for positive pairs compared to negative pairs due to the larger cross section in pp collisions for W^+ than W^- bosons. This affects the predictions of WZ, $W^{\pm}W^{\pm}jj$, and $t\bar{t}W$, while the backgrounds due to ZZ and $t\bar{t}Z$ are the same for the $\mu^+\mu^+$ and $\mu^-\mu^-$ final states. The non-prompt background is expected to be charge symmetric if it originates from pair production of heavy-flavor quarks ($b\bar{b}$, $c\bar{c}$, $t\bar{t}$) with subsequent decays to muons. Non-prompt background contributions originating from W+jets production would, however, be asymmetric.

No significant deviation of the data compared to the Standard Model prediction is observed for either final state. For $\mu^-\mu^-$ the data observation is somewhat higher than the background prediction, however, the discrepancy is maximally 1.3σ, taking into account the total systematic uncertainty on the background estimate as well as the statistical uncertainty for data.

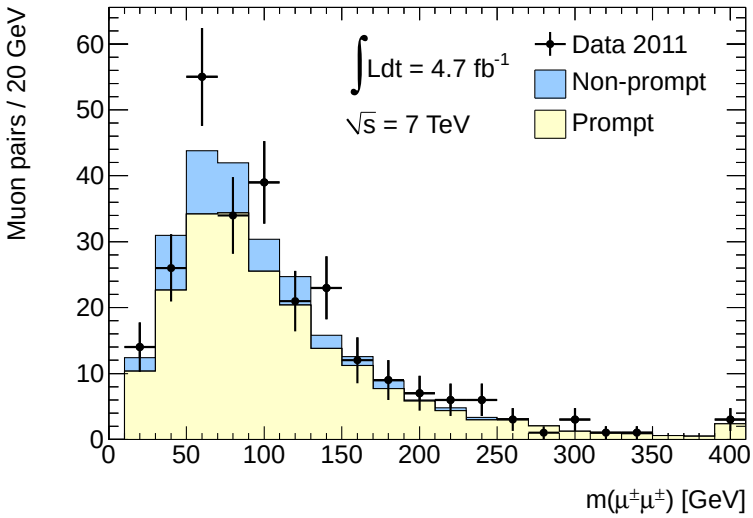

Figure 10.1: Distribution of the like-sign dimuon invariant mass for pairs passing the full event selection. The data are shown as closed circles. The stacked histograms represent the backgrounds composed of pairs of prompt leptons from Standard Model processes and pairs with at least one non-prompt lepton. The last bin is an overflow bin.

Sample	Number of muon pairs with $m(\mu^+\mu^+)$				
	> 15 GeV	> 100 GeV	> 200 GeV	> 300 GeV	> 400 GeV
Non-prompt	22.9 ± 7.6	6.7 ± 2.6	$0.26^{+0.32}_{-0.26}$	$0.00^{+0.28}_{-0.00}$	$0.00^{+0.28}_{-0.00}$
Charge flip	$0.0^{+2.5}_{-0.0}$	$0.0^{+1.3}_{-0.0}$	$0.0^{+0.92}_{-0.00}$	$0.0^{+0.85}_{-0.00}$	$0.0^{+0.83}_{-0.00}$
WZ	92 ± 12	43.9 ± 5.8	10.4 ± 1.5	2.95 ± 0.50	1.11 ± 0.24
ZZ	24.1 ± 3.4	8.1 ± 1.2	1.99 ± 0.32	0.52 ± 0.11	0.19 ± 0.05
$W^\pm W^\pm jj$	4.4 ± 2.2	3.1 ± 1.6	1.15 ± 0.59	0.48 ± 0.25	0.22 ± 0.13
$t\bar{t}W$	2.6 ± 1.3	1.48 ± 0.75	0.43 ± 0.22	0.13 ± 0.07	0.04 ± 0.02
$t\bar{t}Z$	0.96 ± 0.49	0.58 ± 0.30	0.20 ± 0.11	0.05 ± 0.03	0.01 ± 0.01
Total	147 ± 17	$63.7^{+7.7}_{-7.6}$	$14.5^{+2.1}_{-1.9}$	$4.11^{+1.09}_{-0.63}$	$1.57^{+0.92}_{-0.29}$
Data	144	60	16	4	2

Table 10.2: Expected and observed numbers of pairs of isolated like-sign positively-charged muons for various cuts on the dimuon invariant mass. The uncertainties shown are the quadratic sum of the statistical and systematic uncertainties.

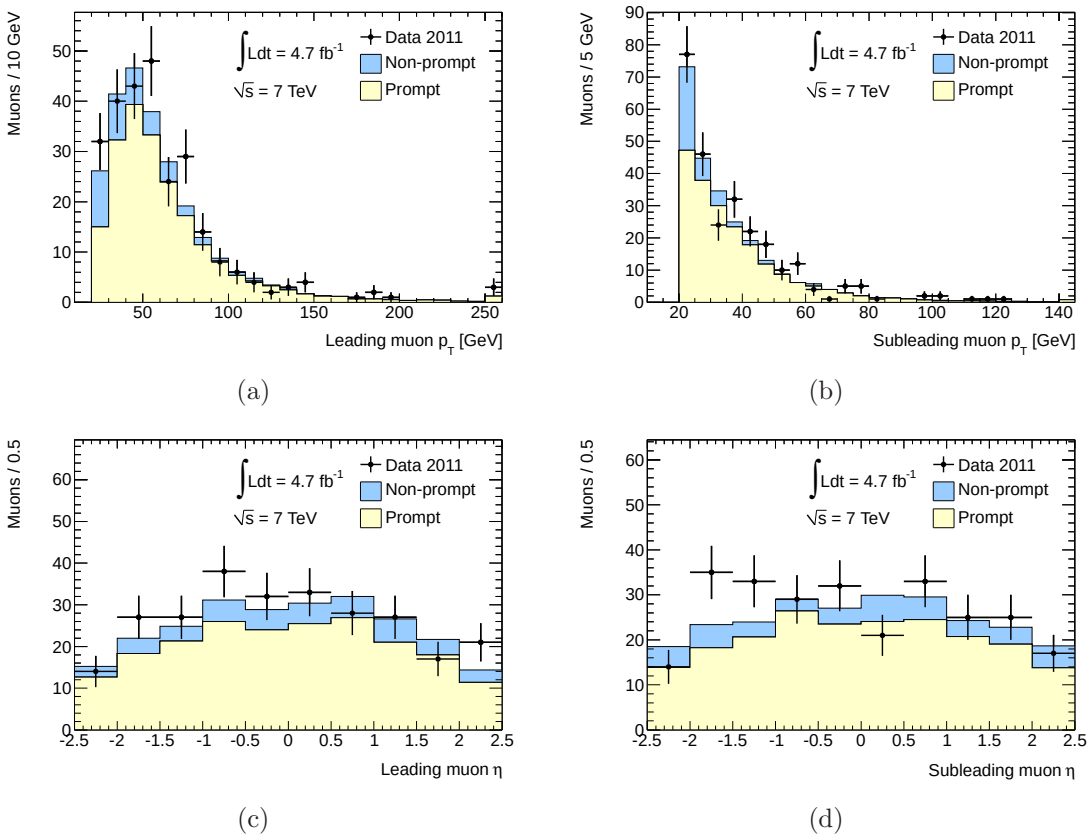

Figure 10.2: Distributions of (a) the leading and (b) the subleading muon p_{T} distributions, and (c) the leading and (d) the subleading muon η distributions. For (a) and (b), the last bin is an overflow bin.

Sample	Number of muon pairs with $m(\mu^-\mu^-)$				
	> 15 GeV	> 100 GeV	> 200 GeV	> 300 GeV	> 400 GeV
Non-prompt	19.6 ± 6.6	5.3 ± 2.3	0.70 ± 0.55	$0.00^{+0.28}_{-0.00}$	$0.00^{+0.28}_{-0.00}$
Charge flip	$0.0^{+2.5}_{-0.0}$	$0.0^{+1.3}_{-0.0}$	$0.0^{+0.92}_{-0.00}$	$0.0^{+0.85}_{-0.00}$	$0.0^{+0.83}_{-0.00}$
WZ	53.8 ± 7.2	23.5 ± 3.2	5.27 ± 0.80	1.01 ± 0.21	0.32 ± 0.10
ZZ	23.4 ± 3.3	7.5 ± 1.1	1.68 ± 0.28	0.47 ± 0.10	0.19 ± 0.05
$W^\pm W^\pm jj$	1.35 ± 0.69	0.85 ± 0.44	0.32 ± 0.17	0.16 ± 0.09	0.06 ± 0.04
$t\bar{t}W$	1.01 ± 0.51	0.49 ± 0.25	0.13 ± 0.07	0.02 ± 0.02	0.01 ± 0.01
$t\bar{t}Z$	0.97 ± 0.49	0.63 ± 0.32	0.19 ± 0.10	0.05 ± 0.03	0.01 ± 0.01
Total	100 ± 12	$38.4^{+5.0}_{-4.8}$	$8.3^{+1.5}_{-1.2}$	$1.71^{+0.94}_{-0.29}$	$0.59^{+0.88}_{-0.13}$
Data	120	50	13	2	0

Table 10.3: Expected and observed numbers of pairs of isolated like-sign negatively-charged muons for various cuts on the dimuon invariant mass. The uncertainties shown are the quadratic sum of the statistical and systematic uncertainties.

The dimuon invariant mass for positively and negatively-charged pairs are shown in Figures 10.3 and 10.4. Distributions of transverse momentum and pseudorapidity are shown in Figures 10.5 and 10.6.

The level of agreement between data and background expectation is evaluated using 1–CL$_b$ [118], defined as the one-sided probability of the background-only hypothesis to fluctuate to at least the observed number of pairs. Statistical and systematic uncertainties and their correlations are fully considered for the calculation. The 1–CL$_b$ values are listed in Table 10.4 for the different search regions. The largest upward deviation is observed for $m(\mu^-\mu^-) > 100$ GeV and > 200 GeV. The observed upward fluctuations occur in these mass bins about 8% of the time in background-only pseudo-experiments.

	1–CL$_b$ for muon pairs with mass				
	> 15 GeV	> 100 GeV	> 200 GeV	> 300 GeV	> 400 GeV
$\mu^\pm\mu^\pm$	0.27	0.24	0.12	0.44	0.47
$\mu^+\mu^+$	0.48	0.53	0.30	0.45	0.35
$\mu^-\mu^-$	0.10	0.08	0.08	0.38	0.79

Table 10.4: 1–CL$_b$ values for each mass bin, describing the one-sided probability of the background-only hypothesis to fluctuate to the number of observed muon pairs.

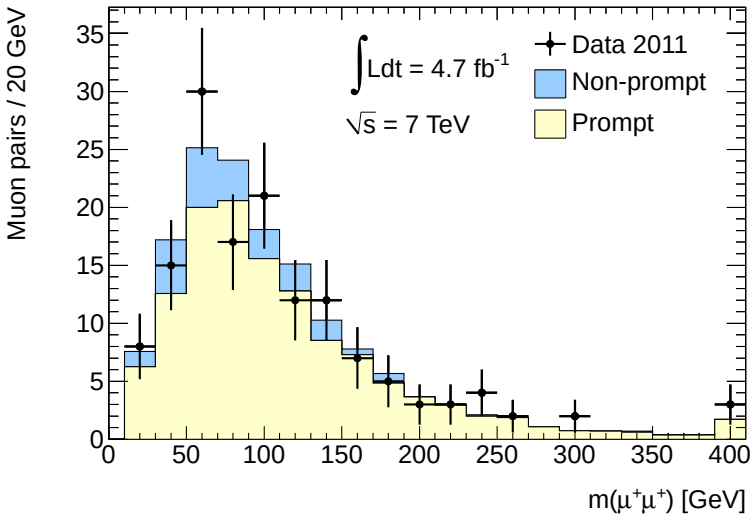

Figure 10.3: Invariant mass distributions for positive-charged muon pairs. The last bin is an overflow bin.

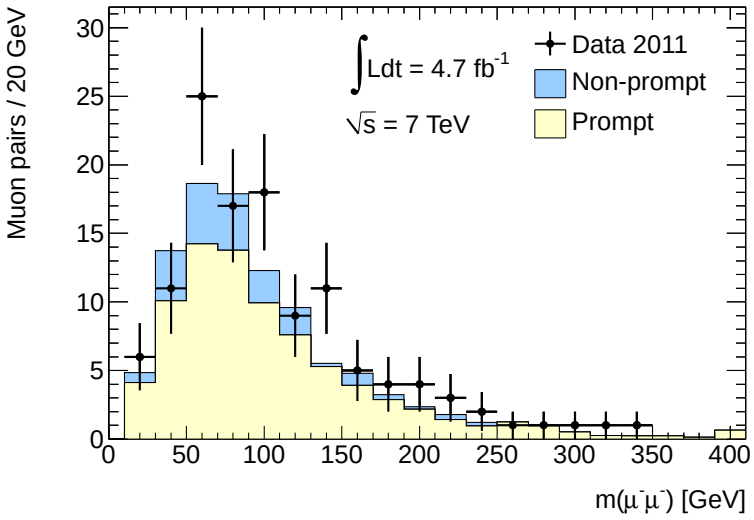

Figure 10.4: Invariant mass distributions for negative-charged muon pairs. The last bin is an overflow bin.

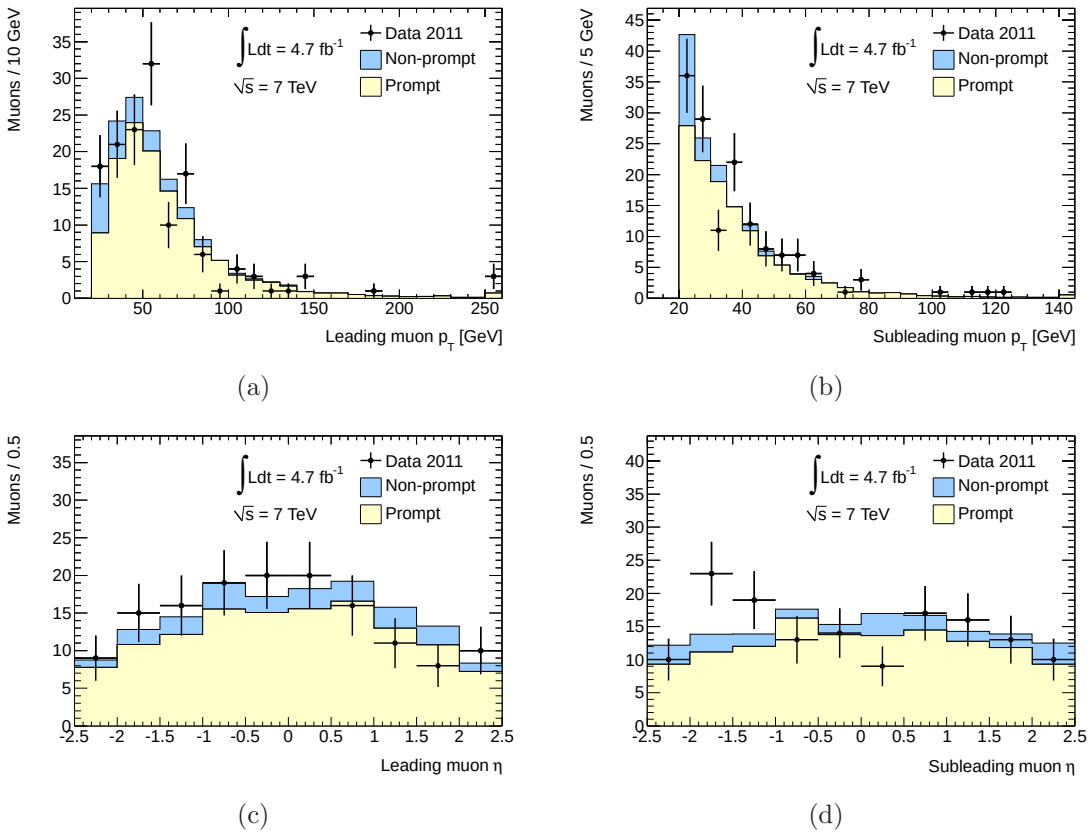

Figure 10.5: Distributions of (a) leading muon p_{T}, (b) subleading muon p_{T}, (c) leading muon η, and (d) subleading muon η for the $\mu^+\mu^+$ signal region. The last bin in (a) and (b) is an overflow bin.

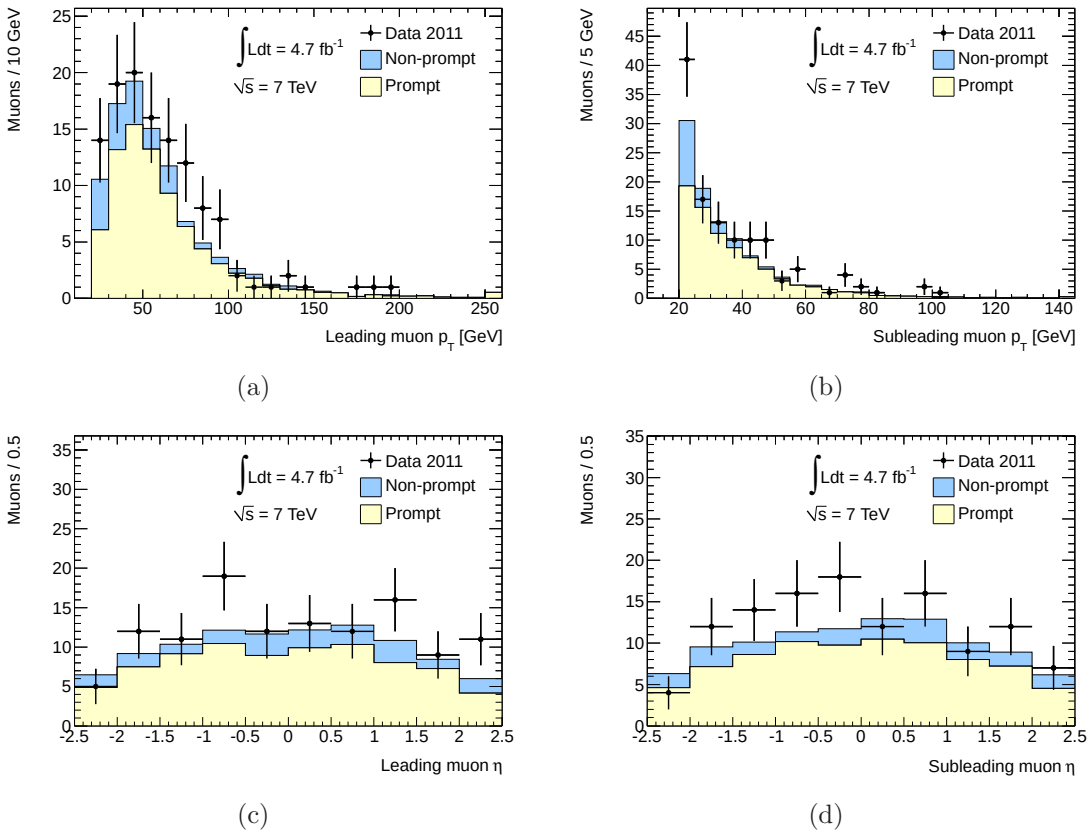

Figure 10.6: Distributions of (a) leading muon p_{T}, (b) subleading muon p_{T}, (c) leading muon η, and (d) subleading muon η for the $\mu^{-}\mu^{-}$ signal region. The last bin in (a) and (b) is an overflow bin.

10.2 Upper Limits on the Cross Section for Prompt $\mu^{\pm}\mu^{\pm}$ Production

No significant deviation is observed in data compared to the background expectation. Constraints are therefore derived on the possible contributions to the signal region due to pairs of like-sign, isolated, high-p_{T} muons originating from beyond the SM processes.

Constraints are first derived on the possible number of muon pairs from non-SM sources which may contribute to the signal region in each of the five invariant mass ranges considered. In order to translate from a limit on the number of muon pairs to a limit on the cross section for such production, the efficiency and acceptance with which non-SM processes enter the signal region must be known. However, since the goal of this analysis is to perform a model-independent search rather than placing limits on a specific model, a derivation of the efficiency times acceptance is not possible. Instead, limits are placed on the production cross section with respect to a *fiducial region*, defined at particle level by a set of criteria emulating the experimental selection as closely as possible.

To translate from an upper limit on the number of muon pairs to an upper limit on the *fiducial cross section*, the cross section with respect to the fiducial region, the *fiducial efficiency* must be derived. The fiducial efficiency is defined as the efficiency for a like-sign muon pair in the fiducial region to pass the experimental selection cuts and enter the signal region. Ideally, the fiducial efficiency would be a model-independent quantity, however, it depends somewhat on the event and muon properties. The fiducial efficiency is studied for a broad range of different new physics models, comparing events with little or high hadronic activity and events with low-p_{T} or high-p_{T} muons. The lowest observed efficiency is used to derive the cross-section limits.

10.2.1 Upper Limits on the Number of Muon Pairs from Non-Standard Model Sources

Upper limits at 95% confidence level (CL) on the number of muon pairs from non-SM sources, N_{95}, is determined using the CL_s method [118]. The ratio between the likelihood of the signal plus background hypothesis and the likelihood of the background-only hypothesis is used as the test statistic. The likelihoods are Poisson distributed for the total number of muon pairs in each search region and are calculated based on the predicted and observed number of pairs. The systematic uncertainties are incorporated into the likelihoods as nuisance parameters with Gaussian probability density functions. For $\mu^{\pm}\mu^{\pm}$, the observed upper limits range from 84 to 4.8 pairs. All limits are listed in Table 10.5.

Mass range	95% CL upper limit on N_{95}					
	expected	observed	expected	observed	expected	observed
	$\mu^{\pm}\mu^{\pm}$		$\mu^{+}\mu^{+}$		$\mu^{-}\mu^{-}$	
$m > 15$ GeV	$67.5^{+24.9}_{-16.8}$	83.7	$42.3^{+17.3}_{-9.3}$	42.8	$34.1^{+12.5}_{-9.9}$	51.9
$m > 100$ GeV	$34.3^{+12.6}_{-8.5}$	42.1	$23.6^{+9.1}_{-6.8}$	22.2	$16.8^{+6.5}_{-5.3}$	28.3
$m > 200$ GeV	$12.1^{+5.2}_{-3.2}$	18.9	$9.9^{+4.4}_{-1.9}$	12.1	$7.7^{+3.2}_{-2.1}$	12.4
$m > 300$ GeV	$6.7^{+2.5}_{-1.9}$	7.2	$5.8^{+2.3}_{-1.4}$	5.9	$4.2^{+2.1}_{-0.8}$	4.9
$m > 400$ GeV	$4.7^{+1.8}_{-1.4}$	4.8	$4.3^{+1.7}_{-0.9}$	5.0	$3.3^{+1.0}_{-0.1}$	3.3

Table 10.5: Upper limit at 95% CL on the number of muon pairs due to non-Standard Model sources for each mass range. The 1σ uncertainties on the expected limits are also given.

10.2.2 Fiducial Efficiency

The fiducial region is defined based on MC generator information such that it is independent of the ATLAS detector environment. The value of the fiducial efficiency generally depends on the considered new physics process, for instance the number of jets that may affect the muon isolation. In order to minimize the dependence, the fiducial region is defined closely related to the analysis selection. At MC generator level, muons are selected as stable particles that originate from a W or Z boson, from a τ lepton, or from an exotic new particle, such as a doubly charged Higgs boson. Generated muons must satisfy a set of p_{T}, η, and isolation requirements, listed in Table 10.6, which mirror the experimental selection requirements. A generator-level track isolation, $p_{\mathrm{T}}^{\mathrm{cone0.4}}$, is defined as the scalar sum of all stable charged particles with $p_{\mathrm{T}} > 1$ GeV in a cone of size $\Delta R_{\mathrm{iso}} < 0.4$ around the muon, excluding the muon itself.

Variable	Requirement
Muon p_{T}	$p_{\mathrm{T}} > 20$ GeV
Muon η	$\lvert\eta\rvert < 2.5$
Isolation	$p_{\mathrm{T}}^{\mathrm{cone0.4}}/p_{\mathrm{T}}(\mu) < 0.06$ and $p_{\mathrm{T}}^{\mathrm{cone0.4}} < (4 + 0.02 \times p_{\mathrm{T}}(\mu))$ GeV
Invariant mass	$m(\mu^{\pm}\mu^{\pm}) > 15$ GeV

Table 10.6: Summary of requirements on generated muons in the fiducial region.

The fiducial efficiency ($\varepsilon_{\mathrm{fid}}$) is defined as the fraction of muon pairs passing this selection that also satisfy the experimental selection criteria described in Chapter 7.

It is determined for a variety of new physics models (see Section 2.2 for details), chosen to cover a broad range of jet multiplicities and muon p_{T} spectra:

- Pair production of doubly charged Higgs bosons, each decaying to a pair of like-sign muons. A broad range of values for the mass of the $H^{\pm\pm}$ boson are considered. Doubly charged Higgs bosons represent event topologies with little activity outside the isolated muons.

- Pair production of like-sign, right-handed top quarks ($t_R t_R$) through a flavor-changing Z' boson. This model yields a considerably busy final state.

- Pair production of heavy down-type fourth generation quarks (b') which both subsequently decay into tW. Samples with $m_{b'} = 300$, 350, 400, 450 and 500 GeV are considered. With many final state jets, this model is used as an example of a busy topology.

- Production of a right-handed W boson (W_R) which subsequently decays into a lepton and a Majorana neutrino (N_R), with the neutrino further decaying into a lepton and jet. A number of Monte Carlo simulated samples with various masses for W_R and N_R are used. This topology provides a broad range of muon transverse momentum.

The fiducial efficiency is calculated for each of the considered samples. A selection of representative resulting efficiencies are shown in Table 10.7. The quoted uncertainty is the statistical uncertainty only, originating from limited size of the Monte Carlo samples. A few samples are listed as "n/a", indicating that the mass range considered is not relevant for that particular sample (for instance, a 100 GeV doubly charged Higgs boson is not relevant to study in a mass range of $m > 300$ GeV).

The fiducial efficiencies range from 59% to about 72%. The lowest observed efficiencies occur for the busy b' or $t_R t_R$ models. The efficiencies are also derived for $\mu^+\mu^+$ and $\mu^-\mu^-$ pairs separately and found to be independent of the charge. To place conservative upper cross-section limits, the lowest efficiency (59%) is used for all mass thresholds.

In addition to the fiducial efficiencies, the fraction of muon pairs satisfying the experimental selection which originates from *outside* the fiducial region are also determined. For the same new physics models, the values range from $< 1\%$ to about 9% as shown in Table 10.8, depending on the final state and the model considered. The efficiency from outside the fiducial region should be small, otherwise the definition of the fiducial region is not optimal.

10.2.3 Upper Fiducial Cross-Section Limits

The upper limit on the number of muon pairs is translated to an upper limit on the cross section with respect to the fiducial region. The fiducial cross section, $\sigma_{95}^{\mathrm{fid}}$,

Model	Fiducial efficiency (%)			
	> 15 GeV	> 100 GeV	> 200 GeV	> 300 GeV
$m(H^{\pm\pm}) = 50$ GeV	72.9 ± 2.0	n/a	n/a	n/a
$m(H^{\pm\pm}) = 100$ GeV	71.1 ± 1.3	n/a	n/a	n/a
$m(H^{\pm\pm}) = 200$ GeV	66.7 ± 1.1	67.6 ± 1.1	n/a	n/a
$m(H^{\pm\pm}) = 300$ GeV	65.3 ± 1.0	65.7 ± 1.0	67.6 ± 1.1	n/a
$m(H^{\pm\pm}) = 400$ GeV	62.6 ± 1.0	62.8 ± 1.0	64.1 ± 1.0	66.0 ± 1.1
$m(H^{\pm\pm}) = 1000$ GeV	59.2 ± 1.0	59.3 ± 1.0	59.5 ± 1.0	60.0 ± 1.0
$t_R t_R$	61.3 ± 2.0	61.1 ± 2.1	62.0 ± 2.4	63.2 ± 3.0
b' (300 GeV)	68.2 ± 2.8	69.5 ± 4	72.4 ± 9.2	n/a
b' (400 GeV)	65.3 ± 2.5	66.6 ± 3.2	67.7 ± 5.4	69.9 ± 9.8
b' (500 GeV)	64.1 ± 2.0	65.4 ± 2.4	67.5 ± 3.7	69.3 ± 6.2
W_R: $m(W_R) = 800$ GeV, $m(N_R) = 100$ GeV	66.6 ± 2.9	66.7 ± 2.9	66.8 ± 3.0	66.2 ± 3.4
W_R: $m(W_R) = 800$ GeV, $m(N_R) = 500$ GeV	68.4 ± 2.0	68.6 ± 2.1	69.0 ± 2.3	67.7 ± 2.8
W_R: $m(W_R) = 1000$ GeV, $m(N_R) = 200$ GeV	65.5 ± 2.2	65.6 ± 2.2	65.9 ± 2.3	66.4 ± 2.4
W_R: $m(W_R) = 1000$ GeV, $m(N_R) = 800$ GeV	65.1 ± 2.8	65.2 ± 2.8	66.0 ± 3.2	65.9 ± 3.9
W_R: $m(W_R) = 1500$ GeV, $m(N_R) = 300$ GeV	63.5 ± 2.1	63.5 ± 2.1	64.1 ± 2.1	64.6 ± 2.2
W_R: $m(W_R) = 1500$ GeV, $m(N_R) = 1300$ GeV	65.8 ± 2.0	66.1 ± 2.0	66.5 ± 2.2	66.7 ± 2.5

Table 10.7: Efficiency (%) with respect to the fiducial region for different new physics models, all producing like-sign dimuons. The quoted uncertainties are statistical only.

Model	Efficiency outside fiducial region (%)			
	> 15 GeV	> 100 GeV	> 200 GeV	> 300 GeV
$m(H^{\pm\pm}) = 50$ GeV	3.2 ± 0.4	n/a	n/a	n/a
$m(H^{\pm\pm}) = 100$ GeV	1.3 ± 0.2	n/a	n/a	n/a
$m(H^{\pm\pm}) = 200$ GeV	0.8 ± 0.1	0.8 ± 0.1	n/a	n/a
$m(H^{\pm\pm}) = 300$ GeV	0.5 ± 0.1	0.5 ± 0.1	0.6 ± 0.1	n/a
$m(H^{\pm\pm}) = 400$ GeV	0.5 ± 0.1	0.4 ± 0.1	0.5 ± 0.1	0.5 ± 0.1
$m(H^{\pm\pm}) = 1000$ GeV	0.3 ± 0.1	0.3 ± 0.1	0.4 ± 0.1	0.3 ± 0.1
$t_R t_R$	2.0 ± 0.4	2.2 ± 0.4	2.6 ± 0.5	3.9 ± 0.7
b' (300 GeV)	2.6 ± 0.5	4.2 ± 0.9	n/a	n/a
b' (400 GeV)	2.1 ± 0.4	2.4 ± 0.6	5.5 ± 1.5	n/a
b' (500 GeV)	2.0 ± 0.3	1.9 ± 0.4	n/a	6.1 ± 1.7
W_R: $m(W_R) = 800$ GeV, $m(N_R) = 100$ GeV	2.9 ± 0.6	2.8 ± 0.6	3.5 ± 0.6	4.1 ± 0.8
W_R: $m(W_R) = 800$ GeV, $m(N_R) = 500$ GeV	0.7 ± 0.2	0.9 ± 0.2	1.4 ± 0.3	2.5 ± 0.5
W_R: $m(W_R) = 1000$ GeV, $m(N_R) = 200$ GeV	1.4 ± 0.3	1.3 ± 0.3	1.7 ± 0.3	1.8 ± 0.4
W_R: $m(W_R) = 1000$ GeV, $m(N_R) = 800$ GeV	0.6 ± 0.3	0.6 ± 0.3	1.4 ± 0.4	3.3 ± 0.8
W_R: $m(W_R) = 1500$ GeV, $m(N_R) = 300$ GeV	0.8 ± 0.2	0.7 ± 0.2	0.8 ± 0.2	1.1 ± 0.3
W_R: $m(W_R) = 1500$ GeV, $m(N_R) = 1300$ GeV	0.8 ± 0.2	1.0 ± 0.2	1.4 ± 0.3	2.4 ± 0.4

Table 10.8: Leakage (%), the fraction of pairs satisfying the experimental selection which originates from outside the fiducial region, shown for different new physics models. The quoted uncertainties are statistical only.

is determined as

$$\sigma_{95}^{\text{fid}} = \frac{N_{95}}{\varepsilon_{\text{fid}} \times \int \mathcal{L} \mathrm{d}t}, \tag{10.1}$$

where ε_{fid} is the fiducial efficiency (59%), N_{95} the upper limit at 95% CL on the number of muon pairs, and $\int \mathcal{L}dt$ the integrated luminosity (4.7 fb^{-1}).

The resulting upper limits at 95% CL on the fiducial cross section are given in Table 10.9. The limits range from 24 fb to 1.7 fb for $\mu^{\pm}\mu^{\pm}$ production, and are generally within 1σ of the expected limits. Upper limits on the $\mu^{+}\mu^{+}$ and $\mu^{-}\mu^{-}$ cross sections are also derived using the same fiducial efficiency as for the inclusive limits and are also listed in Table 10.9. Figure 10.7 shows a pictorial view of the fiducial cross-section limits for $\mu^{\pm}\mu^{\pm}$, $\mu^{+}\mu^{+}$, and $\mu^{-}\mu^{-}$ production.

Mass range	95% CL upper limit [fb]					
	expected	observed	expected	observed	expected	observed
	$\mu^{\pm}\mu^{\pm}$		$\mu^{+}\mu^{+}$		$\mu^{-}\mu^{-}$	
$m > 15$ GeV	$24.0^{+8.9}_{-6.0}$	29.8	$15.0^{+6.1}_{-3.3}$	15.2	$12.1^{+4.5}_{-3.5}$	18.5
$m > 100$ GeV	$12.2^{+4.5}_{-3.0}$	15.0	$8.4^{+3.2}_{-2.4}$	7.9	$6.0^{+2.3}_{-1.9}$	10.1
$m > 200$ GeV	$4.3^{+1.8}_{-1.1}$	6.7	$3.5^{+1.6}_{-0.7}$	4.3	$2.7^{+1.1}_{-0.7}$	4.4
$m > 300$ GeV	$2.4^{+0.9}_{-0.7}$	2.6	$2.0^{+0.8}_{-0.5}$	2.1	$1.5^{+0.8}_{-0.3}$	1.7
$m > 400$ GeV	$1.7^{+0.6}_{-0.5}$	1.7	$1.5^{+0.6}_{-0.3}$	1.8	$1.2^{+0.4}_{-0.0}$	1.2

Table 10.9: Upper limits at 95% CL on the fiducial cross section for like-sign muon pairs from non-SM processes. The expected limits and their 1σ uncertainties are given, as well as the observed limits in data.

Although limits are derived on the generic fiducial cross sections, these can be translated to a limit on a particular model of new physics. Only the acceptance of the new model to enter the fiducial region must be additionally determined. Since the fiducial region is defined at Monte Carlo generator level, without relying on any ATLAS detector simulation, such limits can be determined also by, for instance, a theorist.

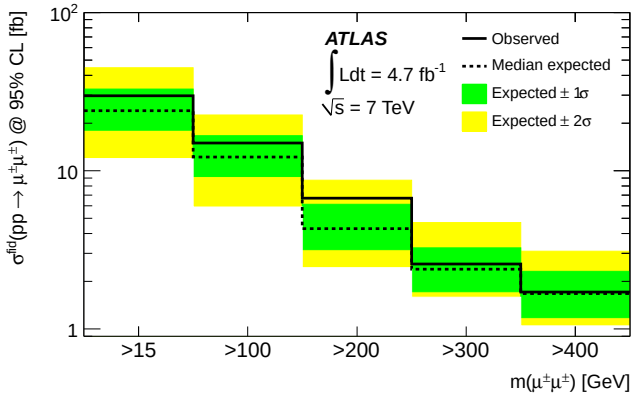

(a)

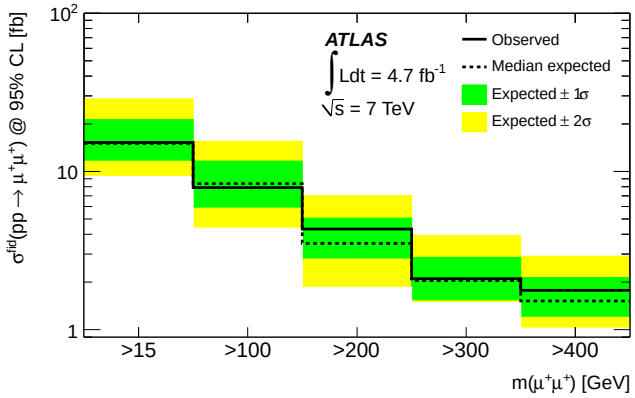

(b) l

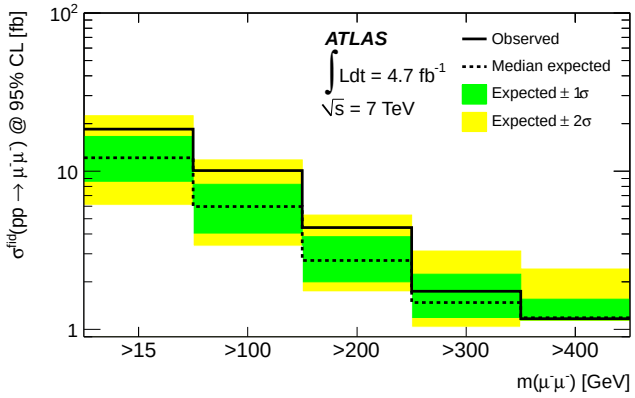

(c)

Figure 10.7: Upper limits at 95% CL on the fiducial cross section for non-SM processes contributing to the fiducial region for (a) $\mu^{\pm}\mu^{\pm}$, (b) $\mu^{+}\mu^{+}$, and (c) $\mu^{-}\mu^{-}$ pairs.

Chapter 11

Results of the Narrow $\mu^{\pm}\mu^{\pm}$ Resonance Search

Some of the models of physics beyond the Standard Model which contain final states with like-sign lepton pairs predict these to result from the decay of a narrow resonance. This chapter describes a search for such narrow resonances, specifically for the production of doubly charged Higgs ($H^{\pm\pm}$) bosons. The search is performed in the like-sign dimuon final state but was published jointly with searches in the $e^{\pm}e^{\pm}$ and $e^{\pm}\mu^{\pm}$ decay modes. The like-sign invariant mass distribution is searched for a narrow peak. No evidence for such resonant production is observed, and constraints are placed on the cross section for pair production of doubly charged Higgs bosons decaying to dimuon final states. Lower limits are also placed on the mass of the $H^{\pm\pm}$ boson.

This chapter describes the signal optimization, where mass bins in which the search is performed are derived, as well as the simulated samples used to study the predicted $H^{\pm\pm}$ boson signal. The narrow resonance search relies on the same event selection criteria and background estimates as the inclusive like-sign dimuon search and are not discussed further here. The results of the narrow resonance search in the $e^{\pm}e^{\pm}$ and $e^{\pm}\mu^{\pm}$ final states are summarized in Appendix B.

11.1 Doubly Charged Higgs Boson Signal

The inclusive like-sign dimuon search is performed in wide mass bins defined by a lower bound on the invariant mass. The narrow resonance search, on the other hand, is performed in narrow mass bins optimized for maximum signal sensitivity. The optimization takes into account the estimated background yields as well as the predicted contribution from the signal. The search is sensitive to any resonance decaying to pairs of like-sign muons but the search is optimized and interpreted specifically for doubly charged Higgs bosons.

Doubly charged Higgs bosons occur naturally in left-right symmetric models, Higgs triplet models, and the little Higgs model (see discussion in Section 2.2.2). Additionally, a $H^{\pm\pm}$-*like* particle can occur as a singlet as proposed in the Zee-Babu model, where it is postulated for the purpose of generating Majorana neutrino masses. The results of the search are interpreted within the left-right symmetric model in which doubly charged Higgs bosons that couple to left-handed and right-handed fermions are distinguished. Monte Carlo simulated samples are produced to study the efficiency with which $H^{\pm\pm}$ bosons decaying to pairs of muons enter the signal region. This section describes the simulated $H^{\pm\pm}$ samples, the search optimization, and the signal efficiency. Additional systematic uncertainties on the signal acceptance, in addition to the sources listed in Chapter 9, are also evaluated.

11.1.1 Simulation of Doubly Charged Higgs Bosons

A set of Monte Carlo simulated samples of the doubly charged Higgs boson signal process are generated using Pythia8 [119]. Samples are generated with $H^{\pm\pm}$ boson masses in 50 GeV increments for the range 50–500 GeV with an additional mass point at 1000 GeV. The samples are simulated using the ATLAS fast simulation packages, AtlFastII, but it was verified at one mass point ($m = 300$ GeV) that the fast-simulation sample completely reproduces the event kinematics of the fully simulated sample.

The search is interpreted within the left-right symmetric model, separating $H^{\pm\pm}$ bosons that couple to left-handed fermions (denoted $H_L^{\pm\pm}$) or to right-handed fermions (denoted $H_R^{\pm\pm}$). The kinematic properties of $H_L^{\pm\pm}$ and $H_R^{\pm\pm}$ bosons are identical, only their cross sections differ. The signal cross sections at leading order (LO) and next-to-leading order (NLO) are listed in Table 11.1 for $H_L^{\pm\pm}$ and $H_R^{\pm\pm}$ bosons [120]. The NLO/LO cross-section ratio (the K-factor) range between 1.24 and 1.37.

11.1.2 Search Optimization

The mass windows in which the search is performed are optimized for maximum signal sensitivity. The intrinsic width of the $H^{\pm\pm}$ resonance peak is narrow for the considered mass range and the measured width of the *reconstructed* mass peak is consequently driven by the detector resolution. For muons, the resolution degrades with increasing muon momentum, from about 2% at $p_{\mathrm{T}} = 20$ GeV to about 10% at $p_{\mathrm{T}} = 1$ TeV. Examples of reconstructed $H^{\pm\pm}$ boson mass peaks in simulation are shown in Figure 11.1.

The width of the invariant mass bins used for the search are determined by maximizing the signal significance. Assuming the data to be Poisson distributed, the approximate signal significance used is defined as [121]

$$Z = \sqrt{2((S+B)\ln(1+S/B) - S)}, \tag{11.1}$$

m [GeV]	$\sigma_{LO}(H_L^{\pm\pm})$ [fb]	$\sigma_{NLO}(H_L^{\pm\pm})$ [fb]	$\sigma_{LO}(H_R^{\pm\pm})$ [fb]	$\sigma_{NLO}(H_R^{\pm\pm})$ [fb]
50	5768	7335	2258	2860
100	321.1	409.0	130.5	165.2
150	65.51	83.98	27.34	34.57
200	19.81	25.39	8.364	10.54
250	7.368	9.411	3.133	3.933
300	3.115	3.960	1.331	1.666
350	1.437	1.817	0.6167	0.7697
400	0.7054	0.8876	0.3041	0.3790
450	0.3631	0.4547	0.1572	0.1959
500	0.1939	0.2396	0.08432	0.1052
1000	9.488×10^{-4}	1.274×10^{-3}	4.354×10^{-4}	5.950×10^{-4}

Table 11.1: Cross sections at leading and next-to-leading order for doubly charged Higgs bosons coupling to left-handed ($H_L^{\pm\pm}$) or right-handed ($H_R^{\pm\pm}$) fermions, as function of the mass.

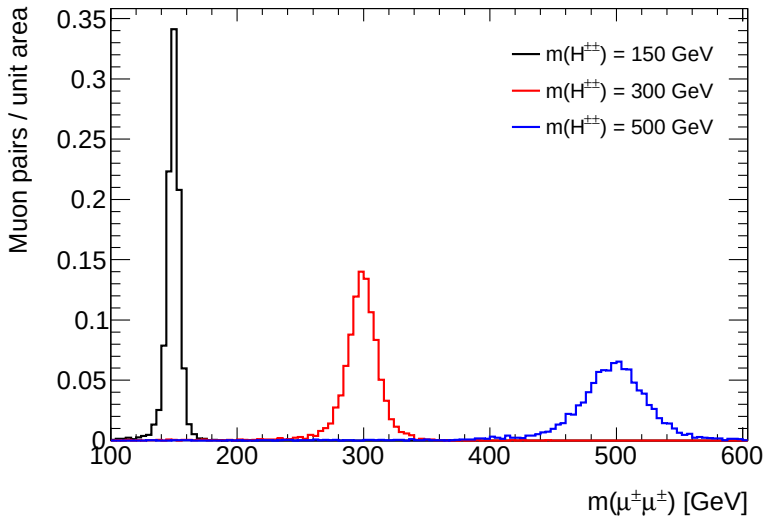

Figure 11.1: Simulated dimuon invariant mass distributions, normalized to unity, for $H^{\pm\pm}$ bosons with masses of 150 GeV, 300 GeV, and 500 GeV.

where S is the number of expected signal events and B is the number of predicted background events. In the limit of $S << B$, this reduces to the more commonly used significance formula $Z = S/\sqrt{B}$.

For each $H^{\pm\pm}$ mass point, the optimal mass window is derived by counting the predicted background yield (B) and the expected signal yield (S), after which the signal significance Z can be determined from Equation 11.1. Examples of the signal and background yields together with the signal significance for different mass windows are shown in Table 11.2 for a $H^{\pm\pm}$ boson with a mass of 300 GeV.

Window [GeV]	Signal	Background	Significance	Comment
$[291, 309]$	11.77	1.37	5.99	$\pm 3\%$
$[288, 312]$	14.19	1.77	6.46	$\pm 4\%$
$[284, 316]$	16.80	2.42	6.79	$\pm 5\%$
$[282, 318]$	17.69	2.57	6.95	$\pm 6\%$
$[278, 322]$	18.93	2.94	7.07	$\pm 7\%$
$[276, 324]$	19.54	3.23	7.06	$\pm 8\%$
$[272, 328]$	20.04	4.06	6.77	$\pm 9\%$
$[269, 331]$	20.27	4.57	6.60	$\pm 10\%$

Table 11.2: Signal and background yields together with the resulting signal significance for a doubly charged Higgs boson with $m = 300$ GeV.

The optimized size of the mass bins as function of $H^{\pm\pm}$ boson mass is shown for ten mass points in Figure 11.2. To extrapolate to intermediate mass points, for which simulated samples are not available, a linear parametrization is used (also shown in the figure). The resulting definition of the mass bins is $\pm[0.06 \times m(H^{\pm\pm}) + 0.7 \cdot 10^{-4} \times m(H^{\pm\pm})^2]$, which corresponds to about a 6% (9%) window for m$(H^{\pm\pm}) = 50$ (500) GeV.

11.1.3 Signal Efficiency

The efficiency with which $H^{\pm\pm}$ bosons would enter the signal search region is estimated for each simulated mass point. The efficiencies for reconstructed muon pairs to fall within the corresponding mass bins (ε_{bin}) are listed in Table 11.3 for each mass point. The acceptance times efficiency, i.e. the total signal efficiency, for $H^{\pm\pm}$ bosons to pass the full analysis selection (ε_{tot}) is also listed. The signal efficiency is calculated as the number of reconstructed muon pairs passing the full analysis selection, including the mass bin requirement described above, with respect to the number of true simulated $H^{\pm\pm}$ decays into pairs of muons.

To interpolate between the simulated mass points, ε_{tot} is fitted using a piecewise,

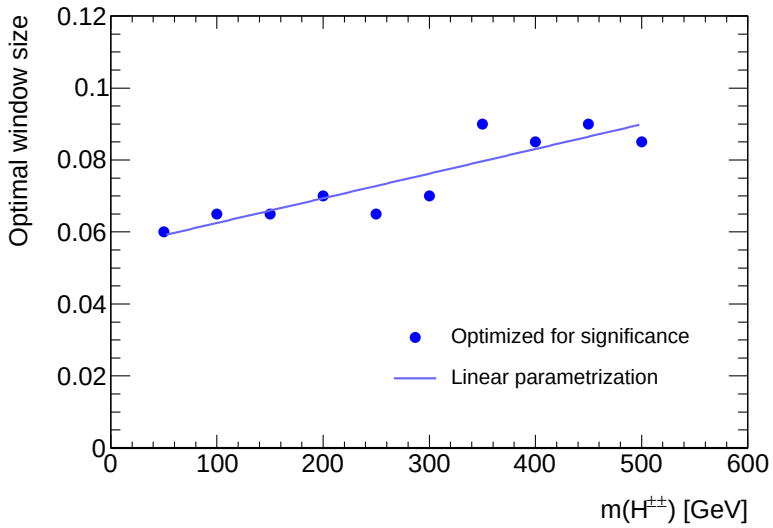

Figure 11.2: Optimized window size as function of $H^{\pm\pm}$ boson mass, together with its linear parametrization.

Mass [GeV]	Window [GeV]	ε_{bin}	ε_{tot}
50	[47, 53]	0.955 ± 0.028	0.201 ± 0.005
100	[93, 107]	0.940 ± 0.019	0.428 ± 0.008
150	[140, 160]	0.920 ± 0.018	0.489 ± 0.008
200	[186, 214]	0.906 ± 0.017	0.507 ± 0.008
250	[231, 269]	0.906 ± 0.017	0.518 ± 0.009
300	[277, 323]	0.897 ± 0.017	0.521 ± 0.009
350	[322, 378]	0.885 ± 0.017	0.508 ± 0.009
400	[366, 434]	0.886 ± 0.017	0.503 ± 0.009
450	[411, 489]	0.878 ± 0.016	0.504 ± 0.009
500	[455, 545]	0.871 ± 0.017	0.492 ± 0.008
1000	[875, 1125]	0.853 ± 0.017	0.462 ± 0.008

Table 11.3: Mass windows and efficiencies for each simulated $H^{\pm\pm}$ mass point. The efficiency for reconstructed muon pairs to fall within the defined mass windows is given by ε_{bin}, while the total acceptance times efficiency is ε_{tot}. The errors shown are statistical only.

empirical functional form. The function is

$$\varepsilon_{\text{tot}}(m) = \begin{cases} p_0(1 - e^{-(m-p_1)/p_2}), & \text{if } m < 300 \text{ GeV} \\ p_3 - p_4 m, & \text{if } m \geq 300 \text{ GeV} \end{cases} \tag{11.2}$$

with the values of the parameters p_i given in Table 11.4. The empirical fit is shown together with the calculated efficiency in Figure 11.3. The fit function agrees with the predicted efficiency within the statistical error for every simulated mass point. Therefore, no additional uncertainty is assessed due to the interpolation function. For the search when scanning the full dimuon mass range, bin centers are spaced apart by about half the bin width.

Parameter	Value
p_0	$5.17 \cdot 10^{-1}$
p_1	$3.04 \cdot 10^{+1}$
p_2	$3.98 \cdot 10^{+1}$
p_3	$5.36 \cdot 10^{-1}$
p_4	$7.60 \cdot 10^{-5}$

Table 11.4: Fitted parameter values for Equation 11.2, which gives $\varepsilon_{\text{tot}}(m)$.

11.2 Systematic Uncertainties

Many sources of systematic uncertainty can effect the signal yield and the background estimate. The prompt muon uncertainties described in Section 9.1 are applied to the signal acceptance for this search. Since the search regions are defined differently for the narrow resonance search compared to the inclusive like-sign search, the effect of the sources of systematic uncertainty must also be evaluated specifically for this search.

Sources of prompt muon uncertainty include the muon identification, trigger, and isolation efficiency. The effect of these uncertainties on the signal yield are shown in Figure 11.4 as function of the $H^{\pm\pm}$ boson mass. The uncertainty on the muon momentum scale, which for the inclusive analysis is $\pm 0.1\%$, is here more prominent (it is maximally 2.5% for a mass of 1000 GeV). The statistical uncertainty is determined separately for each signal search region. The systematic uncertainty on the muon identification and trigger efficiencies are observed to be roughly independent for different mass bins. The uncertainty due to isolation and momentum scale increase with mass, for these the maximum observed value are used.

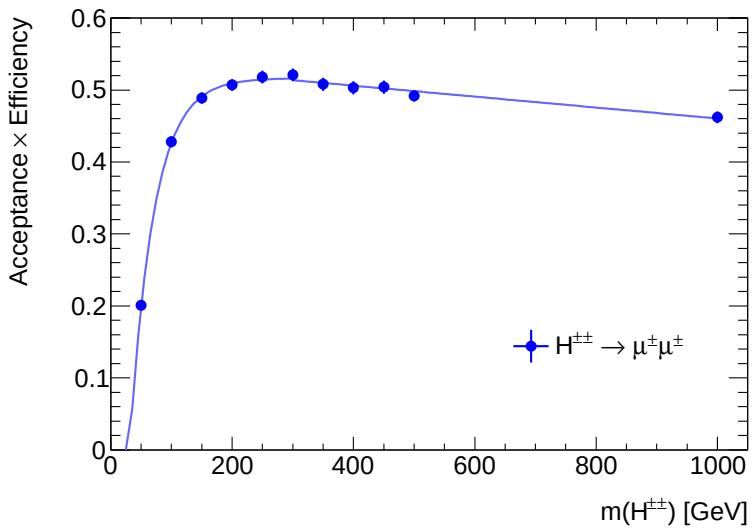

Figure 11.3: Total acceptance times efficiency (ε_{tot}) as function of the simulated $H^{\pm\pm}$ boson mass, fitted with a piecewise empirical function as described in the text.

The different sources of systematic uncertainty as applied to the prompt background yields and the signal acceptance are summarized in Table 11.5. In addition to the prompt muon uncertainties, the impact of the parton distribution functions (PDFs) on the signal acceptance is calculated below to be ±1.6% (see below).

Source of uncertainty	Effect on prediction
Muon identification	±0.6%
Muon isolation efficiency	±4.0%
Muon momentum measurement	±2.5%
Muon trigger efficiency	±0.7%
Luminosity	±3.9%

Table 11.5: Sources of systematic uncertainties affecting both the signal and the prompt backgrounds.

11.2.1 Uncertainty due to Parton Distribution Functions

The simulated doubly charged Higgs boson samples are generated with the leading-order parton distribution function (PDF) CTEQ6L1 [103]. Since no PDF uncertainty set is provided for this PDF, the acceptance uncertainty is instead evaluated using another leading-order PDF, MSTW2008 [122]. The uncertainty is derived by comparing

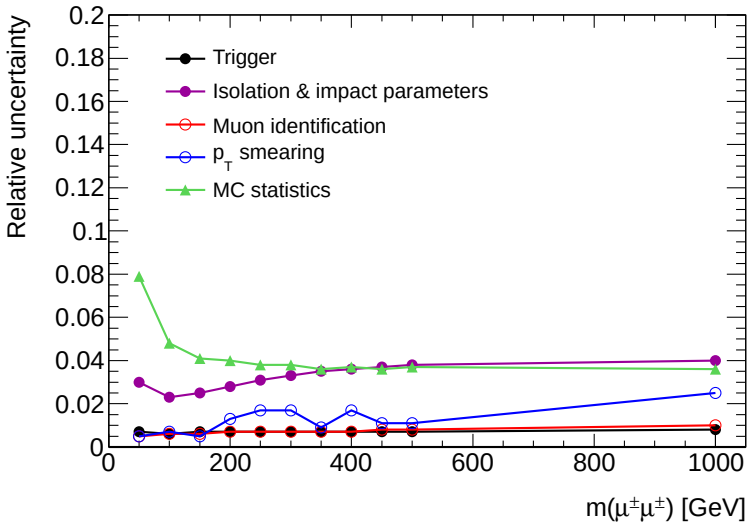

Figure 11.4: Systematic uncertainties as function of $H^{\pm\pm}$ boson mass.

the acceptance found with the central PDF to that found with each of 20 provided positively or negatively varied MSTW2008 90% confidence level (CL) uncertainty sets. The combined uncertainty is deduced using the prescription from Ref. [115]:

$$\begin{aligned} \sigma^{+}_{PDF} &= \sqrt{\sum_{i=1}^{20}[\max(A^{+}_{i}-A_0, A^{-}_{i}-A_0, 0)]^2} \\ \sigma^{-}_{PDF} &= \sqrt{\sum_{i=1}^{20}[\max(A_0-A^{+}_{i}, A_0-A^{-}_{i}, 0)]^2} \end{aligned} \tag{11.3}$$

where $A^{\pm}_{i}$ is the acceptance for a positively or negatively varied PDF set. The resulting uncertainties for different mass points are shown in Table 11.6. The largest uncertainty is observed for $m = 50$ GeV, the lowest mass point considered. The variations result in an uncertainty of $\pm 0.6\%$ for $H^{\pm\pm}$ bosons decaying to $\mu^{\pm}\mu^{\pm}$. Since this search was published jointly with similar searches in the $e^{\pm}e^{\pm}$ and $e^{\pm}\mu^{\pm}$ final states, a common PDF uncertainty was used for the three channels. For the $e^{\pm}e^{\pm}$ channel, a slightly larger uncertainty was observed of +0.9/-1.0%. This value was used also for the $\mu^{\pm}\mu^{\pm}$ search.

In addition to the uncertainty from the PDF uncertainty sets, an uncertainty is derived based on the difference between the acceptance using the MSTW2008 central value and the acceptance derived with CTEQ6L, also shown in Table 11.6. This effect is maximally 0.5% for the $\mu^{\pm}\mu^{\pm}$ final state but 1.2% for $e^{\pm}e^{\pm}$ at 50 GeV. The larger value from the $e^{\pm}e^{\pm}$ channel is again used, resulting in a total uncertainty due to

PDFs of +1.5/-1.6%, which is symmetrized to ±1.6%. Since this uncertainty is small compared to other signal uncertainties, the same ±1.6% uncertainty is applied for all mass points.

m($H^{\pm\pm}$) [GeV]	Uncertainty on ε_{tot}	Diff in central ε_{tot}
50	±0.6%	-0.5%
150	±0.2%	-0.5%
300	±0.1%	-0.2%
500	±0.1%	<0.1%

Table 11.6: Uncertainty on ε_{tot} from the PDF uncertainty set variations using MSTW 2008 LO 90% CL for different $H^{\pm\pm}$ mass points, relative to the central PDF in this set. The difference in ε_{tot} between the CTEQ6L PDF, used to generate the samples, and the central PDF for MSTW 2008 LO is also given.

11.3 Comparison of Data to Background

For the narrow resonance search, the data observation is compared to the background prediction in narrow bins of dimuon invariant mass. No significant discrepancies are observed. Data and background yields are presented for a selection of mass bins in Table 11.7. The predicted and observed invariant mass distributions are shown in Figure 11.5, along with the expected contributions for $H^{\pm\pm}$ bosons at various masses, assuming coupling to left-handed fermions and a 100% branching ratio to muons.

Bin center [GeV]	50	150	250	360	460
Non-prompt	2.3 ± 0.9	1.7 ± 0.9	0.4 ± 0.4	0.1 ± 0.1	$0.0^{+0.3}_{-0.0}$
Charge flips	$0^{+0.00005}_{-0.0}$	$0^{+0.03}_{-0.0}$	$0^{+0.04}_{-0.0}$	$0^{+0.02}_{-0.0}$	$0^{+0.1}_{-0.0}$
Prompt	9.1 ± 1.3	12.5 ± 1.7	5.7 ± 0.8	1.9 ± 0.3	0.8 ± 0.2
Sum of backgrounds	11.4 ± 1.6	14.2 ± 1.9	6.1 ± 0.9	1.9 ± 0.3	$0.8^{+0.4}_{-0.2}$
Data	13	16	8	1	1

Table 11.7: Expected and observed numbers of like-sign muon pairs for various bins in invariant mass. The uncertainties include the statistical and systematic components.

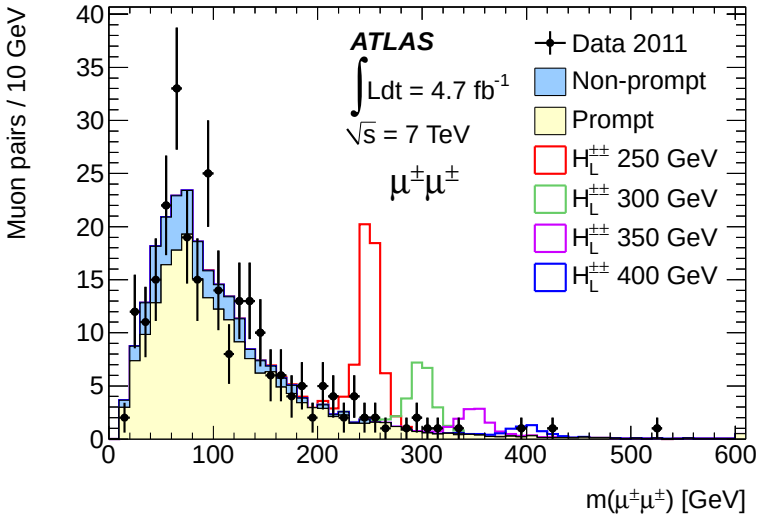

Figure 11.5: Dimuon invariant mass distributions for data and the background predictions. The open histograms show the expected signal from simulated $H_L^{\pm\pm}$ samples, assuming a 100% branching ratio to muons. The last bin is an overflow bin.

11.4 Upper Limits on Doubly Charged Higgs Boson Production

Since the data show no clear peak structure but instead agrees well with the background estimate, constraints are derived on the pair-production cross section of doubly charged Higgs bosons. A limit is first derived on the number of muon pairs originating from $H^{\pm\pm}$ bosons in each mass window (N_H^{rec}) using the CLs technique [118]. Next, this limit is converted to a limit on the cross section times branching ratio for pair production of doubly charged Higgs bosons using the acceptance times efficiency values derived in Section 11.1.3.

The analysis counts muon *pairs* while the pair-production process is constrained, $H^{\pm\pm}H^{\mp\mp}$, where two muon pairs per event can contribute. The translation between the number of events with pair produced $H^{\pm\pm}$ bosons and the number of muon pairs is performed as follows. The cross section for pair production of $H^{\pm\pm}$ bosons, σ_{HH}, is given by

$$\sigma_{HH} = \frac{N_{HH}}{\int \mathcal{L}\mathrm{d}t}, \tag{11.4}$$

where N_{HH} is the true number of events containing a pair of $H^{\pm\pm}$ bosons and $\int \mathcal{L}\mathrm{d}t$ the integrated luminosity. N_{HH} is related to the true number of $H^{\pm\pm}$ bosons, N_H, decaying to a certain decay channel with a branching ratio (BR) via $N_H = 2 \times BR \times$

N_{HH}, from which it follows that

$$\sigma_{HH} \times BR = \frac{N_H}{2 \times \int \mathcal{L} \mathrm{d}t}. \tag{11.5}$$

The number of true $H^{\pm\pm}$ bosons is related to the number of reconstructed $H^{\pm\pm}$ bosons (N_H^{rec}) as $N_H^{\mathrm{rec}} = N_H \times A \times \epsilon$, where $A \times \epsilon$ is the acceptance times efficiency to detect a single $H^{\pm\pm}$ boson. The cross section times branching ratio is then finally given by

$$\sigma_{HH} \times BR = \frac{N_H^{\mathrm{rec}}}{2 \times A \times \epsilon \times \int \mathcal{L} \mathrm{d}t}. \tag{11.6}$$

The expected and observed upper limits at 95% CL on the cross section times branching ratio as a function of the $H^{\pm\pm}$ boson mass are shown in Figure 11.6. The expected limit is determined as the median outcome of simulated pseudo-experiments in the absence of any signal. Also shown are the theoretical cross sections calculated at next-to-leading order for pair production of $H^{\pm\pm}$ bosons with left and right-handed couplings. The uncertainty on these cross sections is $\pm 10\%$ due to scale dependence in the NLO calculation, parton distribution function uncertainties, and neglecting higher-order electroweak corrections. In general the observed and expected limits agree well. The cross-section limits range from 7.6 fb at low mass (64 GeV) to 0.57 fb in the highest mass bin (600 GeV).

By comparing the cross-section limit with the theoretical production cross section, constraints can be derived on the mass of doubly charged Higgs bosons. Assuming pair-production and a branching ratio for $H^{\pm\pm}$ bosons to decay to muons of 100%, doubly charged Higgs bosons which couple to left-handed and right-handed fermions are excluded for masses below 398 GeV and 306 GeV, respectively. Mass limits assuming branching ratios of 100%, 33%, 22%, and 11% are shown in Table 11.8. The mass limits are further derived as function of the branching ratio, shown in Figure 11.7. The stepping behavior, where the same mass limit is valid for a range of branching ratios, is a result of fluctuations in the observed cross-section limit in Figure 11.6. These same mass limits as for $H_L^{\pm\pm}$ apply to the singlet $H^{\pm\pm}$ in the Zee-Babu model, as its production cross section and decay kinematics are the same as for $H_L^{\pm\pm}$ bosons.

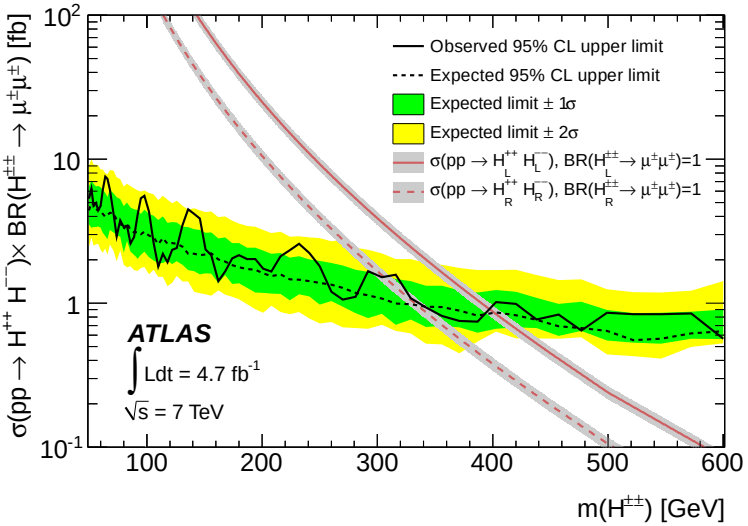

Figure 11.6: Upper limit at 95% CL on the cross section times branching ratio for pair production of $H^{\pm\pm}$ bosons decaying to like-sign muon pairs. The observed and median expected limits are shown along with the 1σ and 2σ variations in the expected limits. Also shown are the theoretical predictions at next-to-leading order for the pair-production cross section for $H_L^{\pm\pm}$ and $H_R^{\pm\pm}$ bosons.

BR to $\mu^\pm\mu^\pm$	$m(H_L^{\pm\pm})$ [GeV]		$m(H_R^{\pm\pm})$ [GeV]	
	expected	observed	expected	observed
100%	401	398	335	306
33%	317	290	247	222
22%	282	282	223	212
11%	234	216	184	176

Table 11.8: Lower mass limits at 95% CL on $H^{\pm\pm}$ bosons decaying to $\mu^\pm\mu^\pm$ pairs. Mass limits are derived assuming a branching ratio of 100%, 33%, 22%, or 11%. Both the expected and observed limits are given.

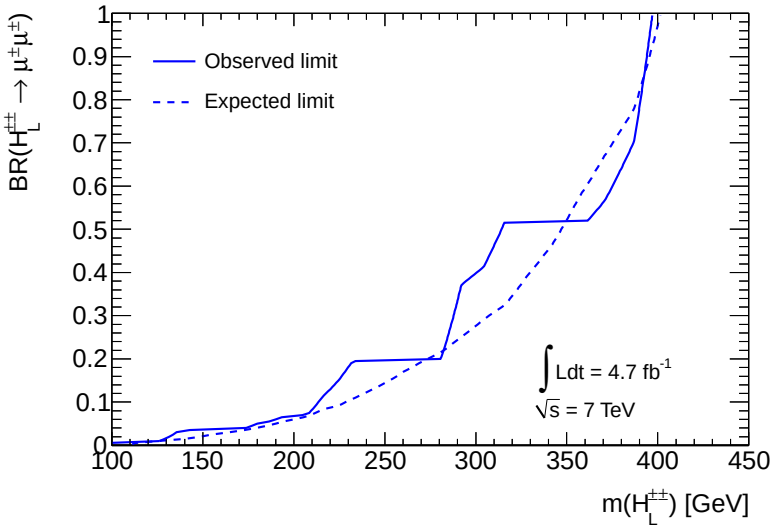

(a)

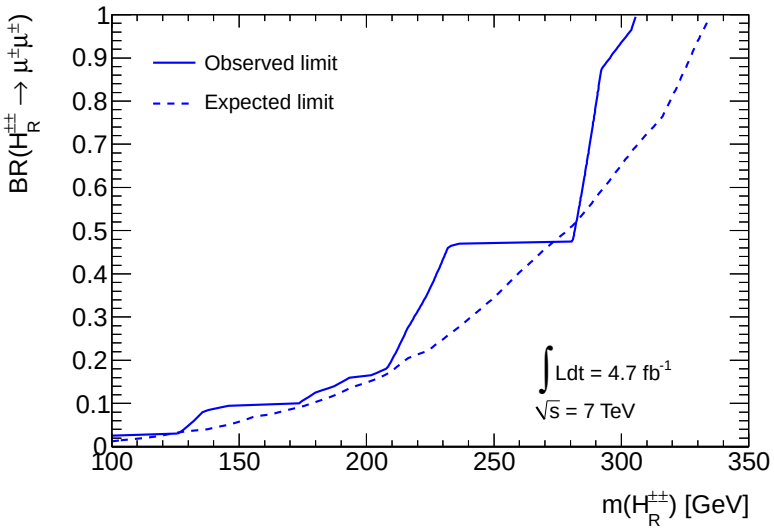

(b)

Figure 11.7: Mass limits as function of branching ratio for (a) $H_L^{\pm\pm}$ and (b) $H_R^{\pm\pm}$ bosons decaying to $\mu^\pm\mu^\pm$. The regions *above* the solid (observed limit) and dashed (expected limit) lines are excluded.

Chapter 12

Conclusions

This dissertation presented a search for physics beyond the Standard Model in events with at least two muons of the same electric charge. The search is performed in a pp collision data sample, collected by the ATLAS experiment at the Large Hadron Collider at $\sqrt{s} = 7$ TeV during 2011, corresponding to a total integrated luminosity of 4.7 fb^{-1}. Like-sign muon pairs are selected by placing tight identification criteria on the muons, with no requirements on other event kinematics.

A search is first performed for anomalous production of like-sign muon pairs, resulting in an overall excess of observed muon pairs with respect to the Standard Model background estimate. Search regions are defined by a lower bound on the dimuon invariant mass, ranging from $m(\mu^{\pm}\mu^{\pm}) > 15$ GeV to $m(\mu^{\pm}\mu^{\pm}) > 400$ GeV. Like-sign muon pairs are additionally considered both inclusively and separated by charge into positively-charged and negatively-charged muon pairs. No statistically significant excess is observed in data for any of the search regions.

Since no excess is observed, the data are used to place upper cross-section limits on the production of like-sign muon pairs due to non-Standard Model sources. The cross-section limits are placed with respect to a fiducial region, defined at truth particle level to closely emulate the experimental selection criteria. The resulting limits at 95% confidence level range between 30 fb and 1.2 fb. These fiducial cross-section limits can be interpreted as cross-section limits on a particular model of new physics phenomena by determining the efficiency with which events enter the fiducial region.

A dedicated search is additionally performed for a narrow like-sign resonance. Such resonant production is predicted by several models of physics beyond the Standard Model, including models with doubly charged Higgs ($H^{\pm\pm}$) bosons, for instance, the left-right symmetric model, Higgs triplet models, and the little Higgs model. The search regions are here defined as narrow bins in the like-sign dimuon invariant mass, determined to optimize the signal sensitivity. No narrow resonance peak is observed in the data, and the results are interpreted as limits on the cross section times branching ratio for pair production of doubly charged Higgs bosons. By comparing the cross-section limits to the theoretical cross-sections, limits are derived on the al-

lowed $H^{\pm\pm}$ boson masses. Within the left-right symmetric model, where different states exist for $H^{\pm\pm}$ bosons coupling to left-handed ($H_L^{\pm\pm}$) and right-handed ($H_R^{\pm\pm}$) fermions, masses are excluded at 95% confidence level below 398 GeV and 306 GeV, respectively, assuming a 100% branching ratio to muons.

Bibliography

[1] CERN, *The CERN Accelerator Complex*, http://public.web.cern.ch/public/en/research/AccelComplex-en.html, 2008.

[2] ATLAS Experiment 2012 CERN, *ATLAS Photos*, http://www.atlas.ch/photos/index.html.

[3] ATLAS Collaboration, *ATLAS Public Luminosity Plots*, https://twiki.cern.ch/twiki/bin/view/AtlasPublic/LuminosityPublicResults.

[4] ATLAS Collaboration, *The ATLAS Experiment at the CERN Large Hadron Collider*, JINST **3** (2008) S08003.

[5] ATLAS Collaboration, *Study of Alignment-Related Systematic Effects on the ATLAS Inner Detector Track Reconstruction*, ATLAS-CONF-2012-141, 2012.

[6] ATLAS Collaboration, *Performance of the ATLAS Muon Trigger in 2011*, ATLAS-CONF-2012-099, 2012.

[7] J. Beringer *et al.* (Particle Data Group), *The Review of Particle Physics*, Phys. Rev. **D 86** (2012) 010001.

[8] L. Evans and P. Bryant (eds.), *LHC Machine*, JINST **3** (2008) S08001.

[9] G. Papotti, *Proceedings of the 2011 Evian Workshop on LHC Beam Operation. Session 1: 2011 Operation*, CERN-ATS-2012-083-rev, December, 2011.

[10] ATLAS Collaboration, *Search for Anomalous Production of Prompt Like-Sign Lepton Pairs at* $\sqrt{s} = 7$ *TeV with the ATLAS Detector*, arXiv:1210.4538 (Accepted by JHEP), 2012.

[11] ATLAS Collaboration, *Search for Doubly-Charged Higgs Bosons in Like-Sign Dilepton Final States at* $\sqrt{s} = 7$ *TeV with the ATLAS Detector*, arXiv:1210.5070 (Accepted by Eur. Phys. J. C), 2012.

[12] ATLAS Collaboration, *Search for Anomalous Production of Prompt Like-Sign Muon Pairs and Constraints on Physics Beyond the Standard Model with the ATLAS Detector*, Phys. Rev. **D 85** (2012) 032004.

[13] ATLAS Collaboration, *Observation of a New Particle in the Search for the Standard Model Higgs Boson with the ATLAS Detector at the LHC*, Phys. Lett. **B 716** (2012) 1.

[14] CMS Collaboration, *Observation of a New Boson at a Mass of 125 GeV with the CMS Experiment at the LHC*, Phys. Lett. **B 716** (2012) 30.

[15] D. Griffiths, *Introduction to Elementary Particles*. WILEY, Second edition, 2008.

[16] M. E. Peskin and D. V. Schroeder, *An Introduction to Quantum Field Theory*. Westview Press, Reprint edition, 1995.

[17] G. Arnison *et al.* (UA1 Collaboration), *Experimental Observation of Isolated Large Transverse Energy Electrons with Associated Missing Energy at* $\sqrt{s} = 540\ GeV$, Phys. Lett. **B 122** (1983) 103.

[18] G. Arnison *et al.* (UA1 Collaboration), *Experimental Observation of Lepton Pairs of Invariant Mass Around 95 GeV/c^2 at the CERN SPS Collider*, Phys. Lett. **B 126** (1983) 398.

[19] Y. Fukuda *et al.* (The Super-Kamiokande Collaboration), *Evidence for Oscillation of Atmospheric Neutrinos*, Phys. Rev. Lett. **81** (1998) 1562.

[20] G. Bertone, D. Hooper, J. Silk, *Particle Dark Matter: Evidence, Candidates and Constraints*, Phys. Rept. **405** (2005) 279.

[21] S. Perlmutter *et al.*, *Measurements of* Ω *and* Λ *from 42 High-Redshift Supernovae*, Astrophys. J. **517** (1999) 565.

[22] A. G. Reiss *et al.*, *Observational Evidence from Supernovae for an Accelerating Universe and a Cosmological Constant*, Astron. J. **116** (1998) 1009.

[23] S. P. Martin, *A Supersymmetry Primer*, arXiv:hep-ph/9709356, 2011.

[24] H. Murayama, *Supersymmetry Phenomenology*, arXiv:hep-ph/0002232, 2000.

[25] E. Eichten, I. Hinchliffe, K. Lane, and C. Quigg, *Supercollider Physics*, Rev. Mod. Phys. **56** (1984) 579.

[26] J. Wess and B. Zumino, *Supergauge Transformations in Four Dimensions*, Nucl. Phys. **B 70** (1974) 39.

[27] S. Dimopoulos and H. Georgi, *Softly Broken Supersymmetry and SU(5)*, Nucl. Phys. **B 193** (1981) 150.

[28] R. M. Barnett, J. F. Gunion, and H. E. Haber, *Discovering Supersymmetry with Like-Sign Dileptons*, Phys. Lett. **B 315** (1993) 349.

[29] J. F. Gunion, H. E. Haber, G. Kane, and S. Dawson, *The Higgs Hunters Guide*, Front. Phys. **80** (2000) 1.

[30] J. F. Gunion, C. Loomis, K. T. Pitts, *Searching for Doubly-Charged Higgs Bosons at Future Colliders*, Proceedings of the 1996 DPF/DPB Summer Study on New Directions for High Energy Physics, 1996.

[31] J. C. Pati and A. Salam, *Lepton Number as the Fourth Color*, Phys. Rev. **D 10** (1974) 275.

[32] R. N. Mohapatra and J. C. Pati, *Left-Right Gauge Symmetry and an Isoconjugate Model of CP-Violation*, Phys. Rev. **D 11** (1975) 566.

[33] G. Senjanovic and R. N. Mohapatra, *Exact Left-Right Symmetry and Spontaneous Violation of Parity*, Phys. Rev. **D 12** (1975) 1502.

[34] T. G. Rizzo, *Doubly Charged Higgs Bosons and Lepton Number Violating Processes*, Phys. Rev. **D 25** (1982) 1355; addendum ibid. **D 27**, (1983) 657.

[35] J.E. Cieza Montalvo, N.V. Cortez, J. Sa Borges, and M.D. Tonasse, *Searching for Doubly Charged Higgs Bosons at the LHC in a 3-3-1 Model*, Nucl. Phys. **B 756** (2006) 1; erratum ibid. **B 796** 422 (2008).

[36] H. Georgi and M. Machacek, *Doubly Charged Higgs Bosons*, Nucl. Phys. **B 262** (1985) 463.

[37] J.F. Gunion, R. Vega and J. Wudka, *Higgs Triplets in the Standard Model*, Phys. Rev. **D 42** (1990) 1673.

[38] N. Arkani-Hamed, A.G. Cohen, E. Katz, A.E. Nelson, T. Gregoire, and J. G. Wacker, *The Minimal Moose for a Little Higgs*, JHEP **0208** (2002) 021.

[39] A. Zee, *Quantum Numbers of Majorana Neutrino Masses*, Nucl. Phys. **B 264** (1986) 99.

[40] K. S. Babu, *Model of Calculable Majorana Neutrino Masses*, Phys. Lett. **B 203** (1988) 132.

[41] M. Nebot, J.F. Oliver, D. Palao, and A. Santamaria, *Prospects for the Zee-Babu Model at the CERN LHC and Low Energy Experiments*, Phys. Rev. **D 77** (2008) 093013.

[42] E. Ma, *Pathways to Naturally Small Neutrino Masses*, Phys. Rev. Lett. **81** (1998) 1171.

[43] M. Magg and C. Wetterich, *Neutrino Mass Problem and Gauge Hierarchy*, Phys. Lett. **B 94** (1980) 61.

[44] J. Schechter and J. W. F. Valle, *Neutrino Masses in SU(2) $\otimes$ U(1) Theories*, Phys. Rev. **D 22** (1980) 2227.

[45] G. Lazarides, Q. Shafi, and C. Wetterich, *Proton Lifetime and Fermion Masses in an SO(10) Model*, Nucl. Phys. **B 181** (1981) 287.

[46] R. N. Mohapatra and G. Senjanovic, *Neutrino masses and mixings in gauge models with spontaneous parity violation*, Phys. Rev. **D 23** (1981) 165.

[47] M. Mühlleitner and M. Spira, *Note on Doubly Charged Higgs Boson Pair Production at Hadron Colliders*, Phys. Rev. **D 68** (2003) 117701.

[48] P. H. Frampton, P. Q. Hung, and M. Sher, *Quarks and Leptons Beyond the Third Generation*, Phys. Rept. **330** (2000) 263.

[49] S. Jung, H. Murayama, A. Pierce, and J. D. Wells, *Top Quark Forward-Backward Asymmetry from New t-Channel Physics*, Phys. Rev. **D 81** (2010) 015004.

[50] CDF Collaboration, *Evidence for a Mass Dependent Forward-Backward Asymmetry in Top Quark Pair Production*, Phys. Rev. **D 83** (2011) 112003.

[51] D0 Collaboration, *Forward-Backward Asymmetry in Top Quark-Antiquark Production*, Phys. Rev. **D 84** (2011) 112005.

[52] CDF Collaboration, *Inclusive Search for New Physics with Like-Sign Dilepton Events in $p\bar{p}$ Collisions at $\sqrt{s} = 1.96$ TeV*, Phys. Rev. Lett. **98** (2007) 221803.

[53] CDF Collaboration, *Search for New Physics in High-p_{T} Like-Sign Dilepton Events at CDF II*, Phys. Rev. Lett. **107** (2011) 181801.

[54] ATLAS Collaboration, *Inclusive Search for Same-Sign Dilepton Signatures in pp Collisions at $\sqrt{s} = 7$ TeV with the ATLAS Detector*, JHEP **10** (2011) 107.

[55] DELPHI Collaboration, *Search for Doubly Charged Higgs Bosons at LEP2*, Phys. Lett. **B 552** (2003) 127.

[56] OPAL Collaboration, *Search for Doubly Charged Higgs Bosons with the OPAL Detector at LEP*, Phys. Lett. **B 526** (2002) 221.

[57] L3 Collaboration, *Search for Doubly-Charged Higgs Bosons at LEP*, Phys. Lett. **B 576** (2003) 18.

[58] CDF Collaboration, *Search for Doubly-Charged Higgs Bosons with Lepton-Flavor-Violating Decays involving Tau Leptons*, Phys. Rev. Lett. **101** (2008) 121801.

[59] D0 Collaboration, *Search for Doubly Charged Higgs Boson Pair Production in $p\bar{p}$ Collisions at $\sqrt{s} = 1.96\ TeV$*, Phys. Rev. Lett. **108** (2012) 021801.

[60] CMS Collaboration, *A Search for a Doubly-Charged Higgs Boson in pp Collisions at $\sqrt{s} = 7\ TeV$*, arXiv:1207.2666, 2012.

[61] SINDRUM Collaboration, *Search for the Decay $\mu^+ \to e^+e^+e^-$*, Nucl. Phys. **B 299** (1988) 1.

[62] M. L. Swartz, *Limits on Doubly Charged Higgs Bosons and Lepton-Flavor Violation*, Phys. Rev. **D 40** (1989) 1521.

[63] ATLAS Collaboration, *ATLAS Detector and Physics Performance. Technical Design Report. Vol 1.*, CERN-LHCC-99-14, 1999.

[64] ATLAS Collaboration, *ATLAS Detector and Physics Performance. Technical Design Report. Vol 2.*, CERN-LHCC-99-15, 1999.

[65] CMS Collaboration, *The CMS Experiment at the CERN LHC*, JINST **3** (2008) S08004.

[66] LHCb Collaboration, *The LHCb Experiment at the CERN LHC*, JINST **3** (2008) S08005.

[67] ALICE Collaboration, *The ALICE Experiment at the CERN LHC*, JINST **3** (2008) S08002.

[68] ATLAS Collaboration, *Luminosity Determination in pp Collisions at $\sqrt{s} = 7\ TeV$ Using the ATLAS Detector at the LHC*, Eur. Phys. J. **C 71** (2011) 1630.

[69] CERN, *Interim Summary Report on the Analysis of the 19 September 2008 Incident at the LHC*, EDMS 973073, 15 October 2008.

[70] ATLAS Collaboration, *ATLAS Pixel Detector Electronics and Sensors*, JINST **3** (2008) P07007.

[71] ATLAS Collaboration, *Improved Luminosity Determination in pp Collisions at $\sqrt{s} = 7\ TeV$ using the ATLAS Detector at the LHC*, ATLAS-CONF-2012-080, 2012.

[72] ATLAS Collaboration, *Performance of the ATLAS Trigger System in 2010*, Eur. Phys. J. C **72** (2012) 1849.

[73] ATLAS Collaboration, *Measurements of the Electron and Muon Inclusive Cross-Sections in Proton-Proton Collisions at $\sqrt{s} = 7$ TeV with the ATLAS Detector*, Phys. Lett. **B 707** (2012) 438.

[74] ATLAS Collaboration, *Electron Performance Measurements with the ATLAS Detector using the 2010 LHC Proton-Proton Collision Data*, Eur. Phys. J. **C 72** (2012) 1909.

[75] T. Cornelissen *et al.*, *Concept, Design and Implementation of the ATLAS New Tracking (NEWT)*, ATL-SOFT-PUB-2007-007, 2007.

[76] ATLAS Collaboration, *The ATLAS Inner Detector Commissioning and Calibration*, Eur. Phys. J. **C 70** (2010) 787.

[77] ATLAS Collaboration, *Performance of Primary Vertex Reconstruction in Proton-Proton Collisions at $\sqrt{s} = 7$ TeV in the ATLAS Experiment*, ATLAS-CONF-2010-069, 2010.

[78] W. Waltenberger, R. Frühwirth, P. Vanlaer, *Adaptive Vertex Fitting*, J. Phys. **G 34** (2007) N343.

[79] ATLAS Collaboration, *Expected Performance of the ATLAS Experiment: Detector, Trigger and Physics*, CERN-OPEN-2008-020, 2008.

[80] R. Nicolaidou, L. Chevalier, S. Hassani, J.F. Laporte, E. Le Menedeu, and A. Ouraou, *Muon Identification Procedure for the ATLAS Detector at the LHC using Muonboy Reconstruction Package and Tests of its Performance using Cosmic Rays and Single Beam Data*, Journal of Physics: Conference Series **219** (2010) no. 3, 032052.

[81] ATLAS Collaboration, *Muon Reconstruction Efficiency in Reprocessed 2010 LHC Proton-Proton Collision Data Recorded with the ATLAS Detector*, ATLAS-CONF-2011-063, 2011.

[82] W. Lampl *et al.*, *Calorimeter Clustering Algorithms: Description and Performance*, ATLAS-LARG-PUB-2008-002, 2008.

[83] M. Cacciari, G. P. Salam, and G. Soyez, *The anti-k_t Jet Clustering Algorithm*, JHEP **0804** (2008) 063.

[84] ATLAS Collaboration, *Jet Energy Measurement with the ATLAS Detector in Proton-Proton Collisions at $\sqrt{s} = 7$ TeV*, arXiv:1112.6426 (Submitted to Eur. Phys. J. C), 2011.

[85] ATLAS Collaboration, *Performance of Missing Transverse Momentum Reconstruction in Proton-Proton Collisions at 7 TeV with ATLAS*, Eur. Phys. J. **C 72** (2012) 1844.

[86] ATLAS Collaboration, *MCP Guidelines for Selection, Scale Factors, and Momentum Smearing*, Described at https://twiki.cern.ch/twiki/bin/view/AtlasProtected/MCPAnalysisGuidelinesEPS2011.

[87] ATLAS Collaboration, *Alignment of the ATLAS Inner Detector Tracking System with 2010 LHC Proton-Proton Collisions at* $\sqrt{s} = 7$ *TeV*, ATLAS-CONF-2011-012, 2011.

[88] ATLAS Collaboration, *Determination of the Muon Reconstruction Efficiency in ATLAS at the Z resonance in Proton-Proton Collisons at* $\sqrt{s} = 7$ *TeV*, ATLAS-CONF-2011-008, 2010.

[89] ATLAS Collaboration, *ATLAS Muon Momentum Resolution in the First Pass Reconstruction of the 2010* $p-p$ *Collision Data at* $\sqrt{s} = 7$ *TeV*, ATLAS-CONF-2011-046, 2011.

[90] M. L. Mangano, M. Moretti, F. Piccinini, R. Pittau, and A. D. Polosa, *ALPGEN, a Generator for Hard Multiparton Processes in Hadronic Collisions*, JHEP **07** (2003) 001.

[91] ATLAS Collaboration, *The ATLAS Simulation Infrastructure*, Eur. Phys. J. **C 70** (2010) 823.

[92] S. Agostinelli *et al.* (GEANT4 Collaboration), *GEANT4: A Simulation Toolkit*, Nucl. Instr. Meth. **A 506** (2010) 250.

[93] ATLAS Collaboration, *Pileup Reweighting*, Described at https://twiki.cern.ch/twiki/bin/view/AtlasProtected/PileupReweighting.

[94] T. Gleisberg, S. Hoeche, F. Krauss, M. Schoenherr, S. Schumann, F. Siegert, and J. Winter, *Event Generation with SHERPA 1.1*, JHEP **0902** (2009) 007.

[95] J. M. Campbell, R. K. Ellis, and C. Williams, *Vector Boson Pair Production at the LHC*, JHEP **07** (2011) 018.

[96] J. Alwall, M. Herquet, F. Maltoni, O. Mattelaer, and T. Stelzer, *MadGraph 5: Going Beyond*, JHEP **1106** (2011) 128.

[97] B. Jäger, C. Oleari, and D. Zeppenfeld, *Next-to-Leading Order QCD Corrections to W^+W^+jj and W^-W^-jj Production via Weak-Boson Fusion*, Phys. Rev. **D 80** (2009) 034022.

[98] T. Melia, K. Melnikov, R. Rontsch, and G. Zanderighi, *Next-to-Leading Order QCD Predictions for W^+W^+jj Production at the LHC*, JHEP **1012** (2010) 053.

[99] J. M. Campbell and R. K. Ellis, *$t\bar{t}W$ Production and Decay at NLO*, JHEP **1207** (2012) 052.

[100] A. Lazopoulos, T. McElmurry, K. Melnikov, and F. Petriello, *Next-to-Leading Order QCD Corrections to $t\bar{t}Z$ Production at the LHC*, Phys. Lett. **B 666** (2008) 62.

[101] M. V. Garzelli, A. Kardos,C. G. Papadopoulos, and Z. Trocsanyi, *Z0-Boson Production in Association with a Top Anti-Top Pair at NLO Accuracy with Parton Shower Effects*, Phys. Rev. **D 85** (2012) 074022.

[102] A. Kardos, Z. Trocsanyi, and C. G. Papadopoulos, *Top Quark Pair Production in Association with a Z-boson at NLO Accuracy*, Phys. Rev. **D 85** (2012) 054015.

[103] J. Pumplin *et al.* (CTEQ Collaboration), *New Generation of Parton Distributions with Uncertainties from Global QCD Analysis*, JHEP **0207** (2002) 012.

[104] M. Guzzi *et al.* (CTEQ Collaboration), *CT10 Parton Distributions and Other Developments in the Global QCD Analysis*, arXiv:1101.0561, 2011.

[105] ATLAS Collaboration, *Search for High-Mass Dilepton Resonances in 5 fb^{-1} of pp Collisions at $\sqrt{s} = 7$ TeV*, ATL-PHYS-INT-2012-073, 2008.

[106] R. Hamberg, W. van Neerven, and T. Matsuura, *A Complete Calculation of the Order α_s^2 Correction to the Drell-Yan K factor*, Nucl. Phys. **B 359** (1991) 343, erratum ibid. **B 644** (2002) 403.

[107] ATLAS Collaboration, *Search for High Mass Dilepton Resonances in pp Collisions at $\sqrt{s} = 7$ TeV with the ATLAS Experiment*, Phys. Lett. **B 700** (2011) 163.

[108] C.M. Carloni Calame, G. Montagna, O. Nicrosini, and A. Vicini, *Precision Electroweak Calculation of the Charged Current Drell-Yan Process*, JHEP **0612** (2006) 016.

[109] C. M. Carloni Calame, G. Montagna, O. Nicrosini, and A. Vicini, *Precision Electroweak Calculation of the Production of a High Transverse-Momentum Lepton Pair at Hadron Colliders*, JHEP **0710** (2007) 109.

[110] S. Frixione and B. R. Webber, *Matching NLO QCD Computations and Parton Shower Simulations*, JHEP **0206** (2002) 029.

[111] G. Corcella, I. Knowles, G. Marchesini, S. Moretti, K. Odagiri, *et al.*, *HERWIG 6: An Event Generator for Hadron Emission Reactions with Interfering Gluons (Including Supersymmetric Processes)*, JHEP **0101** (2001) 010.

[112] M. Aliev, H. Lacker, U. Langenfeld, S. Moch, P. Uwer, M. Wiedermann, *HATHOR: HAdronic Top and Heavy quarks crOss section calculatoR*, Comput. Phys. Commun. **182** (2011) 1034.

[113] A. Sherstnev and R. S. Thorne, *Parton Distributions for LO Generators*, Eur. Phys. J. **C 55** (2008) 553.

[114] P. M. Nadolsky *et al.* (CTEQ Collaboration), *Implications of CTEQ Global Analysis for Collider Observables*, Phys. Rev. **D 78** (2008) 013004.

[115] J. Campbell, J. Huston, and W. J. Stirling, *Hard Interactions of Quarks and Gluons: A Primer for LHC Physics*, Rept. Prog. Phys. **70** (2007) 89.

[116] T. Sjöstrand, S. Mrenna, and P. Skands, *PYTHIA 6.4 Physics and Manual*, JHEP **05** (2006) 026.

[117] ATLAS Collaboration, *Luminosity Determination in pp Collisions at $\sqrt{s} = 7$ TeV using the ATLAS Detector in 2011*, ATLAS-CONF-2011-116, 2011.

[118] A. L. Read, *Presentation of Search Results: the CLs Technique*, J. Phys. **G 28** (2002) 2693.

[119] T. Sjöstrand, S. Mrenna, and P. Skands, *A Brief Introduction to PYTHIA 8.1*, Computer Physics Communications **178** (2008) no. 11, 852.

[120] M. Spira. Private communication.

[121] G. Cowan and E. Gross, *Discovery Significance with Statistical Uncertainty in the Background Estimate*, www.pp.rhul.ac.uk/~cowan/stat/notes/SigCalcNote.pdf, 2008.

[122] A.D. Martin, W.J. Stirling, R.S. Thorne, and G. Watt, *Hard Interactions of Quarks and Gluons: A Primer for LHC Physics*, Eur. Phys. J. **C 63** (2009) 189.

Appendix A

Additional Control Regions

This section shows additional control region figures, used to cross-check the modeling of the non-prompt muon background. These figures are complementary to those shown in Section 8.5.2.

Positively and Negatively-Charged Pairs

Since the signal region is studied separately for positively and negatively charged muon pairs, the control region modeling is cross-checked separating the two charges. Figure A.1 shows the invariant mass distributions for positive pairs and Figure A.2 shows them for negative pairs. The statistics is limited when separating the two charges, however, taking that into account the agreement between observation and prediction is similar for $\mu^+\mu^+$ and $\mu^-\mu^-$ pairs.

Jets and Missing Transverse Momentum

Neither the missing transverse momentum nor the number of reconstructed jets are variables used in the search to select the signal region. However, these variables are useful as an additional cross-check of the non-prompt muon background modeling. Figure A.3 shows the distribution of the missing transverse momentum for the five control regions. Figure A.4 similarly shows distributions of the number of reconstructed jets. Given the significant systematic uncertainties associated with the non-prompt background, the observation and predictions are in agreement. For the control region with like-sign muon pairs where the leading muon is intermediately isolated and the subleading muon is isolated, more pairs are observed than predicted in events with no reconstructed jets. The discrepancy in this control region is, however, only 1.6σ taking the statistical and systematic uncertainties into account.

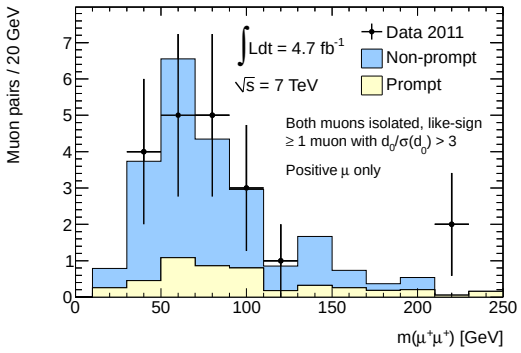

(a) Like-sign $\sigma(d_0)/d_0 > 3$ for ≥ 1 muon

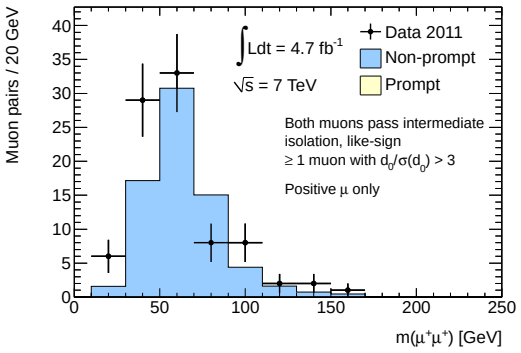

(b) Like-sign intermediate isolation, $\sigma(d_0)/d_0 > 3$ for ≥ 1 muon

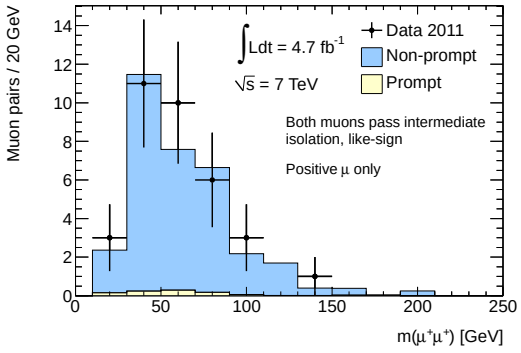

(c) Like-sign intermediate isolation

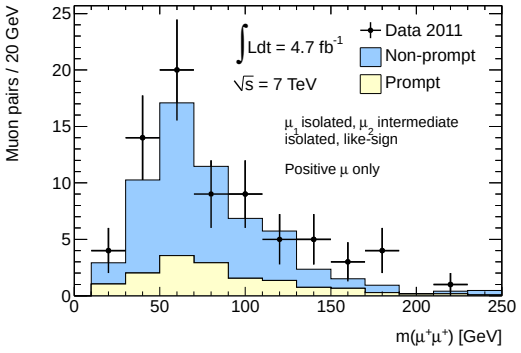

(d) Like-sign muon pairs with leading muon isolated and subleading muon intermediately isolated

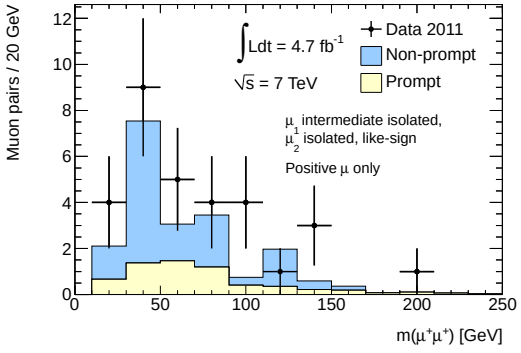

(e) Like-sign muon pairs with leading muon intermediately isolated and subleading muon isolated

Figure A.1: Invariant mass distributions for different control regions enhanced in non-prompt background for positively-charged muon pairs only.

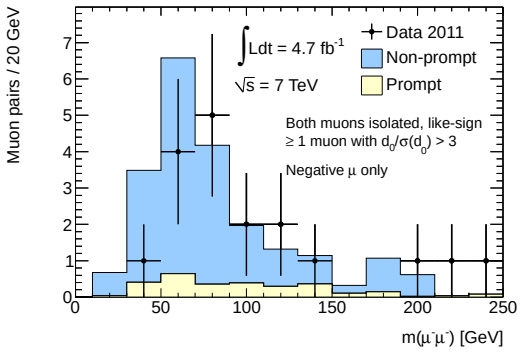

(a) Like-sign $\sigma(d_0)/d_0 > 3$ for ≥ 1 muon

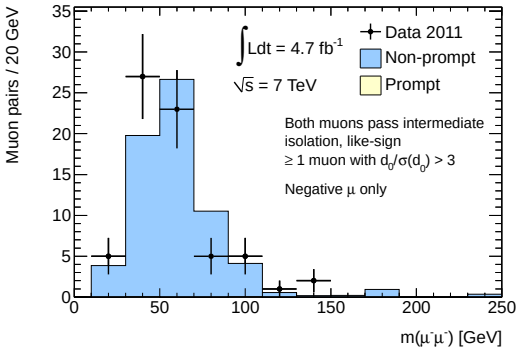

(b) Like-sign intermediate isolation, $\sigma(d_0)/d_0 > 3$ for ≥ 1 muon

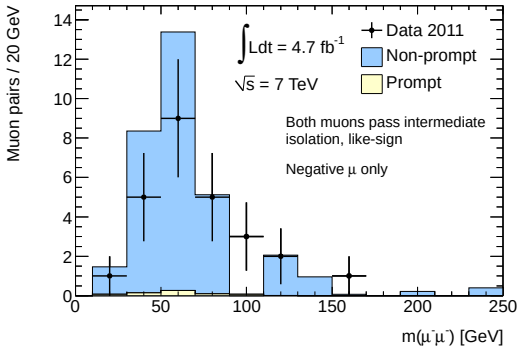

(c) Like-sign intermediate isolation

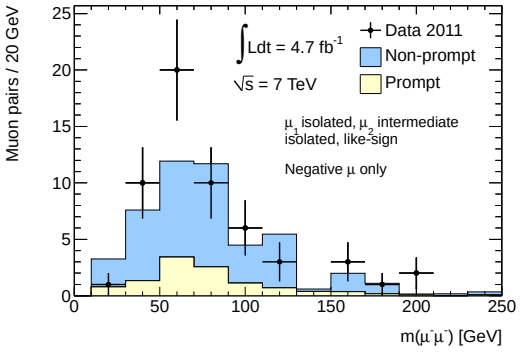

(d) Like-sign muon pairs with leading muon isolated and subleading muon intermediately isolated

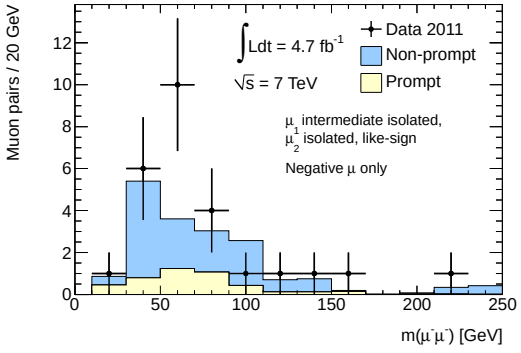

(e) Like-sign muon pairs with leading muon intermediately isolated and subleading muon isolated

Figure A.2: Invariant mass distributions for different control regions enhanced in non-prompt background for negatively-charged muon pairs only.

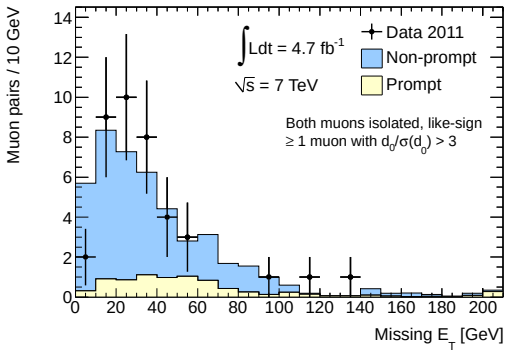

(a) Like-sign $\sigma(d_0)/d_0 > 3$ for ≥ 1 muon

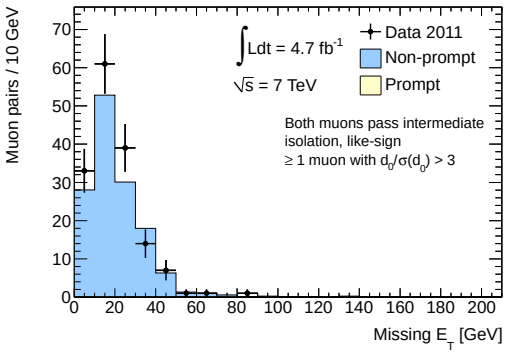

(b) Like-sign intermediate isolation, $\sigma(d_0)/d_0 > 3$ for ≥ 1 muon

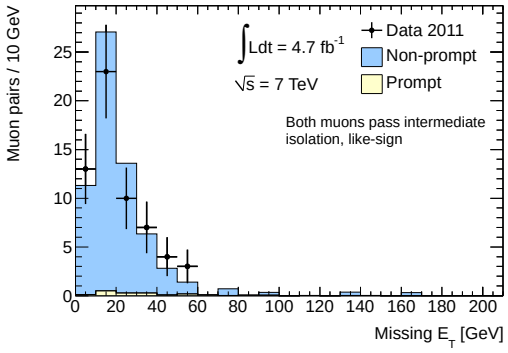

(c) Like-sign intermediate isolation

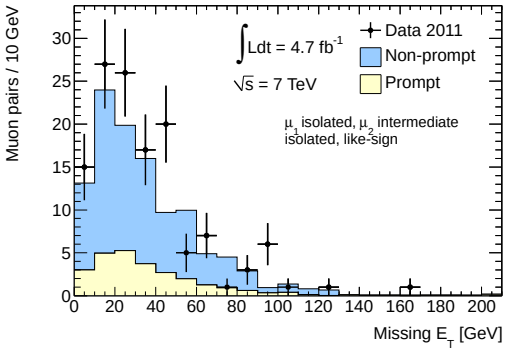

(d) Like-sign muon pairs with leading muon isolated and subleading muon intermediately isolated

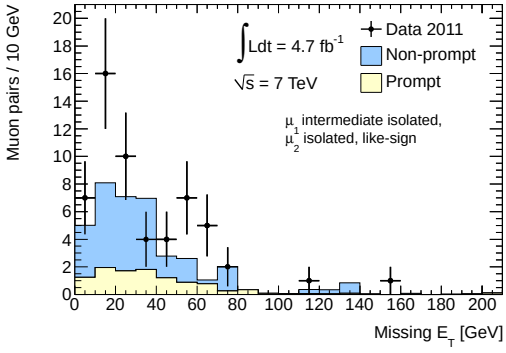

(e) Like-sign muon pairs with leading muon intermediately isolated and subleading muon isolated

Figure A.3: Distributions of missing transverse momentum for different control regions enhanced in non-prompt background.

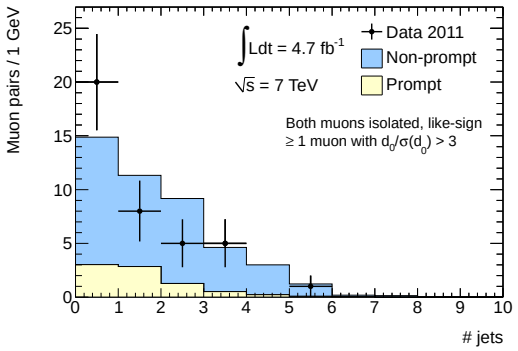

(a) Like-sign $\sigma(d_0)/d_0 > 3$ for ≥ 1 muon

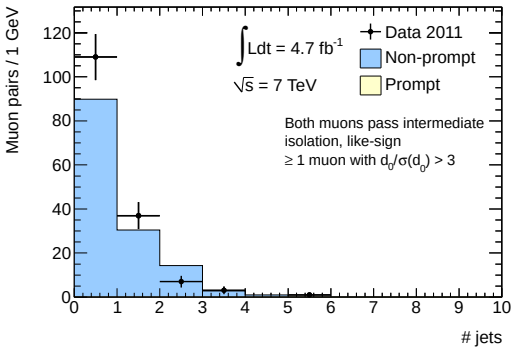

(b) Like-sign intermediate isolation, $\sigma(d_0)/d_0 > 3$ for ≥ 1 muon

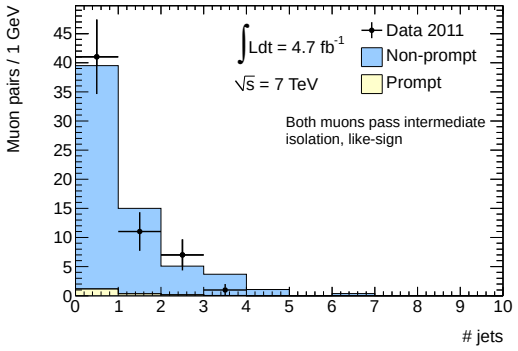

(c) Like-sign intermediate isolation

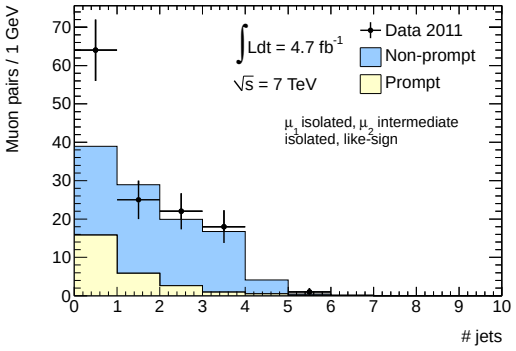

(d) Like-sign muon pairs with leading muon isolated and subleading muon intermediately isolated

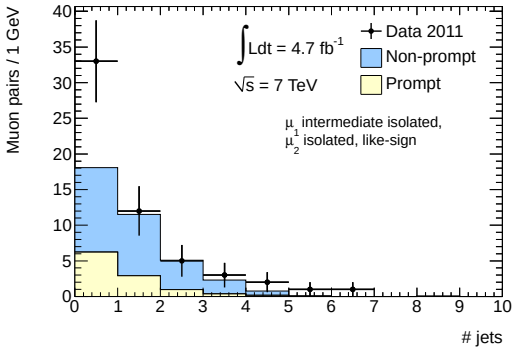

(e) Like-sign muon pairs with leading muon intermediately isolated and subleading muon isolated

Figure A.4: Distributions of the number of reconstructed jets in the event for different control regions enhanced in non-prompt background.

Appendix B

Searches with $e^{\pm}e^{\pm}$ and $e^{\pm}\mu^{\pm}$

The like-sign dimuon search presented in this dissertation was published jointly with searches in the $e^{\pm}e^{\pm}$ and $e^{\pm}\mu^{\pm}$ final states, following the same search strategy [10, 11]. This chapter briefly describes the electron-based searches and summarizes the results of the inclusive search for anomalous production of $e^{\pm}e^{\pm}$ and $e^{\pm}\mu^{\pm}$ pairs, as well as the results of the narrow resonance search in these final states.

Electron Selection

Electrons used in the search are identified as compact showers in the electromagnetic calorimeter which are matched to a reconstructed track in the inner detector using the *tight* identification criteria described in Ref. [74]. Electrons must have $p_{\mathrm{T}} > 20$ GeV. If the highest-p_{T} lepton in a $e^{\pm}e^{\pm}$ or $e^{\pm}\mu^{\pm}$ pair is an electron, it is further required to have $p_{\mathrm{T}} > 25$ GeV due to the trigger requirement[1]. Electrons must have $|\eta| < 2.47$, excluding the transition region between the barrel and endcap calorimeters ($1.37 < |\eta| < 1.52$).

Electrons are required to fulfill the same impact parameter selection as muons (see Section 7.1.2) and to be isolated from nearby hadronic activity in the calorimeters and the tracking system: $E_{\mathrm{T}}^{\mathrm{cone0.3}} < 3$ GeV $+(p_{\mathrm{T}}(e) - 20\ \mathrm{GeV}) \times 0.037$ and $p_{\mathrm{T}}^{\mathrm{cone0.2}}/p_{\mathrm{T}}(e) < 0.1$ are required. The calorimeter-based isolation energy is corrected for the energy of the electron object as well as for energy deposits from pileup interactions. Similarly as for muons, selected electrons must finally be isolated from reconstructed jets.

$e^{\pm}e^{\pm}$ and $e^{\pm}\mu^{\pm}$ pairs are selected if they contain at least two leptons of the same electric charge with invariant mass greater than 15 GeV. For $e^{\pm}e^{\pm}$ pairs, the mass range 70–110 GeV is vetoed due to large backgrounds from opposite-sign electron pairs originating from Z decays, where the charge of one electron is misidentified.

[1] $e^{\pm}e^{\pm}$ pairs are selected using a single-electron trigger with 16 GeV at Level-1 and 20 GeV or 22 GeV at the event filter, depending on the run period. $e^{\pm}\mu^{\pm}$ pairs are selected using a combination of the single-electron and single-muon triggers.

Background Sources

The backgrounds to the $e^{\pm}e^{\pm}$ and $e^{\pm}\mu^{\pm}$ final states are estimated similarly to the $\mu^{\pm}\mu^{\pm}$ channel. The contribution from prompt lepton backgrounds are determined completely analogously (see Section 8.1.4). Electrons suffer from background due to charge misidentification and photon conversions to a much larger extent than muons. The charge misidentification background is measured from simulation with an η-dependent scaling factor applied to correct for an observed overestimate of the charge misidentification in simulation by 15%. The opposite-sign processes which contribute are $Z\gamma^*$, $t\bar{t}$, Wt, and $W^{\pm}W^{\mp}$ production. Production of $W\gamma$ and $Z\gamma$ can also produce $e^{\pm}e^{\pm}$ and $e^{\pm}\mu^{\pm}$ pairs if the photon converts[2].

The estimate of the non-prompt electron background follows the same method as is used to derive the non-prompt muon background (see Section 8.3.2). The non-prompt estimate is derived by reversing either the impact parameter significance cut or by requiring electrons to fail the *medium* electron identification criteria while passing the *loose* criteria, defined in Ref. [74].

Systematic Uncertainties

The sources of systematic uncertainty affecting the signal acceptance and background estimates are similar to those described for the $\mu^{\pm}\mu^{\pm}$ search (see Chapter 9). Systematic uncertainties on the prompt background include lepton identification efficiencies, luminosity uncertainty, and cross-section uncertainties. The muon identification uncertainties were outlines in Section 9.1. The effect on the background yield due to electron identification and electron trigger uncertainties are typically small ($\pm$(3–4)%) and the uncertainty on the electron energy scale impacts the background estimate by up to $\pm$3.5%. Cross-section and luminosity uncertainties are identical to the $\mu^{\pm}\mu^{\pm}$ final state.

The uncertainty on the non-prompt electron background is based on a systematic uncertainty on the electron fake factor, as well as statistical uncertainties in data control samples. The combined non-prompt background uncertainty ranges from about 28% and 31% for $e^{\pm}e^{\pm}$ and $e^{\pm}\mu^{\pm}$ in the mass range $m(\ell^{\pm}\ell^{\pm}) > 15$ GeV to nearly 100% at higher masses.

The uncertainty on the charge-flip background ranges from $\pm$15% to $\pm$23% for $m(\ell^{\pm}\ell^{\pm}) > 15$ GeV to $m(\ell^{\pm}\ell^{\pm}) > 400$ GeV. The uncertainty on the $W\gamma$ and $Z\gamma$ backgrounds is $\pm$(15–18)%, depending on the lower bound on the invariant mass.

Results of the Inclusive Search for $e^{\pm}e^{\pm}$ and $e^{\pm}\mu^{\pm}$ Production

The distributions of the $e^{\pm}e^{\pm}$ and $e^{\pm}\mu^{\pm}$ invariant mass are shown for data and the background estimates in Figure B.1. Figures B.2 and B.3 similarly show the

[2] $W\gamma$ is generated with ALPGEN while the $Z\gamma$ process is included in the simulation of Z/γ^*.

Sample	Number of pairs with $m(e^{\pm}e^{\pm})$				
	> 15 GeV	> 100 GeV	> 200 GeV	> 300 GeV	> 400 GeV
Prompt	101 ± 13	56.3 ± 7.2	14.8 ± 2.0	4.3 ± 0.7	1.4 ± 0.3
Non-prompt	75 ± 21	28.8 ± 8.6	5.8 ± 2.5	$0.5^{+0.8}_{-0.5}$	$0.0^{+0.2}_{-0.0}$
Charge flips & conversions	170 ± 33	91 ± 16	22.1 ± 4.4	8.0 ± 1.7	3.4 ± 0.8
Total	346 ± 44	176 ± 21	42.8 ± 5.7	12.8 ± 2.1	4.8 ± 0.9
Data	329	171	38	10	3

Table B.1: Expected and observed numbers of $e^{\pm}e^{\pm}$ pairs for different lower bounds on the dilepton invariant mass. The uncertainties shown are the quadratic sum of the statistical and systematic uncertainties.

invariant mass for positively-charged and negatively-charged pairs. No significant excess is observed in data compared to the Standard Model background prediction for either of the final states.

The observed number of like-sign lepton pairs in data is compared to the background expectation in Tables B.1 and B.2. The yields are listed for five ranges of invariant mass, defined by a lower bound on the mass, ranging from 15 GeV to 400 GeV. For $e^{\pm}e^{\pm}$ ($e^{\pm}\mu^{\pm}$) pairs, the background from prompt lepton sources is about 30% (50%) in all mass bins. For $e^{\pm}e^{\pm}$ pairs, the largest source of background is due to charge flip and photon conversions. For $e^{\pm}\mu^{\pm}$ pairs, the charge-flip background and the non-prompt background are comparable. The combined background uncertainty on $e^{\pm}e^{\pm}$ pairs ranges from 13% for $m(e^{\pm}e^{\pm}) > 15$ GeV to about 19% for $m(e^{\pm}e^{\pm}) > 400$ GeV. For the same lower invariant mass bounds, the uncertainty ranges from 11% to 20% for $e^{\pm}\mu^{\pm}$ pairs. No indications of physics from non-SM sources contributing to the final state is observed. On the contrary, the observation is in agreement with the background estimate in all mass bins within the statistical and systematic uncertainties.

Table B.3 shows the data compared to the background expectation separately for positively and negatively-charged lepton pairs for the ee and $e\mu$ final states. Again, no significant excess is observed in data compared to the background estimate.

The observed data yields are used to derive upper limits on the number of $e^{\pm}e^{\pm}$ and $e^{\pm}\mu^{\pm}$ pairs from non-SM sources. These limits are then translated to upper limits at 95% CL on the fiducial cross section for such production. The fiducial efficiency is determined similarly as for $\mu^{\pm}\mu^{\pm}$, and is 43% for $e^{\pm}e^{\pm}$ and 55% for $e^{\pm}\mu^{\pm}$. The resulting fiducial cross-section limits are given in Table B.5.

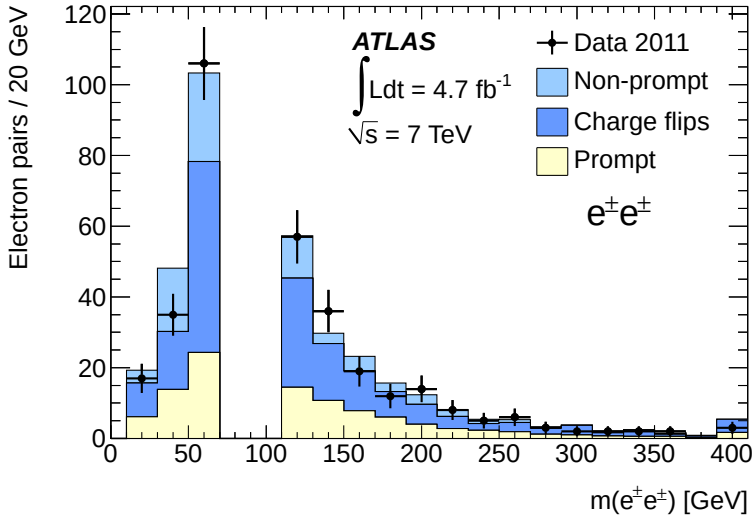

(a)

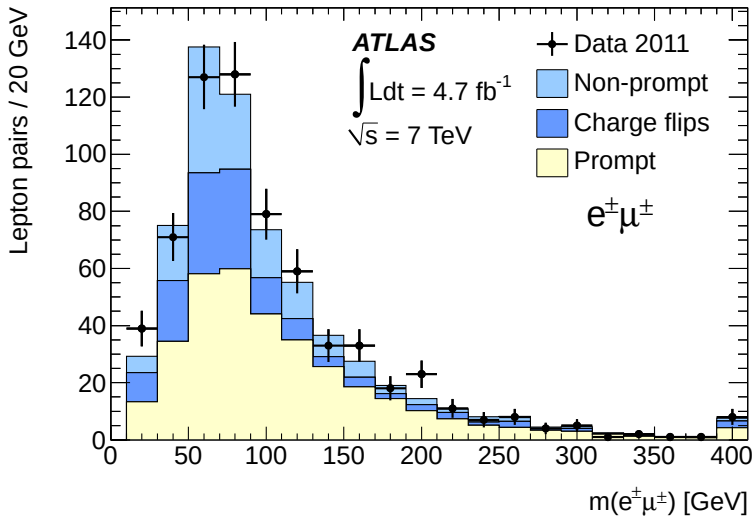

(b)

Figure B.1: Distribution of the like-sign dilepton invariant mass for (a) $e^{\pm}e^{\pm}$ and (b) $e^{\pm}\mu^{\pm}$ pairs passing the full event selection. The last bin is an overflow bin.

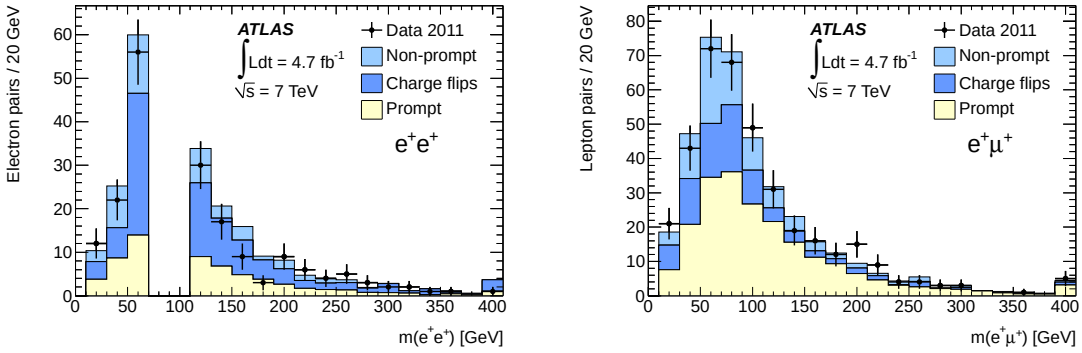

(a) (b)

Figure B.2: Distribution of the like-sign dilepton invariant mass for (a) e^+e^+ and (b) $e^+\mu^+$ pairs passing the full event selection. The last bin is an overflow bin.

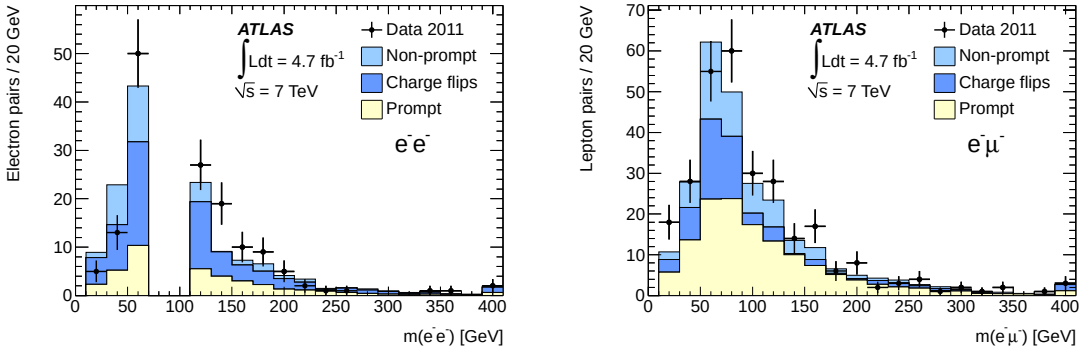

(a) (b)

Figure B.3: Distribution of the like-sign dilepton invariant mass for (a) e^-e^- and (b) $e^-\mu^-$ pairs passing the full event selection. The last bin is an overflow bin.

Sample	Number of pairs with $m(e^{\pm}\mu^{\pm})$				
	> 15 GeV	> 100 GeV	> 200 GeV	> 300 GeV	> 400 GeV
Prompt	346 ± 43	157 ± 20	36.6 ± 4.7	10.8 ± 1.5	3.9 ± 0.6
Non-prompt	151 ± 47	45 ± 13	9.2 ± 4.1	2.6 ± 1.1	1.0 ± 0.6
Charge flips & conversions	142 ± 28	33 ± 7	10.5 ± 2.8	2.9 ± 1.2	2.2 ± 1.1
Total	639 ± 71	235 ± 25	56.4 ± 7.0	16.3 ± 2.3	7.0 ± 1.4
Data	658	259	61	17	7

Table B.2: Expected and observed numbers of $e^{\pm}\mu^{\pm}$ pairs for different lower bounds on the dilepton invariant mass. The uncertainties shown are the quadratic sum of the statistical and systematic uncertainties.

Sample	Number of pairs with $m(\ell^{\pm}\ell^{\pm})$				
	> 15 GeV	> 100 GeV	> 200 GeV	> 300 GeV	> 400 GeV
	e^+e^+ pairs				
Background	208 ± 28	112 ± 14	28.6 ± 4.0	8.5 ± 1.4	3.3 ± 0.7
Data	183	93	26	6	1
	e^-e^- pairs				
Background	138 ± 21	63.3 ± 8.5	14.2 ± 2.3	4.4 ± 0.8	$1.54^{+0.4}_{-0.3}$
Data	146	78	12	4	2
	$e^+\mu^+$ pairs				
Background	381 ± 42	142 ± 15	33.8 ± 5.3	9.8 ± 1.5	4.2 ± 0.9
Data	375	149	39	9	4
	$e^-\mu^-$ pairs				
Background	259 ± 31	93 ± 10	22.6 ± 3.0	6.5 ± 1.3	2.9 ± 1.0
Data	283	110	22	8	3

Table B.3: Expected and observed numbers of positively and negatively-charged $e^{\pm}e^{\pm}$ and $e^{\pm}\mu^{\pm}$ pairs for different lower bounds on the dilepton invariant mass. The uncertainties shown are the quadratic sum of the statistical and systematic uncertainties.

Mass range	95% CL upper limit [fb]					
	expected	observed	expected	observed	expected	observed
	$e^{\pm}e^{\pm}$		$e^{+}e^{+}$		$e^{-}e^{-}$	
$m > 15$ GeV	46^{+15}_{-12}	42	$29.1^{+10.2}_{-8.6}$	22.8	$23.2^{+8.6}_{-5.8}$	25.7
$m > 100$ GeV	$24.1^{+8.9}_{-6.2}$	23.4	$16.1^{+5.9}_{-4.3}$	12.0	$12.0^{+5.3}_{-2.8}$	18.7
$m > 200$ GeV	$8.8^{+3.4}_{-2.1}$	7.5	$7.0^{+2.9}_{-2.2}$	6.1	$4.9^{+1.9}_{-1.2}$	4.0
$m > 300$ GeV	$4.5^{+1.8}_{-1.3}$	3.9	$3.7^{+1.4}_{-1.0}$	2.9	$2.9^{+1.0}_{-0.6}$	2.7
$m > 400$ GeV	$2.9^{+1.1}_{-0.8}$	2.4	$2.3^{+1.1}_{-0.6}$	1.7	$1.8^{+0.8}_{-0.4}$	2.3

Table B.4: Upper limits at 95% CL on the fiducial cross section for ee pairs from non-SM processes. The expected limits and their 1σ uncertainties are given, as well as the observed limits in data.

Mass range	95% CL upper limit [fb]					
	expected	observed	expected	observed	expected	observed
	$e^{\pm}\mu^{\pm}$		$e^{+}\mu^{+}$		$e^{-}\mu^{-}$	
$m > 15$ GeV	56^{+23}_{-15}	64	$34.9^{+12.2}_{-8.6}$	34.1	$26.2^{+10.6}_{-7.6}$	34.4
$m > 100$ GeV	$23.0^{+9.1}_{-6.7}$	31.2	$15.4^{+5.9}_{-4.1}$	18.0	$11.5^{+4.2}_{-3.5}$	16.9
$m > 200$ GeV	$8.4^{+3.4}_{-1.7}$	9.8	$6.6^{+3.5}_{-1.8}$	8.8	$4.6^{+2.1}_{-1.2}$	4.5
$m > 300$ GeV	$4.1^{+1.8}_{-0.9}$	4.6	$3.2^{+1.2}_{-0.9}$	3.2	$2.7^{+1.1}_{-0.6}$	3.5
$m > 400$ GeV	$3.0^{+1.0}_{-0.8}$	3.1	$2.4^{+0.9}_{-0.6}$	2.5	$2.3^{+0.8}_{-0.5}$	2.5

Table B.5: Upper limits at 95% CL on the fiducial cross section for $e\mu$ pairs from non-SM processes. The expected limits and their 1σ uncertainties are given, as well as the observed limits in data.

Results of the Narrow $e^{\pm}e^{\pm}$ or $e^{\pm}\mu^{\pm}$ Resonance Search

For the like-sign narrow resonance search, mass bins in which the search is performed are derived by optimizing the expected signal significance. The mass bins are defined differently for the $e^{\pm}e^{\pm}$ channel due to the improved momentum resolution compared to muons at high invariant mass. As an example, Figure B.5 shows the reconstructed dilepton invariant mass distribution for a 300 GeV $H^{\pm\pm}$ boson, decaying to pairs of electrons or muons.

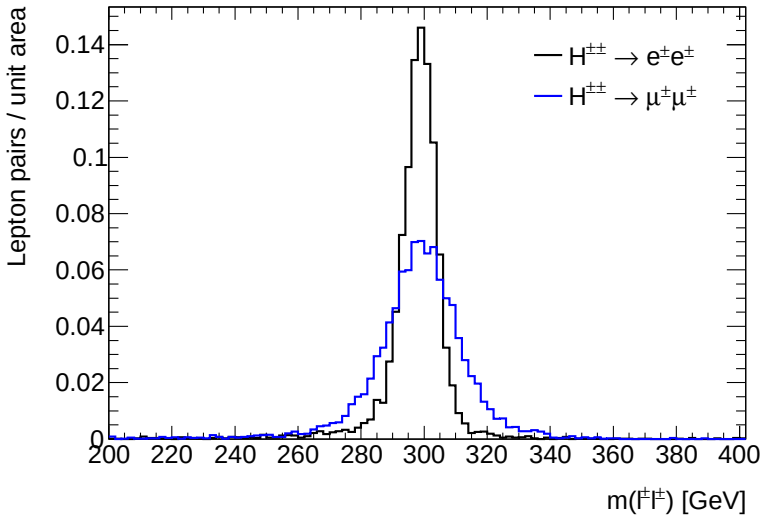

Figure B.4: Simulated invariant mass distribution for a 300 GeV $H^{\pm\pm}$ boson, decaying to pairs of electrons or pairs of muons. Both distributions are normalized to unity.

For the $e^{\pm}e^{\pm}$ final state, lepton pairs are selected with a mass within $\pm 4\%$ of the test $H^{\pm\pm}$ boson mass. For the $e^{\pm}\mu^{\pm}$ final state, the same mass binning is used as for the $\mu^{\pm}\mu^{\pm}$ channel, $\pm[0.06 \times m(H^{\pm\pm}) + 0.7 \cdot 10^{-4} \times m(H^{\pm\pm})^2]$. The acceptance times efficiency for reconstructing a $H^{\pm\pm}$ boson in these mass windows is about 27% (36%) for $e^{\pm}e^{\pm}$ ($e^{\pm}\mu^{\pm}$) for $m(H^{\pm\pm}) = 100$ GeV, and about 50% for $m(H^{\pm\pm}) = 400$ GeV for both final states. The acceptance times efficiency for all three final states is illustrated in Figure B.5.

The observation in data is compared to the background prediction in the narrow dilepton mass bins. No significant discrepancies are observed. The predicted and observed invariant mass distributions are shown in Figure B.6, along with the expected contributions for $H^{\pm\pm}$ bosons at various masses with 100% branching ratio to each decay channel.

The data observation is used to derive constraints on the pair-production cross section of doubly charged Higgs bosons decaying to $e^{\pm}e^{\pm}$ and $e^{\pm}\mu^{\pm}$. The expected

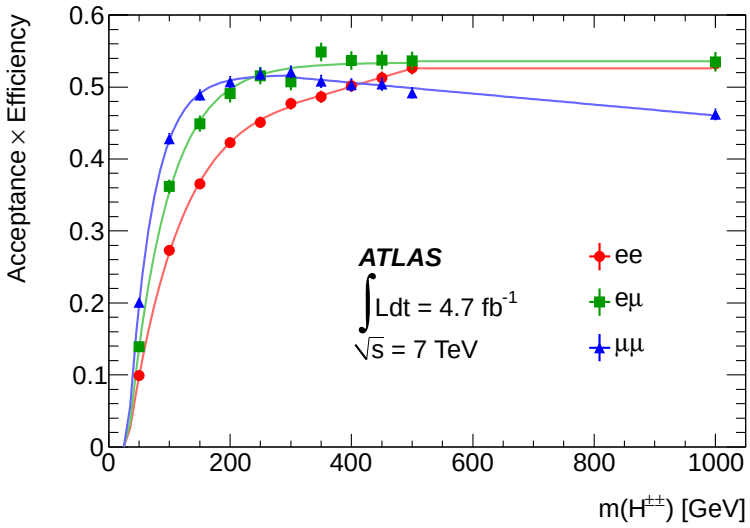

Figure B.5: Total acceptance times efficiency vs simulated $H^{\pm\pm}$ mass for the $e^{\pm}e^{\pm}$, $e^{\pm}\mu^{\pm}$, and $\mu^{\pm}\mu^{\pm}$ channels, fitted with piecewise empirical functions used for interpolation.

and observed upper limits at 95% CL on the cross section times branching ratio as function of the $H^{\pm\pm}$ boson mass are shown in Figure B.7.

By comparing the cross-section limit with the theoretical production cross section, constraints are derived on the mass of doubly charged Higgs bosons. Assuming pair-production and a branching ratio to $e^{\pm}e^{\pm}$ ($e^{\pm}\mu^{\pm}$) of 100%, doubly charged Higgs bosons which couple to left-handed and right-handed fermions are excluded for masses below 409 GeV (375 GeV) and 322 GeV (310 GeV), respectively. Mass limits assuming branching ratios of 100%, 33%, 22%, and 11% are shown in Table B.6. The mass limits are also derived as function of the branching ratio, shown in Figure B.8.

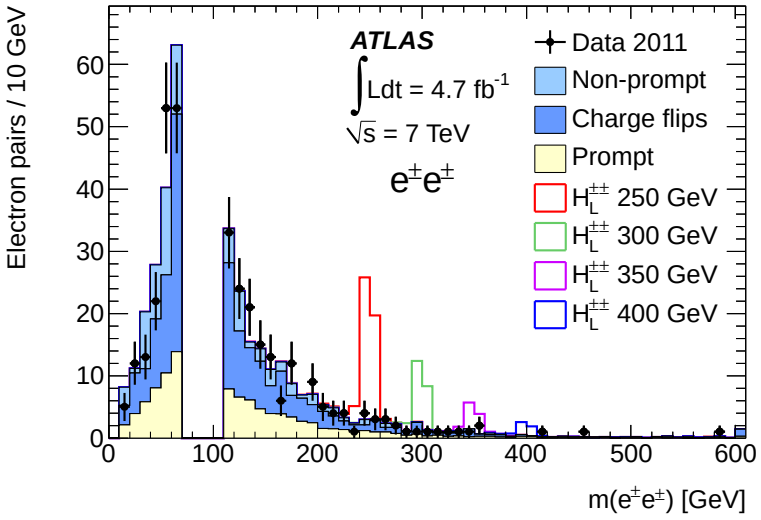

(a)

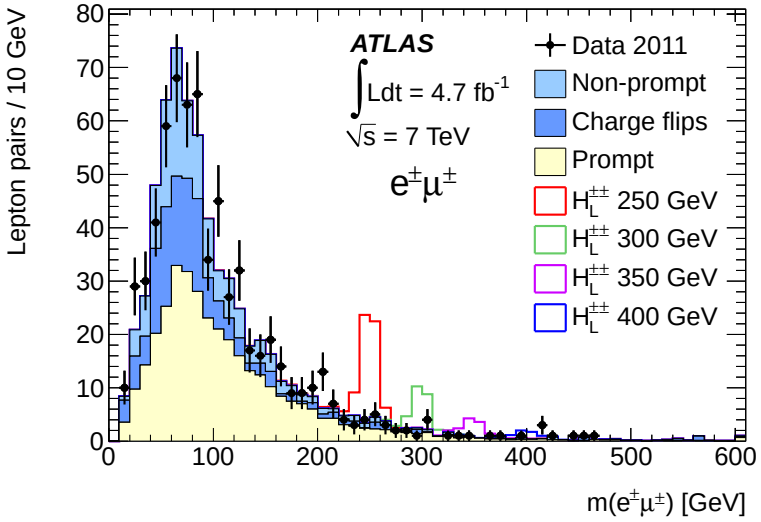

(b)

Figure B.6: Invariant mass distributions for data and background for (a) $e^{\pm}e^{\pm}$ pairs and (b) $e^{\pm}\mu^{\pm}$ pairs. The open histograms show the expected signal from simulated $H^{\pm\pm}$ samples, assuming a 100% branching ratio to the decay channel in question. The last bin is an overflow bin.

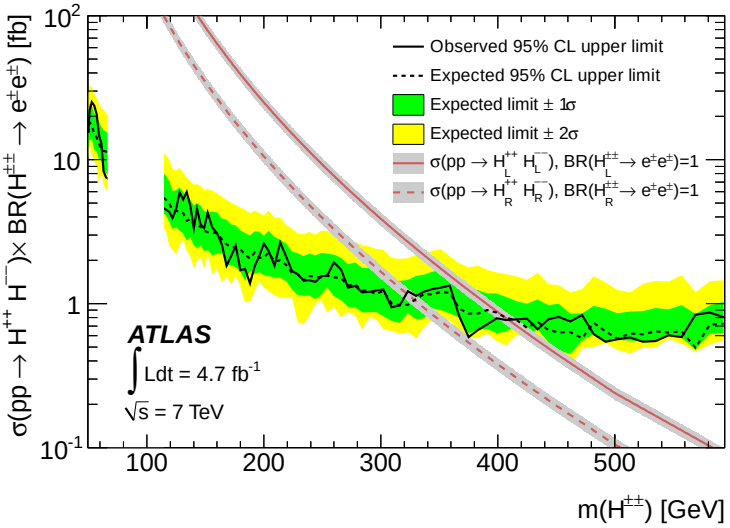

(a)

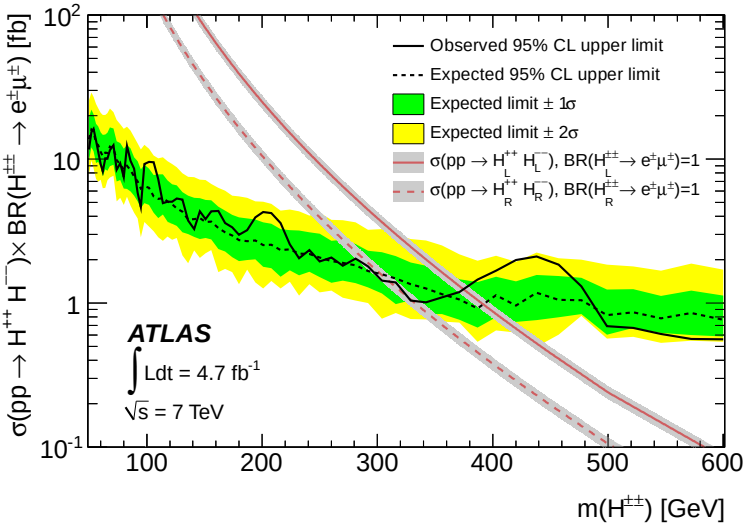

(b)

Figure B.7: Upper limit at 95% CL on the cross section times branching ratio for pair production of $H^{\pm\pm}$ bosons decaying to (a) $e^{\pm}e^{\pm}$ and (b) $e^{\pm}\mu^{\pm}$ pairs. The observed and median expected limits are shown along with the 1σ and 2σ variations in the expected limits. In the range $70 < m(H^{\pm\pm}) < 110$ GeV, no limit is set in the $e^{\pm}e^{\pm}$ channel. Also shown are the theoretical predictions at next-to-leading order for the pair-production cross section for $H_L^{\pm\pm}$ and $H_R^{\pm\pm}$ bosons.

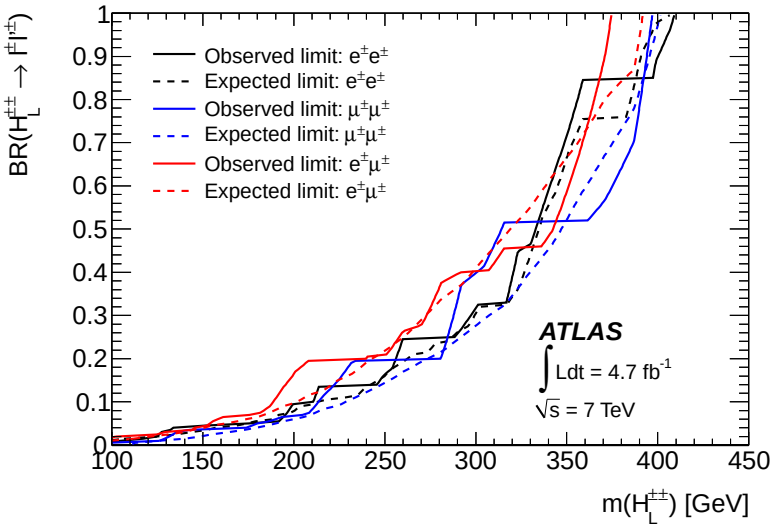

(a)

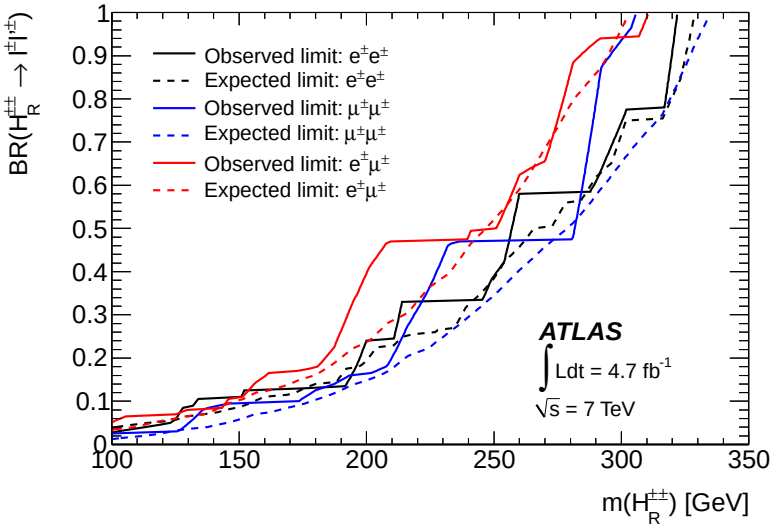

(b)

Figure B.8: Mass limits as function of branching ratio for (a) $H_L^{\pm\pm}$ and (b) $H_R^{\pm\pm}$ bosons decaying to $e^{\pm}e^{\pm}$ or $e^{\pm}\mu^{\pm}$ pairs. For comparison, the mass limits for $H^{\pm\pm}$ bosons decaying to $\mu^{\pm}\mu^{\pm}$ are shown as well. The regions *above* the solid (observed limit) and dashed (expected limit) lines are excluded.

BR($H_L^{\pm\pm} \to \ell^\pm \ell'^\pm$)	95% CL lower limit on $m(H_L^{\pm\pm})$ [GeV]			
	$e^\pm e^\pm$		$e^\pm \mu^\pm$	
	expected	observed	expected	observed
100%	407	409	392	375
33%	318	317	279	276
22%	274	258	250	253
11%	228	212	206	190
BR($H_R^{\pm\pm} \to \ell^\pm \ell'^\pm$)	95% CL lower limit on $m(H_R^{\pm\pm})$ [GeV]			
	$e^\pm e^\pm$		$e^\pm \mu^\pm$	
	expected	observed	expected	observed
100%	329	322	303	310
33%	241	214	220	195
22%	203	199	194	187
11%	160	151	153	151

Table B.6: Lower mass limits at 95% CL on $H^{\pm\pm}$ bosons decaying to $e^\pm e^\pm$ or $e^\pm \mu^\pm$ pairs. Mass limits are derived assuming a branching ratio of 100%, 33%, 22%, or 11%. Both the expected and observed limits are given.

Conclusions

Searches for anomalous production of prompt $e^{\pm}e^{\pm}$ and $e^{\pm}\mu^{\pm}$ production have been performed together with the like-sign dimuon search presented in this dissertation. The electron-based final states have a slight advantage at high mass in searches for a narrow resonance as the mass resolution is better. However, the background to these final states is larger as a consequence of the additional large background due to charge misidentification or photon conversions. Additionally the background is larger in the $e^{\pm}\mu^{\pm}$ final state due to higher prompt background (a phase space factor of two). The inclusive search is thus more sensitive in the like-sign dimuon channel, although, of course, searches in the electron-based channels are as important.